From Femtoseconds to Nanoseconds: Simulation of IBr^- Photodissociation Dynamics in CO_2 Clusters

by

Matthew Alan Thompson

B.A., The Colorado College, 1999

A thesis submitted to the

Faculty of the Graduate School of the

University of Colorado in partial fulfillment

of the requirements for the degree of

Doctor of Philosophy

Department of Chemistry and Biochemistry

2007

This thesis entitled:
From Femtoseconds to Nanoseconds: Simulation of IBr^- Photodissociation Dynamics in CO_2 Clusters
written by Matthew Alan Thompson
has been approved for the Department of Chemistry and Biochemistry

Robert Parson

W. Carl Lineberger

Date

The final copy of this thesis has been examined by the signatories, and we find that both the content and the form meet acceptable presentation standards of scholarly work in the above mentioned discipline.

Thompson, Matthew Alan (Ph.D., Chemistry)

From Femtoseconds to Nanoseconds: Simulation of IBr^- Photodissociation Dynamics in CO_2 Clusters

Thesis directed by Professor Robert Parson

Potential energy curves for the ground and five valence excited states of IBr^- were calculated at the MRCI level using the MOLPRO ab initio package. The Stuttgart large-core MDF ECP was used with an augmented basis set and spin-orbit coupling was calculated via the accompanying spin-orbit ECP. Charge densities, transition moments, and nonadiabatic coupling matrix elements constructed from a distributed multipole analysis of the ab initio wavefunctions were then used to carry out molecular dynamics simulations of the photodissociation of IBr^- in CO_2 clusters with nonadiabatic transitions treated by Tully's fewest-switches surface hopping. Simulations of near-infrared (790-nm) photodissociation show good agreement with experimental product branching ratios. Experimental pump-probe studies have demonstrated a large variation in ground-state recombination times with cluster size—orders of magnitude—which is supported by our simulations. We propose a mechanism of excited-state trapping and a solvent-mediated configurational transition state which leads to similar simulated recombination times on the order of 10-20 ps for a cluster size of 5 solvent molecules, and up to 1-3 ns for sizes of 8 to 10. Simulations have predicted a turnaround in recombination times at larger clusters, a finding which is supported by recent experimental investigations. We also predict that a cluster size of 14 solvent molecules leads to double timescale recombination—picoseconds and nanoseconds—involving a different, excited-state well. Simulations of ultraviolet (355-nm) photodissociation were also carried out. These gave worse agreement, probably due to the larger amounts of kinetic energy release associated with this excitation, and to the absence of a spin-orbit quenching process, thought to be relevant in experiment, from the model.

Dedication

To my grandmother, Ina Thompson, who died before she could see me complete this journey.

Acknowledgements

There have been many people who have helped me on the journey to complete my studies.

First and foremost among these is my adviser, Professor Robert Parson. Under his tutelage I have learned more than I ever thought I would about molecular dynamics, chemistry, and research in general. While I'll never equal his vast knowledge, or his ability to construct Marcus diagrams and picture the movement of excited states, he has helped me be able to at least understand why such a thing is useful. He has given me the ability to research and in the end that is the point of this. Plus, he paid for a lot of this and that's not unimportant either.

Beyond him, I'd like to thank the former members of the Parson group I had the pleasure to interact with either in person or via email. Dr Nikki Delaney was there in the beginning to help shepherd me from grad student who was taking classes to grad student who was doing research. I thank Joseph Fowler for his introduction into the world of quantum chemistry, electronic structure, the programs that do it all, and Linux. Dr James Faeder I thank for his amazing and immense molecular dynamics program that became the boon and bane of my existence these many years. Likewise, in the beginning he was there to answer my many nags about "what does this output mean", or "why does this program hate me". Finally, Prof. Paul Maslen who, besides his knowledge and hard work that went into our molecular dynamics program, provided me with discussions on the nature of his hacks and edits of the MOLPRO quantum chemistry program.

Any theory in chemistry is only as good as the experiments it models and any theoretician is only as good as the experimentalists he interacts with. To that end, I'd like to thank the many

experimentalists in the Lineberger group that have helped explain to me—slowly and patiently—how their experiments worked and why it was my fault my simulations weren't matching with reality. Among these people are Dr Todd Sanford, Dr Jack Barbera, and Joshua Martin, all of whom have variously headed the $IBr^-(CO_2)_n$ fun machine as grad students. Also, I thank the postdocs Drs Vladimir Dribinski, Han Sang Yun, Jeff Rathbone, and Joshua Darr. Also, thanks to Elisa Miller and Dr Lenny Sheps for discussions about IBr^- and photoelectron imaging.

Of course, no mention of the Lineberger group is complete without mention of Professor Lineberger himself. For a man with his many responsibilities, he always seemed ready to discuss various things I saw in my research as well as suggest various simulations I could attempt to reconcile the inevitable theory-experiment discrepancies.

All of this research would not have been possible with out the amazing support staff here at JILA. Foremost among them is Peter Ruprecht who helped me from barely an end-user of Linux to someone who can roll a Linux or Unix box in an afternoon and have it work. In addition, there are the others in the computing department who helped solve the varied questions and problems I had over the years: James McKown, Mark Tamisiea, Alan Dunwell, Nick Metrowsky, Joel Frahm and many more. I also take this time to thank Professor John Bohn and the W. M. Keck Foundation for the use of the Keck cluster here at JILA. I don't think I can figure out how much longer it would have taken me to do the research in this dissertation without it.

I also have to thank Professor Hermann Stoll for his discussions concerning his MDF ECP and basis set which were the cornerstone of a chapter's worth of work. I'd also like to thank the masses of the MOLPRO and GAMESS mailing lists who suffered through my many obvious questions about the programs and their use and interpretation as I was learning.

The fact that I am in grad school right now is due to the many great teachers I have had in my life. As an undergrad, Professors Sally Meyer and Ted Lindeman gave me my first exposures to the world of research, and taught me my foundations of whatever physical chemistry I now know. I also thank Professor Lindeman for showing me all the cool things you can see an do in physical chemistry. I'd also like to thank the Barnes Foundation. Their scholarship was the

only reason I could ever afford to go to a great school like Colorado College.

Before CC and CU, though, there was my first exposure to chemistry. This was due to Dr Bindel and Mr Smiley of Pomona High School. Their infectious enthusiasm for chemistry and science in general was the first step on the path that has led to this moment.

Finally, I'd like to thank my family. Without the support of my mother, father, grandmother, and sister, I probably would never have been able to complete this. Many was the day that I complained to them of some various problem that research, life, the weather, whatever, was causing me, and they took it all in stride and helped keep me sane.

Contents

Chapter

Tables

Table

Figures

Figure

Chapter 1

Introduction

One of the major challenges of physical chemistry—indeed, chemistry as a whole—is to study the effects of solvation on chemical reactions. From the use of a single water molecule to catalyze a reaction to biochemistry, solvation is a basic process whose effects can alter the progress of a reaction. By altering the local environment around a reacting species, solvent can profoundly influence the the course of a reaction. The solvent's effect can be straightforward, such as providing a mechanical block that prevents dissociation, or absorbing the energy released in a reaction into its internal vibrations. At a deeper level, a solvent can perturb the energetics of the reactants, opening up new and interesting dynamics. In this work, we will explore one corner of this vast universe of study: the effects of a solvent on photodissociation of gas-phase clusters. The use of clusters as a way to study condensed-phase solvation dynamics in a microscopic manner is a field with a long and successful history [1, 2]. By avoiding the "averaging" effects which are inherent in the simulation of a reaction in, say, liquid solvent, we are able to explore the solvent's effect in a more detailed manner. We can build a cluster, solvent molecule by molecule, and see how each affects a chemical process.

1.1 Studies of Solvent Effects in I_2 Photodissociation

The study of solvent effects in photodissociation reactions began with the work of Franck and Rabinowitch [3]. In their seminal work, they studied the photodissociation of I_2 in liquid and found that recombination could occur. They attributed this phenomenon to the so-called "cage

effect" due to the collisions of the chromophore with the solvent molecules. Work by Noyes and coworkers [4–7] further explored this phenomenon by determining how altering the photon energy or solvent characteristics affected the caging of the solute. The first time-resolved experiments by Eisenthal [8] of I_2 in carbon tetrachloride and hexadecane determined that the recombination of I_2 was a solvent-dependant process which occurred on the time scale of hundreds of picoseconds.

Modeling of the recombination dynamics by Nesbitt and Hynes [9] in 1982, however, showed that this time scale more accurately accounted for the vibrational relaxation of I_2. Instead, the accepted view [10] from later experiments and theory is that caging and electronic relaxation occurs on time scales of a single picosecond with vibrational relaxation of the chromophore and its interaction with the solvent being responsible for the slower recovery. This demonstrated the need for experiment to be complemented by theory in order to correctly interpret results.

1.2 Studies of Solvent Effects in Dihalide Anion Photodissociation

In the late 1980s, the Lineberger group began a series of studies of dihalide **anion** photodissociation in solvated clusters [11–13]. While the use of a charged solute is useful in that solute-solvent interactions are enhanced, the primary benefit was more practical. By using charged species, the Lineberger group was able to use mass spectrometry to select clusters for study by their size. Thus, the effect of one or two solvent molecules on the photodissociation could be compared to that of tens of solvent molecules. By using size-selected clusters, the experiments could build a more detailed, microscopic picture of the effect of solvent on the solute.

The Lineberger group first began their studies of size-selected clusters with the near-infrared photodissociation of $Br_2^-(CO_2)_n$ and $I_2^-(CO_2)_n$ [12, 14]. In these experiments, a near-infrared photon (720-790 nm) excited the cluster to the repulsive A' state (seen in Figure 1.1(a) for I_2^-) and the resulting dissociated and recombined product ratios were determined. It was found that the caging fraction, the number of products which recombined instead of dissociating,

was a strong function of the number of solvent molecules. By the completion of a full shell of solvent, the caging efficiency was 100% [11–14]. This is in contrast to I_2 in liquid where up to 90% of the solute dissociates in some solvents [10]. Thus, the long-range solute-solvent electrostatic forces in this charged system was able to greatly enhance caging, effects also seen in studies of I_2^- in Ar [15, 16], N_2O [17], and OCS [18–20] as the solvent. In this overview, we will focus mainly on $I_2^-(CO_2)_n$, with brief mentions of I_2^- in argon, as these were the systems modeled by the Parson group.

The first simulations of dihalide anion clusters to include the excited state dynamics in any form were undertaken by Perera and Amar [21, 22] who studied Br_2^- in argon and CO_2. In their model they included only two states where nonadiabatic transitions were included, ad hoc, at long bond lengths and they modeled charge flow by allowing the charge of the resulting dissociating molecule to randomly build to -1 on either the solvated or unsolvated bromine. In the end, they found they needed to include both dissociation possibilities (charge-solvated and -unsolvated) in order to compare to the experimental results.

In the late 1990s, simulation of $I_2^-(CO_2)_n$ bloomed with the independent development by Parson and coworkers [23–29] and Coker and coworkers [30–33] of a model that treated solvation effects in the ground and excited states in a consistent fashion. The difference in the two models are based on the effective Hamiltonian used to evaluate the interactions. Coker and coworkers used a Hamiltonian based on Last and George's Diatomics-in-Ionic-Systems model [34], an augmented form of Bader's Diatomics-in-Molecules method that allowed for polarization by charged atoms. The Parson group's Hamiltonian is based on the ab initio curves for the bare anion being studied [35–37]. The curves calculated by Maslen, Faeder, and Parson for I_2^- and ICl^-, shown in Figure 1.1, include all six spin-orbit states that describe the complete valence energetics. The one-electron density matrix is extracted from these calculations by way of transition distributed multipole analysis [38] which allows us to model the solute response to solvent effects with nonadiabatic transitions handled by Tully's surface-hopping method [39]. A brief description of this model is provided in Chapter 2 and can be found in greater detail in the

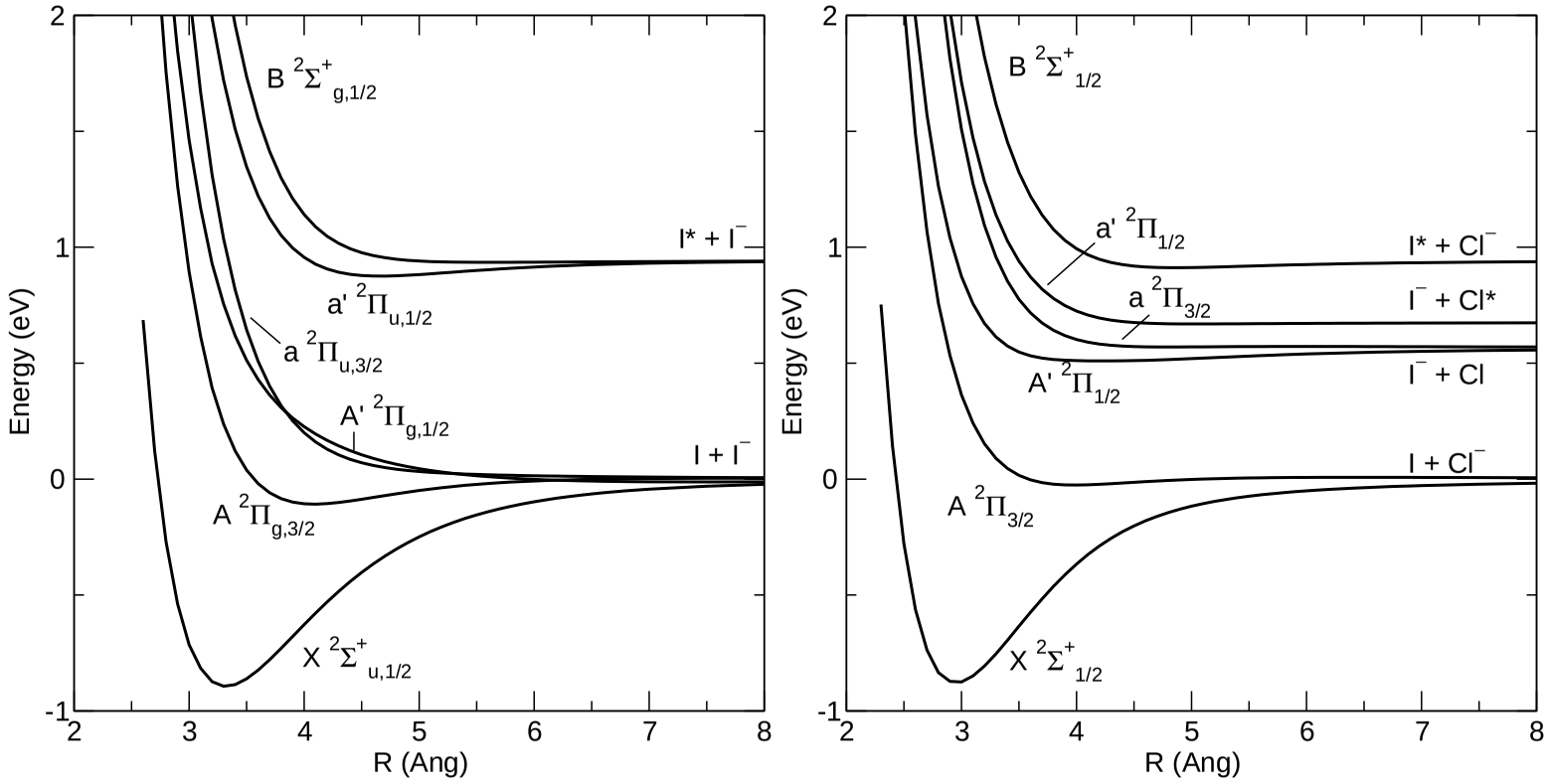

Figure 1.1: Potential energy curves for the six lowest spin-orbit states of (a) I_2^- and (b) ICl^- including spin-orbit coupling [35–37]. The Hund's case (a) labels used here are approximately valid near R_e.

appropriate publications [27, 37]. Section 2.2 will detail the construction of ab initio curves for IBr^- that are integrated into Maslen, Faeder, and Parson model for the simulations presented in this work.

Simulations of I_2^- near-infrared photodissociation in CO_2 and argon by Parson and coworkers have been quite successful in duplicating the photoproduct branching ratios. The simulations showed that the high caging efficiency seen in the experiments of $I_2^-(CO_2)_n$ is due to concerted charge and solvent flow in the clusters, all due to the perturbation of the solvent. For example, although the A' state in I_2^- is repulsive, see Figure 1.1(a), the inclusion of a single CO_2 solvent molecule makes the state no longer dissociative. Rather, nonadiabatic transitions to lower states are needed for both dissociation and recombination. In systems using argon as a solvent, the dissociated products often had a bimodal mass spectrum which the simulations reproduced. The simulations showed that this structure is due to argon's much weaker interaction with iodine compared to CO_2, that dissociation could occur on A' or after nonadiabatic transition to a lower state. The energy transferred to the solvent upon hopping to a lower state allowed more solvent to boil off of the cluster and led to two different fragment mass patterns.

The Lineberger group also carried out experiments of $I_2^-(CO_2)_n$ using ultraviolet excitation to the B state [18, 19]. It was found that ultraviolet photoexcitation of $I_2^-(CO_2)_n$ led to three product channels, a recombined product and two dissociation channels leading to I^- accompanied by both spin-orbit excited iodine neutrals and ground-state (quenched) neutrals. The experiments saw these two dissociation channels as a bimodal distribution in the mass distribution of the product anions after 7-8 solvent molecules were present. The higher mass fragments were accompanied by spin-orbit excited iodine neutral ($^2P_{1/2}$), while the lower mass products were accompanied by quenched ($^2P_{3/2}$) neutral. The recombined products were found to be strongly dependent on the number of solvent molecules, with 7-8 CO_2 needed before spin-orbit quenching could occur.

Parson and coworkers' simulations of the ultraviolet photodissociation of $I_2^-(CO_2)_n$ [40, 41] quite nicely reproduced the findings of experiment and confirmed that the bimodal distri-

bution was indeed a signature of the two I^- channels. Likewise, the recombination channel was found to be quite efficient at higher masses. In fact, the simulations preceded experiment and predicted the onset of the extensive spin-orbit quenching. Beyond just good agreement in photoproduct branching ratios, the simulations were able to provide a mechanism for the onset of the spin-orbit quenching in $I_2^-(CO_2)_n$: solvent-mediated charge transfer. It was found that when the clusters had 8-9 CO_2 molecules, the solvent asymmetry in the cluster was large enough to overcome the 0.94 eV spin-orbit splitting before the I-I bond grew too large for the accompanying charge transfer to not occur. An extension of a Marcus parabola model derived from the theory of electron transfer in solution [42], first used to help explain the near-infrared simulations, provided an additional visual explanation why large solvent asymmetries were necessary for spin-orbit quenching to begin in $I_2^-(CO_2)_n$.

Dihalide anion systems have also been studied by the Lineberger group in the time-domain using an near-infrared photon to begin dissociation and then a second pulse to probe the recombination dynamics as the cluster begins to reform [16, 43–48]. It was found that the absorption recovery occurred on a 10-20 ps time scale, a finding also supported by experiment of I_2^- in various liquids by Barbara and coworkers [49–52]. One odd feature of the recovery experiments was the appearance of a peak at 2 ps, much faster than the overall recovery signal. While this was first attributed to recombination on the A state, the simulations on the ultraviolet photodissociation of $I_2^-(CO_2)_n$, vide infra, were able to provide the correct mechanism.

Similarly, the Neumark group has carried out many photoelectron spectroscopy experiments of I_2^- [53–74] where after the pump pulse to begin dissociation of I_2^-, an ultraviolet photon detaches the electron. The excess electron kinetic energy is monitored against the pump-probe delay which allows for complementary dynamical information to the absorption recovery experiments. Their experiments on $I_2^-(CO_2)_n$ [58, 65, 67, 69, 71] also confirm the 10-20 ps recovery times.

Parson and coworkers have also modeled the absorption recovery for near-infrared photoexcitation of I_2^- [23, 75] as well as the time-resolved photoelectron spectrum [25] with success.

The experimental and simulated findings that spin-orbit quenching in $I_2^-(CO_2)_n$ is very efficient helped to explain a minor mystery in the Lineberger group's study of the 720-nm pump/720-nm probe absorption recovery dynamics [44,45,47]. This mystery involved the assignment of a peak at 2 picoseconds in the otherwise much longer recombination of $I_2^-(CO_2)_n$. It was originally attributed to passage of recombining clusters in strong absorption regions in an excited state, namely $a \leftarrow A$ transitions near the repulsive wall, a mechanism similar to that seen in studies of I_2^- in liquids [49,50]. Instead, very large-scale simulations [75] found that the 2-ps peak was caused by probe absorption of recombining trajectories from the ground X state at long bond length ($R_{I-I} > 3.7$ Å) to the spin-orbit excited B and a' states. The efficient spin-orbit quenching in $I_2^-(CO_2)_n$ then allows for the experimentally seen two-photon fragments. The belief that spin-orbit quenching in $I_2^-(CO_2)_n$ would be inefficient led to the dismissal of this mechanism in the earlier experimental work [45, 47]. This success of the molecular dynamics simulations to help explain puzzling recombination dynamics presages findings in this thesis where simulations of $IBr^-(CO_2)_n$ ground-state recombination are able to explain surprising experimental results.

Less well understood than $I_2^-(CO_2)_n$ are the dynamics of $ICl^-(CO_2)_n$ clusters. With the breaking of the solute symmetry by using a heteronuclear chromophore, mass spectrometry can now distinguish two dissociated products, I^- and Cl^-, along with recombined ICl^-, see Figure 1.1(b). Both near-infrared and ultraviolet photodissociation experiments carried out by the Lineberger group [46, 76, 77] show that once again the solvent has a strong effect on the recombination and spin-orbit relaxation dynamics.

Compared to $I_2^-(CO_2)_n$, the dynamics of $ICl^-(CO_2)_n$ demonstrate different behavior. Recombined ICl^- products are seen in clusters as small as one solvent molecule and peaking at $ICl^-(CO_2)_5$. With larger clusters, though, ICl^--based product rapidly decreases and dissociated Cl^- product becomes dominant and the sole product channel open with a full solvent shell. Simulations by Faeder and Parson group [37] have shown that this large-cluster Cl^- product is actually produced adiabatically with spin-orbit excited iodine. Unfortunately, this large cluster behavior along with a low two-photon absorption cross-section for $ICl^-(CO_2)_n$ has made time-

resolved studies of recombination dynamics problematic. We hope, however, that the research presented in this thesis will be able to shed light on the less-understood $ICl^-(CO_2)_n$ dynamics.

1.3 Dissertation Overview

It was hoped that IBr^- could provide a bridge between the well understood dynamics of homonuclear $I_2^-(CO_2)_n$ and the less successful partnership of modeling and experiment in heteronuclear $ICl^-(CO_2)_n$. The studies of $ICl^-(CO_2)_n$ provided glimpses that suggest that breaking the solute symmetry could lead to new and interesting solvation dynamics. But the large difference in the solvation characteristics of iodine and chlorine has made interpretation of the simulations with respect to experiment difficult. The study of $IBr^-(CO_2)_n$ could therefore provide a gentler system to study solvation dynamics in an asymmetric solute.

This dissertation hopes to show that this was indeed the case. In Chapter 2, we will introduce the background of the simulations of $IBr^-(CO_2)_n$ photodissociation presented herein. We will begin with a brief overview of the molecular dynamics method we use for our simulations. Then, we will present the results of quantum chemistry calculations on the six lowest spin-orbit states of IBr^- which provide our molecular dynamics program with the necessary input to perform the nonadiabatic molecular dynamics. We will use this new data, along with Lennard-Jones parameters determined for the $Br\cdots CO_2$ interaction, to simulate the absorption spectra for IBr^- and compare it to experiment. We will also explore the properties of minimum energy clusters for $IBr^-(CO_2)_n$ and $Br^-(CO_2)_n$ and how the gradual build-up of solvent affects the energetics of these systems.

In Chapter 3, we will present the findings of our simulations of near-infrared (790-nm) photodissociation product branching ratios of $IBr^-(CO_2)_n$ in comparison to experiment [78,79]. We will see that while 50-ps long simulations (a time scale commonly used in previous simulations) seemed to provide a good agreement with experiment, they actually obscured interesting behavior. We will see that after 50 ps, clusters like $IBr^-(CO_2)_8$ were in fact trapped on an excited state. We will use extrapolations of long-time simulations performed for later work to

show the correct long-time branching ratios for our simulations. We will also examine the sensitivity of our photoproduct ratios to photoexcitation wavelength and Lennard-Jones short-range parameters.

One of the main reasons that $IBr^-(CO_2)_n$ was selected for study after $ICl^-(CO_2)_n$ was that it was hoped that time-resolved experiments could be carried out. The low absorption cross-section of $ICl^-(CO_2)_n$ in the wavelengths available for femtosecond study had prevented a detailed study of the ground-state recombination dynamics of an asymmetric solute. However, when the first attempt was made to study the ground-state recombination dynamics of $IBr^-(CO_2)_8$, the first cluster which exhibits total recombination in the photoproduct studies, it was found that the recombination occurred on a time scale of nanoseconds [77,79], very different to the picosecond scale of $I_2^-(CO_2)_n$. Subsequent experiments [80] found that the ground-state recombination recovery times depend strongly upon the number of solute molecules, and in an unexpected fashion. The addition of two solvent molecules, from $IBr^-(CO_2)_6$ to $IBr^-(CO_2)_8$, increases the recovery time by two orders of magnitude. In Chapter 4, we will present a survey of simulated results which attempts to explain the large effects of the solvent on the ground-state recombination dynamics. With these simulations, we extend our group's success in using our model to help explain puzzling results in experiments, as seen with the 2-ps peak in the $I_2^-(CO_2)_n$ time-resolved studies [75]. We will also present simulations on larger $IBr^-(CO_2)_n$ clusters which predict a turnaround in recovery times from the nanosecond scale of $IBr^-(CO_2)_8$ back to tens of picoseconds.

In Chapter 5 we will focus on the ultraviolet (355-nm) photodissociation of $IBr^-(CO_2)_n$ and compare the experimental product ratios to our simulations. While our simulations will show worse agreement with experiment than the near-infrared simulation did, we will see that an analysis of the ultraviolet simulations still provide insight into understanding the experimental results. At large cluster size, our simulations predict the appearance of ground-state recombination IBr^- product as a major channel, something not supported in experiment which sees dissociation as the major product even at the largest cluster sizes. We will present a hy-

pothesis for the possible reason for this discrepancy: deactivation of spin-orbit excited bromine by the vibrations of the solvent. Previously, it was discussed how simulations of the ultraviolet photodissociation of $I_2^-(CO_2)_n$ by Parson and coworkers [40, 41] supported a mechanism of solvent-mediated charge transfer for the efficient spin-orbit quenching of iodine. We will see that this same process is the mechanism of spin-orbit quenching present in our simulations of the ultraviolet photodissociation of $IBr^-(CO_2)_n$. Since the experimental results seem to preclude this mechanism by the lack of ground-state recombined product, we will hypothesize that our model must neglect a competing process. We will argue that the presence of an efficient spin-orbit quenching process between bromine and the vibrations of CO_2—which is treated as rigid in our model—is a viable candidate.

Finally, Chapter 6 will explore possible future directions for our simulations and their relationship to previous work by our group and ongoing and future work in the Lineberger group. Among these will be the modeling of the time-dependent photoelectron spectra of $IBr^-(CO_2)_n$, a present area of study experimentally, as well as revisiting the dynamics of $ICl^-(CO_2)_n$ given the knowledge and experience gained by the work with $IBr^-(CO_2)_n$ presented in this thesis.

Chapter 2

Theoretical Methods

In this chapter we will present both the theoretical methods used in our simulations of $IBr^-(CO_2)_n$ photodissociation and applications of these methods to basic properties of $IBr^-(CO_2)_n$ and $Br^-(CO_2)_n$ clusters.

First, we will present a brief overview of the nonadiabatic molecular dynamics (MD) method developed in our group by Paul Maslen, James Faeder, and Robert Parson [26,27,36,37], hereafter referred to as MFP. This will consist of a summary of both the effective Hamiltonian and dynamics methods in our model.

We will then present the quantum chemistry calculations which were necessary for simulations of $IBr^-(CO_2)_n$. While previous workers had calculated the ab initio potential energy surface (PES) and associated properties needed for our MD method for I_2^- and ICl-$^-$ [36], no such calculations were done for IBr^-. We will present internally-contracted multireference configuration interaction (icMRCI) calculations for the lowest six spin-orbit states for IBr^- and compare the resulting energetics with experimental values. We will also document the calculation of the necessary short-range Lennard-Jones (LJ) parameters needed for our effective Hamiltonian.

With these new parameters, we will then explore calculated properties of the $IBr^-(CO_2)_n$ system. First, we will analyze a calculated absorption spectrum for IBr^- and compare it to experimental findings. Then, we will explore the properties of minimum energy clusters for both the $IBr^-(CO_2)_n$ and $Br^-(CO_2)_n$ systems and how our model compares to experiment.

2.1 Molecular Dynamics

All the dynamics simulations presented in this thesis are an application of a nonadiabatic molecular dynamics (MD) method first developed for use in investigating solvated I_2^-. This model was the result of many years of work by MFP, and the associated publications [26,27,36] and Dr Faeder's thesis [37] are the complete reference to the model. We present here a brief summary of this model in reference to the $IBr^-(CO_2)_n$ simulations.

2.1.1 Effective Hamiltonian

Assuming the Born-Oppenheimer (BO) approximation, the electronic Hamiltonian is expressed for the solute-solvent system as a function of the nuclear coordinates by means of distributed multipole analysis (DMA) [38,81–85]. In the distributed multipole (DM) expansion, several sites are chosen within each molecule and then the multipoles for the entire molecule are divided into contributions from each atom at each site. In the case of IBr^-, the expansion sites selected were the two atom centers and two point equidistant to the nuclei along the internuclear bond. At each site, the moments are expanded in real spherical tensor moments [86].

As an example, the intermolecular electrostatic energy for non-overlapping charge distributions takes the form:

$$E_{electrostatic} = \frac{1}{2} \sum_{A_i,B_j,t,u} Q_t^{A_i} T_{tu}^{A_i B_j} Q_u^{B_j} \tag{2.1}$$

where the sum runs over the sites, A_i, B_j, and multipole orders, t, u, on each pair of molecules in the system, with the factor of $1/2$ compensating for double counting. The elements in the interaction tensor, T, are complicated but have been tabulated [38, 86, 87] and are efficiently calculated [88–91]. Note that single molecule terms, $T^{A_i A_j}$, are always zero as it is assumed these effects are accounted for in the intramolecular energy.

If the components of the electronic Hamiltonian are then expressed in terms of DM **operators**, one can construct the electrostatic Hamiltonian operator:

$$\hat{H}_{electrostatic} = \frac{1}{2}\mathsf{Q} \cdot \mathsf{T} \cdot \mathsf{Q} + \mathsf{q} \cdot \mathsf{T} \cdot \mathsf{Q} \tag{2.2}$$

where we have switched to a more compact tensor notation. In Equation 2.2, Q and q are the DM operator tensors for the solvent and solute respectively, and T is the DM interaction tensor. Finally, one can introduce a generalized potential for the solvent V defined as

$$\mathsf{V} \equiv \mathsf{T} \cdot \mathsf{Q} \tag{2.3}$$

and a corresponding solute generalized potential v

$$\mathsf{v} \equiv \mathsf{T} \cdot \mathsf{q}. \tag{2.4}$$

The generalized potentials contain the electrostatic potential and all derivatives at every point in the solvent-solute system.

With this framework, the full effective Hamiltonian due to MFP [26, 27, 36, 37] is:

$$\begin{aligned} \hat{h}_{eff} = & E_{intra} + \hat{h}_{isolute} + \hat{h}_{short-range} \\ & + \frac{1}{2}(\mathsf{Q}+\mathsf{q}) \cdot \mathsf{T} \cdot (\mathsf{Q}+\mathsf{q}) \\ & - \frac{1}{2}(\mathsf{Q}+\mathsf{q}) \cdot \mathsf{T} \cdot \boldsymbol{\chi} \cdot \mathsf{T} \cdot (\mathsf{Q}+\mathsf{q}) \end{aligned} \tag{2.5}$$

which in the generalized potential nomenclature becomes

$$\begin{aligned} \hat{h}_{eff} = & E_{intra} + \hat{h}_{isolute} + \hat{h}_{short-range} \\ & + \frac{1}{2}(\mathsf{Q}+\mathsf{q}) \cdot (\mathsf{V}+\mathsf{v}) \\ & - \frac{1}{2}(\mathsf{V}+\mathsf{v}) \cdot \boldsymbol{\chi} \cdot (\mathsf{V}+\mathsf{v}). \end{aligned} \tag{2.6}$$

where we have introduced three new terms, $E_{intra} + \hat{h}_{isolute} + \hat{h}_{short-range}$, and a new operator tensor, $\boldsymbol{\chi}$,the generalized electric susceptibility which describes the electronic polarization response of the solvent/solute to the generalized potential. For further details, we once again refer back to the appropriate publications [26, 27, 36, 37] but state here that the second line of the effective Hamiltonian, Equation 2.6, deals with the electrostatic energy due to interaction of the permanent moments and the third line is the induction-dispersion energy associated with the induced moments.

Of the other three terms in the first line of Equation 2.6, E_{intra} describes the solvent

internal degrees of freedom. In our model, we use rigid CO_2 molecules and we set this term to zero.

The second term, $\hat{h}_{isolute}$ is the Hamiltonian of the isolated solute and is decomposed as

$$\hat{h}_{isolute} = \hat{h}_a + \hat{h}_{SO}. \tag{2.7}$$

$\hat{h}_a$ refers to the Hund's case (a) states for the solute and $\hat{h}_{SO}$ is the spin-orbit (SO) operator that transforms them into Hund's case (c) states. We note that in the case of I_2^- and ICl^- the ab initio energies were calculated in case (a), with an empirical one-electron SO operator added on a posteriori as the quantum chemistry program used at the time did not reliably calculate SO operators. In the case of IBr^-, the spin-orbit operator used was a SO effective core potential (ECP), as detailed below. However, in order to be used by our MD program, the case (a) and spin-orbit operators were extracted from the quantum chemistry program that we used.

Finally, $\hat{h}_{short-range}$ is included to account for the short-range interactions that our DMA approximation neglects: the dispersion forces and exchange-repulsion forces. This operator is partitioned as follows:

$$\hat{h}_{short-range} = \hat{h}^{solute-solvent}_{short-range} + E^{solvent-solvent} \tag{2.8}$$

where the solvent-solvent interaction energy, $E^{solvent-solvent}$, is assumed to be independent of the solute wavefunction and is just a function of the solvent nuclear separation. For all interactions, it is assumed that the electrostatic terms will dominate both mixing and long-range effects. Moreover, although short-range effects are dependent on the state of the solute, we assume that this state dependence will be small and thus use state-independent empirical parameters.

The short-range interactions are represented as a sum of pair-wise Lennard-Jones (LJ) potentials,

$$\hat{H}_{short-range} = \sum_{i<j} 4\epsilon_{ij} \left(\frac{\sigma_{ij}^{12}}{R_{ij}^{12}} - \frac{\sigma_{ij}^{6}}{R_{ij}^{6}} \right) \tag{2.9}$$

where the $CO_2 \cdots CO_2$ and $I \cdots CO_2$ parameters are taken from MFP [26, 27, 36, 37] and the $Br \cdots CO_2$ interactions are calculated and tabulated below in Section 2.2.2.

2.1.2 Overview of Molecular Dynamics Methods

We now present a short description of how the effective Hamiltonian is used to compute the molecular dynamics performed in our method. As always, further reference may be found in the appropriate publications [26, 27, 36, 37].

In our method, classical dynamics are performed on the current adiabatic states calculated from the effective Hamiltonian with nonadiabatic transitions ("hops") to other states treated via a surface-hopping algorithm briefly described below. At each step in the trajectory, the eigenvectors and eigenstates of $\hat{h}_{eff}$ are obtained by diagonalization of Equation 2.6. All solute state energies and DM operators are obtained via splined data evaluated at the current configuration. Then, forces on the current adiabatic state are calculated from derivatives of the effective Hamiltonian with respect to the nuclear coordinate, $\mathbf{R}$, using the Hellmann-Feynman theorem

$$\mathbf{F} = -\nabla_{\mathbf{R}} \langle \psi | \hat{h}_{eff} | \psi \rangle = -\langle \psi | \nabla_{\mathbf{R}} \hat{h}_{eff} | \psi \rangle. \tag{2.10}$$

Using these forces the trajectories are propagated according to the velocity Verlet algorithm [92].

In order to simulate the nonadiabatic dynamics during a trajectory Tully's surface-hopping method [93] is used. In this method quantum amplitudes are integrated using the time-dependent Schrödinger equation (TDSE)

$$\imath\hbar\dot{c}_i = \sum_j c_j \left(E_i \delta_{ij} - \imath\hbar \dot{\mathbf{R}}(t) \cdot \mathbf{d}_{ij} \right) \tag{2.11}$$

where c_i is the quantum amplitude for state i, E_i is the energy of state i, $\dot{\mathbf{R}}(t)$ is the nuclear velocity vector, and $\mathbf{d}_{ij}$ is the nonadiabatic coupling vector between states i and j. At each time step, the hopping probability between states is computed and transitions are made according to Tully's "fewest-switches" algorithm [93]. This algorithm minimizes the number of hops while making sure that the ensemble per-state probabilities approach the probabilities from the TDSE. Following previous work [26, 27, 36, 37], we also use a quantum decoherence reset interval of 200 fs to prevent spurious coherence effects [93, 94].

The quantum amplitudes are integrated using an adaptive Runge-Kutta method [95] at a

much smaller time step than that used for the classical dynamics (1.0 fs in this work). In regions of strong nonadiabatic coupling, the classical timestep is also shortened to ensure accuracy in the transition zones. Further specifics of each ensemble's MD setup will be provided when examining the results of the simulations.

2.2 Quantum Chemistry

All quantum chemistry calculations in the following section were performed using MOLPRO 2002.6 [96], a high-level ab initio quantum chemistry application. The MOLPRO code was modified in analogy to changes made by Paul Maslen to MOLPRO94 [97], to allow for calculation of transition distributed multipoles, a major component of our molecular dynamics (MD) simulation program.

2.2.1 Potential Energy Surface for IBr^-

As a dihalide anion, IBr^-, behaves like a one-electron molecule with the valence hole taking the place of the electron. Considering the valence s subshell as closed, the electronic structure is determined by 11 valence p electrons in 6 valence p orbitals. In the absence of spin-orbit coupling, this corresponds to 4 levels from 12 molecular states, $2^2\Sigma$ and $2^2\Pi$, which dissociate to a ^1S anion and a ^2P neutral. These are the Hund's case (a) states and they are examined in Section 2.2.1.4. The spin-orbit (SO) coupling breaks the degeneracy of the ^2P neutral into $^2P_{3/2}$ and $^2P_{1/2}$ states giving rise to four case (c) asymptotes.

The potential energy surface (PES) for the lowest six states for IBr^- including spin-orbit interaction is presented in Figure 2.1. The PES was constructed using MOLPRO 2002.6 [96] and provides the isolated solute Hamiltonian, $\hat{h}_{isolute}$, Equation 2.7, needed in the effective Hamiltonian, Equation 2.6. Note that although only six states are shown, each state is, in reality, doubly degenerate in accordance to Kramers' theorem [98, 99]. In our MD model we rigorously keep track of all twelve states, but for practical purposes we refer here in this thesis only to the six states of IBr^-. Though we use case (a) labels for the states of IBr^-, which, as

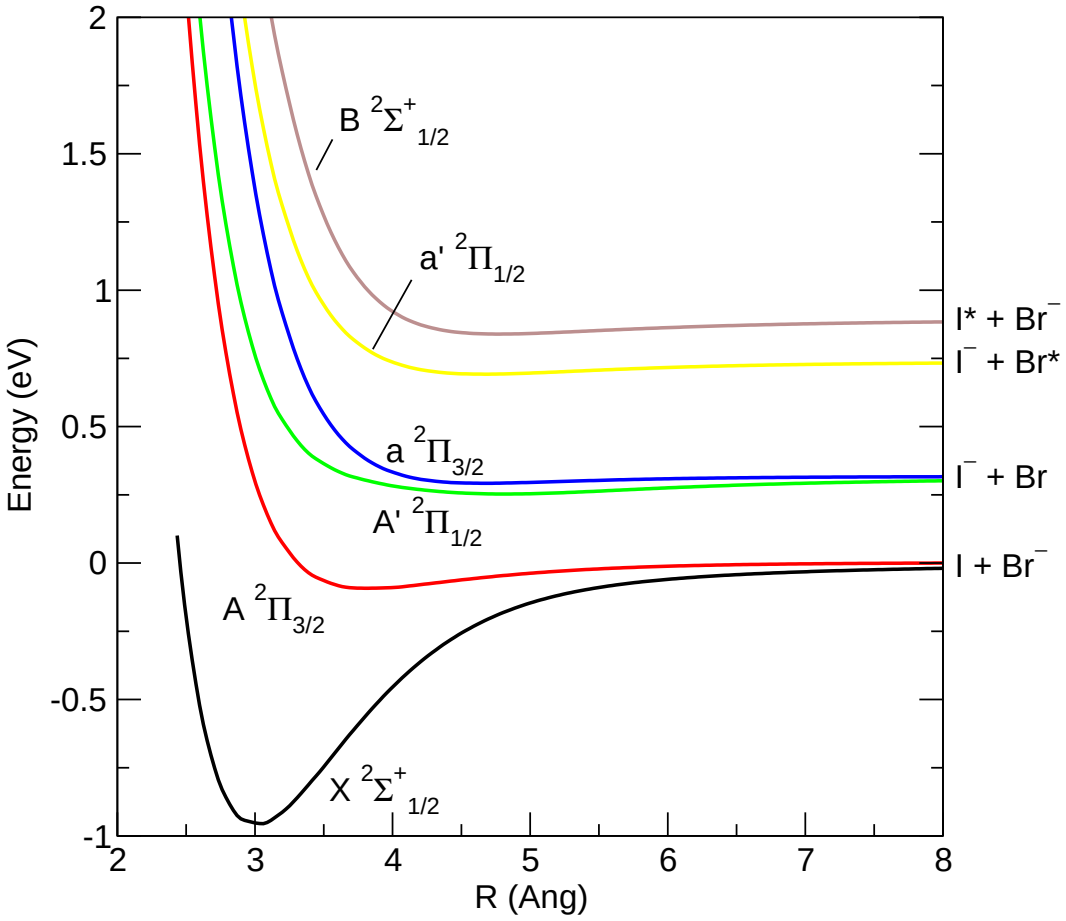

Figure 2.1: Potential energy curves for the six lowest spin-orbit states of IBr^-. The Hund's case (a) labels used here are approximately valid near R_e.

shown in Section 2.2.1.4 are approximately valid around R_e, the only rigorously good quantum number in case (c) is Ω, the projection of the total angular momentum along the bond axis. The $X, A, \ldots$ labels are nevertheless retained here since they are widely used in the literature. As in our group's previous studies of I_2^-, above the ground X state, upper case labels are used for states that are "bright" with respect to absorption, while the lower case labels are "dark" (Figure 1.1(a)). While this "bright/dark" distinction may not hold for IBr^-, as it was for I_2^-, we continue this scheme in our studies of $IBr^-(CO_2)_n$ as much of the discussion in former and future publications is couched in terms of, e.g., near-infrared (IR) excitation as a $A' \leftarrow X$ transition.

For IBr^-, only the ground state is strongly attractive, with higher states either repulsive or slightly bound. The six states lead to four asymptotes. The lowest four states dissociate to atomic states corresponding to ^1S and $^2P_{3/2}$ and are split by the electron affinity difference of bromine and iodine. The fourth and fifth excited states, corresponding to ^1S and spin-orbit excited $^2P_{1/2}$ at dissociation, are separated from the lower asymptotes by the spin-orbit splitting of bromine and iodine.

Finally, we note the coloring scheme used in Figure 2.1 with black representing the ground state, red the first excited state, and so on. This scheme will become important in plots of trajectories that will be presented in later sections concerning the photodissociation dynamics of $IBr^-(CO_2)_n$. In most of these plots, the coloring can usually be counted on to correspond to the like bare ion states; however, our plot and figure generation tools assign colors strictly on the basis of energy ordering. Since the solvent strongly perturbs the electronic states of the bare anion, the color-coded states in the figures will not always correspond to the color-coded states of the bare anion. Instances in which this is important will be noted in the text.

2.2.1.1 Basis Set and Effective Core Potentials Used

Our calculations for IBr^- use the energy-consistent effective core potential (ECP) of the Stuttgart-Bonn group [100]. Specifically, we use the large-core MDF ECPs which are based upon multiconfigurational Dirac-Hartree-Fock (MCDHF) calculations of the neutral atom (sometimes

called ECPnMDF where n is the number of electrons replaced). These also include a spin-orbit ECP and a core polarization potential (CPP). The CPP models the charge-induced dipole interaction of the core and are included in our calculations.

The basis set used is an augmented form of the standard basis set included with the Stuttgart MDF ECPs. The stock basis set for this ECP is $(6s6p)/[4s4p]$, but an augmented $(7s7p3d2f)/[5s5p3d2f]$ basis, which was used in the original paper [100], was graciously supplied by the authors [101]. The extra functions for iodine are an s function with an exponent of 0.030; a p function with an exponent of 0.023; three d functions with exponents of 0.3550, 0.1851, and 0.1025; and, two f functions with exponents of 0.4330 and 0.2026. The extra functions for bromine are an s function with an exponent of 0.041; a p function with an exponent of 0.030; three d functions with exponents of 0.7063, 0.2639, and 0.1047; and, two f functions with exponents of 0.5515 and 0.2580. This augmented basis was used primarily because our transition distributed multipole analysis (DMA) includes quadrupole terms which are better described using d and f functions. Electronic accuracy also increased with the augmented basis.

Use of the newer small-core MDF-based aug-cc-pVnZ-PP potentials and basis sets [102] were also explored. Naively, it was assumed that the much larger basis set combined with the inclusion of more electrons with a small-core ECP would enhance energetic performance, albeit at the expense of computational time. However, it was found that the spin-orbit ECPs included with these sets gave poorer energetics than the large-core MDF used in this study.

Finally, in previous work, surfaces for I_2^- and ICl^- were calculated by Maslen, et al [36] using the MOLPRO94 [97] program, see Figure 1.1. In that work, the medium-size polarized all-electron basis sets of Sadlej [103,104] were used. With the suggested additional polarization functions, the sets were $(13s10p4d)/[7s5p2d]$ and $(19s15p12d4f)/[11s9p6d2f]$ for chlorine and iodine, respectively, where chlorine's first contracted d function was scaled by 0.9195 to reduce the error in the electron affinity difference of I and Cl [36,37]. ECPs were avoided due to doubts of their accuracy at the time. Calculations of IBr^- were undertaken using the Sadlej basis and MOLPRO 2002's SO code but the energetics were found to be much worse than with the

large-core MDF and computational performance greatly suffered due to the immense size of the basis set, so these basis sets were not used.

2.2.1.2 Details of Calculation Theory

The internally-contracted multireference configuration interaction (icMRCI) program of MOLPRO [96] was used for calculation of the curves and all properties. First, a state-averaged multiconfigurational self-consistent field (SA-MCSCF) of all six states of IBr^- is done. Three 2-state icMRCI calculations were then carried out, one for each symmetry (done at C_{2v}). The icMRCI method is a singles-and-doubles multireference configuration interaction (MRCISD) in which the pairs are internally contracted to reduce the size of the configuration interaction (CI) matrix [105–107]. During the MRCISD calculation, the two valence s and six valence p orbitals are correlated. The size-consistency errors inherent in configuration interaction calculations are ameliorated through use of Pople's cluster correction [96, 108].

Beyond this, transition DMA, complete active-space self-consistent field (CASSCF) angular momentum, nonadiabatic coupling matrix elements (NACMEs), and SO calculations were also carried out, each of which is required by our MD program.

2.2.1.3 Analysis of the IBr^- Potential Energy Surface Properties

In Table 2.2.1.3, the calculated energetics and properties of the IBr^- PES are compared to available experimental data. The first sets of data deal with the atomic data that can be extracted from the asymptotes of the IBr^- PES, compared to the known spin-orbit splitting and electron affinities of the isolated atoms.

Our calculations underestimate the SO splittings by 30-50 meV, a relative error of 5-7%. Likewise, the calculated electron affinity difference between iodine and bromine is found to be within 4% of the actual value. Considering we are using a large-core ECP and SO ECP, this performance is quite remarkable given the small size of our multireference configuration interaction (MRCI) active space.

		Calc. (eV)	Expt. (eV)	Δ(Expt. - Calc.)
Spin-Orbit Splittings:	Br:	0.4237	0.4569[a]	0.0331
	I:	0.8932	0.9427[a]	0.0495
	ΔEA[b]:	0.3156	0.3045[c]	-0.0111
	D_0:	0.948[d]	1.10(4)[e]	0.152
			0.954(6)[f]	0.006
	EA(IBr^-):	2.494	2.500(6)[f]	0.006
	R_e (Å):	3.05	3.06(3)[f]	0.01

[a]: Ref. 109.
[b]: Electron affinity difference between I and Br.
[e]: Ref. 110.
[d]: Calculated using $\omega_e = 118$ cm^{-1}, see text.
[e]: Ref. 79.
[f]: Preliminary results, Ref. 111.

Table 2.1: Summary of the energetics and properties from ab initio calculations of IBr^-.

The molecular properties of IBr^- are compared to experiments in the second part of Table 2.2.1.3. Our calculations give a calculated well depth, D_e, of 0.956 eV at an equilibrium bond length, R_e, of 3.05 Å. Translational energy-release spectroscopy at a series of wavelengths from 660 and 790 nm has provided an experimental value for D_0 of 1.10 ± 0.04 eV [79]. More recent photoelectron spectroscopy experiments by the Lineberger group have found a more accurate D_0 value for IBr^- of 0.954 ± 0.006 eV [111]. This is obviously an impressive match to our calculated value for D_e, however, we feel that this is more likely the result of error cancelation in the calculations rather than implicit verification of our method. Our calculations were not designed around finding the ground-state binding energy of IBr^- but rather properties of all the valence states.

In order to more fairly compare the experimental and calculated well depth, a value for the vibrational frequency of $\omega_e = 118$ cm^{-1} was obtained by analysis of the ground state using Le Roy's LEVEL 7.7 program [112]. This value is only an estimate as the LEVEL program does not do half-integer rotational values, so the vibrational levels predicted are actually for $J = 0$, whereas in the case of IBr^- the ground state is $\Omega = 1/2$ so that the first state would correspond to $J = 1/2$. Nevertheless, we can use an $\omega_e \approx 118$ cm^{-1} to estimate that the difference between D_e and D_0 for our PES is about 8 meV, leading to a calculated $D_0 = 948$ meV. An experimental vibrational frequency of 136 cm^{-1} was obtained in solution [79], but no known gas-phase measurement has been made.

A difference of 144 meV could be significant for the dynamics of photodissociation. A shallower well in simulations for the same photon energy corresponds to a larger kinetic energy release (KER) in our simulations, c.f. experiment. In order to assess the effect of this error, simulations were carried out at an excitation energy of 840 nm and compared to those run at 790 nm. This was done rather than scaling the curves which might adversely affect the excited states.

Likewise, the newer experimental D_0 value leads to a smaller KER in our simulations since the zero-point energy (ZPE) is not included in our simulations. In order to assess this

error, simulations were carried out at 770 nm. While this does overestimate the ≈ 8 meV ZPE offset, it will provide a test of the effect of less KER in the simulations. The results of this analysis are presented in Sections 3.4 and 4.6.

2.2.1.4 Mixing of the Hund's Case (a) States Due to Spin-Orbit Coupling in the IBr^- PES

The Hund's case (a) ab initio potential energy curves for IBr^- are presented in Figure 2.2. Since SO coupling is by definition not included, there are only four distinct curves leading to two distinct asymptotes as the ^2P degeneracy of the neutral atom has not been lifted. The curves show that, as in case (c), only the Σ state is strongly bound with the other states repulsive or slightly attractive at longer bond lengths. As in ICl^- [36,37], there is a crossing between the Σ^* and Π^* curves due to the interaction between the quadrupole moment of the neutral atom and the charge on the ion. The interaction is attractive for all the Σ states and repulsive for the Π states.

In addition to the curves for case (a), we also tabulate in Table 2.2.1.4 the case (a) mixing coefficients for the case (c) curves in Figure 2.1. Since Ω is a conserved quantum number, there is no mixing between the Σ and Π states for the $\Omega = 3/2$ states at any internuclear separation. For the $\Omega = 1/2$ states, however, mixing can be very strong as the bond length increases. Table 2.2.1.4 shows that the case (a) labels are approximately valid for the SO coupled curves around R_e. Each state at R_e is $> 90\%$ Σ or Π and so those labels are valid. This is especially true for the ground-state which is 98% case (a) at the equilibrium bond length. In comparison to ICl^- [36,37], there is more mixing in IBr^- due to the stronger spin-orbit coupling in bromine than in chlorine.

The mixing at R_e also has great importance for the photodissociation experiments. At R_e the A' and a' states have some mixing with Σ^* and it is this mixing that allows for transition into these states. The perpendicular $\Sigma \rightarrow \Pi$ transition is far too weak to be used for experiment,

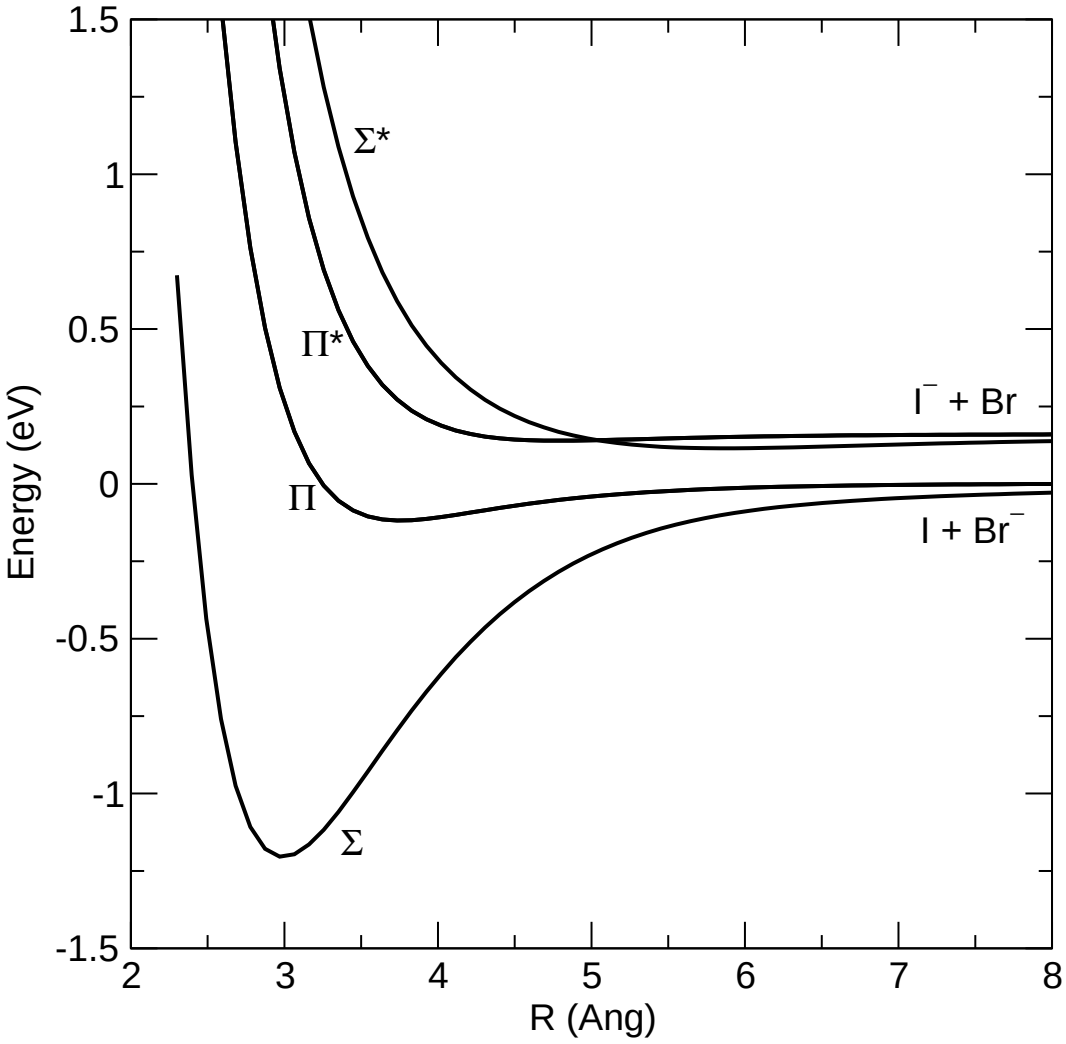

Figure 2.2: Hund's case (a) ab initio potential energy curves for IBr^-.

State	R (Å)	% of Basis Function Character			
		Σ	Σ^*	Π	Π^*
$^2\Sigma^+_{1/2}$ (X)	R_e	98.0	0.0	1.0	1.0
	5.3	71.6	2.6	24.1	1.6
	∞	66.7	0.0	33.3	0.0
$^2\Pi_{3/2}$ (A)	R_e	0.0	0.0	99.6	0.4
	5.3	0.0	0.0	99.6	0.4
	∞	0.0	0.0	100.0	0.0
$^2\Pi_{1/2}$ (A')	R_e	0.9	3.4	95.0	0.8
	5.3	5.8	62.5	8.0	23.8
	∞	0.0	66.7	0.0	33.3
$^2\Pi_{3/2}(a)$	R_e	0.0	0.0	0.4	99.6
	5.3	0.0	0.0	0.4	99.6
	∞	0.0	0.0	0.0	100.0
$^2\Pi_{1/2}$ (a')	R_e	1.1	0.6	0.4	97.8
	5.3	5.2	20.6	0.0	74.1
	∞	0.0	33.3	0.0	66.7
$^2\Sigma^+_{1/2}$ (B)	R_e	0.0	96.0	3.6	0.4
	5.3	17.4	14.3	67.8	0.5
	∞	33.3	0.0	66.7	0.0

Table 2.2: Case (a) composition of the spin-orbit coupled states of IBr^- as a function of the bond length.

while the parallel $\Sigma \rightarrow \Sigma^*$ transition, i.e., $B \leftarrow X$, is always strong. However, the small amount of Σ^* character that is mixed into the A' state at R_e is what gives the $A' \leftarrow X$ peak its intensity, and thus makes the near-IR experiment possible. In Section 2.2.3, an absorption spectrum is calculated from the ground state for IBr^- (Figure 2.9). The three largest peaks are, in order, $B \leftarrow X$, $A' \leftarrow X$, and $a' \leftarrow X$ just as the case (a) mixing coefficients imply.

As the bond is extended just slightly to 5.3 Å, the mixing changes quite rapidly. The case (a) labels become less appropriate as more mixing occurs. This is especially true for states A' and B which switch from nearly all Π and Σ^* around R_e to being mainly Σ^* and Π, respectively, all in 2.3 Å! Also, with this change, the polarization of these states also changes signs as each changes its R_e bonding/antibonding character.

Finally, as we approach dissociation, the case (a) mixing eventually approaches the case (c) proportions associated with the $^2P_{3/2}$ and $^2P_{1/2}$ neutral atoms. This is expected as at long bond lengths, spin-orbit coupling dominates, whereas near R_e the SO coupling is effectively "quenched" by molecular bonding interactions.

2.2.1.5 Assessment of Potential Energy Surface Quality

Although our simulations were designed to be used in collaboration with the Lineberger group, the group of Andrei Sanov has also used our PES for IBr^- [113]. Their work on time-resolved photoelectron imaging of I_2^- and IBr^- used the PES in Figure 2.1 for semiclassical simulations of the photodissociation of IBr^-.

By use of their experimental results on the $A' \leftarrow X$ photodissociation of IBr^- in conjunction with classical trajectories, they were able to transform time-versus-electron kinetic energy (eKE) data into R-versus-A' state energy with the results presented in the color contour map in Figure 2.3. This mapping was constructed by first solving Newton's second law

$$\mu \frac{d^2R}{dt^2} = -\frac{dV^{A'}_{IBr^-}(r)}{dR} \tag{2.12}$$

where R is the internuclear distance, μ is the reduced mass, and $dV^{A'}_{IBr^-}(R)$ is the A' state

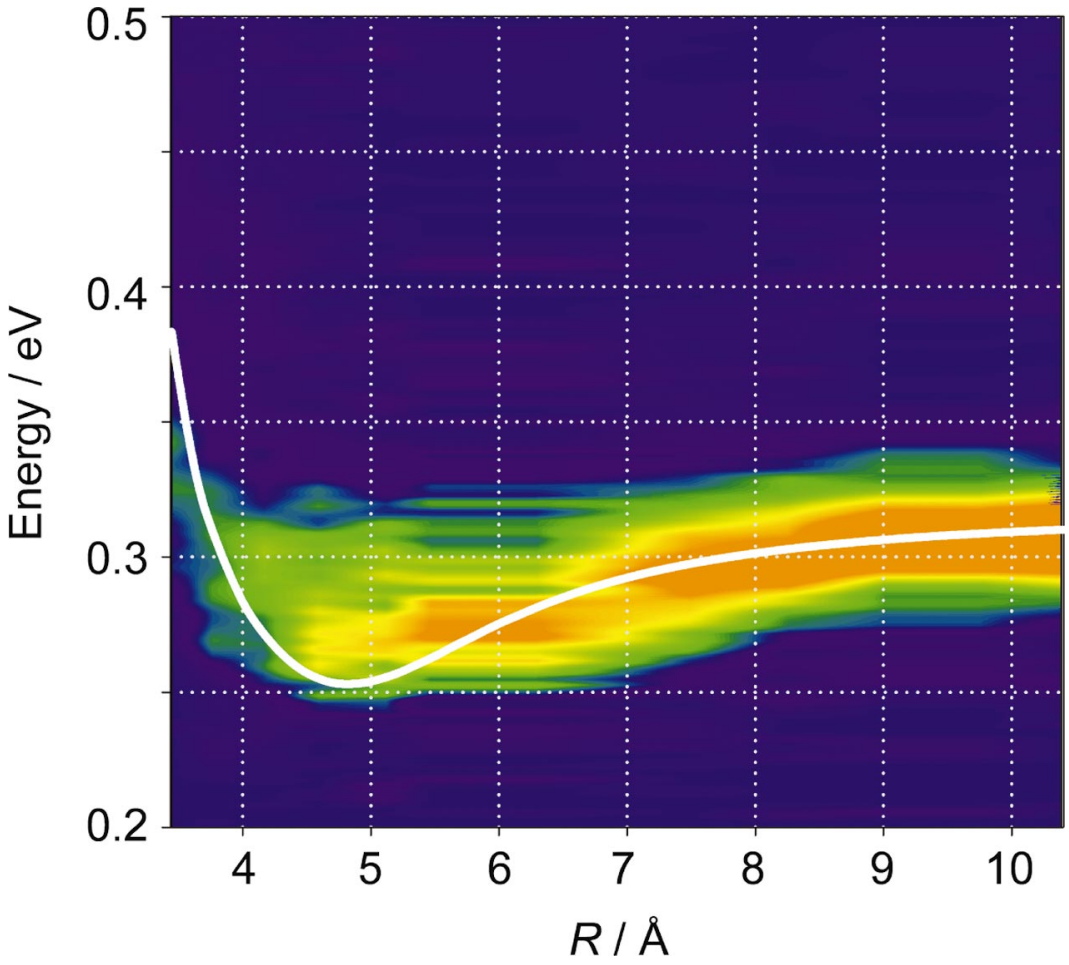

Figure 2.3: Comparison of the theoretical IBr^- A' state potential energy curve (white line) with experimental data from Mabbs, et al [113]. Reproduced with permission from Dr Sanov.

potential for IBr^- (The curves were scaled to match the experimental ground-state well depth, $D_0 = 1.10 \pm 0.04$ eV [79]. By integrating Equation 2.12, trajectories $R(t)$ were obtained which allowed construction of an eKE(t) trajectory. Since each point on in time corresponds to a specific expectation value of $R(t)$, it is possible to transform the (t, eKE) photoelectron data into (R, eKE) according to

$$\mathrm{eKE}(R) = \left[h\nu + V^{A'}_{\mathrm{IBr}^-}(R)\right] - V_{\mathrm{IBr}}(R), \tag{2.13}$$

where $V_{\mathrm{IBr}}(R)$ is the neutral IBr energy curves. In this case, the neutral states considered were the A and C states of IBr [114] and the subsequent trajectory was an average of both states' contributions. Then, using an average of the A and C IBr potential curves as a single "reference" neutral state, the (R, eKE) data was transformed into the (R, $V^{A'}_{\mathrm{IBr}^-}$) phase space.

Also included in Figure 2.3 is an overlay of the A' curve from our PES of IBr^-. There is reasonable agreement between the ab initio calculations and their experimental "rebuild" of the surface for A' state. The fact that this agreement is seen in an **excited** state of IBr^-, provides extra support for our electronic structure. This is important since the near-IR photodissociation studied by the Lineberger group modeled in this work is based on the $A' \leftarrow X$ excitation.

2.2.2 Lennard-Jones Parameters for $IBr^-(CO_2)_n$

In the effective Hamiltonian in our MD method, Section 2.1.1, the ab initio operator is only the first of several terms. While the DMA calculated along with the PES takes care of the rest of the solute-solvent electrostatic and induction effects, an operator for the short-range dispersion and exchange-repulsion forces between solvent and solute, and between solvent molecules not included in the DMA prescription is needed as well. As stated before, these forces will be included with the addition of pair-wise Lennard-Jones forces on each of the atoms. The values of the parameters used for the $IBr^-(CO_2)_n$ work are tabulated in Table 2.3.

The C-O, C-C, O-O, I-O, and I-C parameters used in our model for $IBr^-(CO_2)_n$ remain the same as formulated in previous efforts. While it should be suspected that perhaps the

Molecular Geometry		
R_{C-O} (Å)	1.16	
Charge distribution[b]	charge (au)	distance from C (Å)
$q_1 = q_5$	0.1216	1.523
$q_2 = q_4$	−0.6418	1.066
q_3	1.0404	0.000
Polarizability[a]		
α_{zz} (Å^3)	4.487	
$\alpha_{xx} = \alpha_{yy}$ (Å^3)	2.127	
LJ parameters	σ (Å)	ϵ (meV)
C–C[b]	2.824	2.256
O–O[b]	3.026	6.477
C–O[b]	2.925	3.823
C–I[c]	3.805	16.33
O–I[c]	3.200	12.56
C–Br	3.751	16.00
O–Br	3.016	10.00

[a] Ref. 115.
[b] Ref. 116.
[c] Ref. 37.

Table 2.3: Short-range potential parameters for $IBr^-(CO_2)_n$.

parameters for the $CO_2 \cdots CO_2$ should remain the same, we are currently using a very different basis set than was used in the studies of I_2^- and ICl^-. However, this turns out not to be a concern as shown in Figure 2.4 which is a Lennard-Jones (LJ) fit for the $I^- \cdots CO_2$ T-shaped configuration that can be extracted from our MD program using the IBr^- ab initio dataset.

However, values for the $Br \cdots CO_2$ interaction need to be obtained. To this end, coupled cluster with single, double, and iterative triple excitations (CCSD(T)) calculations were calculated for the $Br^- \cdots CO_2$ T-shaped and linear configurations using the MOLPRO quantum chemistry program [96], with the resulting curves in Figure 2.5. The MDF ECP [100] was used for bromine, as was used for the IBr^- PES. For the carbon and oxygen, the aug-cc-pVTZ basis set [118, 119] was used. The C-O bond length was fixed at 1.16 Å. The $Br^- \cdots CO_2$ separation was then varied at 46 different bond lengths from 2.5 to 100 Å.

Figure 2.5 contains both the "T-shaped" configuration and the "linear" configuration. T-shaped refers to a configuration where the bromine anion and carbon in CO_2 are collinear with the oxygens perpendicular to the Br-C line. The linear configuration is one in which the all four atoms of the $Br^- \cdots CO_2$ system are collinear. As in $I^- \cdots CO_2$ and $Cl^- \cdots CO_2$, the anion energetics in the T-shaped geometry are attractive due to the strong interaction of the ion with the CO_2 quadrupole. Also, the slightly negative oxygens are repelled by the anion causing a bend in the true structure of $Br^- \cdots CO_2$. This bend is about 7° in $Br^- \cdots CO_2$, between the values of 5° in $I^- \cdots CO_2$ and 10° in $Cl^- \cdots CO_2$ [53]. However, in both the CCSD(T) calculations and in our simulations, the solvent is considered rigid.

Using our MD program, similar surfaces for $Br^- \cdots CO_2$ were generated in order to extract from these surfaces the "quantum" energies, defined as the contribution to the energetics due to the whole effective Hamiltonian, Equation 2.6, less $\hat{h}_{short-range}$. These values were then subtracted from the CCSD(T) curves to obtain the short-range energies. We then attempted to find best Br-O and Br-C parameters which would duplicate the CCSD(T) LJ curves in Figure 2.5. Unfortunately, it was found that an attempt to exactly duplicate, say, the T-shaped $Br^- \cdots CO_2$ CCSD(T) curves with one set of LJ parameters led to a poor fit with the linear $Br^- \cdots CO_2$

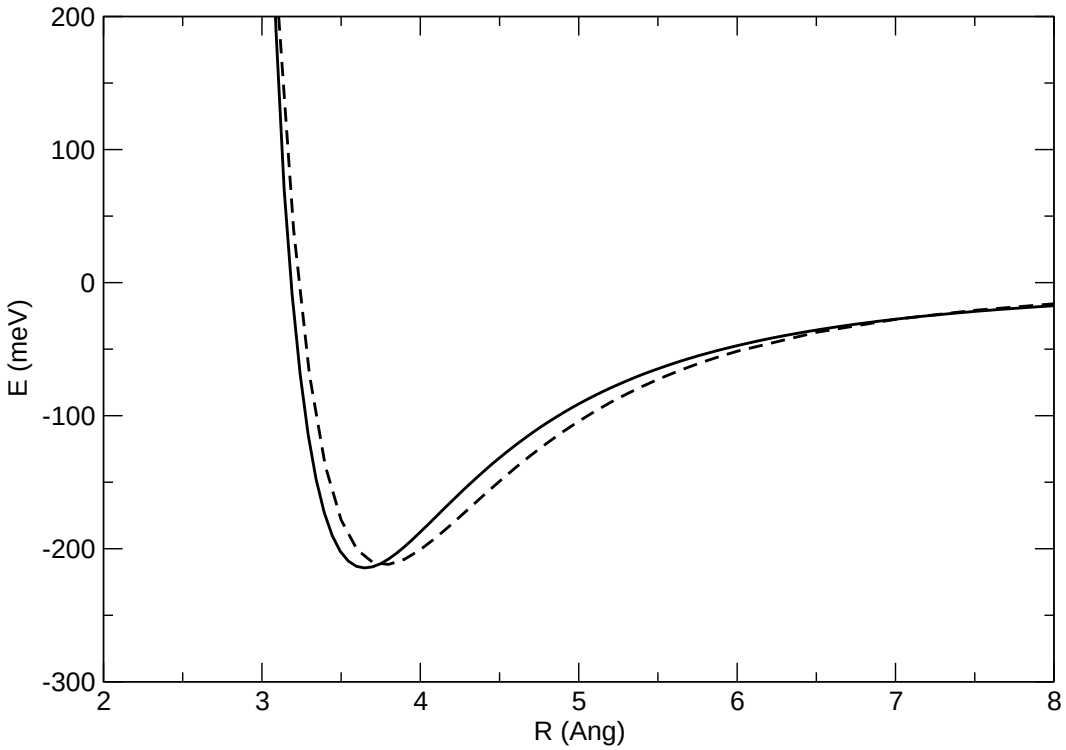

Figure 2.4: Comparison of the standard Lennard-Jones fit tabulated in Table 2.3 (solid) to $I^- \cdots CO_2$ potential energy surfaces from experiment [117] (dashed).

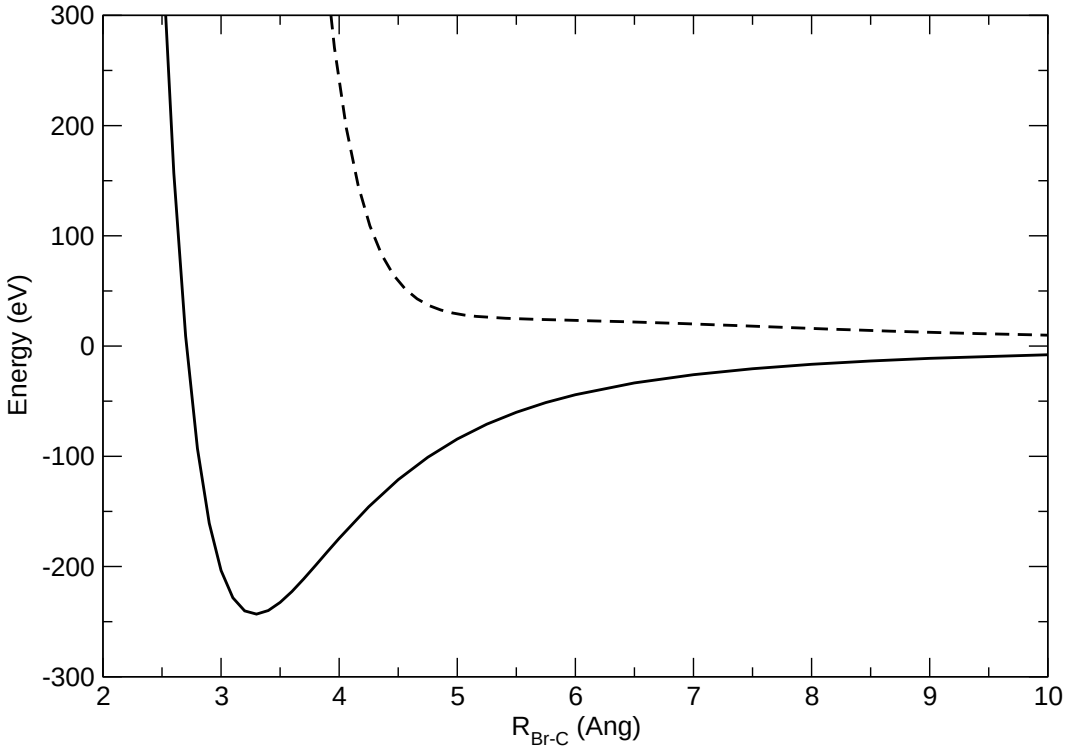

Figure 2.5: Calculated CCSD(T) T-shaped (solid) and linear (dashed) $Br^- \cdots CO_2$ potential energy surfaces using the Stuttgart-Bonn MDF effective core potential [100] for Br and aug-cc-pVTZ basis [118, 119] for C and O.

interaction and vice versa. Therefore, a compromise set of LJ parameters were chosen and they are the values tabulated in Table 2.3. These parameters give the short-range interactions seen in Figure 2.6. These LJ parameters for Br-O and Br-C then lead to the T-shaped surface in Figure 2.7 and the linear surface in Figure 2.8.

In Figures 2.7 and 2.8, the solid line is the curve our MD program outputs for the $Br^- \cdots CO_2$ interaction at that geometry. This curve, when compared to the CCSD(T) curves, is not perfect as the parameters used were a compromise to achieve the best of both geometries. While both geometries show that our MD program overestimates the $Br^- \cdots CO_2$ distance by about 0.25 Å, our major concern is the underestimation of the energy in the T-shaped geometry. To assuage these concerns, a second set of LJ parameters were constructed such that the energy of the $Br^- \cdots CO_2$ T-shaped well matched that of the CCSD(T) well, and a third set that matched the shallower well calculated using the icMRCI method. In this case, the effect on the linear $Br^- \cdots CO_2$ interaction was not considered.

The influence the choice of LJ parameters on the $IBr^-(CO_2)_n$ system is explored in several parts of this thesis. First, the effect on $Br^-(CO_2)_n$ clusters is analyzed in Section 2.2.5 in comparison to experimental results. Also the sensitivity of $IBr^-(CO_2)_n$ properties choice of LJ parameters will be examined: the effect on the near-IR photoproduct ratios in Section 3.5, the effect on the ground-state recombination (GSR) of the near-IR photodissociation in Section 4.7, and the effect on the ultraviolet (UV) photodissociation product ratios in Section 5.3.

2.2.3 Calculated Absorption Spectrum for IBr^-

Electronic absorption spectra from the ground electronic state were computed from the calculated potential energy surface shown in Figure 2.1. These calculations use a modified reflection approximation [120] due to Heller [121]. The absorption cross section at frequency ω is given by

$$\sigma_{if}(\omega) = 4\pi^2 \alpha a_0^2 \omega \left| V_f^{'}(q_T) \right|^{-1} \left| \mu_{if}(q_T) \psi_i(q_T) \right|^2 \tag{2.14}$$

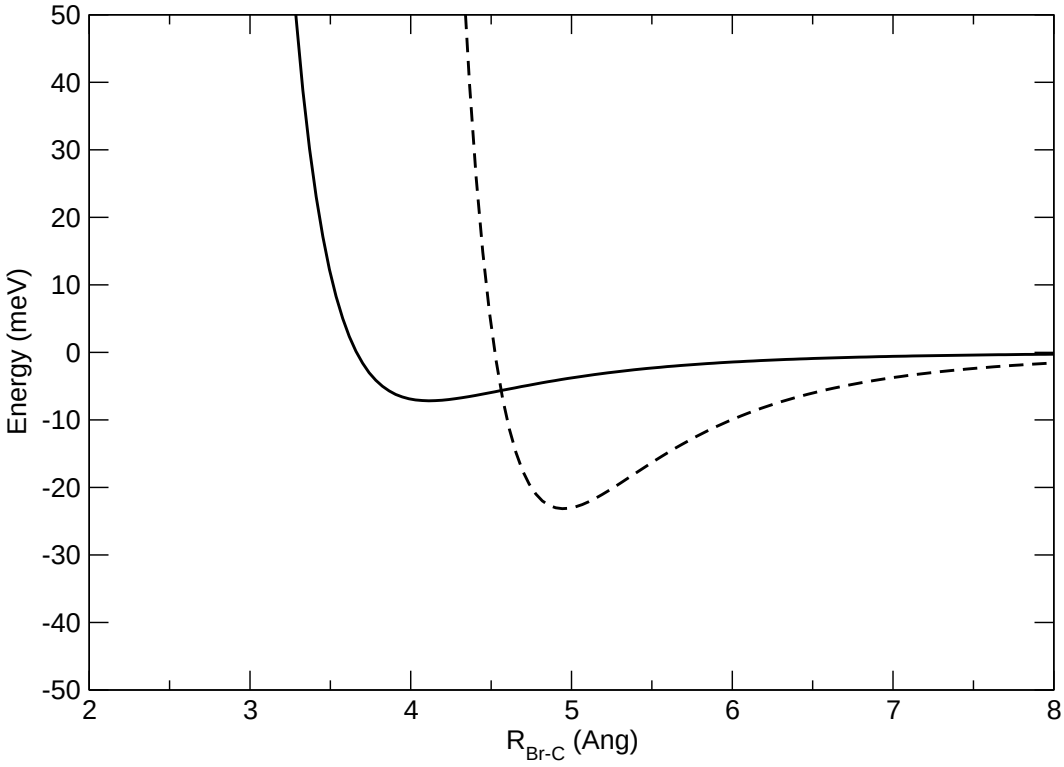

Figure 2.6: Curves for the $Br^- \cdots CO_2$ Lennard-Jones T-shaped (solid) and linear (dashed) short-range interactions using the Lennard-Jones parameters from Table 2.3.

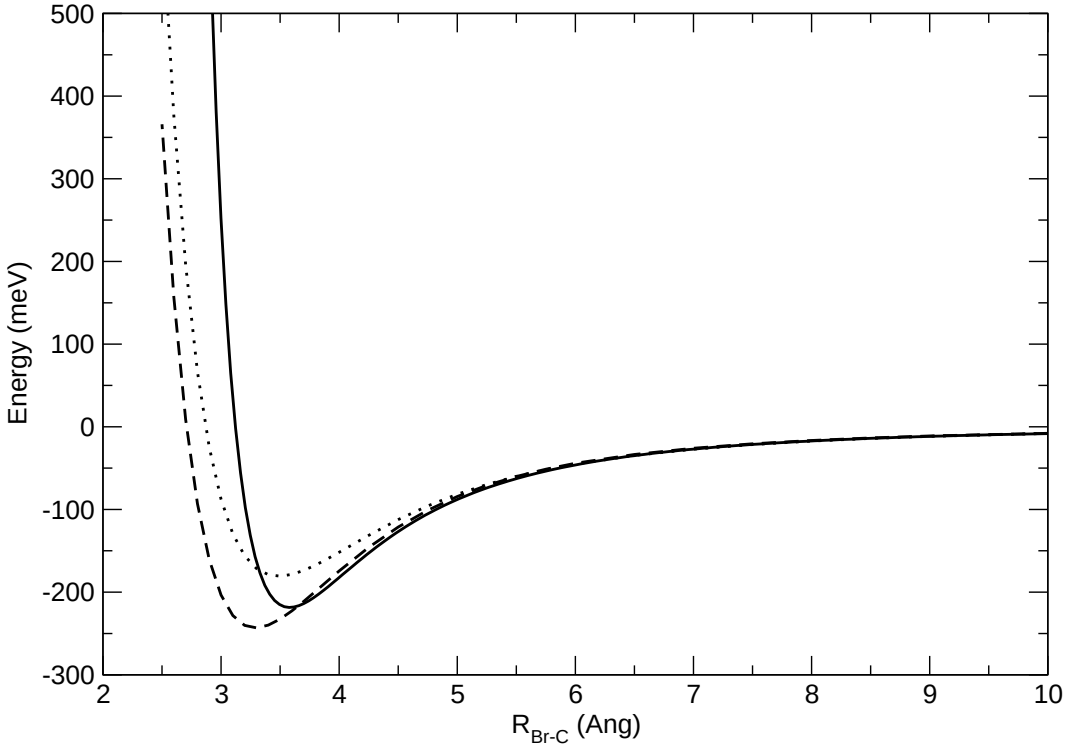

Figure 2.7: T-shaped $Br^- \cdots CO_2$ potential energy surface using the standard Lennard-Jones fit tabulated in Table 2.3 (solid) compared to MRCI (dotted) and CCSD(T) (dashed) curves calculated using the MDF effective core potential [100] for Br and aug-cc-pVTZ basis [118, 119] for C and O.

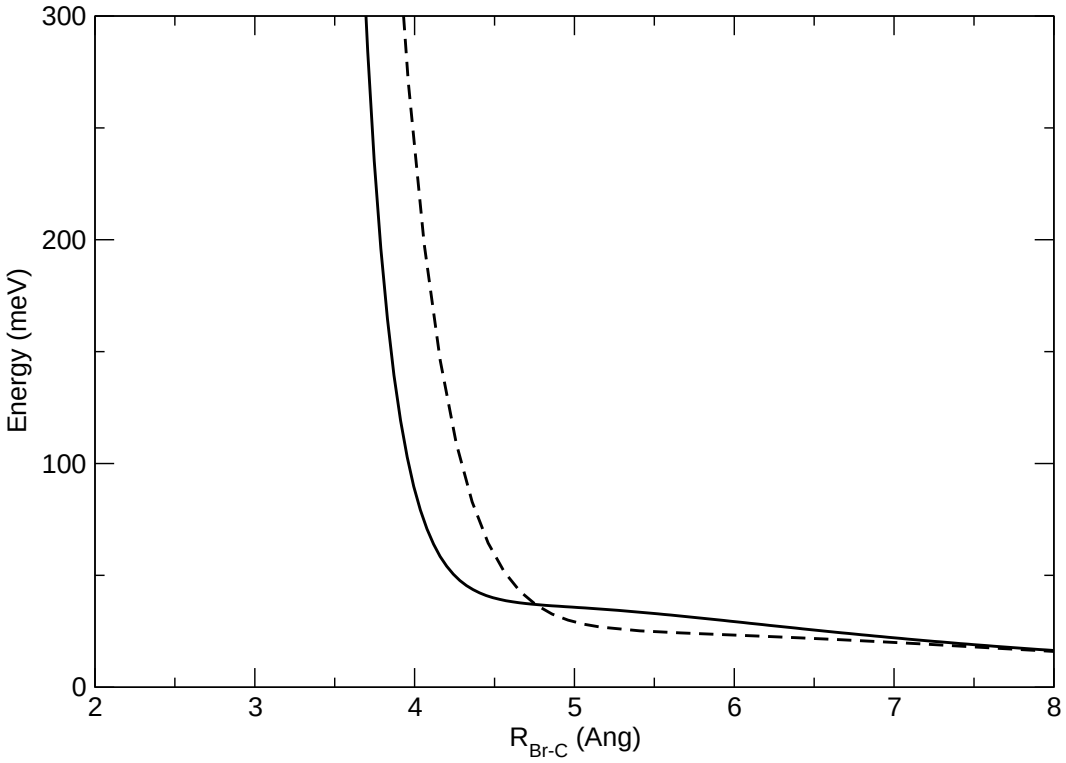

Figure 2.8: Linear $Br^- \cdots CO_2$ potential energy surface using the standard Lennard-Jones fit tabulated in Table 2.3 (solid) compared to CCSD(T) (dashed) curves calculated using the MDF effective core potential [100] for Br and aug-cc-pVTZ basis [118, 119] for C and O.

where μ_{if} is the $f \leftarrow i$ transition moment, ψ_i is the lower-state vibrational wavefunction, $V_f(q_T)$ is the higher-state potential at the classical turning point q_T. At a given lower-state energy E_i, the turning point is defined by $E_i + \hbar\omega = V_f(q_T)$. The ground vibrational state is approximated by a harmonic oscillator whose frequency is determined from the ground-state potential for the cluster configuration under study. Thus, in an $IBr^-(CO_2)_4$ configuration, the oscillator's frequency is determined from the IBr^- potential in the cluster, not that of the bare ion. The harmonic approximation is justified by the fact that the anharmonicity for the ground state is found to be on the order of a wavenumber.

The absorption spectrum for bare IBr^-, Figure 2.9, was calculated according to the above prescription. The spectrum is generated by averaging over 100 configurations of bare IBr^- at 60 K in the ground state, the same temperature at which we sample configurations for our photodissociation simulations. As discussed in Section 2.2.1.4, the major peak in the spectrum, $B \leftarrow X$, is strong due to the parallel $\Sigma \rightarrow \Sigma^*$ charge transfer transition. The other peaks in the spectrum would be quite small if Σ and Π were good quantum numbers (Hund's case (a)). When SO coupling is included, the case (a) states mix, allowing for some Σ^* character to mix into otherwise perpendicular states. Since the spectrum in Figure 2.9 is taken from configurations in the ground-state well, the relevant lines to focus on in Table 2.2.1.4 are those that indicate the degree of mixing at R_e. We find, as expected, that state B contains the largest amount of Σ^* character and is the largest peak, but that states A' and a' also display some Σ^* character, with A' having more than a'. Figure 2.9 shows that the $A' \leftarrow X$ peak is larger than the $a' \leftarrow X$ peak (which is barely visible on the main ordinate's scale).

Sanford [77] measured the absorption cross-section for the $A' \leftarrow X$ transition of IBr-$^-$ and determined that the peak was approximately Gaussian and centered at 740 nm with a full-width half-maximum (FWHM) of approximately 50 nm. The calculated spectrum has its peak value near 770 nm and has a FWHM of 60 nm. Thus, the calculated spectrum is slightly red-shifted from experiment. This red-shift is not unexpected. As stated in Section 2.2.1.3, the calculated ground-state for IBr^- has a shallower well depth, $D_e = 0.956$ eV, than that

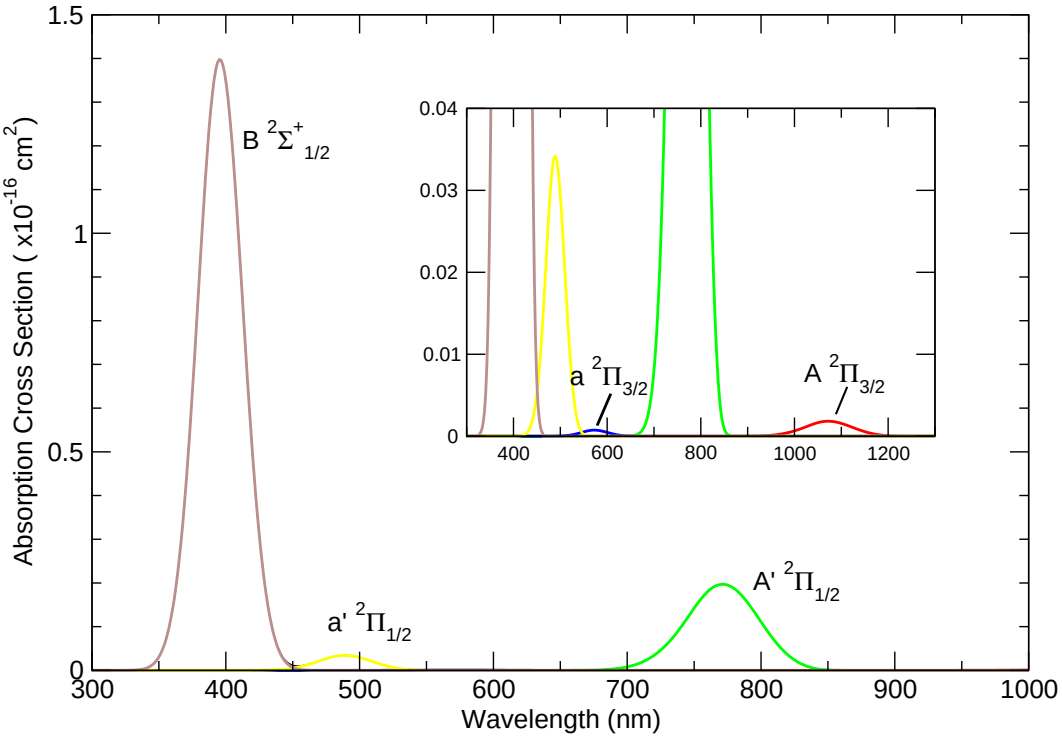

Figure 2.9: Calculated absorption spectrum for IBr^-. Coloring corresponds to the coloring of the bare ion curves in Figure 2.1. 10^{-16} cm^2 = 1 Å^2.

determined by measurements [79], $D_0 = 1.10 \pm 0.04$ eV. As the well depth is less, all simulated excitations could require less energy depending on whether the excited states also shift and by how much.

An absolute cross section for IBr^- was also measured by Sanford [77]. At 760 nm, the absolute cross section was found to be $6.9 \cdot 10^{-18}$ cm^2. Using their relative cross section measurements this implies an absolute cross section of $3 \cdot 10^{-18}$ cm^2 at 790 nm, the wavelength used in the near-IR photostudies. The simulated spectrum predicts a cross section of $16 \cdot 10^{-18}$ cm^2, which reflects both the red-shift of our simulation as well as a generally taller peak.

As a point of comparison for the calculated spectrum of IBr^-, we present the calculated spectra [36, 37] for I_2^-, Figure 2.10, and ICl^-, Figure 2.11. As expected the $B \leftarrow X$ peak is the largest of the peaks. Relative to the $B \leftarrow X$ peak, the $A' \leftarrow X$ peak is largest in I_2^-, smaller in IBr^-, and smallest in ICl^-. This follows the expected pattern when compared to the IX^- mixing, at R_e for the A' state. The most mixing occurs in I_2^- and the least in ICl^-. The $a' \leftarrow X$ peak in the simulated spectrum for I_2^- is not seen as this is a dipole-forbidden transition ($g \nleftrightarrow u$). This selection rule is lifted in the heteronuclear IX^- species and the mixing predicted from the spin-orbit operator introduces a peak in both IBr^- and ICl^-.

2.2.4 Minimum Energy $IBr^-(CO_2)_n$ Clusters

The minimum energy $IBr^-(CO_2)_n$ structures for the $IBr^-(CO_2)_n$ (n = 0-16), Figure 2.12, are constructed by sampling 201 configurations from a 1-ns trajectory on the IBr^- ground state having an average temperature of 80 K. These configurations are then quenched to local minima using Newton-Raphson minimization [95]. The energetic properties of the complete range of $IBr^-(CO_2)_{1-16}$ clusters are shown in Table 2.2.4.

To examine the energetics of $IBr^-(CO_2)_n$, we define a sequential binding energy,

$$\Delta_n = \mathrm{PE}_{n-1} - \mathrm{PE}_n \tag{2.15}$$

where PE_n is the potential energy of the cluster with n solvent molecules. In Table 2.2.4, we

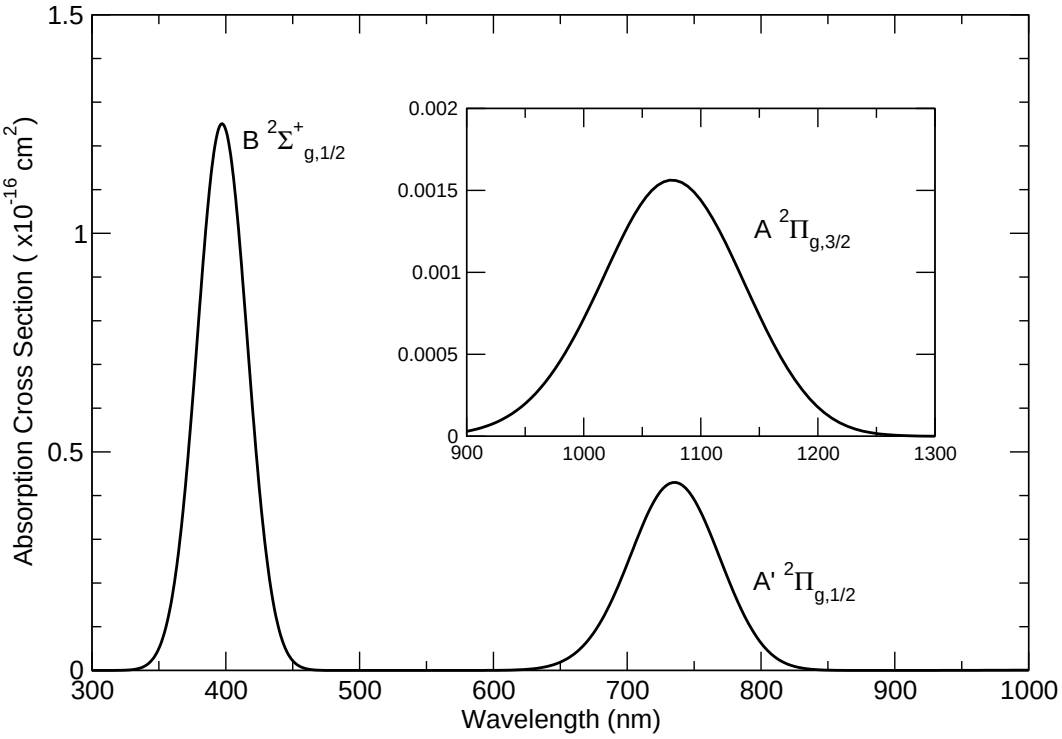

Figure 2.10: Calculated absorption spectrum for I_2^-. 10^{-16} cm^2 = 1 Å^2.

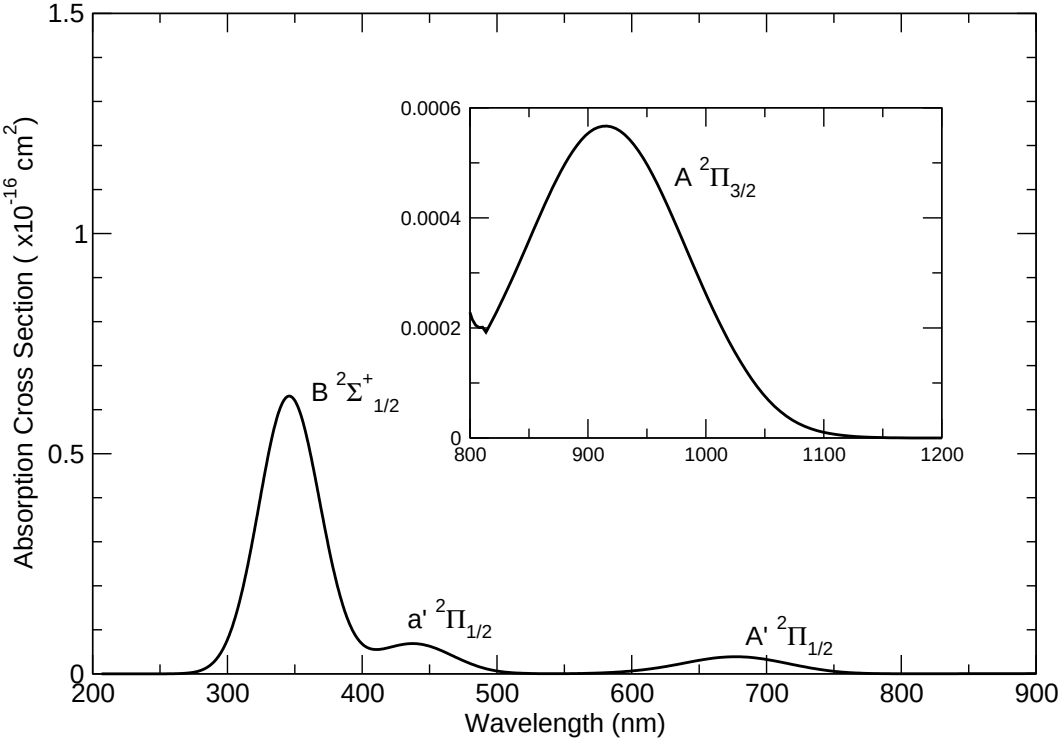

Figure 2.11: Calculated absorption spectrum for ICl^-. 10^{-16} cm^2 = 1 Å^2.

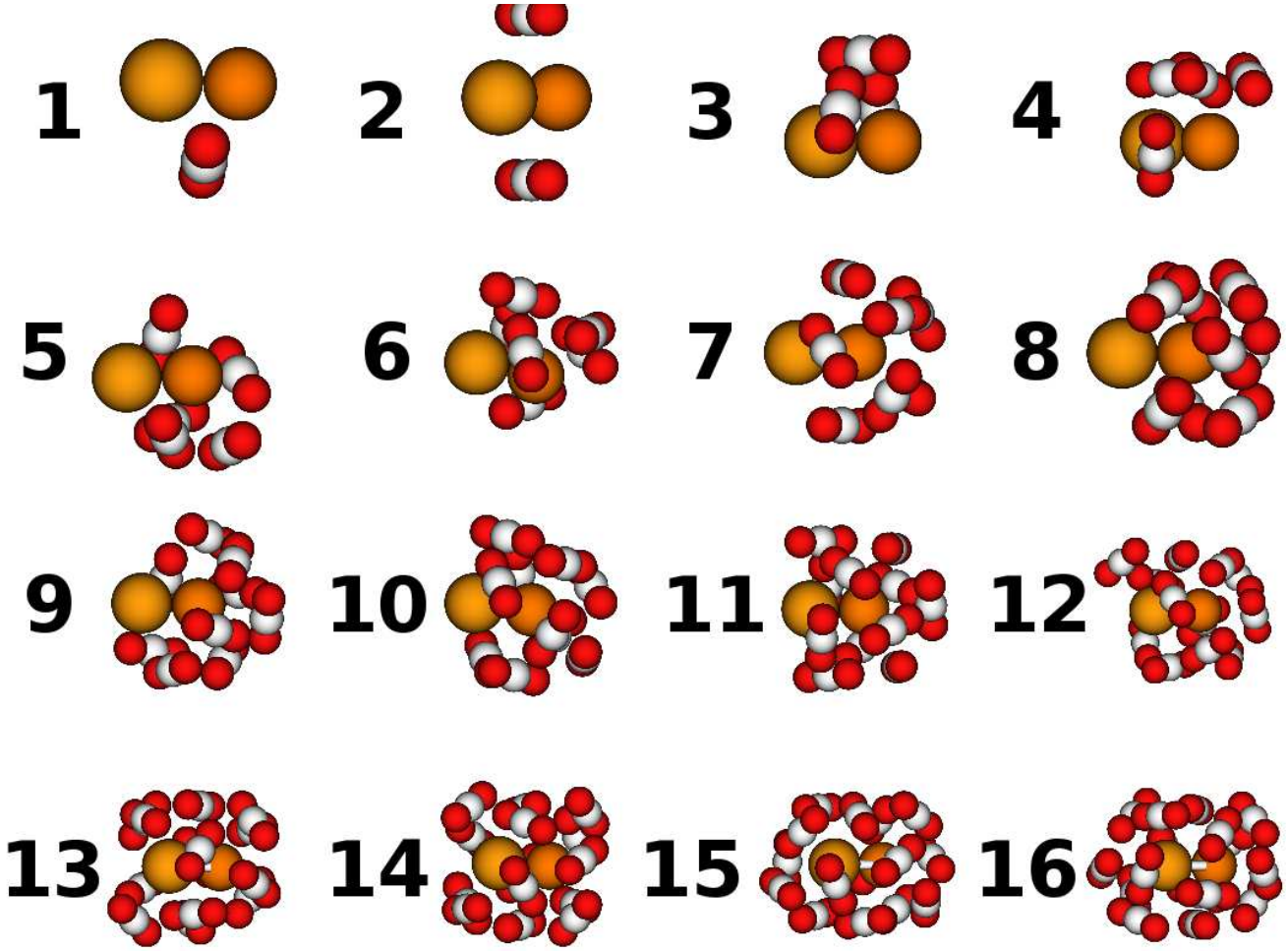

Figure 2.12: Minimum energy structures for $IBr^{-}(CO_2)_n$. The pattern for CO_2 filling is first around the I-Br bond, then the Br end, and finally the I end.

see the sequential binding energies for the minimum energy structures for $IBr^-(CO_2)_n$.

The first two clusters of $IBr^-(CO_2)_n$ in Table 2.2.4 show a Δ_n similar to that of I_2^- (Table 2.5); each cluster builds similarly at low n primarily due to similar energetics. $IBr^-(CO_2)_1$ and $I_2^-(CO_2)_1$ both have one CO_2 perpendicular to the bond at the bond center; with $n = 2$, the second is placed opposite the first CO_2, again perpendicular. These early sequential binding energies also compare reasonably well to previous measurements of $Br^-(CO_2)_{1-2}$ [54], although the calculated values are a bit lower than experiment, see also Subsection 2.2.5.

With the third CO_2, differences are seen as the filling is no longer at the bond center. Rather, the three solvent molecules interact favorably not just with each other, but with the bromine, lowering the sequential binding energy (SBE) in regards to $n = 1, 2$. A SBE of approximately 220 meV is seen until $n = 8$ where a particularly stable half-filled solvation shell is formed with maximum interaction with bromine. After this, the filling proceeds around the iodine end of IBr^- as the $I\cdots CO_2$ interaction takes over. Throughout the filling, the $CO_2\cdots CO_2$ interaction controls the solvent cage conformation. Starting with $IBr^-(CO_2)_3$, the favored T-shaped $CO_2\cdots CO_2$ geometry can be seen as the slightly negative oxygens prefer to point to carbons on other solvent molecules.

Experimentally, it was found that the average energy removal per CO_2 evaporated from IBr^- was 263 ± 12 meV [77]. A statistical model [122] estimated the kinetic energy associated with solvent evaporation at 40 meV, giving an average SBE of 223 meV for 7-15 solvent molecules on IBr^-. This compares favorably with the calculated values in Table 2.2.4.

2.2.4.1 Comparison to $I_2^-(CO_2)_n$ and $ICl^-(CO_2)_n$

Figure 2.13 and Table 2.5 show that $IBr^-(CO_2)_n$ is intermediate between I_2^- and ICl^-. In $I_2^-(CO_2)_n$, the clusters built predictably with SBEs on the order of 190-200 meV. In comparison, $ICl^-(CO_2)_n$ shows a strong contrast between the solvation of chlorine versus that of iodine. The CO_2 bind to the chlorine with approximately 280 meV until the "half-shell" of solvation around it is filled at $n = 6$. There are two reasons for this high SBE in the early solvation of ICl^-. First,

n	PE (meV)[a]	Δ_n (meV)[b]	-PE/n (meV)	$\Delta\Phi$ (meV)	# local minima
1	-205	205	205	-16	1
2	-406	201	203	-35	23
3	-627	222	209	-316	22
4	-852	225	213	-229	47
5	-1074	222	215	-340	65
6	-1301	227	217	-503	98
7	-1525	224	218	-936	104
8	-1775	251	222	-1113	63
9	-2009	233	223	-922	64
10	-2248	240	225	-784	112
11	-2483	234	226	-691	135
12	-2680	198	223	-444	111
13	-2917	237	224	-136	126
14	-3157	240	225	-144	143
15	-3380	223	225	54	131
16	-3588	208	224	-84	140

[a] Not including IBr^- bond energy (0.956 eV).
[b] See Eqn. 2.15

Table 2.4: Properties of minimal energy clusters of $IBr^-(CO_2)_n$ generated at 80 K.

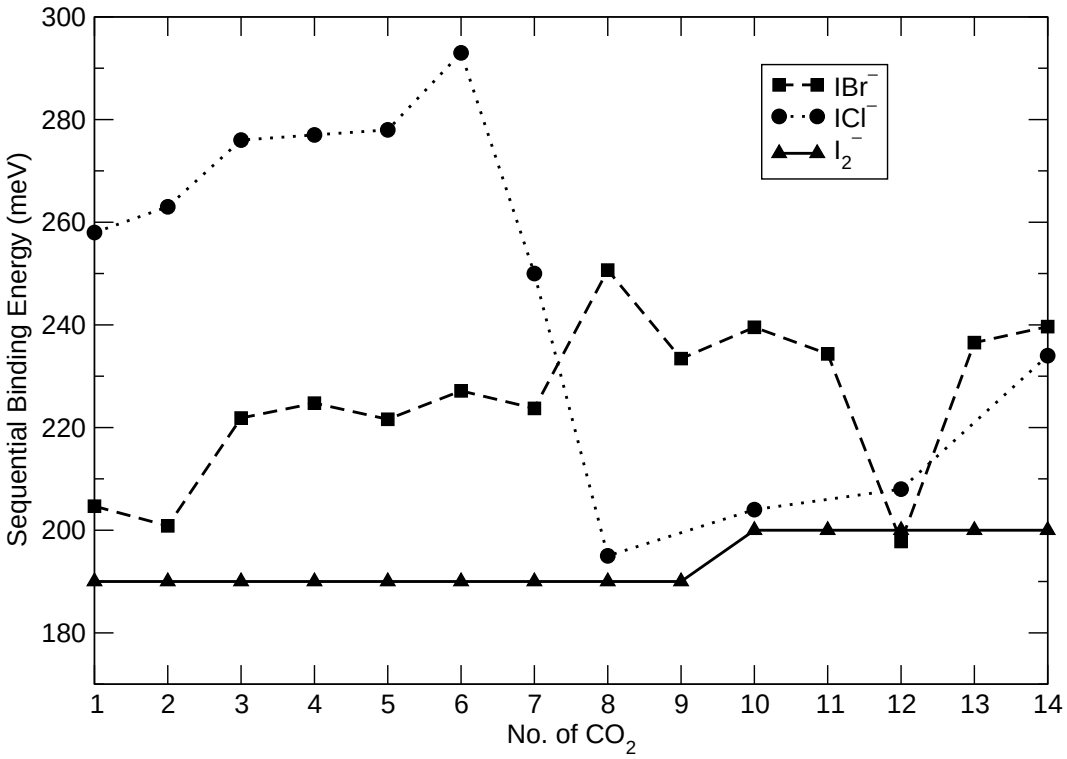

Figure 2.13: Sequential binding energies for $IBr^-(CO_2)_n$, $ICl^-(CO_2)_n$, and $I_2^-(CO_2)_n$ in meV.

n	$IBr^-(CO_2)_n$	$ICl^-(CO_2)_n$	$I_2^-(CO_2)_n$
1	205	258	190
2	201	263	190
3	222	276	190
4	225	277	190
5	222	278	190
6	227	293	190
7	224	250	190
8	251	195	190
9	233		190
10	240	204	200
11	234		200
12	198	208	200
13	237		200
14	240	234	200
15	223		200
16	208		200

Table 2.5: Sequential binding energies, Δ_n, for $IBr^-(CO_2)_n$, $ICl^-(CO_2)_n$ and $I_2^-(CO_2)_n$ in meV.

the chlorine is more electronegative and has a greater attraction to the solvent. Second, Cl^- is a small anion allowing tighter packing of CO_2 leading to more $CO_2 \cdots CO_2$ interactions. There is rapid decrease in SBE after $n = 6$ as the CO_2 find themselves solvating the iodine, which is less electronegative and larger. Finally, there is a slight increase at larger clusters as the CO_2 molecules are able to pack more efficiently.

For $IBr^-(CO_2)_n$, the first two CO_2 fill around the I-Br bond similar to $I_2^-(CO_2)_n$. From $n = 3$ to $n = 8$, $IBr^-(CO_2)_n$ then fills around the bromine, leading to a higher SBE due to favorable interactions. $IBr^-(CO_2)_8$ can be viewed as similar to $ICl^-(CO_2)_6$ as both mark the most asymmetric clusters in each system. At that point, the solvent shell is most concentrated around the more electronegative atom. Unlike $ICl^-(CO_2)_n$, $IBr^-(CO_2)_n$ does not have the large drop-off in SBE as the CO_2 begin to fill around the iodine. Indeed, the SBE slowly increases as solvent-solvent interactions become more favorable as in $I_2^-(CO_2)_n$.

The lone exception is $IBr^-(CO_2)_{12}$ which has a low SBE compared to other large clusters. This indicates that compared to both $n = 11$ and 13, that CO_2 does not form a particularly stable, minimum energy structure. To show this, we define the asymmetry of the solvent configuration, $\Delta\Phi$, as the energy required to move a charge of $-e$ from the I end to the Br end of a cluster [24]. Negative values describe a solvation that favors bromine, while positive values are those that favor iodine. Using this measure of solvent asymmetry, Figure 2.14 shows that $IBr^-(CO_2)_{12}$ has a labile ground-state configuration reflecting its less rigid solvent-shell structure. The labile configuration of $IBr^-(CO_2)_{12}$ will become important in later studies of ground-state recombination in Section 4.5.1.

2.2.5 Properties of $Br^-(CO_2)_n$ Solvation

The building of the minimal energy $IBr^-(CO_2)_n$ clusters is not the only cluster property that can be compared to previous work. The Neumark group [53,54] has explored the structure of $Br^-(CO_2)_n$ clusters which provides another check of the LJ parameters tabulated in Table 2.3. Table 2.6 presents the sequential binding energies for calculations of $Br^-(CO_2)_{1-16}$ for our

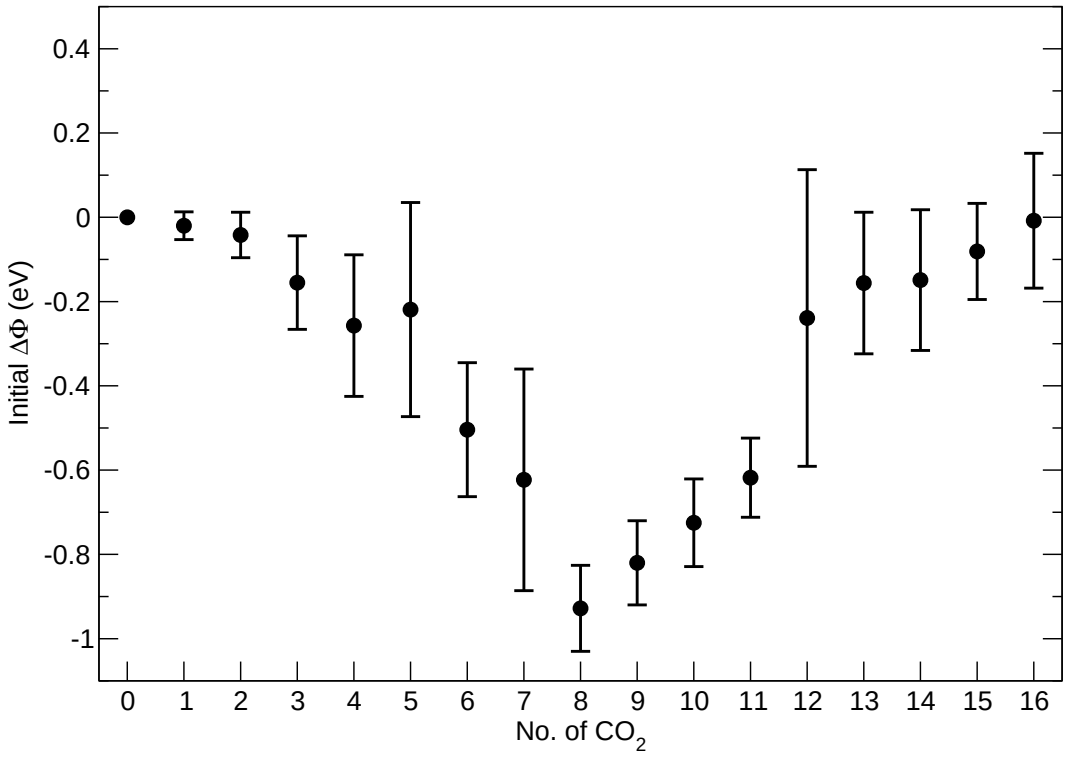

Figure 2.14: Average $\Delta\Phi$ in eV for 100, 60-K configurations of $IBr^{-}(CO_2)_{0-16}$ in the ground state. Error bars represent one standard deviation of the mean.

model, compared to experimental values.

While it is not immediately apparent from Table 2.6, our model predicts the completion of a solvent shell at $Br^-(CO_2)_{13}$. This was confirmed by viewing the cluster directly and seeing that in larger clusters the solvent molecules began filling in a second shell. At $Br^-(CO_2)_{13}$, the SBE suddenly decreases indicating that the solvent molecules are no longer binding with the more favorable $Br\cdots CO_2$ and $I\cdots CO_2$ interactions but rather through $CO_2\cdots CO_2$ interactions. Also, the calculated SBEs for the $Br^-(CO_2)_n$ filling are larger than that seen in experiment. The calculated values tend to average 250 meV or more over the first solvent shell, compared to around 200 meV in experiment.

Moreover, experiment predicts that the first solvent shell is complete at $Br^-(CO_2)_8$, much earlier than our simulated results. While this seems odd considering the higher calculated SBE, it is not entirely unexpected. As discussed in Section 2.2.2, our model's LJ parameters exhibit a $Br^-\cdots CO_2$ interaction that is both weaker and at a larger distance than the CCSD(T) calculations predicted, see Figure 2.7, in the T-shaped geometry.

To test whether this could be causing the larger solvent shell seen in Table 2.6, an alternate set LJ parameters were determined so that the MD model would return the same attraction as seen in the CCSD(T) curve from Figure 2.7. This CCSD(T) LJ fit shown in Figure 2.15 would then allow for tighter $Br^-\cdots CO_2$ binding which would lead to earlier $Br^-(CO_2)_n$ solvent shell completion. The new solvent binding pattern shown in Table 2.2.5 shows that this is indeed the case. Using the new CCSD(T) LJ fit, the $Br^-(CO_2)_n$ simulated clusters now complete a solvent shell at $Br^-(CO_2)_{10}$, 3 solvent molecules than before. This smaller solvent shell, however, is at the cost of an even larger average SBE for $Br^-(CO_2)_n$ interactions. (We do not calculate the $Br^-(CO_2)_n$ interactions for the MRCI fit seen in Figure 2.7 as this would lead us to even larger solvent shells.)

These findings might lead one to suspect that the LJ values used in the simulations, Table 2.3, will fail to work for $IBr^-(CO_2)_n$. Sections 3.4 and 4.7 will demonstrate that this is not true. The small amount of extra $Br\cdots CO_2$ binding energy the CCSD(T) LJ fit would provide

n	PE	Δ_n^a	-PE/n	$\Delta_n^{expt,b}$
1	-219	219	219	230
2	-470	251	235	219
3	-748	279	249	219
4	-1010	262	253	224
5	-1268	258	254	181
6	-1536	268	256	173
7	-1807	270	258	158
8	-2081	274	260	159*
9	-2342	261	260	77
10	-2629	287	263	79
11	-2857	228	260	21
12	-3090	234	258	...
13	-3296	206*	254	...
14	-3475	179	248	...
15	-3631	156	242	...
16	-3852	221	241	...

* First solvation shell complete.
[a] See Eqn. 2.15.
[b] Refs. 53 and 54.

Table 2.6: Properties of minimal energy $Br^-(CO_2)_n$ clusters. All energies in meV.

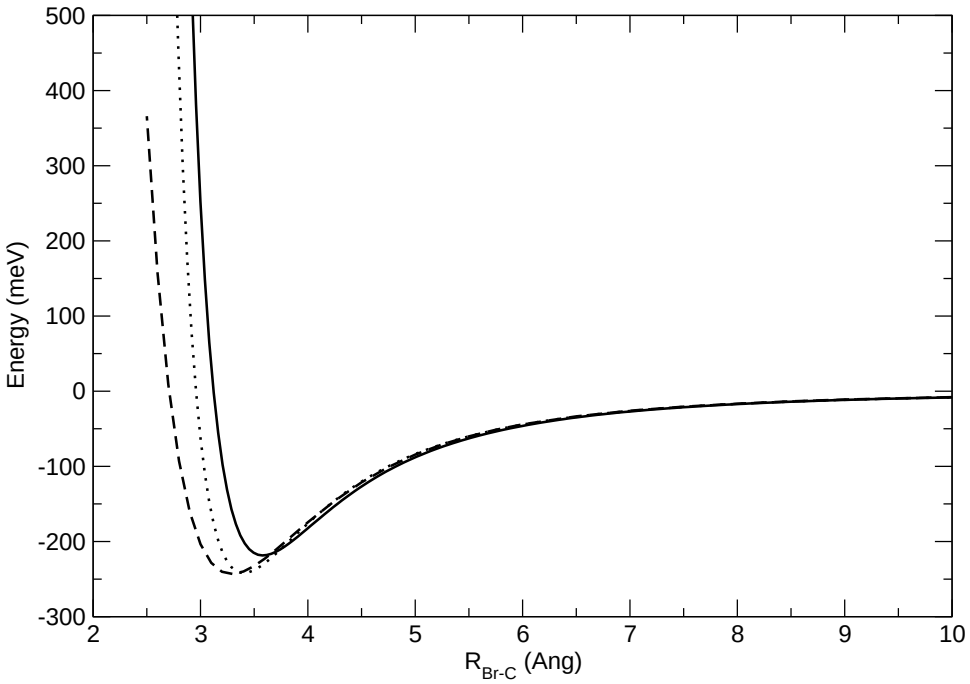

Figure 2.15: $Br^- \cdots CO_2$ potential energy surface calculated using the standard Lennard-Jones fit (solid) tabulated in Table 2.3 and the best Lennard-Jones fit (dotted) compared to CCSD(T) $Br^- \cdots CO_2$ interaction calculated using the MDF ECPs [100] for Br and aug-cc-pVTZ basis [118, 119] for C and O (dashed).

n	Δ_n^a	Δ_n^{CCFit}	$\Delta_n^{expt,b}$
1	219	242	230
2	251	269	219
3	279	295	219
4	262	279	224
5	258	274	181
6	268	280	173
7	270	300	158
8	274	273	159*
9	261	296	77
10	287	216*	79
11	228	199	21
12	234	169	...
13	206*	196	...
14	179	204	...
15	156	189	...
16	221	195	...

* First solvation shell complete.
[a] See Eqn. 2.15.
[b] Refs. 53 and 54.

Table 2.7: Comparison of sequential binding energies of minimal energy $Br^-(CO_2)_n$ clusters using standard $Br^- \cdots CO_2$ fit tabulated in Table 2.3 and a tight fit ("CCFit") to CCSD(T) calculations, see Figure 2.7. All energies in meV.

greatly affects the photodissociation dynamics of $IBr^-(CO_2)_n$, especially in larger clusters. This is due to the formation of an excited-state $IBr^-(CO_2)_n$ species which dominates the larger cluster dynamics, and the extra $Br\cdots CO_2$ binding leads to these excited-state $IBr^-(CO_2)_n$ species being **too** stable.

2.3 Conclusions

In summary, this chapter has described the techniques used to incorporate IBr^- into the molecular dynamics method first used by Maslen, Faeder, and Parson [26, 27, 36, 37] to explore the dynamics of I_2^- and ICl^- in various solvents. Quantum chemistry calculations of the six lowest spin-orbit states of IBr^- were performed using energy-consistent ECPs and it was found that, despite the small size of the basis set—compared to the size of all-electron basis sets for large halogens—very good energetic performance was achieved. When compared to recent photoelectron spectroscopy measurements of the ground-state binding energy, our calculations matched quite well. Likewise, photoelectron imaging experiments on the near-infrared (IR) excitation of IBr^- demonstrated reasonable agreement with our excited A' state energetics. Both of these have prime import when considering the near-IR (i.e., excitation to the A' state) simulations of the photodissociation of $IBr^-(CO_2)_n$.

With this potential energy surface and other associated properties of IBr^- calculated, we then proceeded to demonstrate how our model performs when calculating various properties of both the bare anion and clusters with solvating CO_2. Our calculated absorption spectrum for IBr^- had fair agreement with experimental findings and showed the expected periodic progression of peak strength when compared to I_2^- and ICl^- in line with the calculated spin-orbit mixing for these three ions.

We also showed the derivation of Lennard-Jones (LJ) parameters to help model the $Br\cdots CO_2$ interaction necessary for us to simulate $IBr^-(CO_2)_n$ dynamics. Calculations of the minimum energy clusters of $IBr^-(CO_2)_n$ using these compared favorably with the experimentally-found binding energy of CO_2 solvating IBr^-. Calculations of the $Br^-(CO_2)_n$ minimum

energy cluster properties had a lesser match with experiment, but were still fairly good.

Indeed, it is these differences with experiment that will be an important area of study in the following chapters detailing the near-IR and ultraviolet (UV) photodissociation dynamics of $IBr^-(CO_2)_n$. The differences in the ground-state well energetics for the bare ion will provide a test of the effect of excitation wavelength on the dynamics. Likewise, we saw in this chapter that our "standard" LJ parameters were chosen as a compromise between the calculated T-shaped and linear $Br^- \cdots CO_2$ interactions. However, as we saw when looking at the properties of the $Br^-(CO_2)_n$ clusters, there are tighter fits to our ab initio calculations of the $Br^- \cdots CO_2$ interaction that improved the match between the formation of the first solvent shell compared to experiment. We will see in future chapters that the dynamics of $IBr^-(CO_2)_n$ photodissociation are quite sensitive to model parameters and successes in $Br^-(CO_2)_n$ properties to not always imply success with the dynamics of $IBr^-(CO_2)_n$.

Chapter 3

Dynamics of $IBr^-(CO_2)_n$ Near-Infrared Photodissociation

In this chapter we will explore the dynamics of $IBr^-(CO_2)_n$ photodissociation following excitation at 790 nm in the near-infrared. We will first summarize the simulation methods used in constructing and running the trajectories used in our research. We will then present our simulated results for the product branching ratios for near-infrared (IR) photodissociation at 790-nm excitation and compare these results to experiment. We will also analyze the average number of CO_2 molecules lost after photodissociation.

After that, two sensitivity tests are described. As mentioned in Section 2.2.1.3, the calculated well depth for the ground state of bare IBr^- is shallower than that found in experiment. We will use a redder, 840-nm excitation in simulations to determine the effect of our standard curves on the photoproduct ratios. Likewise, in Section 2.2.2, we noted that the standard $Br^- \cdots CO_2$ Lennard-Jones (LJ) parameters used for simulation, tabulated in Table 2.3, do not exactly match the energetics of the calculated coupled cluster with single, double, and iterative triple excitations (CCSD(T)) $Br^- \cdots CO_2$ interaction. We will test the effects of different LJ parameters on the photodissociation product ratios and compare them to our standard fit.

3.1 Near-Infrared Trajectory Simulation Methods

All trajectories in this chapter use the molecular dynamics (MD) methods detailed in Section 2.1. Ensembles for near-infrared (IR) MD simulations are constructed via the following process. First, using the calculated minimum energy structures (Section 2.2.4), the cluster is

heated for 40 ps at a temperature of 60 K, followed by a 100-ps run on the ground state to test that the cluster energetics are stable. After that, ensembles are constructed by running a 2-fs time-step trajectory on the ground state that is sampled every 5 ps until 100 configurations are constructed. A long trajectory with a wide sample window is used in order to assure that the starting configurations for the simulations have sufficiently random geometries.

To start the photoproduct trajectories, the configurations of the constructed ensemble have their I-Br bond lengths adjusted to match the experimental photon energy of 790 nm. Since each of these excitations lies in the $A' \leftarrow X$ absorption band (Figure 2.9), only small adjustments are needed, on the order of 0.1-0.2 Å.

Trajectories are then run for a maximum of 50 ps. If the bond length exceeds 40 a_0, the trajectory is terminated and classified as dissociated. If more than 20 crossings of the ground-state well occur, the trajectory is considered to have recombined. A step-size of 1 fs is used for all trajectories which results in energy conservation on the order of $10^{-3}E_h$.

3.2 Simulated Near-Infrared Photodissociation Results

The first simulated 790-nm photodissociation results for 50-ps simulations of $IBr^-(CO_2)_n$ are compared to experimental results [79] in Figure 3.1. This figure details the three photoproduct channels of $IBr^-(CO_2)_n$ dissociation: I^--based, Br^--based, and IBr^--based products. As noted, these are the simulated product branching ratios for $IBr^-(CO_2)_n$ after **50 ps** of simulation run times. Unfortunately, it turns out that, despite the fairly good agreement to experiment, near-infrared (IR) photodissociation has additional complications which makes these results less useful. As will be detailed in Chapter 4, $IBr^-(CO_2)_{7-15}$ exhibit trapping on the A' state which can last for nanoseconds. The tools used to extract the simulated branching ratios shown in Figure 3.1 naively assumed that all IBr^--based product is ground-state recombination (GSR) product. However, a more detailed analysis of the 50-ps results shows that after 50 ps not all of the IBr^--based product has recombined in the ground state. The results of this analysis are shown in Figure 3.2.

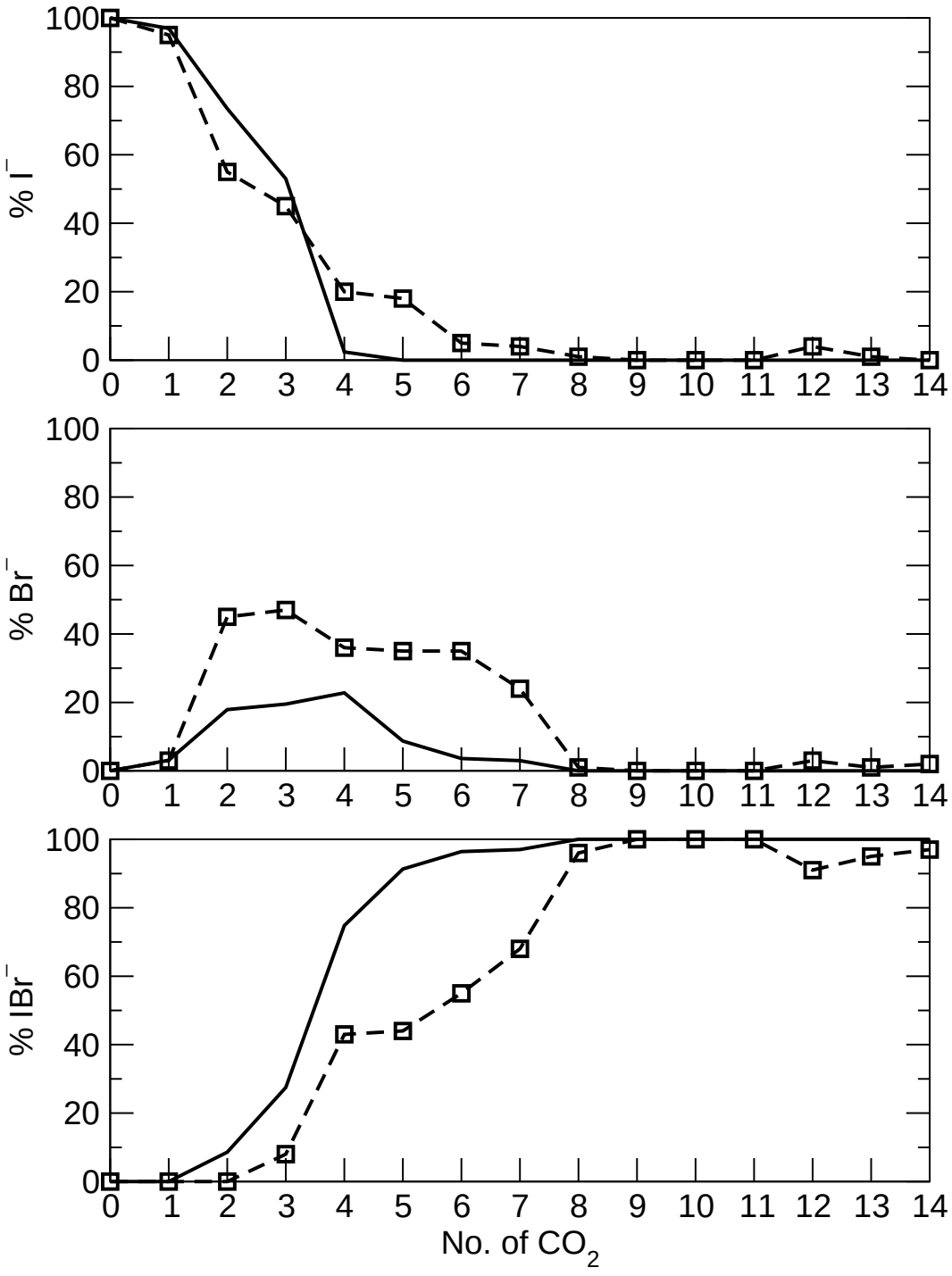

Figure 3.1: Near-infrared (790 nm) 50-ps simulated (dashed with squares) photodissociation product branching ratios for $IBr^-(CO_2)_n$. Experimental results (solid) from Sanford, et al [79].

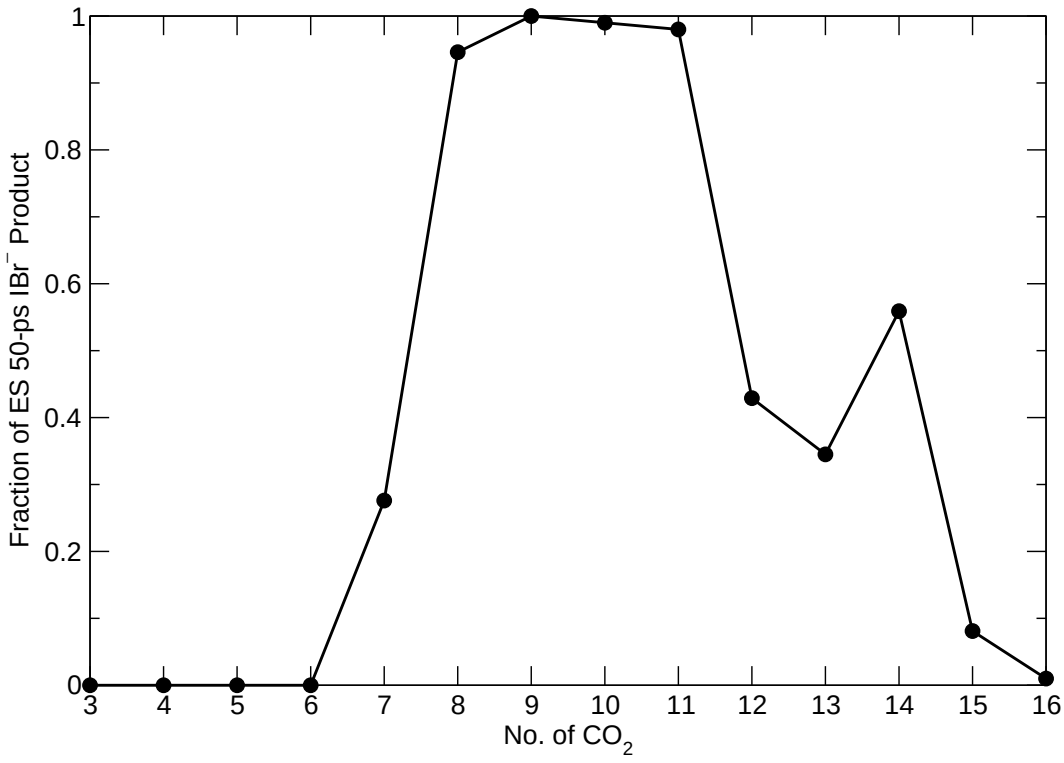

Figure 3.2: Fraction of IBr^- product trapped in the A' state at 50 ps as a function of cluster size.

Figure 3.2 shows the fraction of IBr^- products that are still trapped in the excited state after 50 ps over the range of 5-16 solvent molecules. It shows that beginning with $IBr^-(CO_2)_7$, the IBr^- product shown in Figure 3.1 are more correctly referred to as **excited-state trapped** IBr^-! The trapping dominates short-time dynamics up to $IBr^-(CO_2)_{12}$, beyond which the "fast" ground-state recombination channel begins to predominate.

The experimental products are counted after 5-10 μs of travel time to the mass spectrometer, by which time any IBr^- product has presumably relaxed to the ground state. The photodissociation experiments found that the recombined IBr^- products are produced with 5-6 CO_2 solvent molecules [77]. The average energy removal per CO_2 evaporated from IBr^- was determined to be 263 ± 12 meV. A statistical model [122] estimated the kinetic energy associated with solvent evaporation at 40 meV, giving an average sequential binding energy (SBE) of 223 meV for 7-15 solvent molecules on IBr^-, which, as previously discussed (Section 2.2.4) compares favorably with our simulated binding energies. Dissipation of a photon energy of 1.57 eV, 790 nm, would then require approximately 6 CO_2 evaporating at an SBE of 263 meV. Thus, a comparison of the simulated 50-ps results to experiment is not exact. Rather, a fairer comparison between simulation and experiment can be accomplished by extrapolating the product ratios to "infinite" time as seen in Figure 3.3. The extrapolated results were tabulated by use of nanosecond-long trajectories performed to simulate the ground-state recovery signal of $IBr^-(CO_2)_n$ [80] the details of which are described in Chapter 4.

Longer simulations performed for the clusters which demonstrate trapping show that the trapped products eventually dissociate or recombine in the ground state. We therefore hypothesize that the final dissociated/recombined product ratios after nanoseconds of simulation time are the same as that at completion. Any remaining trapped product is apportioned according to the fraction that finished in each product channel. With this procedure, Figure 3.3 shows only final ground-state IBr^- product, and not both excited- and ground-state product. While it would be preferable to run simulations until all trajectories had transited through the excited state, in some cases this would require tens of nanoseconds of simulation. This extrapolation

procedure provides our best estimate of how the simulations would conclude if run to completion.

This new extrapolated data allows us to better compare the simulations to experiment. We see that, unlike experiment where the I^--channel closes at $IBr^-(CO_2)_5$, the simulations show it to be open to $IBr^-(CO_2)_{13}$. Second, the Br^--channel is both exaggerated in number in simulation and stays open in larger clusters. This is especially true in smaller clusters where simulation predicts a larger fraction of Br^- than seen in experiment. By comparing the pattern of the additional Br^- product to what is "missing" from the IBr^- channel, the larger bromine product seems to be at the expense of what experimentally is recombined product. This suggests that the model might underemphasize the strength of the $I\cdots Br$ interaction or, perhaps, the solute-solvent interactions allow for too facile dissociation. Nevertheless, the simulations show a similar pattern of Br^--product increase and decrease up to $IBr^-(CO_2)_7$.

With the larger clusters, $IBr^-(CO_2)_8$ and beyond, both experiment and simulation predict that the major product will be ground-state recombined IBr^-. One significant difference is that simulation still reports small amounts (approximately 5%) of I^- and larger amounts of Br^- product at nearly every cluster size, while, experimentally, the atomic anion channels are closed at $IBr^-(CO_2)_8$.

Overall, however, there is reasonable agreement between the trends displayed in the simulations and experiments. While both I^- and Br^- products are more prevalent in simulation, the simulated product ratios correctly predict the patterns of each channel.

3.2.1 A Closer Look at the Three Product Channels

In this section, we investigate the three product channels for $IBr^-(CO_2)_n$ in more depth. Figure 3.4 presents the smallest and simplest cluster for which both dissociation channels appear, $IBr^-(CO_2)_1$. These plots document the adiabatic energies (top), the charge character of the cluster (middle), and the I-Br bond length over the run-time of the simulation. Both trajectories exhibit rapid dissociation of the cluster along with charge localization onto the io-

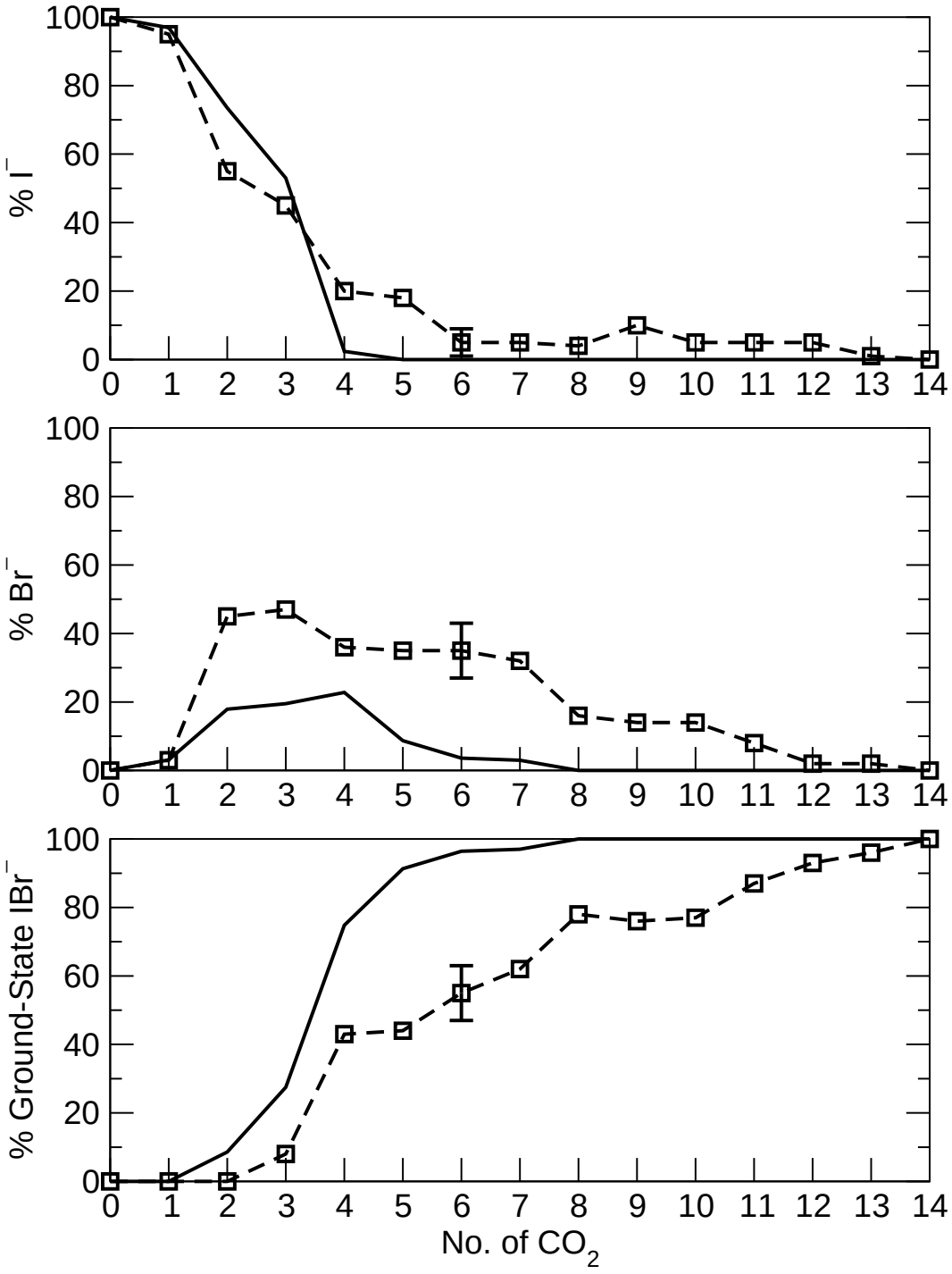

Figure 3.3: Near-IR (790 nm) photodissociation product branching ratios for $IBr^-(CO_2)_n$. Simulated results (dashed with squares) based on an "infinite" time scale extrapolation. Experimental results (solid) from Sanford, et al [79]. Error bars are 1σ sampling error for $n = 6$ and is representative of that at other cluster sizes.

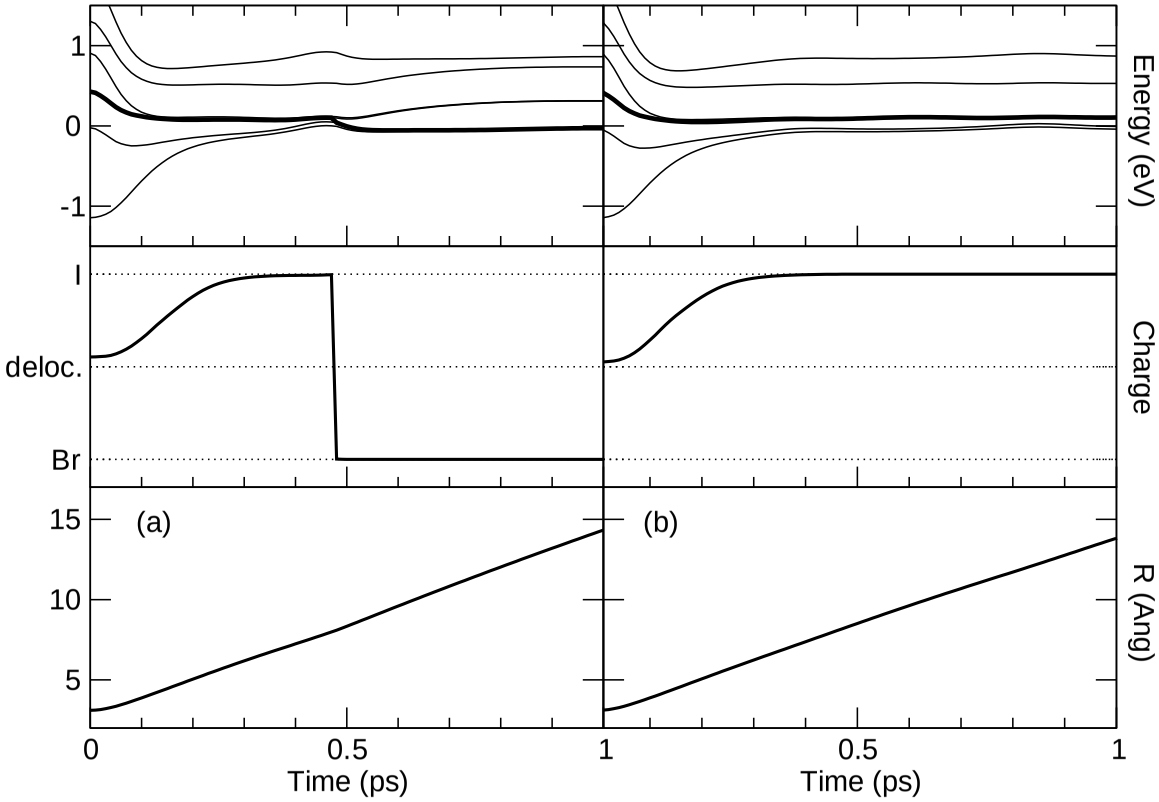

Figure 3.4: Near-infrared (790-nm) photodissociation of two exemplar $IBr^-(CO_2)_1$ trajectories. The adiabatic energies are plotted in the first row as a function of time with the bold line being the occupied state. The second row plots the charge character of the trajectory over time. The third row plots the I-Br bond length over time. (a) shows a trajectory that dissociates to Br^- and (b) shows a trajectory that dissociates to I^-.

dine, as the bond extends. Figure 3.4(b) shows a trajectory which then continues along the A' state producing I^- product. Figure 3.4(a), however, is an example trajectory where the solvent interaction causes a nonadiabatic hop to a lower state. This hop, which occurs around 500 fs, causes an immediate charge transfer in the solute reflecting the different character of the new state. The cluster then dissociates leading to Br^-. In each case, the trajectories dissociate on the expected states from the IBr^- bare ion potential energy surface (PES), Figure 2.1.

The simple picture provided by the $IBr^-(CO_2)_1$ trajectories begins to break down as the clusters grow larger. The greater and more numerous solute-solvent interactions lead to more complicated dynamics. Three exemplar trajectories for $IBr^-(CO_2)_6$ that result in the three product channels —Br^-, I^-, and ground-state recombined product—are presented in Figure 3.5.

The exemplar trajectory that results in Br^- dissociation, Figure 3.5(a), shows a trajectory that dissociates (i.e., reached 40 a_0) to $Br^-(CO_2)_4$ in 16 ps. This trajectory exhibits rather interesting dynamics. After excitation, the solute begins to dissociate reaching over 6 Å before the solvent arrests the escape. At the same time, the charge fluctuates on the solute until it localizes on the bromine. At that point, the cluster "explores" a region at 4-7 Å before finally dissociating at 8 ps. This sort of "exploration" is not uncommon as the solvent is exerting forces on both solute atoms to contain the cluster. Indeed, as in Figure 3.5(a), the charge can be completely localized on one solute atom, and yet the strong solute-solvent interactions are enough to hold the cluster together for several picoseconds. This is contrasted to the $IBr^-(CO_2)_1$ trajectories, Figure 3.4, where the single solvent molecule can cause a nonadiabatic hop, but there aren't enough interactions to stop dissociation.

Figure 3.5(b) shows an example of a trajectory that dissociates to $I^-(CO_2)_6$, with dissociation being so rapid that no solvent is able to escape before the 40 a_0 limit is reached. In contrast to the previous Br^- trajectory, though, this trajectory does not "explore" but rather explodes apart as the charge localizes on the iodine, reaching 10 Å in just over 2 ps. One interesting thing to note in Figure 3.5(b) is the energetics. As the charge localizes on the iodine and the I-Br bond dissociates, the cluster is on the **lowest** energetic state. This might be surprising

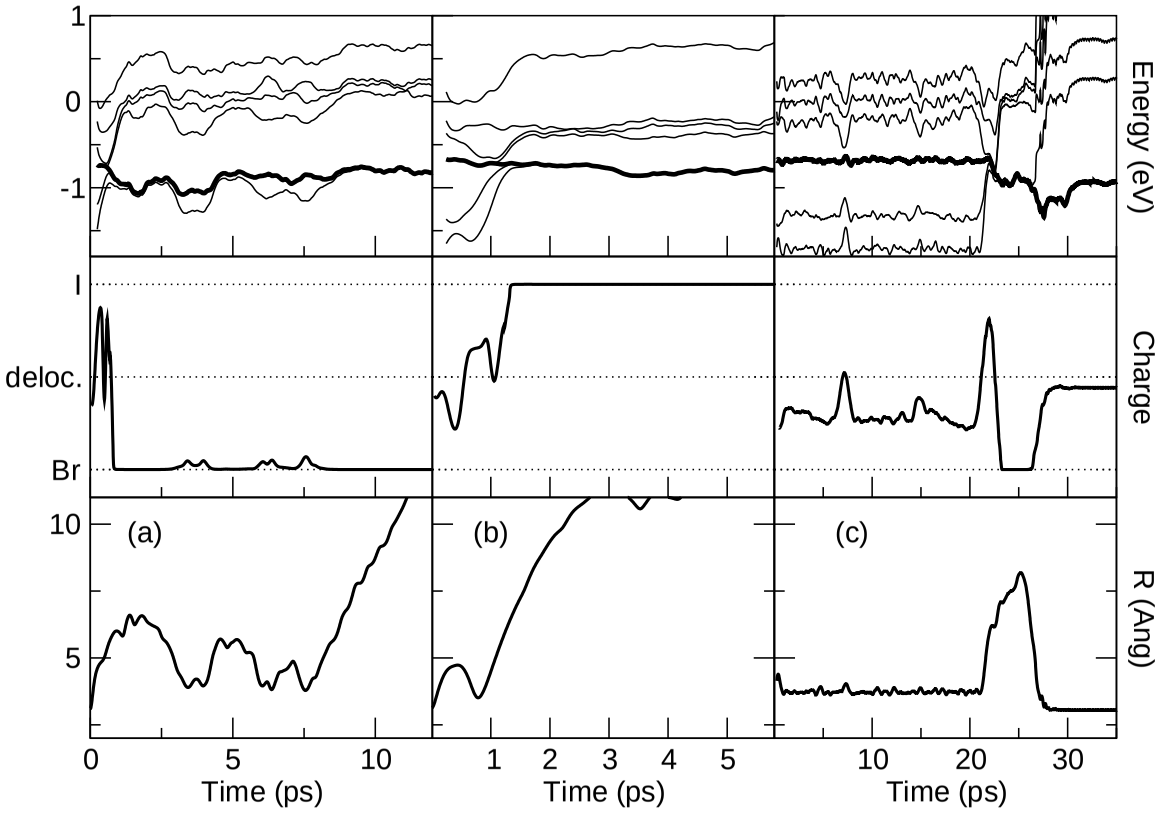

Figure 3.5: Near-infrared (790-nm) photodissociation of three exemplar $IBr^-(CO_2)_6$ trajectories. The adiabatic energies are plotted in the first row as a function of time with the bold line being the occupied state. The second row plots the charge character of the trajectory over time as a 10-point moving average to smooth out some fluctuations. The third row plots the I-Br bond length over time. (a) shows a trajectory that dissociates to Br^-. (b) shows a trajectory that dissociates to I^-. (c) shows a trajectory that recombines in the ground state, with the energies being plotted as a 50-point moving average to eliminate vibrational grassiness.

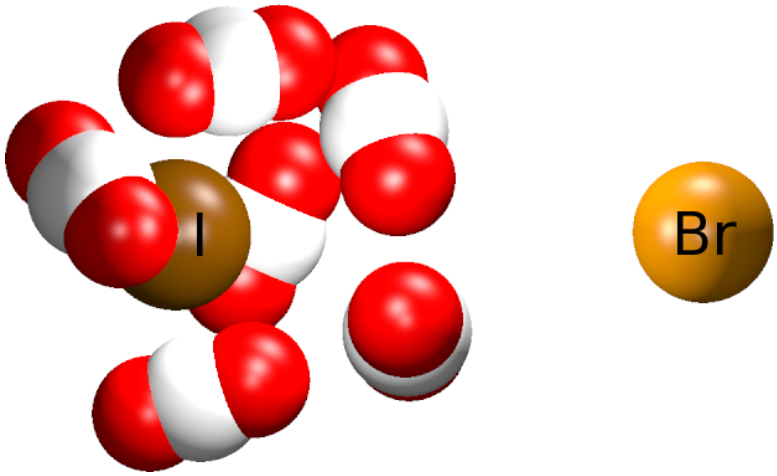

Figure 3.6: Example dissociating $IBr^-(CO_2)_6$ cluster showing solvated I^-, qv. Figure 3.5(b).

given our expectation that I^- product should dissociate on the second-lowest asymptote of our bare ion PES, Figure 2.1. However, one must remember that that PES is for the **bare** anion. In Figure 3.5(b), the state energies show the effect of the solvent configuration at each point in the trajectory. Since this trajectory dissociates to I^-, at later times, the configuration is one with solvent surrounding the I^-, Figure 3.6. In this configuration, states corresponding to Br^- are therefore in a less favorable solvent configuration and are **higher** in energy. The lowest energy state for this solvent configuration has the charge on iodine, and it is this state upon which dissociation takes place. The analogous phenomenon in Br^- dissociation can be seen in Figure 3.5(a,top). After the charge localizes on bromine following the hop to the lower state, the state corresponding to I^- is suddenly less energetically favored and it increases in energy relative to the Br^- states.

Figure 3.5(c) is an example of a trajectory that ends as IBr^- recombined on the ground state after 30 ps. Viewing all three sets of data together, for the first 20 ps, the cluster seems to be trapped on the A' state around roughly 4 Å in a delocalized charge state. Then, suddenly, the cluster hops to a lower state and the I-Br bond begins to stretch. From the charge localization plot, the cluster assumes a Br^- character but it is prevented from dissociating by the solvent which reforms IBr^-. The cluster then hops to the ground state where it falls into the well and

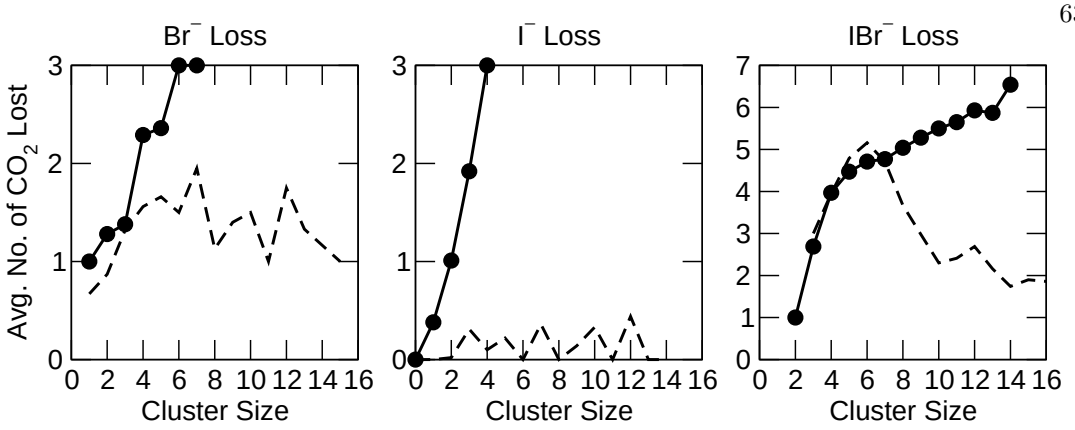

Figure 3.7: Experimental (solid line with circles) and simulated (dotted line) results for the average CO_2 loss for $IBr^-(CO_2)_n$, $n = 0 - 16$. Experimental results from Sanford [77].

vibrationally relaxes, evaporating solvent molecules. At this point the solute has reformed and the charge is widely delocalized, albeit polarized towards bromine as electronegativity would predict for the ground state. This phenomenon of excited-state trapping becomes a major theme for $IBr^-(CO_2)_{7-11}$, where solvent flow plots, previously developed by our group [24], are used to better analyze the trajectories that are trapped and how they escape and recombine to the ground state. These ideas are developed in Chapter 4 which examines the ground-state recombination dynamics for near-IR trajectories.

3.3 Average CO_2 Loss in Near-Infrared Photodissociation

In this section the average solvent loss at the end of a simulation is compared to the products seen in experiment. These results are presented in Figure 3.7. The poor match between the experimental and simulated results in Figure 3.7 might perhaps raise a cause for alarm given our group's success with solvent loss prediction in $I_2^-(Ar)_n$ [23]. Argon, however, is a much more loosely bound solvent than CO_2. In the experiment, the clusters have microseconds of travel time to reach the mass spectrometer detector. In comparison, the simulations end in two ways that could affect our modeling of solvent loss. First, with the dissociated product, the simulations end once the I-Br bond length exceeds 40 a_0 in length since recombination at that distance is

simply not possible. Second, for recombined products, the simulations end after 20 "crossings" of the ground state. In either case, these criteria are met in picoseconds of simulation time once either process has begun, even if there were nanoseconds of trapping. Thus, with the recombined products, the process of vibrational relaxation of the solute, which would result in boiling of the solvent as the cluster relaxed to the bottom of the ground state well, is cut off from the time it needs to complete the process. Moreover, the time required to simulate equilibrium mass distributions is extremely long. Even when IBr^- is fully relaxed, it can take a long time for evaporation to take place. For this reason, simulation of the mass distribution for CO_2 clusters has never been reliable.

In order to test these hypotheses, a few simple simulations were run. Simulation of $IBr^-(CO_2)_4$ were run and the dissociated products were allowed to run to double the normal dissociation I-Br separation, 80 a_0. Doing so increased the numbers of CO_2 lost by almost half a solvent molecule. While this doesn't prove much, it does show that a "longer" dissociation threshold does result in the expected behavior.

Likewise, to test the recombined process, simulations of $IBr^-(CO_2)_{13}$, a large cluster with a fast ground-state recombination (GSR) time, were run with parameters of 100 and 500 ground-state crossings. The results showed that from $20 \rightarrow 100 \rightarrow 500$ crossings, the average CO_2 loss grew from $1.33 \rightarrow 2.98 \rightarrow 3.96$, just as would be expected.

3.4 Sensitivity of Near-Infrared Photoproduct Ratios to Excitation Wavelength

In Section 2.2.1.3, the question was raised as to whether the calculated ground-state well depth, when compared to experiment, would present difficulties when it came time to simulate the dynamics of $IBr^-(CO_2)_n$ photodissociation. The existence of two measures of the experimental D_0 for IBr^- leads to two logical tests. First, we will assess the effect of less kinetic energy release in the photodissociation of $IBr^-(CO_2)_n$ by using a redder, 840-nm excitation to model the deeper, experimental well. Then, we will test the more recent findings of a D_0 almost

equal to the calculated D_e for IBr^- by incorporating the effect of zero-point energy (ZPE) offset by using a slightly bluer, 770-nm excitation.

In order to test these effects, trajectories were assembled for $IBr^-(CO_2)_{1-14}$. Each ensemble was composed of 100 trajectories assembled in the same fashion as before. The trajectories ran with a classical time-step of 1.0 fs for durations of 100 ps for $IBr^-(CO_2)_{1-6}$, 400 ps for $IBr^-(CO_2)_{7,12,13}$, and 5000 ps for $IBr^-(CO_2)_{8-11,14}$. If the bond length exceeds 40 a_0, the trajectory was terminated and classified as dissociated. If more than 20 crossings of the ground-state well occur, the trajectory was considered to have recombined.

The resulting product ratios for the 840-nm and 770-nm runs are compared to the 790-nm and experimental results in Figure 3.8. The differences between the 840-nm, 770-nm, and 790-nm runs are minimal. Indeed, the I^- and Br^- product channels at 840 nm seem to be only slightly worse when compared to experiment than the results from the 790-nm studies. The slightly larger kinetic energy release (KER) provided by the 770-nm excitation does lead to results that are slightly better than the 790-nm simulations at small cluster sizes, but the effect is negligible at larger clusters. Indeed, the 770-nm and 840-nm photoproduct ratios seem to be roughly within the sampling error of the 790-nm results.

Thus, the possible under- or overestimation of the calculated ground-state well depth of IBr^- with respect to experiment has little effect on the near-infrared (IR) photodissociation branching ratios for $IBr^-(CO_2)_n$. However, this is not the final test of excitation wavelength on the dynamics of $IBr^-(CO_2)_n$ photodissociation. As stated above, the intermediate-size and larger clusters of $IBr^-(CO_2)_n$ (i.e., $n \geq 8$) demonstrate trapping on the excited A' state which necessitated the use of extrapolated results. We will see in Section 4.6 that the effects of excitation wavelength on the ground-state recombination (GSR) recovery dynamics are more profound.

We note for completeness that the 840-nm photoproduct branching ratio results for $IBr^-(CO_2)_{8-11}$ are not included in Figure 3.9. These trajectories were so long-lived that only around 10 of the 100 trajectories set up ran to completion in the allotted run-time after a month

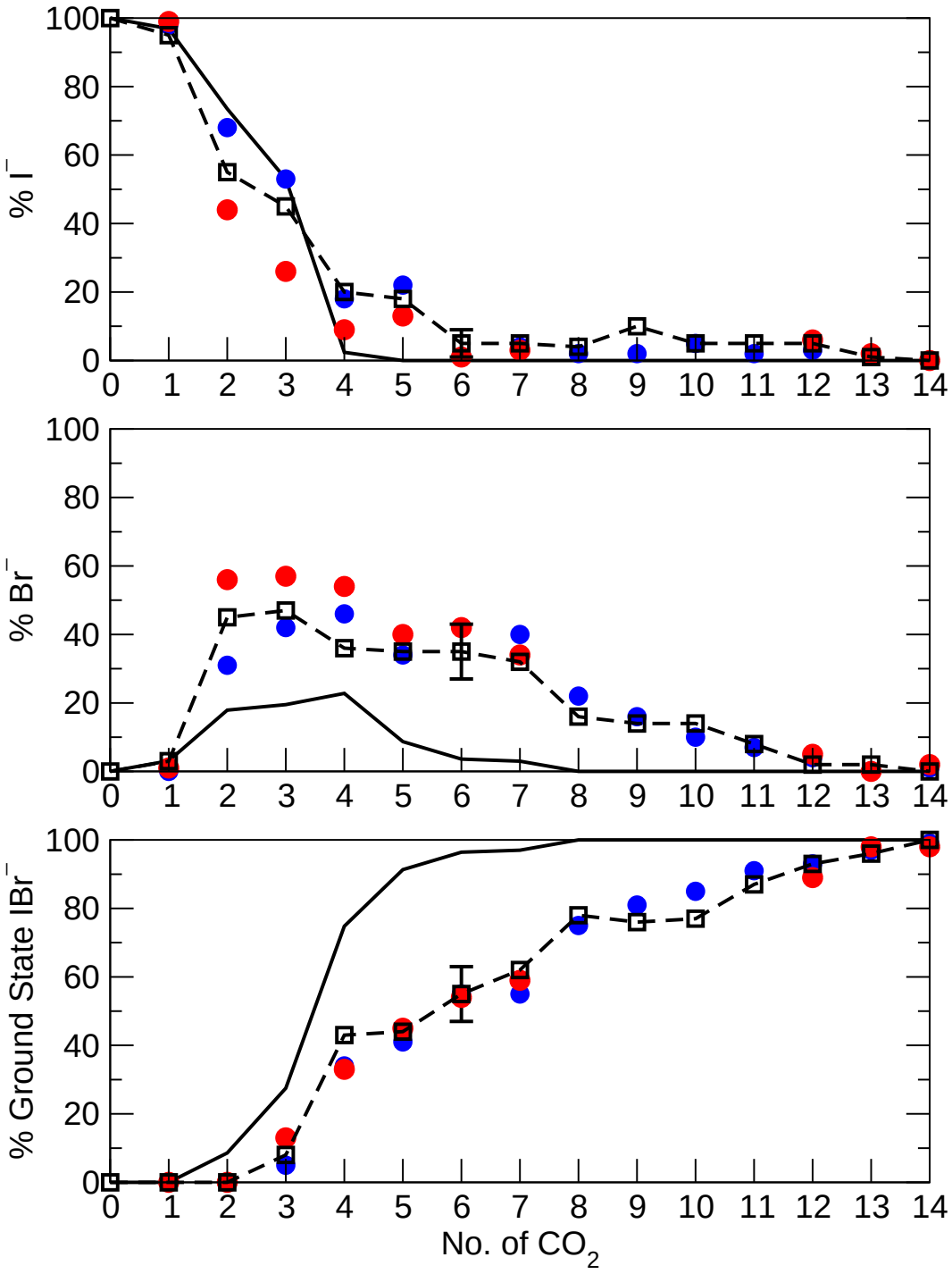

Figure 3.8: Near-infrared simulated 790-nm (dash with square), 840-nm (red circle), and 770-nm (blue circle) photodissociation product branching ratios for $IBr^-(CO_2)_n$. Simulated results based on an "infinite" time scale extrapolation. Experimental results (solid line) from Sanford, et al [79]. Error bars are 1σ sampling error for $n = 6$ and is representative of that at other cluster sizes.

of compute time. The reason for this extremely long duration is explored in Chapter 4 which examines the GSR dynamics of $IBr^-(CO_2)_n$. The 840-nm excitation has a much greater impact on the GSR dynamics compared to the photoproduct branching ratios. However, we would expect that the 840-nm results for $IBr^-(CO_2)_{8-11}$ would approximate the 790-nm and 770-nm results as the reported ratios do.

3.5 Sensitivity of Near-Infrared Photoproduct Ratios to Lennard-Jones Parameters

In Section 2.2.2 it was noted that the standard Lennard-Jones (LJ) parameter fit to the $Br^- \cdots CO_2$ interaction, tabulated in Table 2.3, was slightly less attractive than the well depth for the $Br^- \cdots CO_2$ T-shaped geometry calculated at the coupled cluster with single, double, and iterative triple excitations (CCSD(T)) level of theory (Figure 2.7). In order to explore the effect of this on the dynamics simulations, an alternate set of LJ parameters was determined that matched the energetics of the CCSD(T) fit as shown in Figure 2.15. A similar set of LJ parameters was determined that matched the $Br^- \cdots CO_2$ T-shaped energetics predicted by a multireference configuration interaction (MRCI) calculation of the system. This MRCI prediction is shown in Figure 2.7 and it is shallower even than the standard LJ fit.

In order to test the effect of the LJ fit parameters on photoproduct ratios, trajectories were assembled for $IBr^-(CO_2)_{1-14}$. Each ensemble was composed of 100 trajectories assembled in the same fashion as before. The trajectories were run with a classical time-step of 1.0 fs for durations of 50 ps for $IBr^-(CO_2)_{1-6}$ and 3000 ps for $IBr^-(CO_2)_{7-14}$. If the bond length exceeded 40 a_0, the trajectory was terminated and classified as dissociated. If more than 20 crossings of the ground-state well occur, the trajectory was considered to have recombined. The results of these simulations are shown in Figure 3.9.

For the smaller clusters, the influence of the alternative LJ parameters appears negligible. For $n \leq 6$, the coupled cluster (CC) fit leads to much the same ratios as the standard fit for all the product channels. The configuration interaction (CI) fit seems to give better results for

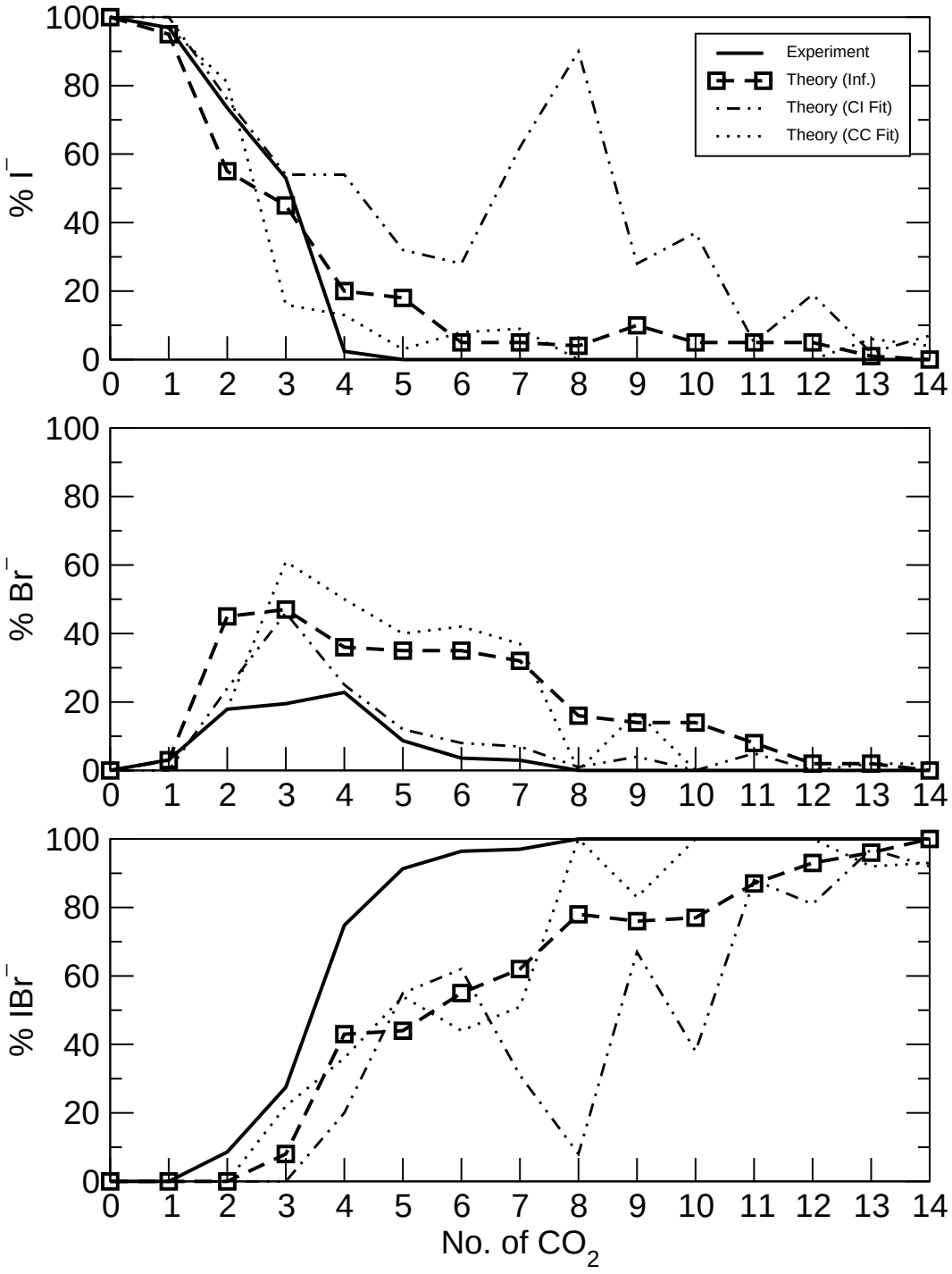

Figure 3.9: Branching ratios for near-infrared (790-nm) photodissociation including results for tight Lennard-Jones fits to MRCI (dot-dash) and CCSD(T) (dot) $Br^- \cdots CO_2$ data as seen in Figure 2.7, as well as the normal Lennard-Jones fit from Table 2.3 (dash with squares) and experimental data from Sanford, et al [79].

the Br^- channel, but at the expense of the I^- channel which is much too prevalent. This can be explained by the fact that the CI fit leads to a $Br^- \cdots CO_2$ interaction that is less attractive than the $I^- \cdots CO_2$ interaction, thus favoring the I^- channel.

In larger clusters, the CI fit results in more extreme behavior. The I^- channel is much too large at the expense of the ground-state recombination (GSR) IBr^- channel, especially for $IBr^-(CO_2)_8$ where the CI fit leads to near total domination of the I^- channel with severe depletion of the IBr^- products. This larger I^- channel trend continues even up to $IBr^-(CO_2)_{12}$.

Comparing the CC fit results to the standard fit in Figure 2.15, it would seem that the tighter CC fit would provide the best LJ parameters. As the cluster size grows, the IBr^- channel dominates the product ratios much faster than the standard fit, although there is less agreement when comparing the Br^- channel in $IBr^-(CO_2)_{3-7}$. For this channel, the overproduction of Br^- product from the standard fit is enhanced making it worse. Despite this overenhancement of the Br^- channel, though, the better fit with ground-state recombination (GSR) IBr^- product would seem to favor the use of the CCSD(T) LJ parameters.

However, as shown in Chapter 4, the CC fit results in ground-state relaxation times that are much too long compared to experiment, whereas the standard fit provides a better match to the experimental trends. For consistency, we have therefore relied primarily upon the standard fit for analyzing the time-independent data in this chapter.

3.6 Conclusions

Simulations of the near-infrared (IR) photodissociation of $IBr^-(CO_2)_n$ were performed and compared to experiment. We found that 790-nm excitation to the A' state leads to dynamics in larger clusters that cannot be studied on the tens-of-picoseconds scale. As will be shown in Chapter 4, these dynamics correspond to trapping on the A' state which can occur for many nanoseconds. By extrapolating long-duration simulations to predict their products if run to completion, our simulations show reasonable agreement to experiment, Figure 3.3. The simulations tend to overestimate dissociation at the expense of ground-state recombined IBr^-

product, but the general pattern demonstrated in experiment is largely duplicated. Using exemplar trajectories for $IBr^-(CO_2)_1$ and $IBr^-(CO_2)_6$, we were able to detail how increasing solvent begins to alter the properties of the system. The larger solvent environment of $IBr^-(CO_2)_6$ led to interesting dynamics such as rapid charge localization leading to state energetics that differed from expectations if one were to only use the bare ion curves, Figure 2.1, as reference.

Sensitivity tests on the near-IR photodissociation dynamics were also described. The first explored the use of a redder, 840-nm excitation to model a shallower, calculated ground-state well depth compared experiment which leads to less kinetic energy release (KER) upon excitation. We found that the 840-nm excitation had little effect on the photoproduct channels of $IBr^-(CO_2)_n$. Newer photoelectron spectroscopy experiments on IBr^- have provided a different, shallower D_0 value which, when zero-point energy is taken into account means the standard 790-nm simulation is too red. To model this effect, a slightly bluer, 770-nm excitation was modeled and the photoproduct ratios of $IBr^-(CO_2)_n$ again showed little effect. A greater effect was seen in the other sensitivity test described, that of the Lennard-Jones (LJ) parameters used in the molecular dynamics (MD) model. We found that a more attractive, tighter fit to the calculated coupled cluster with single, double, and iterative triple excitations (CCSD(T)) T-shaped $Br^- \cdots CO_2$ interaction led to slightly better photoproduct ratios than that of the standard fit presented in Table 2.3.

However, tests performed on the sensitivity of the ground-state recombination recovery times of $IBr^-(CO_2)_n$ in Chapter 4 to both excitation wavelength and the LJ parameters will show a more profound effect. The small effects seen on the photoproduct ratios due to excitation wavelength will contrast with the large effects seen on the ground-state recovery times, often improving our performance relative to experiment in contrast to the findings in this chapter. Likewise, we will show that the CCSD(T) fit leads to a worse match with the experimental ground-state recombination recovery times. This shows the need to balance various criteria when selecting parameters for the MD model. If we had selected the tighter CCSD(T) fit as our primary parameters based on its performance in the photoproduct ratios, the successes that

will be seen in Chapter 4 using the standard fit may have been missed.

Chapter 4

Ground-State Recombination Dynamics in $IBr^-(CO_2)_n$ Near-Infrared Photodissociation

In this chapter we will focus on the ground-state recombination (GSR) dynamics of $IBr^-(CO_2)_n$ near-infrared (IR) photodissociation. We hinted that these dynamics were the source of the oddities seen in the short-time photoproduct ratios in the previous chapter. We will begin by laying down a brief overview of the theoretical methods we will be using in these simulations.

We will start our investigation not with the smallest $IBr^-(CO_2)_n$ clusters that demonstrate GSR, but rather with the cluster that started the investigation historically in experiment: $IBr^-(CO_2)_8$. During this analysis, we will explore the excited-state trapping that characterizes the long-time recombination dynamics. We will also introduce our main tool to view these trajectories, the solvent flow plot, which allows us to view the interplay of solute and solvent geometries over the course of a trajectory. With these plots, we will plainly see the trapping as well as the transition state whose barrier we believe causes the dynamics to occur at longer times than was assumed.

After the focus on $IBr^-(CO_2)_8$, we will then survey the range of $IBr^-(CO_2)_n$ clusters by moving from the smaller clusters to the largest studied. In this survey, we will focus again on two clusters, $IBr^-(CO_2)_{12}$ and $IBr^-(CO_2)_{14}$. The former is representative of the dynamics seen in most of the larger clusters, the latter exhibits a unique double time scale which includes both fast and slow recovery trajectories. A summary of the ground-state recombination dynamics

for $IBr^-(CO_2)_{5-16}$ can be found in Appendix B. A similar, smaller tabulated summary will be presented in each of the three sections of the survey below.

During this survey, we will compare our predicted GSR recovery times to those observed experimentally. However, as we progress to the larger clusters, we will see that experiment is no longer able to provide comparative data. Using simulations of absorption spectra for $IBr^-(CO_2)_{12}$, we will propose an explanation on energetic grounds for the difficulties that the experimentalists have encountered in trying to obtain recombination results.

Finally, we will perform two sensitivity experiments on our simulations. As mentioned in Section 2.2.1.3, the calculated well depth for the ground state of bare IBr^- is shallower than that found in experiment. We will use a redder, 840-nm excitation in simulations to determine the effect of our standard curves on the GSR recovery times for $IBr^-(CO_2)_n$ photodissociation. Likewise, in Section 2.2.2, we noted that our standard $Br^- \cdots CO_2$ Lennard-Jones (LJ) parameters used for our simulations, tabulated in Table 2.3, do not exactly match the energetics of the calculated coupled cluster with single, double, and iterative triple excitations (CCSD(T)) $Br^- \cdots CO_2$ interaction. We will show the effects of using different LJ parameters which match the CCSD(T) $Br^- \cdots CO_2$ interaction on the simulated GSR recovery times, as well as a different fit to a less attractive multireference configuration interaction (MRCI) $Br^- \cdots CO_2$ interaction.

4.1 Theoretical Methods of Ground-State Recombination

Long-time nonadiabatic molecular dynamics (MD) simulations of $IBr^-(CO_2)_{5-16}$ were carried out to obtain simulated time constants for ground-state recombination (GSR), see Figure 4.1. All simulations used a time step of 1 fs, while the length of simulations ranged from 20 ps for $IBr^-(CO_2)_5$ to 2 ns for $IBr^-(CO_2)_{8,10}$ with ensemble sizes ranging from 100 trajectories to more than 1700 for $IBr^-(CO_2)_5$.[1]

Time constants were calculated via single-exponential fit of the number of total recom-

[1] The extra-large ensemble size for $IBr^-(CO_2)_5$ was used in order to help resolve short-time behavior in this system.

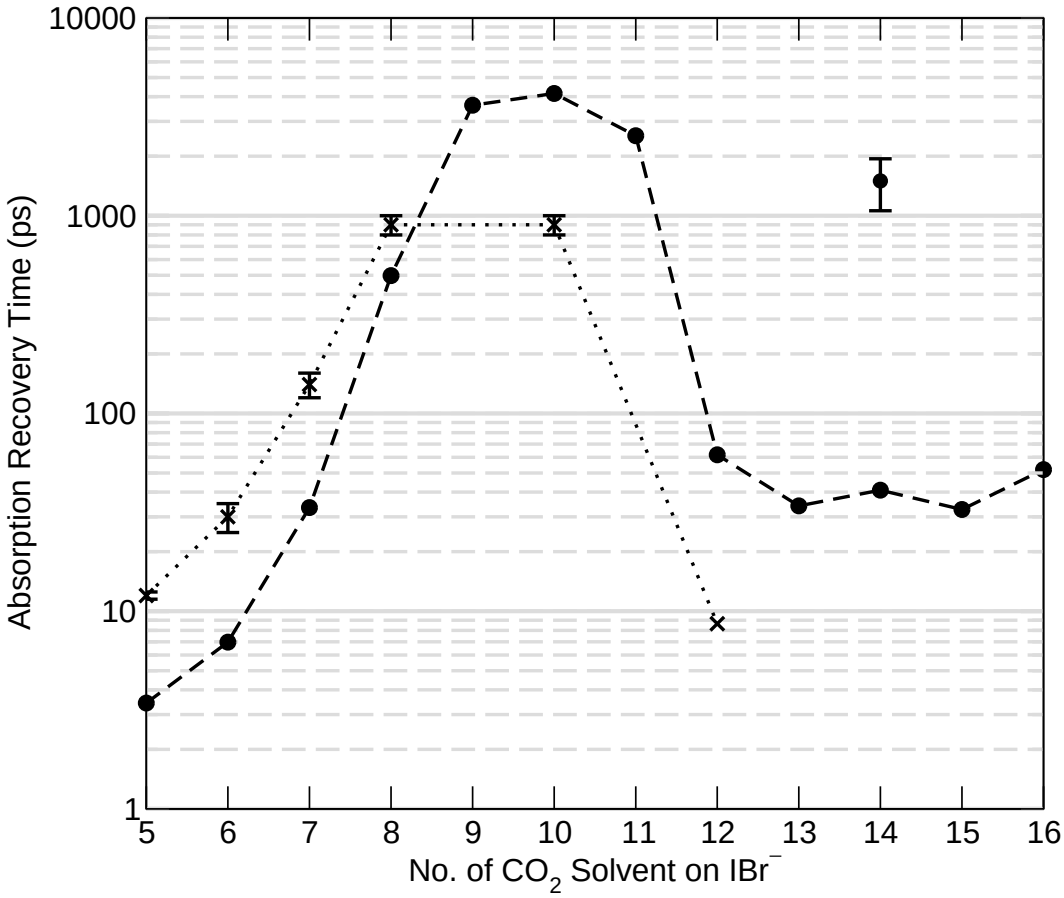

Figure 4.1: Experimental [80] (dotted with X) and simulated (dashed with circles) ground-state recombination recovery times for near-infrared (790 nm) photoexcitation of $IBr^-(CO_2)_n$. Error bars for simulations are within the size of the circle, save for the long-time $IBr^-(CO_2)_{14}$ point. Experimental $n = 12$ point is unreported and provisional.

bined trajectories over time:

$$N(t) = A_0 \left[1 - e^{(-t/\tau)}\right]. \tag{4.1}$$

A trajectory was considered "recombined" when the IBr bond length had reached 3.3 Å on the ground state. The lone exception to the single-exponential fit was $IBr^-(CO_2)_{14}$ which required the use of two time constants, see Figure 4.25. The preexponential factor, A_0, in Equation 4.1 was used in order to both achieve the best fit and as a check to see if the distribution achieved the correct "infinite-time" behavior. That is, if simulations showed that 70 trajectories recombined by the end of the time scale considered, as $t \to \infty$, $N(t) \to 70$, and so $A_0 \to 70$. If this trend was not seen, A_0 was adjusted so long-time behavior was met. Also, with the smaller clusters, $IBr^-(CO_2)_{5,6}$, it was necessary to offset the time axis due to a delay in GSR rise, so Equation 4.1 was modified:

$$N(t) = A_0 \left[1 - e^{(-(t-t_0)/\tau)}\right] \tag{4.2}$$

where t_0 accounts for the shift. This shift was fit along with A_0 and τ and will be given when necessary. Finally, all error bars included in the simulated results below are based on the 95% confidence interval for the asymptotic standard errors of the fits.

We note that technically speaking, our time constant does not correspond exactly to that measured in the experiment. The simulated results count the populations of trajectories that reach a particular configuration on a specific electronic state; they do not directly simulate the pump-probe recovery. While there is no guarantee that these should lead to the same results, we believe the evidence presented below shows that this population recovery analysis of the simulations is valid. The time scale of the trajectories in reaching the ground-state (often, hundreds of picoseconds to nanoseconds) are much longer than any subsequent time scales for dynamics on the ground state. We expect any vibrations, vibrational relaxation, etc., to be complete within a few picoseconds so we do not worry about the time necessary to reach the ground-state absorption window.

4.2 $IBr^-(CO_2)_8$: The Troublemaker That Started It All

Following the $IBr^-(CO_2)_n$ photoproduct studies of the Lineberger Group [77,79], the first time-resolved pump-probe recombination experiments were conducted on $IBr^-(CO_2)_8$. This cluster was chosen because it was the smallest cluster to demonstrate complete recombination to the ground state, see Figure 3.3. By analogy to $I_2^-(CO_2)_n$ [45], an absorption recovery time of 10-30 ps was expected. As shown in Figure 4.2, however, no probe absorption signal was seen over the first 200 ps, the maximum delay possible on the setup at that time. In order to extend the experiment, a crude delay-line was set up to gather points from 5-8 ns. These long-time delays showed that the recombination had essentially completed by 5 ns.

When this discrepancy was discovered, our original 50-ps simulations, see Figure 3.1, were reexamined as they had seemed to show recombination on a 50-ps time scale at least. It was found that the script used to assign the products was grouping all IBr^--based products together, instead of counting only the **ground-state** IBr^- products. A further analysis, shown in Figure 3.2, revealed that clusters from $IBr^-(CO_2)_7$ to $IBr^-(CO_2)_{15}$ all had excited-state trapped IBr^- product at the end of 50 ps; indeed, for $IBr^-(CO_2)_{8-11}$ nearly all the product was trapped in the excited-state well!

In an attempt to reconcile experiment and simulation, long-time trajectories of near-infrared (IR) photodissociation were undertaken for $IBr^-(CO_2)_8$. An ensemble of 100 trajectories was propagated for 2 ns using a timestep of 1.0 fs. Of those 100 trajectories, 75 recombined in the ground-state in 2 ns, leading to a fitted time constant of 498 ± 23 ps, Figure 4.3. Subsequent time-resolved experiments led to a time scale of 900 ± 100 ps.

This long-time relaxation behavior is attributed to the presence of a well on the excited A' state in the solvated ion that inhibits the expected fast ground-state recovery signal. One attempt to visualize this well is shown in Figure 4.4, which is an example potential energy surface (PES) for $IBr^-(CO_2)_8$. These curves were generated by using as input the minimal energy structure for $IBr^-(CO_2)_8$, shown in Figure 2.12. In this configuration, the iodine in

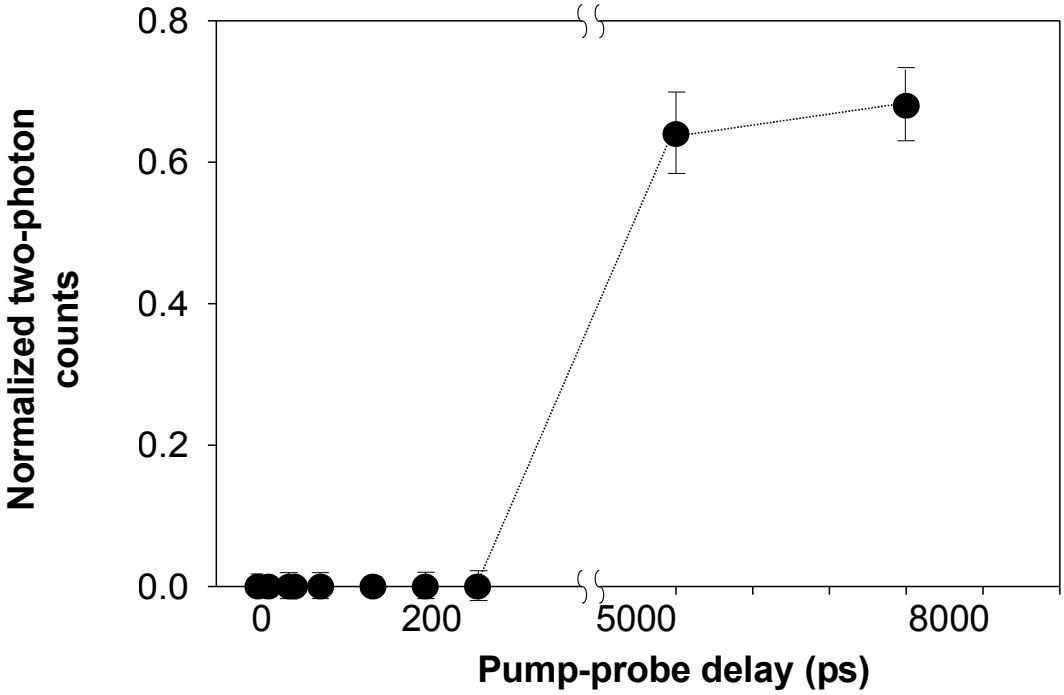

Figure 4.2: Ground-state recombination probability of $IBr^-(CO_2)_8$ as a function of time. The time scale is broken in order to indicate the large difference. Dotted line provided as a guide for the eyes. Figure reproduced with permission from Sanford [77].

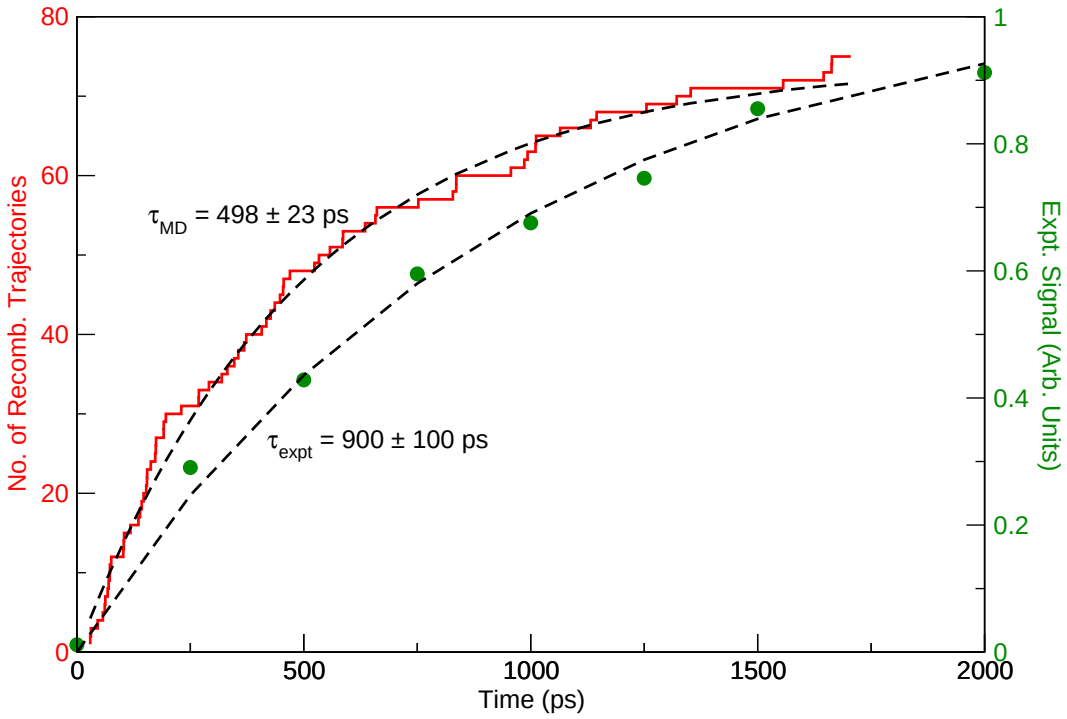

Figure 4.3: Ground-state recombination dynamics for $IBr^{-}(CO_2)_8$. The red line represents theoretical results and the green dots represent experimental data. Dotted lines represent single-exponential fits to the data, see Equation 4.1. Experimental results from Dribinski, et al [80].

the cluster is not hindered by any solvent, so the iodine is "pulled" from the cluster and the resulting state energies plotted as a function of the I-Br separation. The arrow in Figure 4.4 roughly corresponds to a 790-nm photon excitation from the ground-state. This arrow is mainly included as a guide to show that the energetics, even in a naive comparison with this PES, show that trapping in the solvent-generated well on the excited state is possible. In fact, as a test, 50-ps simulations of $IBr^-(CO_2)_8$ were run using a 730-nm photon and the extra kinetic energy release (KER) provided by this more energetic photon allowed most of the IBr^- product to recombine in the ground state within 50 ps.

However, these curves are not the best way to interpret the trajectories on the excited state. The problem is that these curves are generated only for one solvent configuration for the cluster; moreover, this solvent configuration is the minimal energy configuration for the ground state. This is a configuration that would rarely, if ever, be seen after warming the cluster to 60 K, let alone after excitation with a 790-nm photon. Instead, to visualize the trajectories, a technique used previously by the Parson group [41, 75] is adopted, in which trajectories are analyzed in terms of two coordinates, solute bond length and a collective solvent coordinate. We define this solvent coordinate, $\Delta\Phi$, as the change in energy when a charge of $-e$ is moved from one solute atom to another. In IBr^-, a negative $\Delta\Phi$ broadly represents a solvent configuration that is concentrated around the bromine atom, while a positive $\Delta\Phi$ corresponds to a configuration concentrated around the iodine. A larger absolute value of $\Delta\Phi$ represents more solvent asymmetry, Figure 4.5 (bottom), while a $\Delta\Phi$ near zero represents a more symmetric solvent configuration, Figure 4.5 (top). Note that, unlike a symmetric solute system like $I_2^-(CO_2)_n$, $\Delta\Phi = 0$ does not exactly equal a symmetric solvent configuration as the two solute atoms are not the same. Also, while $\Delta\Phi$ is a measure of the energy for a cluster geometry, it does not directly specify the nuclear separation. Many different solute-solvent configurations correspond to the same value of $\Delta\Phi$.

While these plots will allow analysis of the concerted motion of the solute and solvent over the length of the trajectory, the energy landscape will have to be inferred from the limitations of

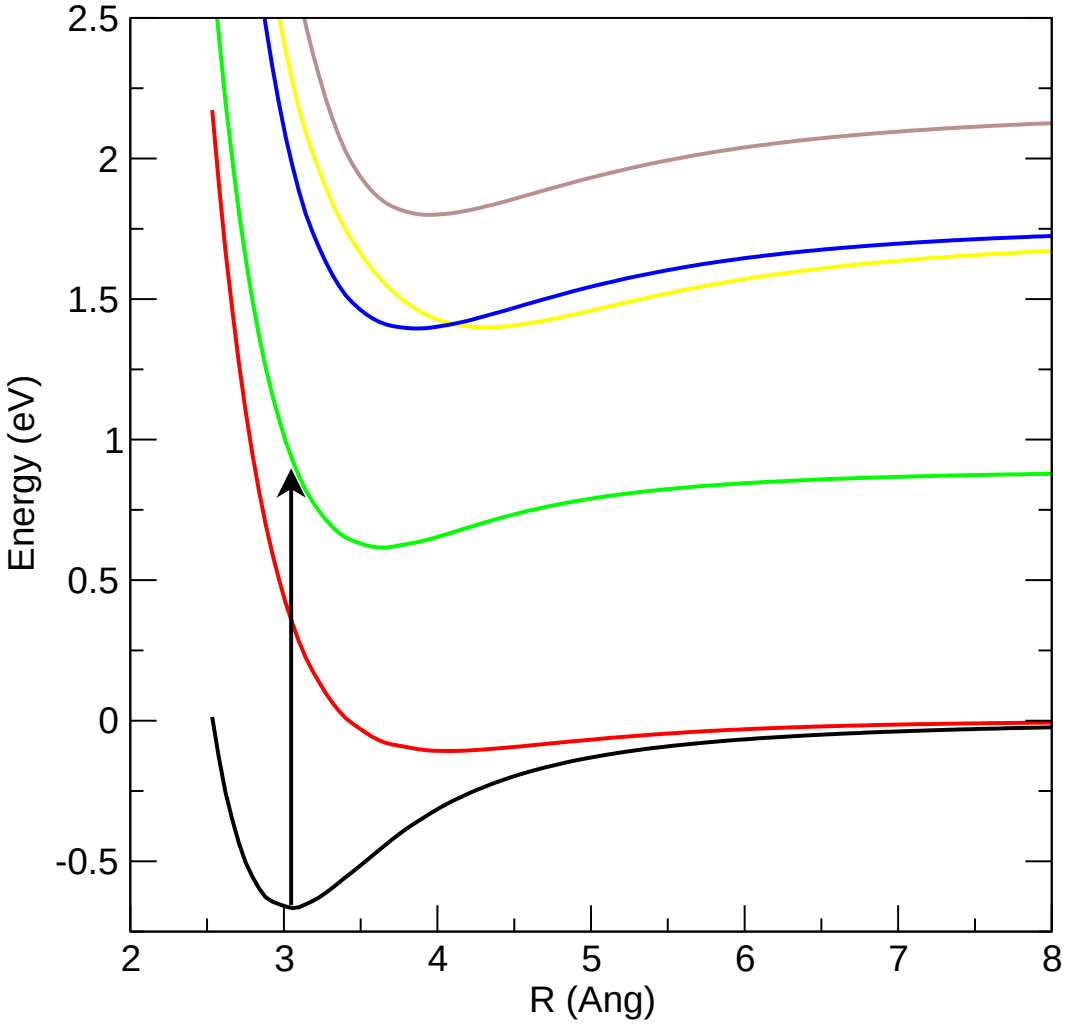

Figure 4.4: Potential energy surface for $IBr^{-}(CO_2)_8$ generated by "pulling" the iodine from the $IBr^{-}(CO_2)_8$ minimal energy structure seen in Figure 2.12 and plotting the energy as a function of separation. Arrow roughly shows a 790-nm excitation as a guide for the eyes.

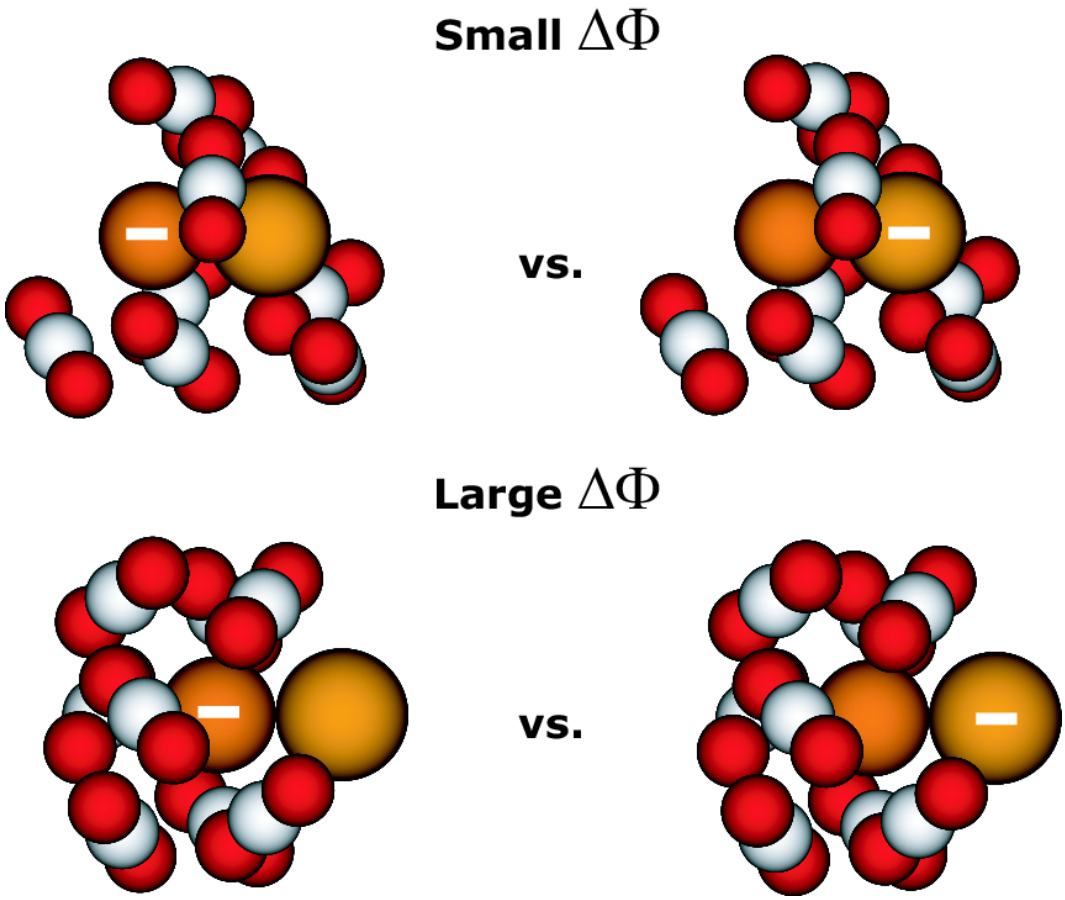

Figure 4.5: Visual representation of the solvent coordinate, $\Delta\Phi$, using $IBr^{-}(CO_2)_8$ clusters (bromine on left, iodine on right of solute). Symmetric solvent configuration, top, small $\Delta\Phi$. Asymmetric solvent configuration, bottom, large $\Delta\Phi$.

this movement on the landscape. That is, wells and valleys of the energy landscape will appear as trajectories trapped either in small, compact areas (wells) or long, slim areas (valleys) of movement. Finally, included in these plots is an extra dimension of analysis: the state which a trajectory currently occupies is color-coded according to the scheme used in the bare IBr^- PES, Figure 2.1, where green, red, and black represent the second- and first-excited states and the ground state, respectively.

To demonstrate the utility of these solvent flow plots, two examples for $IBr^-(CO_2)_8$, are presented that allow analysis of the ground-state recombination (GSR) dynamics. The first of these plots, Figure 4.6, is an example of a trajectory that was trapped over its 50-ps lifetime. After excitation to the excited state (the point roughly at 3 Å), the solute begins to dissociate, and the solvent becomes more asymmetric around the solute. At this point it becomes trapped in a well located at about 3.8 Å. While the trajectory does make an attempt to dissociate, the turning point implies the existence of a wall to dissociation as the I-Br bond length increases.

In comparison to this trapped trajectory, one that achieves ground-state recombination in shown in Figure 4.7. In this case, while the cluster was initially trapped in the same excited-state well, it eventually achieved a more symmetric solvent configuration which allowed it to cross over to a configuration in which I_2^- is solvated (positive $\Delta\Phi$). At this point it was able to increase its bond length to a point where a nonadiabatic transition to lower states was possible (shown as a color change from green to red). After the hop was made, the trajectory quickly (on the order of a few ps) hopped to the ground state and recombined in the ground-state well.

Thus, the long-time dynamics of $IBr^-(CO_2)_8$ are attributed to the need for the solvent to reorganize, passing through a more symmetric configuration in order to reach the area of the surface where nonadiabatic transitions to lower states and, later, relaxation to the ground state can occur.

To better show the location of this configurational transition state, a solvent flow plot of all 75 trajectories that relaxed to the ground state during the 2-ns runs, overlaid into one plot, is presented in Figure 4.8. This plot shows that every single trajectory that eventually relaxes

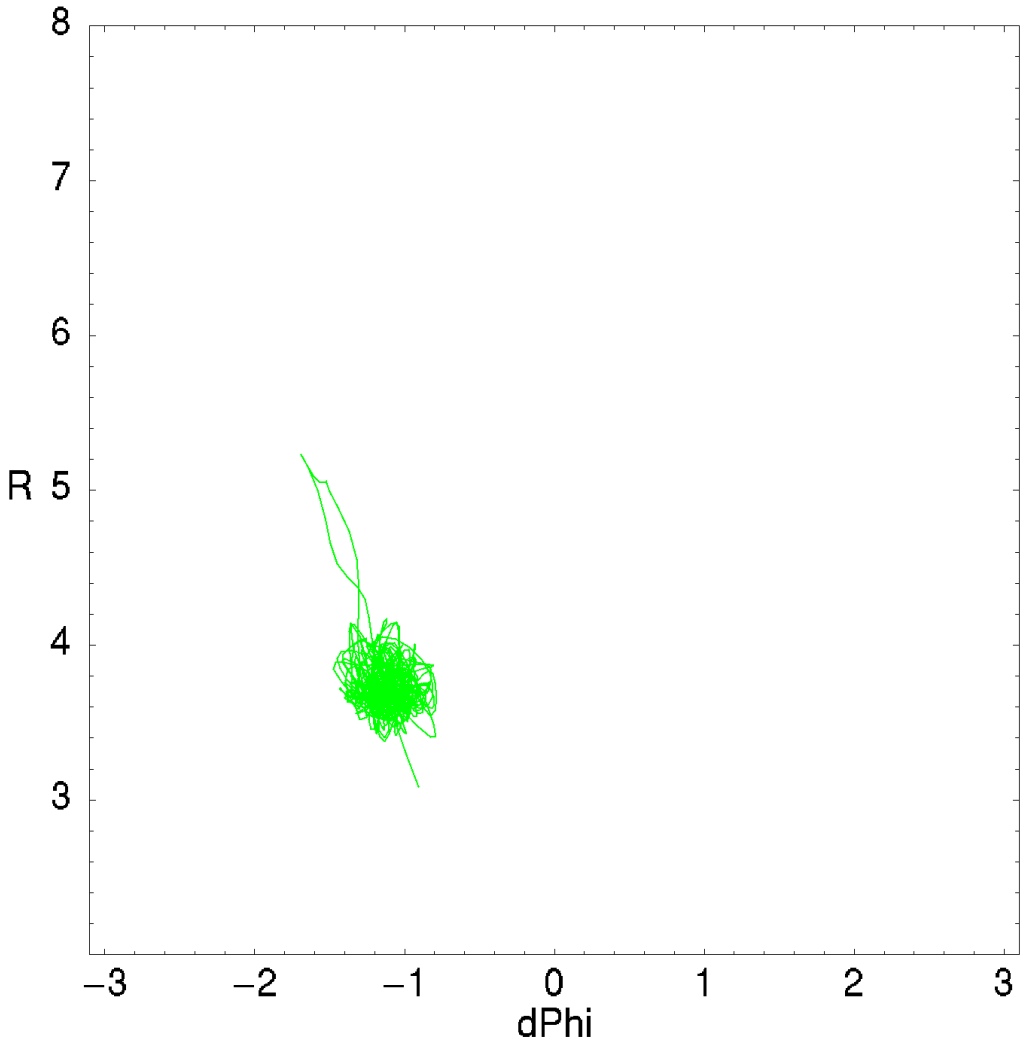

Figure 4.6: Plot of solvent coordinate, $\Delta\Phi$, versus solute bond length for a trapped trajectory for $IBr^-(CO_2)_8$. Green represents trajectory dynamics on the second-excited state. dPhi ($=\Delta\Phi$) is in eV and R is in Angstroms.

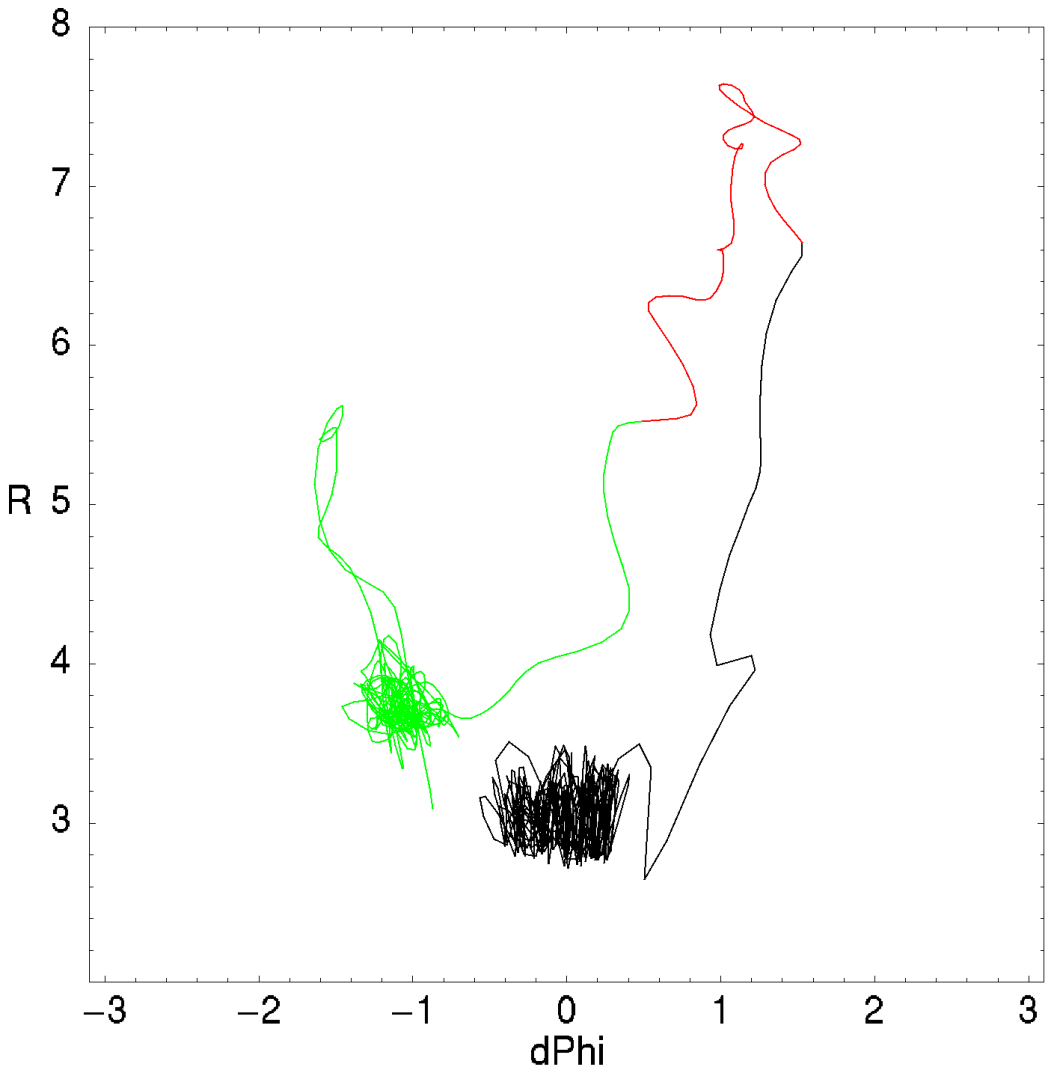

Figure 4.7: Plot of solvent coordinate, $\Delta\Phi$, versus solute bond length for a trapped trajectory for $IBr^{-}(CO_2)_8$. Black, red, and green represent trajectory dynamics on the ground, first-, and second-excited states, respectively dPhi ($=\Delta\Phi$) is in eV and R is in Angstroms.

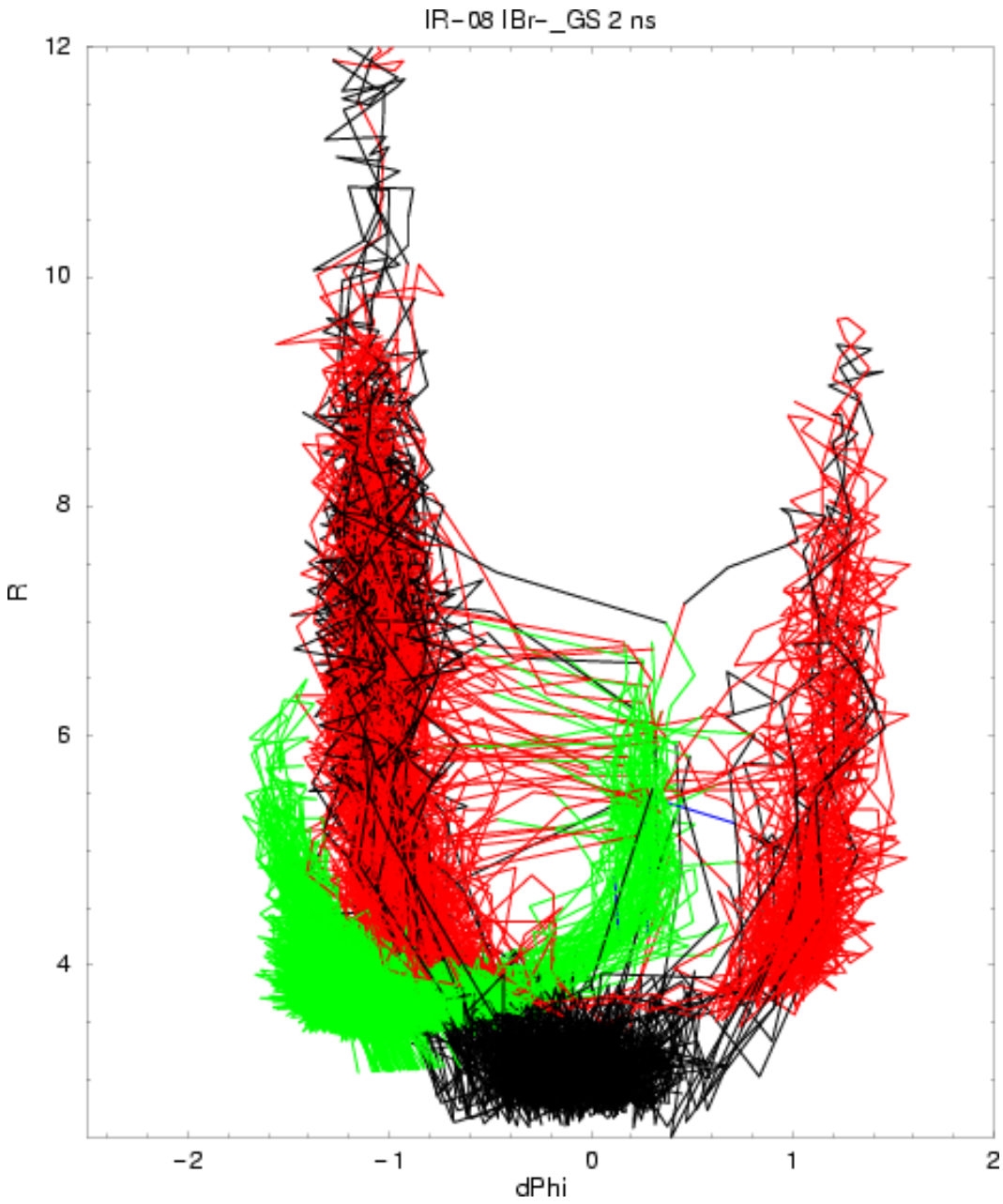

Figure 4.8: Plot of solvent coordinate, $\Delta\Phi$, versus solute bond length for 2-ns trajectories for $IBr^-(CO_2)_8$ that end as IBr^- product in the ground state. Black, red, and green represent trajectory dynamics on the ground, first-, and second-excited states, respectively dPhi (=$\Delta\Phi$) is in eV and R is in Angstroms.

to the ground state must pass through a transition state located at roughly at $\Delta\Phi = -0.3$ eV and R = 3.9 Å. There appears to be a very narrow range of solvent configurations that will afford escape from the excited state well. Furthermore, Figure 4.8 also allows a more complete mapping of the energy surface seen by $IBr^-(CO_2)_8$ during its trajectories. First, the excited-state well, while concentrated around 4 Å of solvent separation, isn't so compact that trajectories can't reach bond lengths of up to 6 Å, although that seems to be the limit. In other words, the excited state is bound, but only loosely. At longer bond lengths, the A' state seems to evolve from a single well structure to a double well structure. This seems to be crucial as it allows the clusters to reach the valley in the A' state located at zero $\Delta\Phi$ where the nonadiabatic $A' \rightarrow A$ transitions occur. Likewise, the long-bond length double-valley structure extends to both the A state and ground-state. As discussed in earlier studies of $I_2^-(CO_2)_n$ [24, 29], the double-wells in the X and A states correspond to localized charge distributions (solvated-I^- and bromine and iodine and solvated-Br^-), whereas the single well on the X state at short bond lengths corresponds to a delocalized, molecular charge distribution. The delocalized distribution wins out at short separations where the chemical bonding interactions are stronger than the X^--solvent interactions. In the A state, the chemical forces are weak for all R, so the charge remains localized at nearly all internuclear distances.

In fact, it is this double-valley configuration that provides clues into the mechanisms of both Br^- dissociation, Figure 4.9, and I^- dissociation, Figure 4.10, in $IBr^-(CO_2)_8$. As in Figure 4.8, these are composites of all trajectories that led to Br^- and I^- products before 2 ns was reached. The mechanism for both Br^- and I^- dissociation follows that for GSR. Both channels begin with trapping in the excited-state well that is escaped only by crossing the same configurational transition state needed to reach the area of nonadiabatic transition. The clusters then enter either the -$\Delta\Phi$ valley and dissociate to form Br^- product or they enter the +$\Delta\Phi$ valley and dissociate to form I^- product. Interestingly, in Figure 4.9, evidence is seen of the A state forming a single-well structure at shorter bond lengths as a few trajectories were actually able to transition from the +$\Delta\Phi$ valley to the -$\Delta\Phi$ valley by moving to a tighter solute

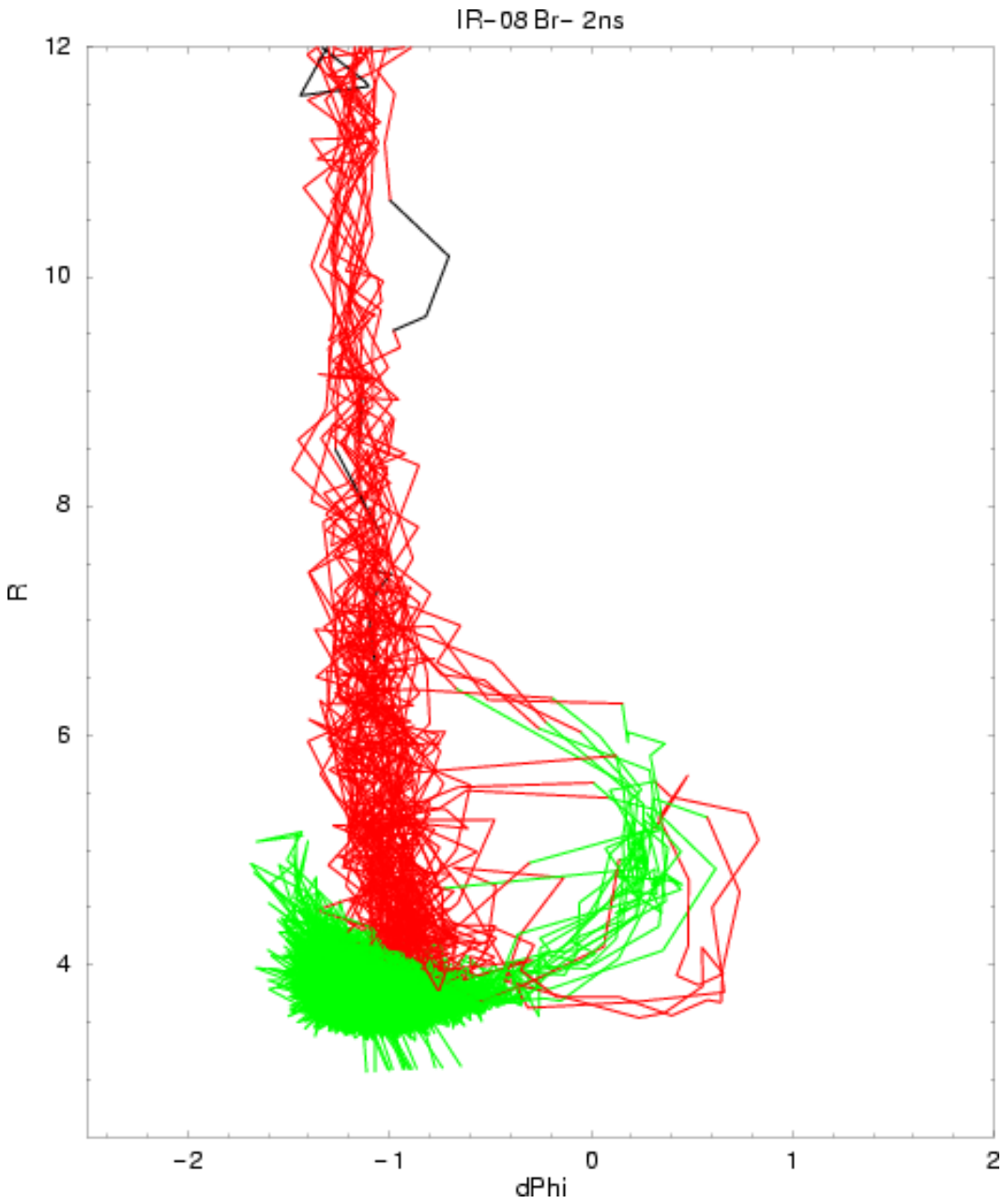

Figure 4.9: Plot of solvent coordinate, $\Delta\Phi$, versus solute bond length for 2-ns trajectories for $IBr^-(CO_2)_8$ that end as Br^- product. Black, red, and green represent trajectory dynamics on the ground, first-, and second-excited states, respectively dPhi (=$\Delta\Phi$) is in eV and R is in Angstroms.

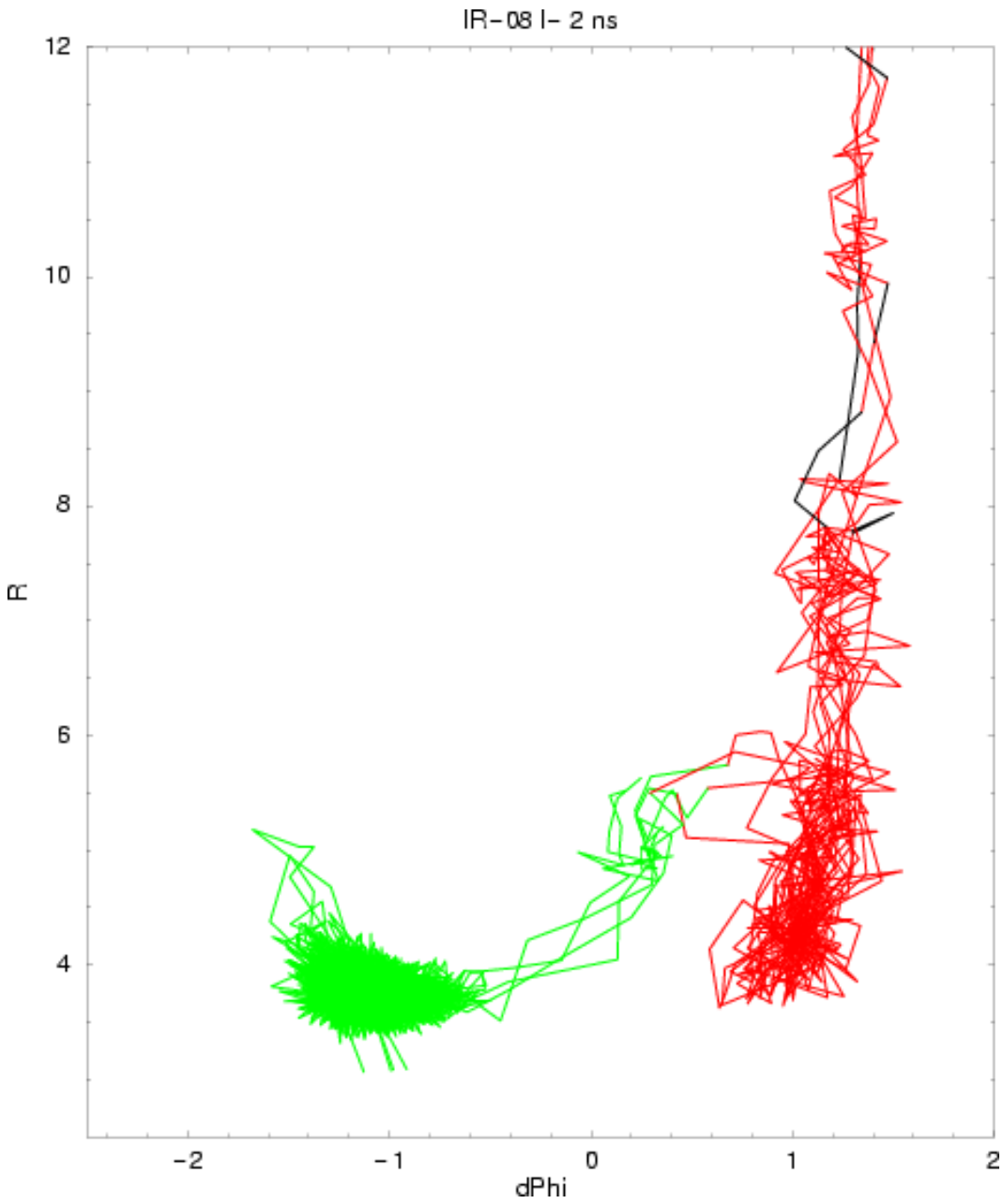

Figure 4.10: Plot of solvent coordinate, $\Delta\Phi$, versus solute bond length for 2-ns trajectories for $IBr^{-}(CO_2)_8$ that end as I^{-} product. Black, red, and green represent trajectory dynamics on the ground, first-, and second-excited states, respectively dPhi (=$\Delta\Phi$) is in eV and R is in Angstroms.

No. of CO_2	Duration (ps)	No. of Traj.	No. of GSR Product	τ_{sim} (ps)	t_0 [a] (ps)	τ_{expt} [b] (ps)
5	20	1796	711	3.43 ± 0.06	0.7	12 ± 0.5
6	20	1000	440	6.97 ± 0.18	1.65	30 ± 5
7	200	237	155	33.4 ± 0.7	—	140 ± 20

[a] t_0 shift in Eqn. 4.2
[b] Ref. 80

Table 4.1: Summary of ground-state recombination (GSR) recovery dynamics of near-IR (790 nm) photodissociation of $IBr^-(CO_2)_{5-7}$. All simulations performed with 1.0 fs time step. A trajectory was considered dissociated once I-Br bond length reached 40 a_0 or recombined after 20 crossings of the ground state well.

configuration. This facilitated a solvent reorganization allowing entry into the Br^- channel.

One final note about the long-time solvent flow plots shown above is that when compared to the 50-ps plots in Figures 4.6 and 4.7 is that they seem "coarser" in their representation of a trajectory. This is an artifact of the resolution: while the same 1.0-fs time-step was used in all nonadiabatic runs, for these long-time runs the properties associated with the trajectory were only reported every few picoseconds in order to reduce the disk space needed to store these runs. If a multi-nanosecond run reported properties at the same rate as the shorter runs, each trajectory could consume hundreds or thousands of megabytes each. It was felt that some coarseness would not seriously impede the ability to analyze the properties of any trajectory.

4.3 Ground-State Recombination Dynamics in Smaller Clusters

The behavior of $IBr^-(CO_2)_n$ ground-state recombination (GSR) in the smaller clusters is a good starting point to view how the long-time dynamics change as the clusters grow more asymmetric. As the cluster size increases from $IBr^-(CO_2)_5$ to $IBr^-(CO_2)_7$—only two CO_2 molecules—the GSR time increases by an order of magnitude. Table 4.3 summarizes the both the ensemble starting statistics and resulting simulated GSR dynamics results for the small clusters. In all cases in this and subsequent sections, a time-step of 1.0 fs was used. If the bond length exceeded 40 a_0, the trajectory was terminated and classified as dissociated. If more than 20 crossings of the ground-state well occurred, the trajectory was considered to have recombined.

The investigation begins with $IBr^-(CO_2)_5$, the smallest cluster considered here for examination of GSR dynamics. As seen in Figure 3.3, experiment observes over 90% ground-state recombination (GSR) in $IBr^-(CO_2)_5$, while in simulation, both IBr^-- and Br^--based products are significant. It was found that the simulated GSR time for $IBr^-(CO_2)_5$ was 3.43 ± 0.06 ps, compared to the experimental value of 12 ± 0.5 ps (Figure 4.11). For the simulated fit in Figure 4.11, the shifted exponential, Equation 4.2, was used with a shift of $t_0 = 1.71$ ps.

The reason such a large number of trajectories were included in the $IBr^-(CO_2)_5$ (and, vide infra, $IBr^-(CO_2)_6$) ensemble was that the experimentalists had noted that the GSR signal began to rise only after a time delay of ≈ 0.7 ps. Previous simulations used ensembles too small to definitively see this delay in the data, so the larger ensemble was run, resulting in 711 of the 1796 trajectories relaxing to the ground state by 20 ps. With this larger data set, the simulations were able to confirm this delay in the GSR rise although the simulations see it occurring at ≈ 1.0 ps. We attribute this difference in the short-time dynamics between simulation and experiment to the fact that, as stated above, we count the populations of trajectories that reach a certain configuration on a specific electronic state. The experiment, rather, measures the appearance of the probe absorption signal which may (and most likely does) occur in a different area of the potential energy surface. This difference in the short-time dynamics could therefore be a reflection of our differing methods of obtaining the time constant. This delay was accounted for in the calculation of the simulated time constant by the use of the shifted exponential, Equation 4.2, $t_0 = 0.7$ ps, for the fit.

Analysis of recombined trajectories attribute this time delay to the basic mechanics of the system. A trajectory that recombines on the ground state needs approximately one picosecond to physically reorganize the solvent, nonadiabatically transition to the ground state, and reach the 3.3 Å separation wherein it is counted as a ground-state product. The reason this delay is only noticed, and therefore studied, for $IBr^-(CO_2)_{5,6}$ is that they are the only systems whose simulated GSR time scales are small enough for the phenomenon to be observed. As will be seen later in this chapter, larger clusters undergo trapping on the excited-state where this dynamical

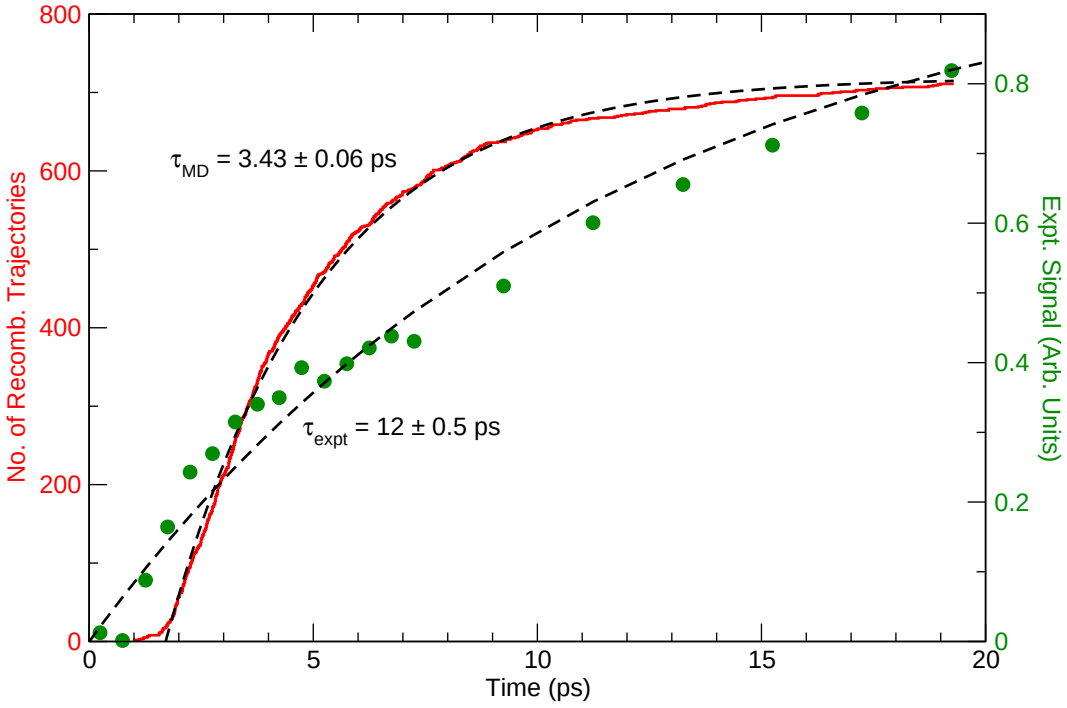

Figure 4.11: Ground-state recombination dynamics for $IBr^{-}(CO_2)_5$. The red line represents theoretical results and the green dots represent experimental data. Dotted lines represent single-exponential fits to the data, see Equation 4.1. Experimental results from Dribinski, et al [80].

delay is precluded from being studied. Likewise, in experimental studies [80], the low GSR signal at early times in larger clusters precludes the study of delayed onset in those systems. Note, though, that there is no reason to assume such a short-time delay wouldn't occur in larger systems.

Similar GSR behavior is seen in simulations of $IBr^-(CO_2)_6$, see Figure 4.12. The simulated GSR time was found to be 6.97 ± 0.18 ps compared to the experimental value of 30 ± 5 ps. For the simulated fit in Figure 4.12, the shifted exponential, Equation 4.2, was used with a shift of $t_0 = 1.65$ ps. The addition of one solvent molecule has thus doubled the GSR time in simulation, with an even larger increase seen in the experiment. This difference is attributed to the extra solvent asymmetry built in the cluster which has further stabilized the excited state well. Figure 2.14 shows that when the clusters grows from $IBr^-(CO_2)_5$ to $IBr^-(CO_2)_6$, the ground-state solvent asymmetry becomes much more negative; that is, the bromine is solvated more effectively. This can be observed pictorially in Figure 2.12 which charts the building of the $IBr^-(CO_2)_n$ clusters.

The trapping in $IBr^-(CO_2)_6$, however, is not as severe as that seen $IBr^-(CO_2)_8$. In $IBr^-(CO_2)_8$, the long-time trapping was caused by the need to reach a more symmetric configuration so transit to the nonadiabatic transition region could be made. But, from Figure 2.12, the $IBr^-(CO_2)_6$ cluster, though asymmetric, needs much less concerted solvent motion in order to reach a symmetric solvent geometry.

That said, one should not depend too much on the minimum energy cluster geometries and ground-state $\Delta\Phi$ trends to predict trends in GSR. From our experience with $IBr^-(CO_2)_5$ and $IBr^-(CO_2)_6$, one would expect that the difference from $IBr^-(CO_2)_6$ to $IBr^-(CO_2)_7$ would not be as drastic. The ground-state $\Delta\Phi$ does not change much and the ground-state solvent geometries are not drastically different. Yet, when GSR simulations of $IBr^-(CO_2)_7$ were run (Figure 4.13), the recovery time was found to be 33.4 ± 0.7 ps in simulation compared to a time of 140 ± 20 ps seen in experiment. Although the solvent configuration difference in the ground state between $IBr^-(CO_2)_6$ and $IBr^-(CO_2)_7$ is not that great, the GSR recovery time has more

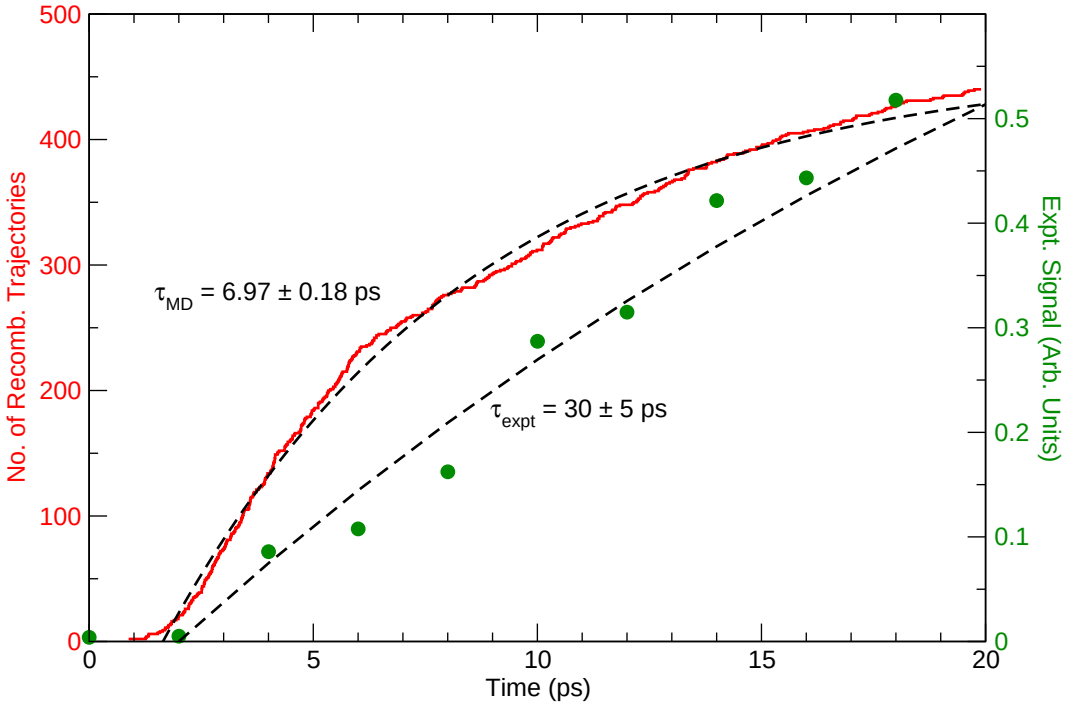

Figure 4.12: Ground-state recombination dynamics for $IBr^{-}(CO_2)_6$. The red line represents theoretical results and the green dots represent experimental data. Dotted lines represent single-exponential fits to the data, see Equation 4.1. Experimental results from Dribinski, et al [80].

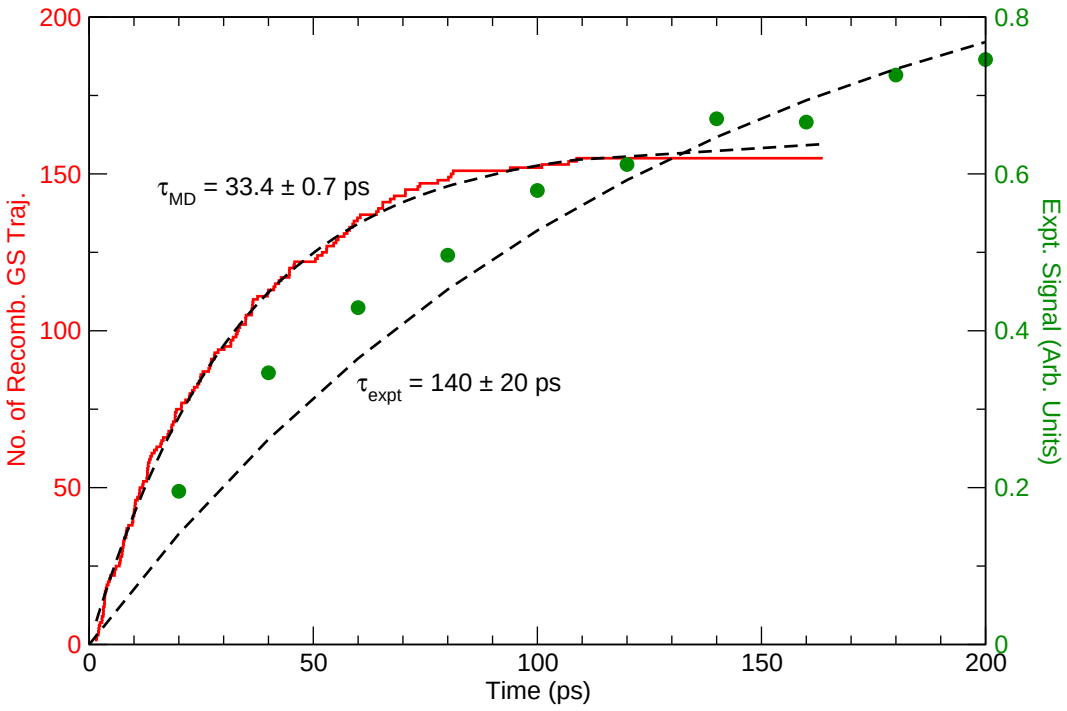

Figure 4.13: Ground-state recombination dynamics for $IBr^{-}(CO_2)_7$. The red line represents theoretical results and the green dots represent experimental data. Dotted lines represent single-exponential fits to the data, see Equation 4.1. Experimental results from Dribinski, et al [80].

No. CO_2	Duration (ps)	No. of Traj.	No. of GSR Product	Extrap. GSR Product[a]	τ_{sim} (ps)	τ_{expt}[b] (ps)
8	2000	100	75	—	498 ± 23	900 ± 100
9	4000	100	54	76	3620 ± 60[c]	—
10	4000	90	44	70	4150 ± 120[c]	900 ± 100
11	3000	100	74	87	2540 ± 60[c]	—

[a] A_0 in Eqn. 4.1
[b] Ref. 80
[c] Lower bound to time constant

Table 4.2: Summary of ground-state recombination (GSR) recovery dynamics of near-IR (790 nm) photodissociation of $IBr^-(CO_2)_{8-11}$. All simulations performed with 1.0 fs time step. A trajectory was considered dissociated once I-Br bond length reached 40 a_0 or recombined after 20 crossings of the ground state well.

than tripled. The reason is that the additional solvent molecule has a much larger impact upon the solvation of the excited state than the ground state. Figure 4.18 will be crucial in explaining the dynamics of the larger clusters, but it can also help explain the smaller cluster increases as well. As the cluster size increases from $IBr^-(CO_2)_6$ to $IBr^-(CO_2)_{10,11}$, the average $\Delta\Phi$ of the **excited-state** well grows in magnitude. Thus, the excited state cluster's configuration is more asymmetric than a casual glance at the minimum energy structures in the ground state, Figure 2.12, would predict. And since the cluster must reorganize to symmetric solvent configurations in order to reach the transition state, the GSR recovery time is lengthened.

4.4 Ground-State Recombination Dynamics of Intermediate-Sized Clusters

As the size of the $IBr^-(CO_2)_n$ clusters increase from $n = 5 \rightarrow 8$, the ground-state recombination (GSR) recovery time increases from $5 \rightarrow 500$ ps in simulation and $10 \rightarrow 1000$ ps in experiment. This is remarkable agreement with both predicting a change of 2 orders of magnitude. However, the simulations of the intermediate-sized clusters, $IBr^-(CO_2)_{9-11}$, begin to diverge from experiment. Table 4.4 summarizes both the ensemble starting statistics and resulting simulated GSR dynamics results for the intermediate-sized clusters.

The first two intermediate-sized clusters, $IBr^-(CO_2)_9$ and $IBr^-(CO_2)_{10}$, represent the

peak of GSR times in simulation. It was found that the simulated GSR time for $IBr^-(CO_2)_9$ was at least 3.62 ± 0.06 ns (Figure 4.14. This number is based on the assumption that the product ratio at 4 ns was the same at it would be at infinite time, and so the preexponential factor, A_0 in Equation 4.1, was set to 76 as the infinite extrapolation predicted an additional 23 trajectories recombining. No experiments were carried out at $IBr^-(CO_2)_9$, but it is suspected that the simulations overestimate the GSR time for this cluster. This assumption is made by visual inspection of the overall GSR trends in Figure 4.1 where it appears that there is a turnaround in GSR time between $IBr^-(CO_2)_8$ and $IBr^-(CO_2)_{10}$. If this is true, the experimental time constant is likely on the order of 1-3 ns compared to the simulations which give a lower bound near 4 ns.

Likewise, simulations of $IBr^-(CO_2)_{10}$ were run, and it was found that the simulated GSR time had a lower bound of at least 4.15 ± 0.12 ns (Figure 4.15). Like $IBr^-(CO_2)_9$, $IBr^-(CO_2)_{10}$ had many trajectories that did not escape the excited-state well. This recovery time is based on the assumption that the product ratio at 4 ns was the same at it would be at infinite time, and so the preexponential factor, A_0 in Equation 4.1, was set to 70 as the infinite extrapolation predicted an additional 26 trajectories recombining. Unlike $IBr^-(CO_2)_9$, there is some experimental data for $IBr^-(CO_2)_{10}$ which has shown a GSR time constant of 900 ± 100 ps, roughly the same time scale as $IBr^-(CO_2)_8$.

The simulations of $IBr^-(CO_2)_9$ and $IBr^-(CO_2)_{10}$ predict GSR recovery times on the order of at least 4-5 ns. When compared to the experimental data for these two clusters, a GSR recovery time for $IBr^-(CO_2)_{10}$ of less than a nanosecond, the simulations have overestimated the recovery time. This seems to indicate that our model creates too large a barrier for the solvent reorganization. Our ability to analyze the reasons for this difference are hindered by the extremely long simulation times needed. The 4-ns simulations referenced above took a month of computation time to run just 100 trajectories...many of which did not even escape the excited state! That said, there is no evidence that the mechanism for $IBr^-(CO_2)_{9,10}$ GSR is any different than that shown for $IBr^-(CO_2)_8$ in Section 4.2. In each case it is the solvent reorganization to

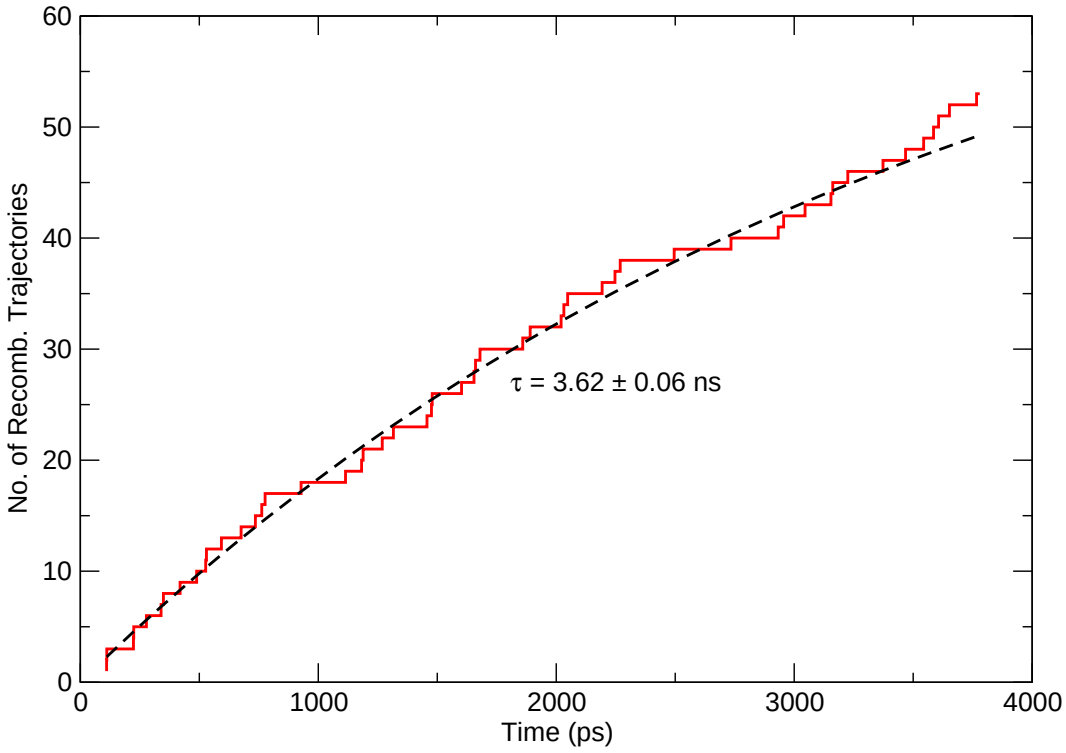

Figure 4.14: Ground-state recombination dynamics for $IBr^{-}(CO_2)_9$. The red line represents theoretical results. Dotted lines represent single-exponential fits to the data, see Equation 4.1.

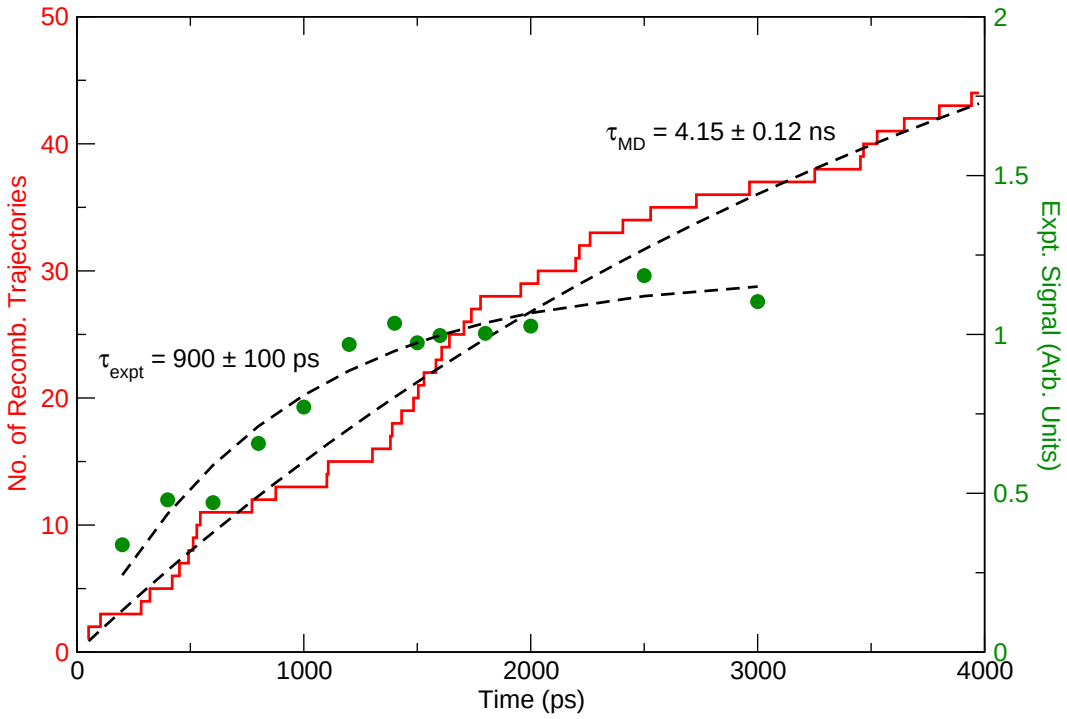

Figure 4.15: Ground-state recombination dynamics for $IBr^{-}(CO_2)_{10}$. The red line represents theoretical results. Dotted lines represent single-exponential fits to the data, see Equation 4.1. Experimental results from Dribinski, et al [80].

No. of CO_2	Duration (ps)	No. of Traj.	No. of GSR Product	τ_{sim} (ps)	τ^a_{expt} (ps)
13	300	250	199	34.1 ± 1.6	—
14	3000	100	96	40.9 ± 1.9 1500 ± 440	—
15	150	100	99	32.7 ± 2.8	—
16	150	100	97	52.0 ± 3.1	—

[a] Ref. 80

Table 4.3: Summary of ground-state recombination (GSR) recovery dynamics of near-IR (790 nm) photodissociation of $IBr^-(CO_2)_{12-16}$. All simulations performed with 1.0 fs time step. A trajectory was considered dissociated once I-Br bond length reached 40 a_0 or recombined after 20 crossings of the ground state well.

a small range of symmetric geometries that is stalling the recovery.

Fortunately, $IBr^-(CO_2)_{9,10}$ turned out to yield the longest GSR times in this cluster. When simulations of $IBr^-(CO_2)_{11}$ were run, with the results shown in Figure 4.16, it was found that the simulated GSR time was still long, but was only at least 2.54 ± 0.06 ns. While this is not a drastic drop-off in recovery time, it does presage the change in dynamics in larger clusters shown in Figure 4.1. Like $IBr^-(CO_2)_9$, the GSR time constant for $IBr^-(CO_2)_{11}$ was calculated using the same "infinite-time" extrapolation where it was assumed that of the 15 trajectories still trapped at 4 ns, 13 would undergo GSR, so the preexponential factor, A_0 in Equation 4.1, was set to 87.

4.5 Ground-State Recombination Dynamics of Larger Clusters

The dynamics of the larger clusters, $IBr^-(CO_2)_{12-16}$, differ markedly from those of the intermediate-sized clusters, $IBr^-(CO_2)_{8-11}$. Table 4.5 summarizes both the ensemble starting statistics and resulting simulated ground-state recombination (GSR) dynamics results for the large clusters.

4.5.1 Focus on $IBr^-(CO_2)_{12}$: A Transitional Cluster

Simulations of $IBr^-(CO_2)_{12}$ found the GSR time was not on the order of multiple nanoseconds, as was true for just one fewer solvent molecule, but rather 61.8 ± 2.1 ps (Figure 4.17).

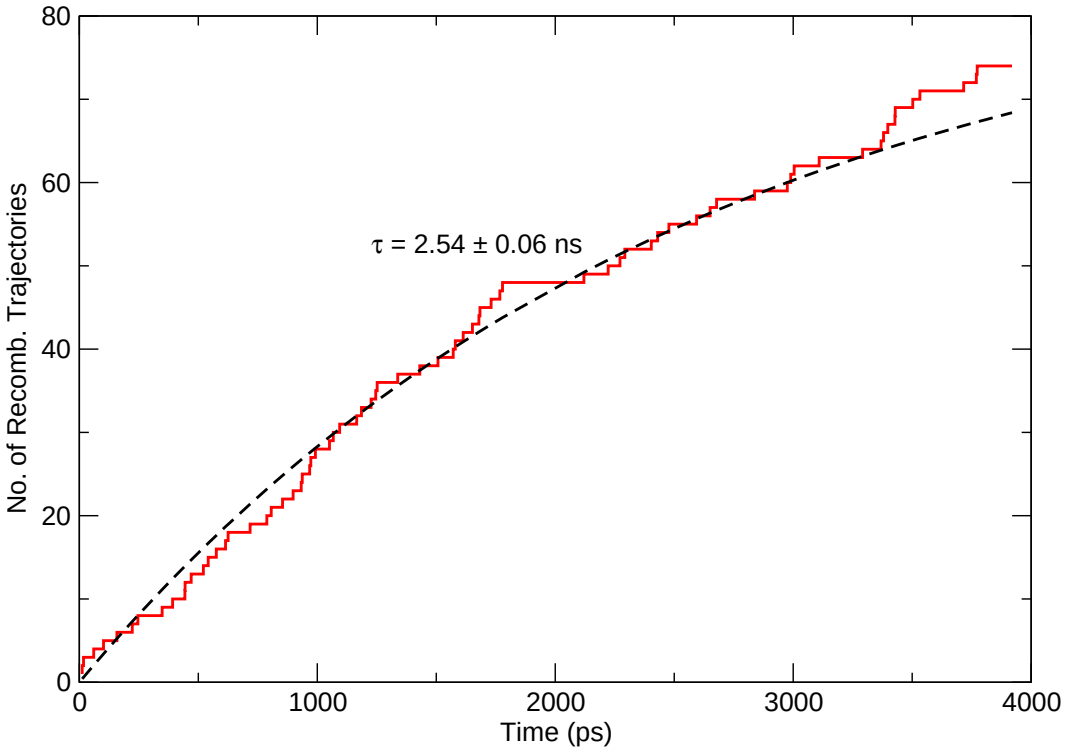

Figure 4.16: Ground-state recombination dynamics for $IBr^{-}(CO_2)_{11}$. The red line represents theoretical results. Dotted lines represent single-exponential fits to the data, see Equation 4.1.

Obviously, something dramatic has occurred to the solvent environment of the cluster.

First, recalling the ground-state $\Delta\Phi$ statistics shown in Figure 2.14, $IBr^-(CO_2)_{12}$ has a particularly labile solvent configuration in the ground state. Its average structure has nearly the same $\Delta\Phi$ as $IBr^-(CO_2)_5$ and it can sometimes have a structure that is nearly symmetric. Thus, like $IBr^-(CO_2)_5$, $IBr^-(CO_2)_{12}$ does not start in a solvent configuration that greatly favors the bromine end. In fact, $IBr^-(CO_2)_{12}$ seems to act as a "bridge" between the intermediate-sized clusters, characterized by large $|\Delta\Phi|$, and the larger clusters which begin to approach a symmetric configuration (small $|\Delta\Phi|$).

Similar trends are seen in the excited state. The average excited-state well $\Delta\Phi$ values for $IBr^-(CO_2)_n$ are plotted in Figure 4.18, while the average $IBr^-(CO_2)_n$ excited-state solute geometry is plotted in Figure 4.19. The most dramatic statistic is the average excited-state solvent configuration for $IBr^-(CO_2)_{12}$ in Figure 4.18; once again, $IBr^-(CO_2)_{12}$ can be seen as a bridge between smaller and larger clusters.

For $IBr^-(CO_2)_{6-11}$, the large negative $\Delta\Phi$ values in the ground-state configuration imply that after excitation the cluster dynamics begin on the -$\Delta\Phi$ side of the excited state. As we have seen in the previous sections, trajectories in this region are easily trapped. However, $IBr^-(CO_2)_{12}$ has much more freedom of movement in its solvent configuration and can begin to access the +$\Delta\Phi$ side of the excited state. To see this more clearly, Figure 4.20 shows the solvent flow dynamics of short-time (50-ps) trajectories which were trapped on the excited state for $IBr^-(CO_2)_{12}$. From this plot, there are in fact two wells identified that $IBr^-(CO_2)_{12}$ can access once promoted to the excited state. Focusing on the starting points for the trajectory near 3.6 Å, which side of the excited state it enters appears to be a function of the initial configuration on the ground state. Those that began with the bromine end solvated, end up in a well that favors that configuration, and similarly for iodine. In fact, the $IBr^-(CO_2)_{12}$ clusters having $\Delta\Phi > 0$ on the ground state are already in that part of the excited state after excitation, where, following $IBr^-(CO_2)_8$, transitions to lower states occur. Analysis of GSR trajectories shows that many of the rapidly relaxing clusters come from this side, although that is not a certainty

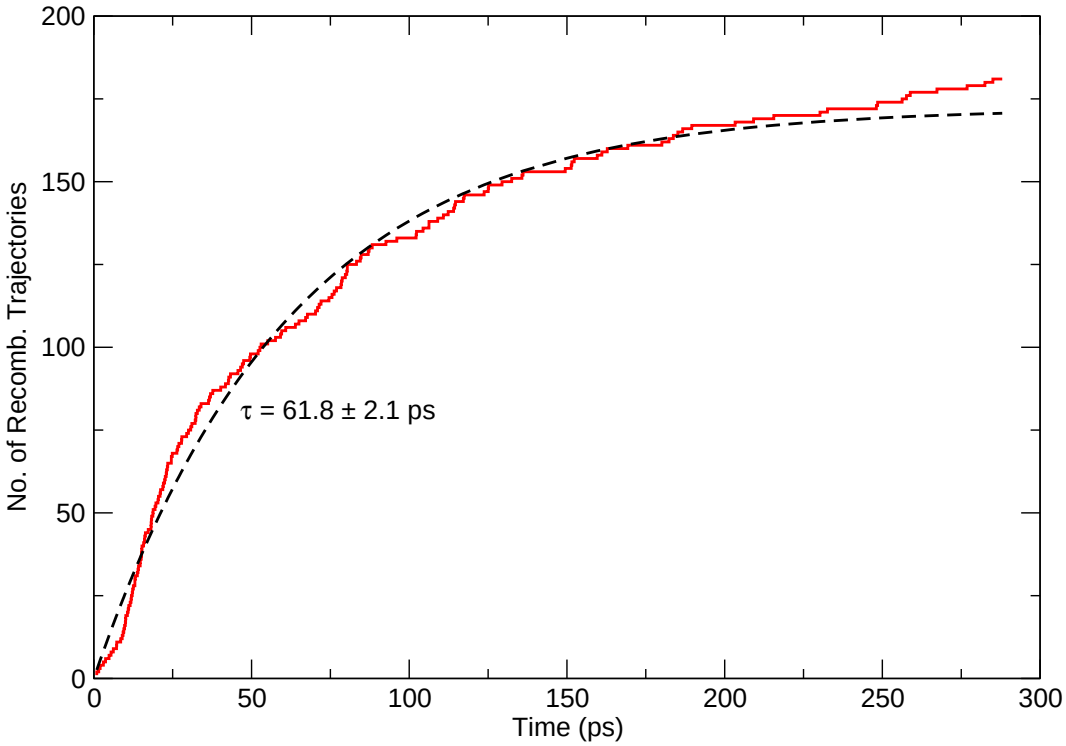

Figure 4.17: Ground-state recombination dynamics for $IBr^{-}(CO_2)_{12}$. The red line represents theoretical results. Dotted lines represent single-exponential fits to the data, see Equation 4.1.

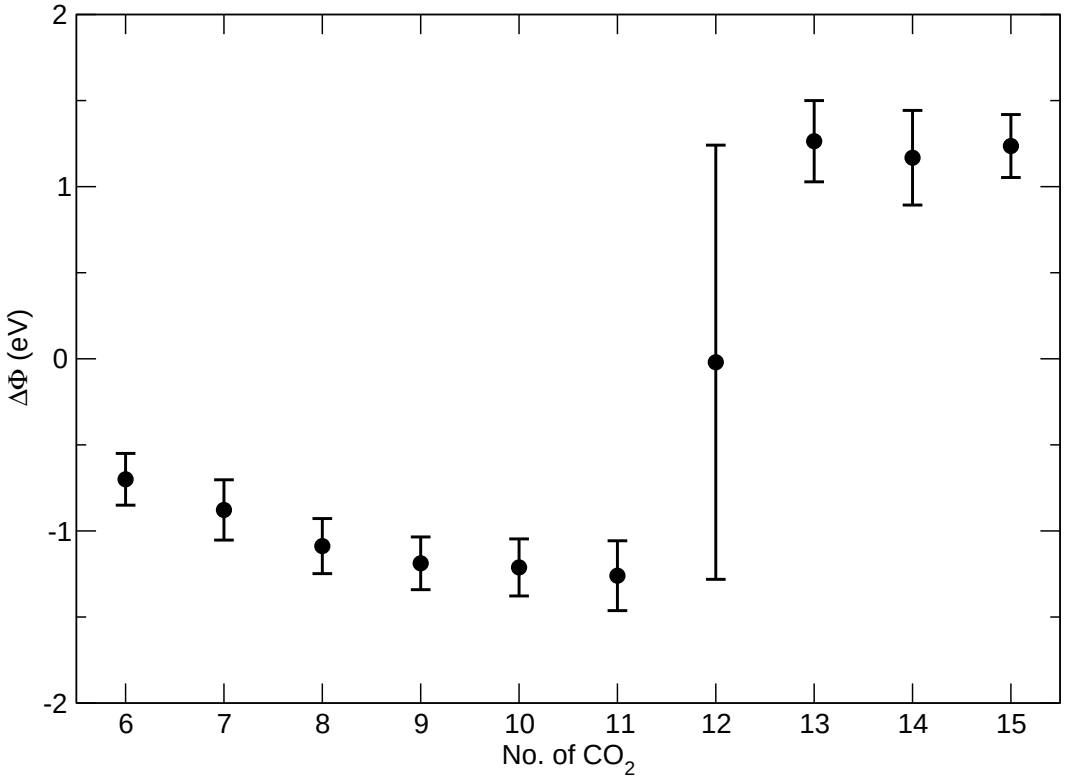

Figure 4.18: Average solvent coordinate ($\Delta\Phi$) of the excited-state well in $IBr^-(CO_2)_{6-15}$ simulations. Error bars represent one standard deviation of the mean.

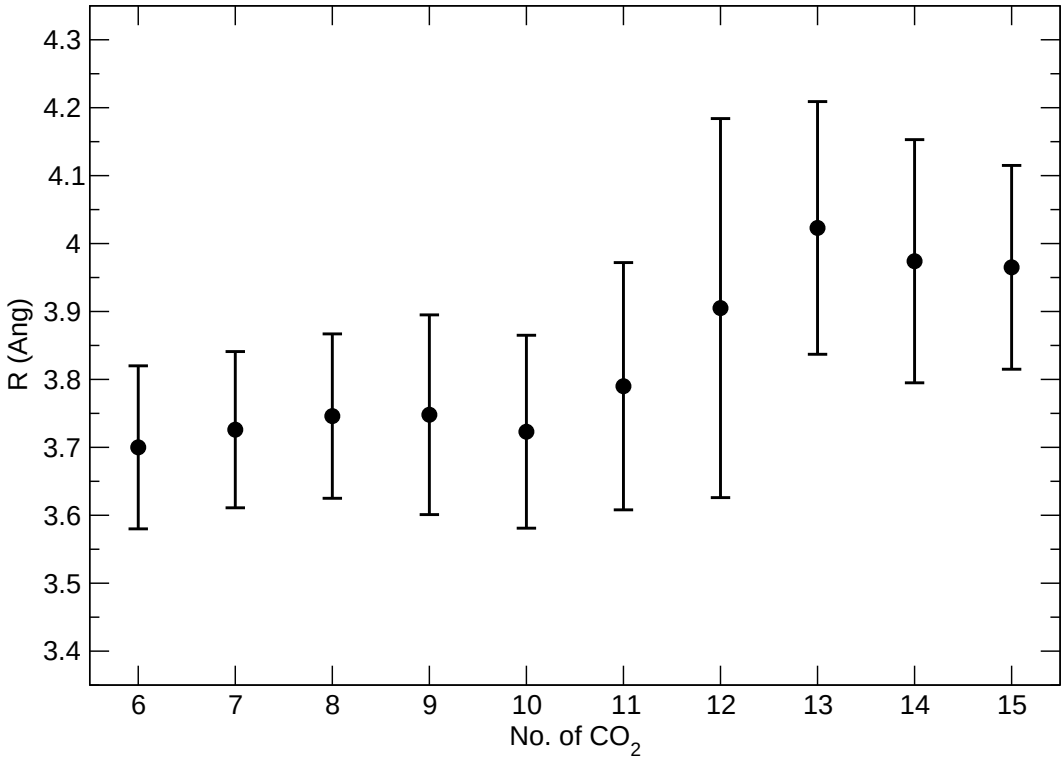

Figure 4.19: Average solute bond length of the excited-state well in $IBr^-(CO_2)_{6-15}$ simulations. Error bars represent one standard deviation of the mean.

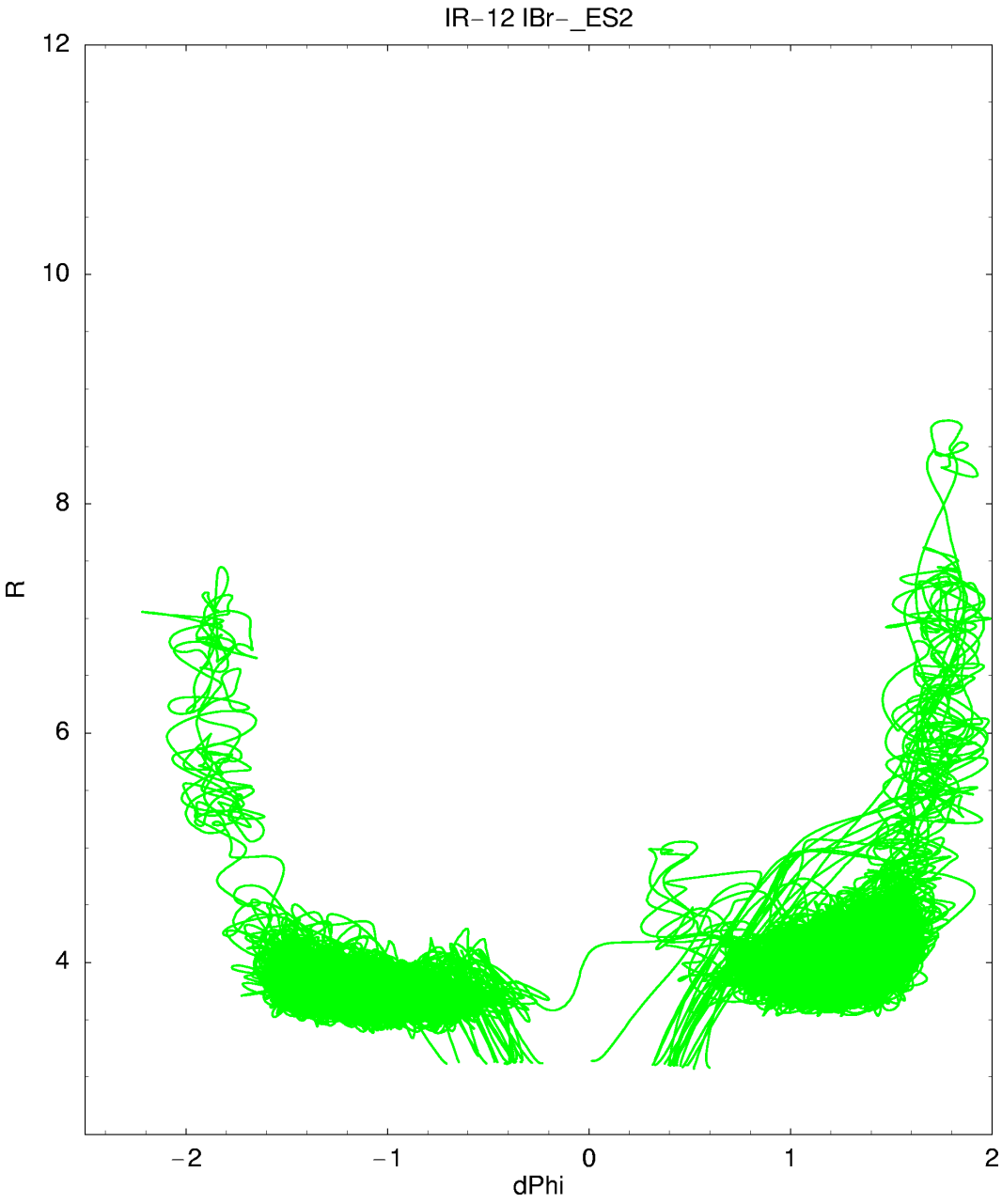

Figure 4.20: Plot of solvent coordinate versus solute bond length for $IBr^-(CO_2)_{12}$ short-length trajectories that were trapped on the excited state. Green represents trajectory dynamics on the second-excited state. dPhi (=$\Delta\Phi$) is in eV and R is in Angstroms.

as long excursions can occur on the lower states. Also, since $IBr^-(CO_2)_{12}$ has a fairly fast GSR recovery time, the transition state barrier for the -$\Delta\Phi$ $IBr^-(CO_2)_{12}$ trajectories is probably not as large as for the intermediate-sized clusters.

In Figure 4.21, the solvent flow dynamics are plotted for $IBr^-(CO_2)_{12}$ trajectories that relax to the ground state. While messy, the figure gives an overall picture of the process that $IBr^-(CO_2)_{12}$ uses to recombine. Unlike $IBr^-(CO_2)_8$ (Figure 4.8), $IBr^-(CO_2)_{12}$ is able to easily reorganize the solvent shell so that it can access the transition zone at $\Delta\Phi \approx 0.3$ eV and around 5 Å. After that, though, the dynamics are quite similar. Both quickly move to either bromine or iodine solvated configurations in the A state and then relax to the ground state and recombine. This helps confirm that the barrier seen in $IBr^-(CO_2)_{8-11}$ exists because of the fairly rigid solvent configurations that these clusters can easily access in the excited state.

Finally, preliminary studies [123] have shown a possible experimental recovery time for $IBr^-(CO_2)_{12}$ on the order of 10 ps which is indicated in Figure 4.1. While this data has not been confirmed with additional experiments, it does provide evidence that our predicted turnaround in the GSR recovery time at $IBr^-(CO_2)_{12}$ has an experimental counterpart. As discussed in Section 4.5.4, experimental studies in this regime are difficult to carry out.

4.5.2 The Large Clusters: $IBr^-(CO_2)_{13,15,16}$

The clusters whose GSR dynamics can be considered to be typical of large clusters are $IBr^-(CO_2)_{13,15,16}$. Analysis of $IBr^-(CO_2)_{14}$ is deferred until Section 4.5.3 due to its unique double time scale dynamics. First, the simulated dynamics of $IBr^-(CO_2)_{13}$ (Figure 4.22) continue the rapid recovery seen in $IBr^-(CO_2)_{12}$. It was found that the simulated GSR time for $IBr^-(CO_2)_{13}$ was 34.1 ± 1.6 ps. Thus, $IBr^-(CO_2)_{13}$ undergoes GSR at a faster rate than $IBr^-(CO_2)_{12}$. This phenomenon can be explained, for $IBr^-(CO_2)_{13}$ as well as $IBr^-(CO_2)_{15,16}$, by referring back to the excited-state statistics in Figure 4.18. Unlike $IBr^-(CO_2)_{12}$, there is not a component of the dynamics in the -$\Delta\Phi$ side of the excited state. Instead, **all** the clusters begin their recombination dynamics on the same side of the excited state as the transition zone

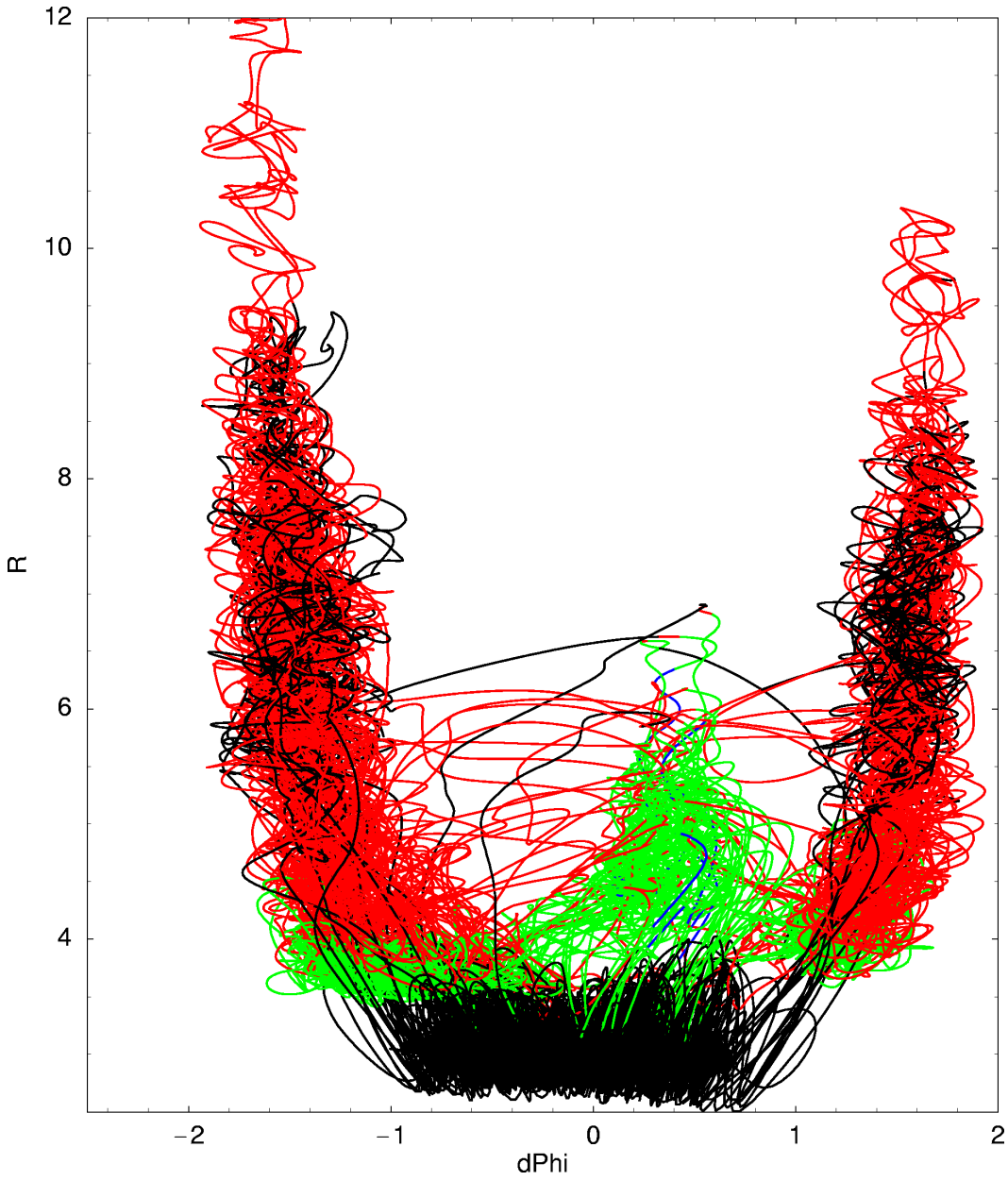

Figure 4.21: Plot of solvent coordinate versus solute bond length for $IBr^{-}(CO_2)_{12}$ trajectories that relax to the ground state. Black, red, and green represent trajectory dynamics on the ground, first-, and second-excited state. dPhi (=$\Delta\Phi$) is in eV and R is in Angstroms.

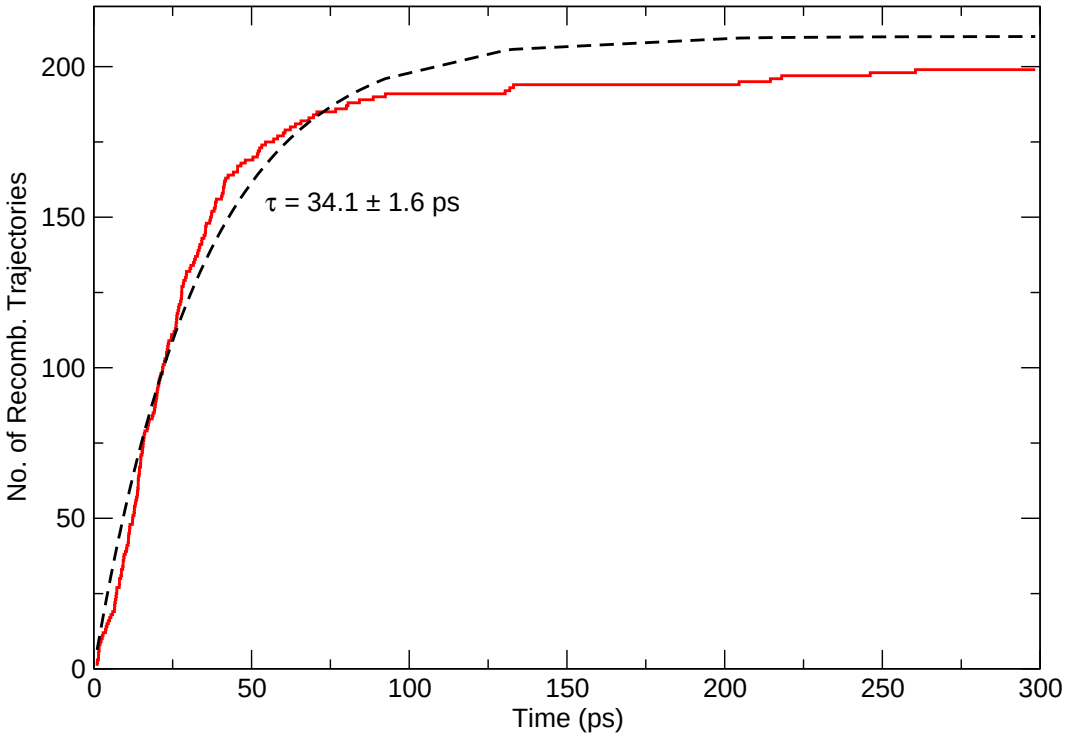

Figure 4.22: Ground-state recombination dynamics for $IBr^{-}(CO_2)_{13}$. The red line represents theoretical results. Dotted lines represent single-exponential fits to the data, see Equation 4.1.

located at $+\Delta\Phi$. This means that while there might be some movement in an excited state well, there exists little to no barrier to solvent reorganization, so that the solvent configurations where nonadiabatic transitions occur are readily reached.

Similar dynamics are seen in $IBr^-(CO_2)_{15}$ and $IBr^-(CO_2)_{16}$. Simulations of $IBr^-(CO_2)_{15}$ were run (Figure 4.23) and it was found that the simulated GSR time for $IBr^-(CO_2)_{15}$ was 32.7 ± 2.8 ps. Also, simulations of $IBr^-(CO_2)_{16}$ were run (Figure 4.24) and it was found that the simulated GSR time for $IBr^-(CO_2)_{16}$ was 52.0 ± 3.1 ps. Thus, for the largest clusters studied, the simulations show that GSR becomes both fast and the dominant channel for near-infrared (IR) photodissociation. Except, that is, for $IBr^-(CO_2)_{14}$.

4.5.3 The Curious Case of $IBr^-(CO_2)_{14}$

The most interesting larger cluster of $IBr^-(CO_2)_n$ is that of $IBr^-(CO_2)_{14}$, which simulation predicts has a double time scale for ground-state recombination (GSR). Shorter, 150-ps runs similar to those done for the other larger clusters showed a significant number of trajectories still trapped on the excited state at the end of the run-time. In order to fully test this phenomenon, an ensemble of 100 trajectories was run for 3 ns with the results for GSR shown in Figure 4.25. The GSR data for $IBr^-(CO_2)_{14}$ could only be reliably fit to a **double** exponential with time constants of 40.9 ± 1.9 ps and 1500 ± 440 ps. Thus, there appear to be two different processes present in $IBr^-(CO_2)_{14}$. One is much like the fast recovery process seen in the larger clusters, while the other is slow like that seen in $IBr^-(CO_2)_{8-11}$.

In order to investigate this double "personality" of $IBr^-(CO_2)_{14}$, solvent flow plots for two different recombined trajectories are presented below that demonstrate the two mechanisms. Figure 4.26 shows a trajectory that gets caught in an excited-state well on the A' state. This well is the $+\Delta\Phi$ mate to the -$\Delta\Phi$ well seen in $IBr^-(CO_2)_8$ trajectories. Like $IBr^-(CO_2)_8$ there again appears to be a configurational transition state that must be crossed in order to reach the nonadiabatic transition valley. And, as before, the hopping region lies in a configuration that is more symmetrical than that of the trapped species.

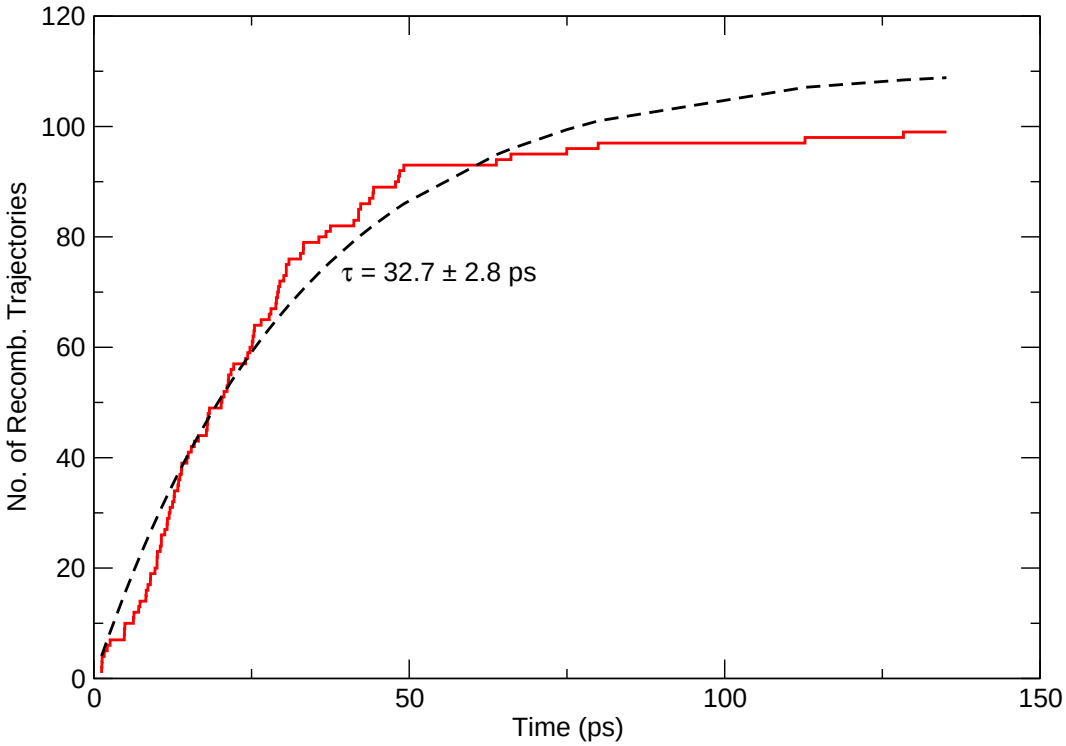

Figure 4.23: Ground-state recombination dynamics for $IBr^{-}(CO_2)_{15}$. The red line represents theoretical results. Dotted lines represent single-exponential fits to the data, see Equation 4.1.

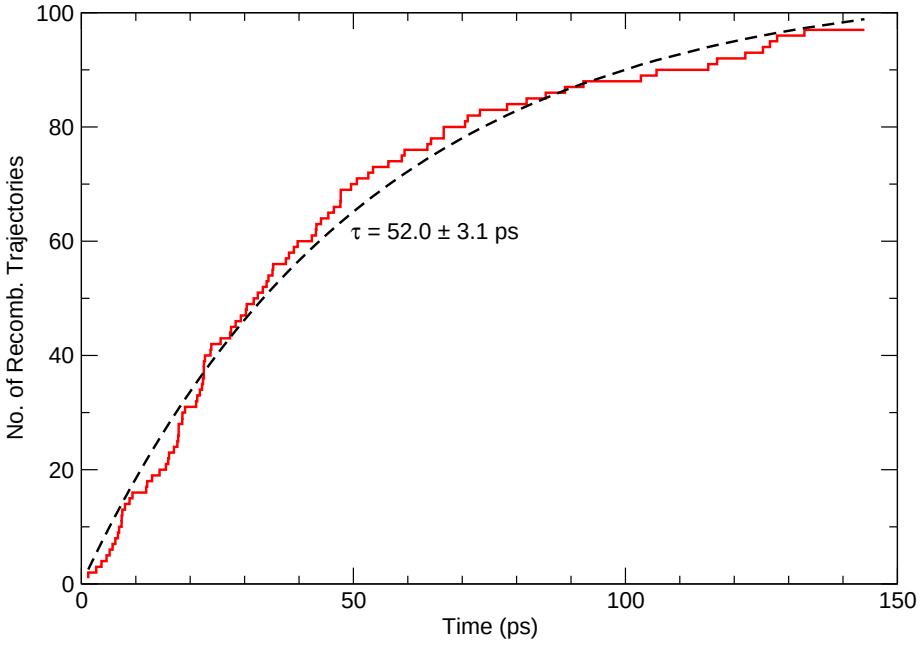

Figure 4.24: Ground-state recombination dynamics for $IBr^{-}(CO_2)_{16}$. The red line represents theoretical results. Dotted lines represent single-exponential fits to the data, see Equation 4.1.

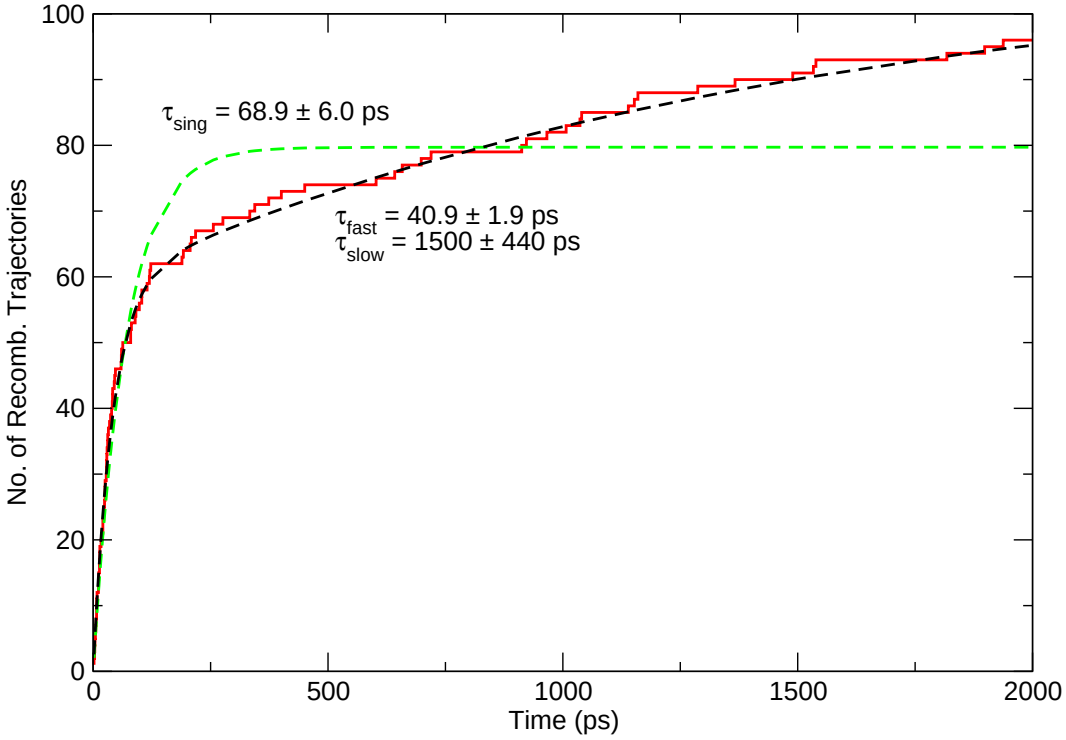

Figure 4.25: Comparison of single- and double-exponential fits to the ground-state recombination time of $IBr^{-}(CO_2)_{14}$. The red line represents the theoretical results. The green-dashed and black-dashed lines are single- and double-exponential fits, respectively. Ensemble composed of 100 3-ns trajectories.

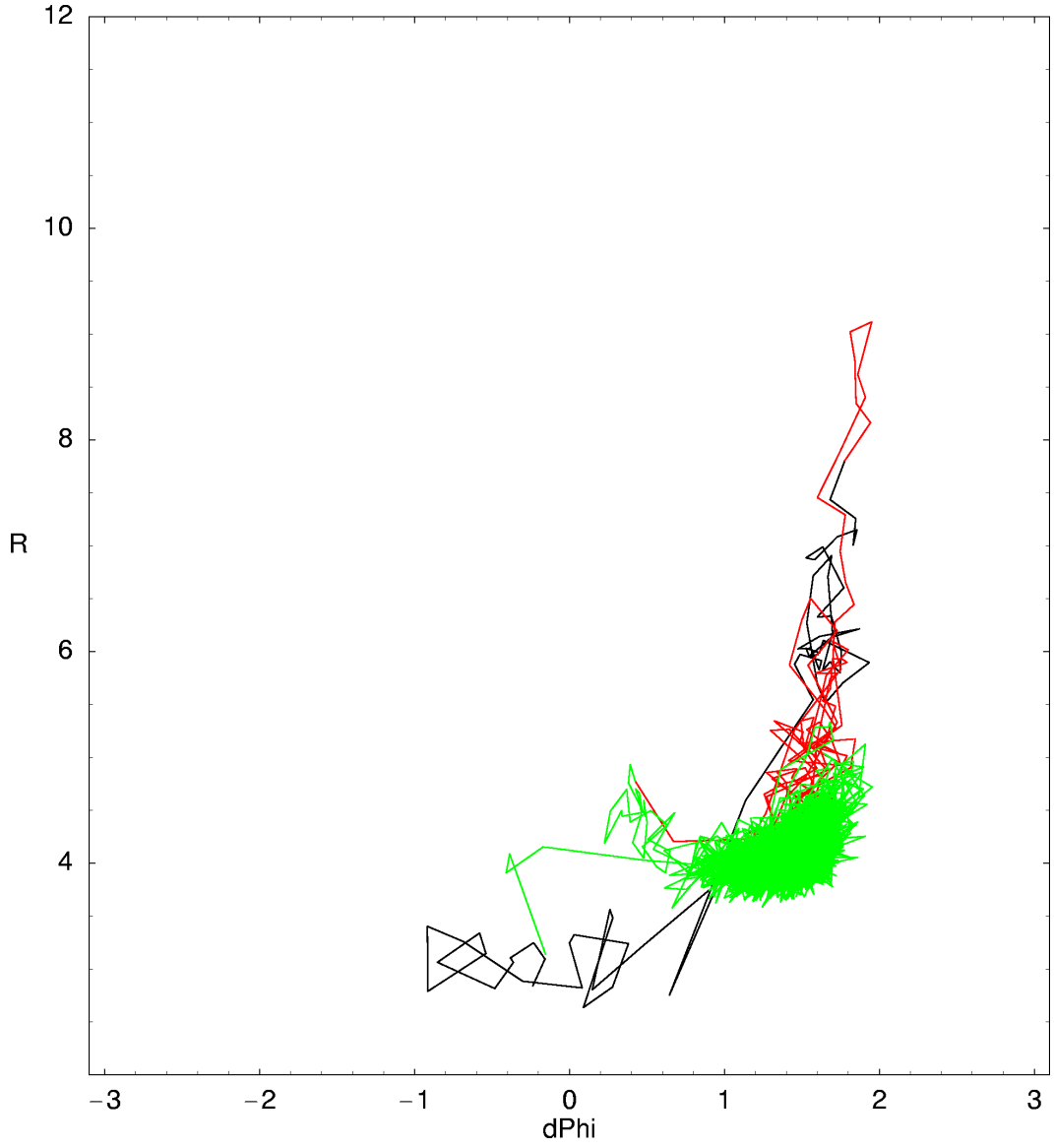

Figure 4.26: Plot of solvent coordinate versus solute bond length for a long $IBr^-(CO_2)_{14}$ trajectory that ends as IBr^- on the ground state. Black, red, and green represent trajectory dynamics on the ground, first-, and second-excited states, respectively dPhi (=$\Delta\Phi$) is in eV and R is in Angstroms.

Conversely, a larger proportion of the $IBr^-(CO_2)_{14}$ GSR product actually proceeds in a fashion similar to other large clusters. As seen in Figure 4.27, the trajectory manages to avoid being trapped in the A' well and instead proceeds with a fast recombination to the ground state. The reason why $IBr^-(CO_2)_{14}$ can proceed by a fast process is obviously that it is similar in its near-symmetric configuration like that of $IBr^-(CO_2)_{13,15}$. The solvent-mediated transition state shown for the long-time GSR recovery is most likely lower than the one seen in $IBr^-(CO_2)_{8-11}$ since even the long-time component is faster than the "fastest" intermediate-sized cluster, $IBr^-(CO_2)_{11}$. This is most likely due to the location of the nonadiabatic transition zone. As seen in both Figure 4.26 and Figure 4.8, the transition zone is located at positive values of $\Delta\Phi$. Thus, the $IBr^-(CO_2)_{8-11}$ clusters must wholly change their solvent character from bromine- to iodine-solvated before the recombination process can begin. $IBr^-(CO_2)_{14}$, on the other hand, is already solvated on the iodine and need less solvent motion as a consequence. What is still unclear, however, is why $IBr^-(CO_2)_{14}$ shows a long-time process at all and whether this is an artifact of the simulations or is based in reality.

As a test of the simulations, in analogy to $IBr^-(CO_2)_8$, runs for $IBr^-(CO_2)_{14}$ were made using a bluer, 730-nm photon with the results shown in Figure 4.28. These simulations consisted of 100 total trajectories, of which 99 recombined in the ground state by the end time of 2000 ps. A trajectory was considered complete when 2000 ps had elapsed, an I-Br separation of 40 a_0 was reached, or 20 crossings of the ground state had occurred. Using a 730-nm excitation, simulations predict a single GSR recovery time of 54.3 ± 1.3 ps. This is in contrast to the double time scale for recovery seen using the 790-nm excitation. Thus, it is possible that the excited-state well seen for $IBr^-(CO_2)_{14}$ is perhaps just a coincidence of the energetics. However, in the favor of trapping is the fact that the ground-state well depth predicted by our calculations, Figure 2.1, is shallower than in experiment. Thus, even a 790-nm excitation could be too blue! An experimental test is needed to successfully resolve this oddity.

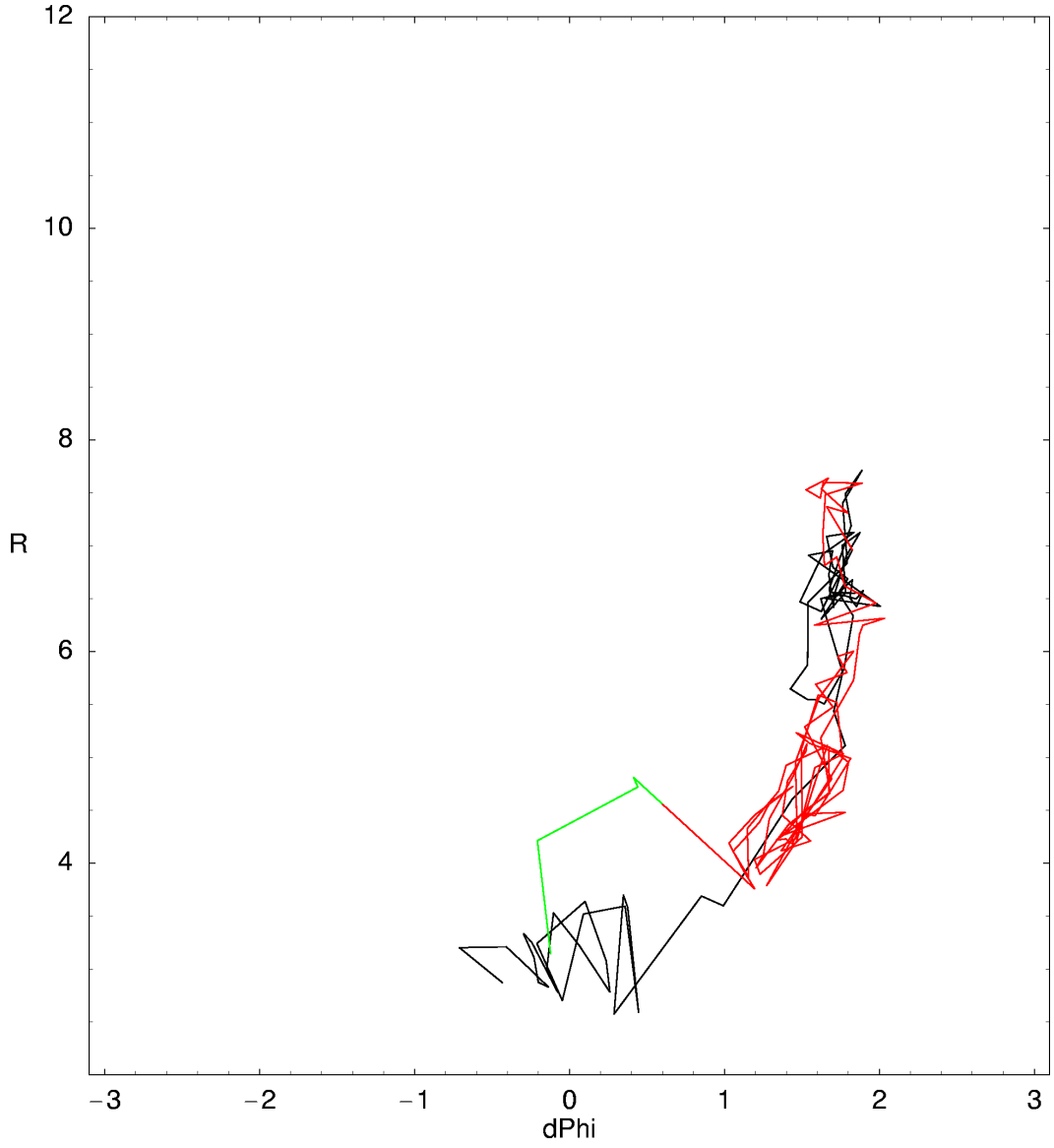

Figure 4.27: Plot of solvent coordinate versus solute bond length for a short $IBr^-(CO_2)_{14}$ trajectory that ends as IBr^- on the ground state. Black, red, and green represent trajectory dynamics on the ground, first-, and second-excited states, respectively dPhi (=$\Delta\Phi$) is in eV and R is in Angstroms.

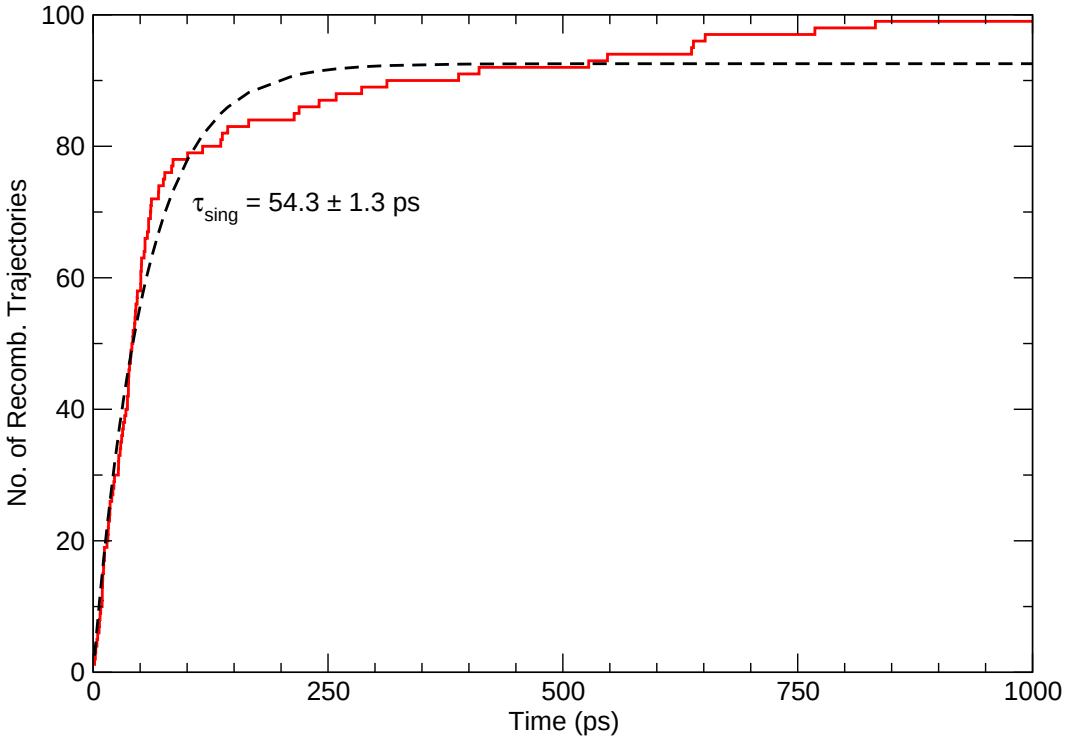

Figure 4.28: Ground-state recombination dynamics of $IBr^{-}(CO_2)_{14}$ excited with a 730-nm photon. The red line represents the theoretical results. The dotted line represents single-exponential fit to the data, see Equation 4.1.

4.5.4 Experimental Difficulty with Large $IBr^-(CO_2)_n$ Clusters

The theoretical predictions of a recombination time turnaround at large cluster size and of a possible double time scale for recombination in $IBr^-(CO_2)_{14}$ have yet to be verified by experiment. Unfortunately, several factors combine to make such experiments very difficult.

To begin with, generation of these clusters is difficult. As the size of the clusters increases, the yield of starting clusters decrease. For example, $IBr^-(CO_2)_{12}$ is generated at a rate one-fourth that of $IBr^-(CO_2)_{6-8}$. Various changes to the experimental setup including more powerful electron guns, valve orifice size alterations, and pulse variance have led to no improvement, and indeed, sometimes resulted in a decrease in signal. [123]

Moreover, as the cluster size increases, our simulated absorption spectra indicate that the peak for $A' \leftarrow X$ absorption is blue-shifted away from that of bare IBr^- (Figure 4.29). As the excitation laser used for the near-IR experiments is only slightly adjustable around the 790-800 nm range, by the time the cluster size increases to $IBr^-(CO_2)_{12}$, the absorption cross section is essentially gone. Moreover, as the calculated ground-state well depth is shallower than that in the experiment [79], the calculated values for all $IBr^-(CO_2)_n$ spectra are redshifted by default, q.v. Section 2.2.3. This means the experimentalists are "doubly-damned" when attempting to effect absorption of large clusters.

While this does presage difficulty in experimental verification of larger cluster dynamics, the calculated $IBr^-(CO_2)_{12}$ spectrum, Figure 4.29, does have some interesting features that are worth exploring. From the inset, the $A' \leftarrow X$ peak for $IBr^-(CO_2)_{12}$ appears to be a combination of two peaks. As seen in Figures 2.14 and 4.18, $IBr^-(CO_2)_{12}$ presents itself in simulation as a "bridge" between the highly asymmetric clusters of $IBr^-(CO_2)_{8-11}$ and the more symmetric larger clusters, $IBr^-(CO_2)_{13-16}$. To show this phenomenon in the spectrum, spectra for $IBr^-(CO_2)_{11}$ and $IBr^-(CO_2)_{16}$ were calculated and their $A' \leftarrow X$ peaks were plotted in comparison to that of $IBr^-(CO_2)_{12}$. As seen in the inset of Figure 4.29, the $IBr^-(CO_2)_{12}$ peak is a combination of two peaks, corresponding to asymmetric and symmetric clusters. Likewise,

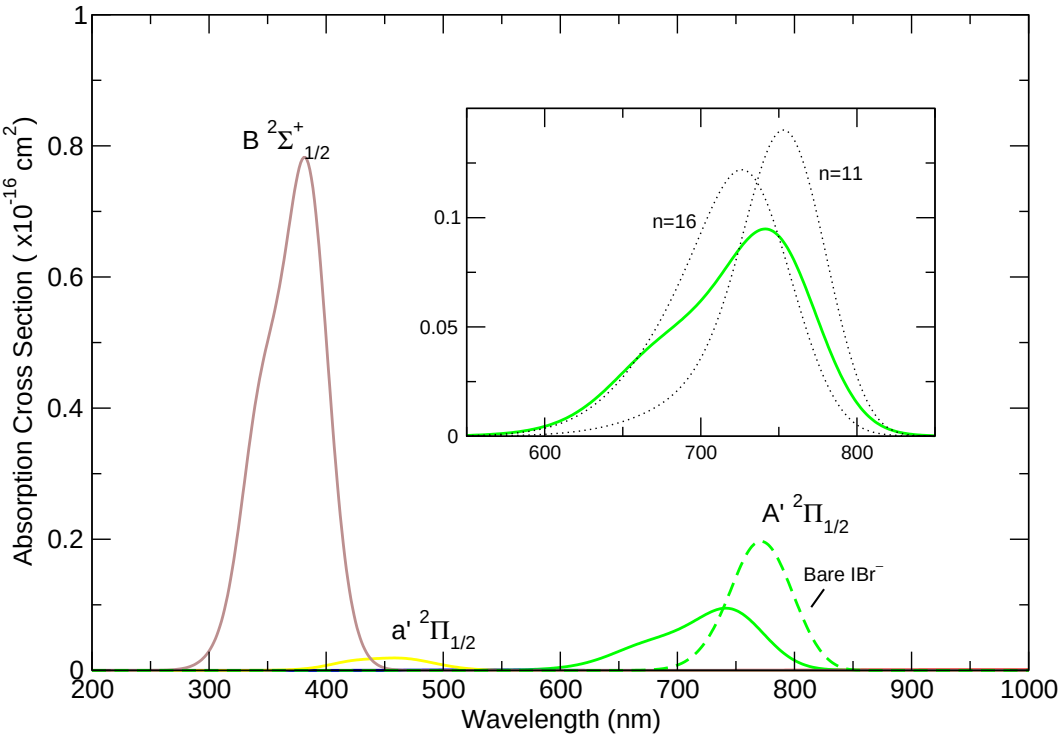

Figure 4.29: Calculated absorption spectrum for $IBr^-(CO_2)_{12}$. Inset shows peaks on A' state for $IBr^-(CO_2)_{11,16}$, dotted. Spectrum is average of 100 configurations sampled at 60 K.

the $B \leftarrow X$ also has the double-peak shape that can be attributed to this phenomenon. We note with caution that existence of this phenomenon in experiment could depend sensitively on cluster energetics (real v. simulated model) and cluster temperature, which is not well known.

4.6 Ground-State Recombination Sensitivity to Excitation Wavelength

This section will explore how the calculated well depth difference, see Section 2.2.1.3, affects the ground-state recombination (GSR) dynamics of $IBr^-(CO_2)_n$. Earlier experimental results [79] have shown that the D_0 for bare IBr^- is 1.10 ± 0.04 eV while the calculations give a D_e of 0.956 eV. Thus, when a 790-nm photon is used to model experiments undertaken at 790-nm, the simulations are providing the cluster with a larger kinetic energy release than in reality. More recent experimental results have demonstrated a D_0 for IBr^- of 0.954 ± 0.006 eV [111]. As this is a much closer match to our calculated value of D_e, we must take into account the possible zero-point energy (ZPE) offset which would account for smaller kinetic energy release (KER) in simulation using a 790-nm photon.

To assess the effect of a lower KER upon excitation, simulations were run using an 840-nm photoexcitation. Likewise, 770-nm photoexcitation simulations were also carried out to model the effect of slightly more KER in $IBr^-(CO_2)_n$. Section 3.4 demonstrated that adjusting the excitation wavelength had minimal impact on the photodissociation product ratios. Figure 3.8 shows that in the "infinite-time" extrapolation that the 770-nm and 840-nm product ratios closely matched that of the 790-nm simulations and were essentially within the sampling error. However, there could still be a significant effect on the relaxation dynamics. The previous results in this chapter suggest that the GSR recovery dynamics for $IBr^-(CO_2)_n$ are determined by the rate of passage across a transition state barrier. In that vein, one would expect any change that affects the energy either needed to cross that barrier or the energy available to the system to have an exponential effect on the dynamics [124].

In order to test this effect, trajectories were assembled for $IBr^-(CO_2)_{5-16}$. Each en-

semble was composed of 100 trajectories assembled in the same fashion as detailed previously in Section 3.1. The trajectories ran with a classical time-step of 1.0 fs for durations of 100 ps for $IBr^-(CO_2)_{5,6}$, 400 ps for $IBr^-(CO_2)_7$, 5000 ps for $IBr^-(CO_2)_{8,9}$, and 400 ps again for $IBr^-(CO_2)_{12-16}$. The results of the simulations were then modeled according to the prescriptions in Section 4.1 and the resulting time constants are shown in Figure 4.30.

Lowering the photoexcitation to mimic a lower KER does appear to have an effect. As expected, lowering the energy available to traverse the configurational transition state barrier increases the recovery times at all cluster sizes. For $IBr^-(CO_2)_{5-7}$, the simulated results more closely match the experiment, with a near match at $IBr^-(CO_2)_7$. In all cases, the 840-nm photoexcitation has had the expected effect of lengthening the GSR recovery time.

In the larger clusters, however, the effect of the redder excitation becomes one of overcorrection, significantly increasing GSR recovery times. The 840-nm results shown for $IBr^-(CO_2)_8$, $IBr^-(CO_2)_9$, and $IBr^-(CO_2)_{11}$ are shown in Figure 4.30 as 5 ns for convenience only. In reality, as in the intermediate clusters above, see Section 4.4, these numbers are a **lower bound** for the true recovery times. The lowering of the photon energy, and, thus, the KER, has had the effect of greatly strengthening the effect of the A' well; so much so, that only approximately 10 trajectories for each cluster size completed their run-time in two weeks of calculations. This is also the reason that no results for $IBr^-(CO_2)_{10}$ are included in Figure 4.30.

However, in $IBr^-(CO_2)_n$, with $n > 12$, the situation returns to being similar to the 790-nm results. $IBr^-(CO_2)_{12}$ is once again a bridge between the long-time trapping clusters and the faster, larger clusters. Like the $IBr^-(CO_2)_{5,6}$, there is once again a slight increase in the calculated GSR recovery times. Again, this is the expected effect of less KER from the redder excitation. And, as seen in the 790-nm simulations, $IBr^-(CO_2)_{14}$ exhibits a double time scale and both time constants show the expected effect. The short-time dynamics are slightly longer, with the long-time dynamics greatly enhanced.

When compared to the 790-nm results, the 770-nm simulations again show the expected behavior for increasing the KER after excitation. In the smaller clusters, $IBr^-(CO_2)_{5-7}$, the

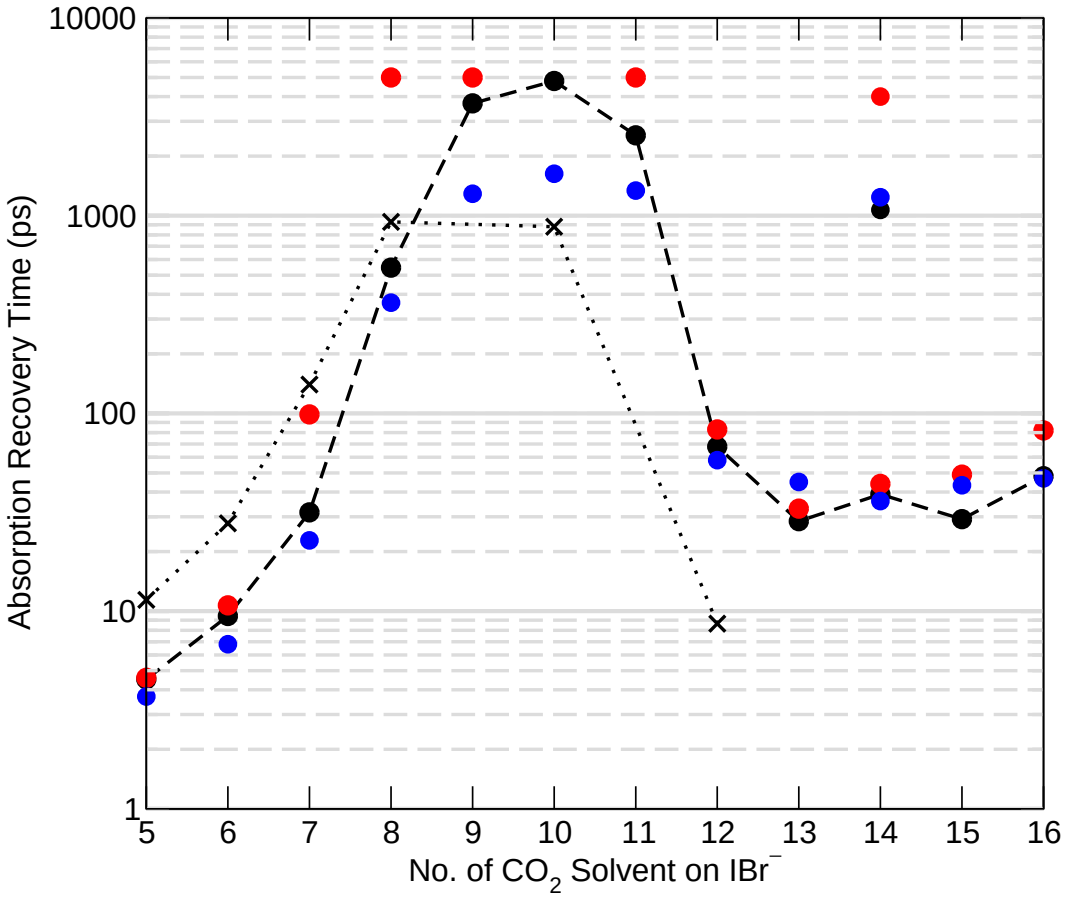

Figure 4.30: Simulated 790-nm (black solid with circles), 840-nm (red circles), 770-nm (blue circles) and experimental (dotted with X's) ground-state recombination times for $IBr^-(CO_2)_n$ photodissociation. Experimental results from Dribinski, et al [80].

simulated GSR recovery times are slightly less than those found in the 790-nm simulations. Since more kinetic energy should lead to faster dynamics out of the well, this is as we expect. But, since our calculated 790-nm GSR recovery times were already too fast compared to experiment, this is a less than desirable pattern. Likewise, in the larger clusters we see much the same with slightly smaller recovery times for the 770-nm excitation. One possible exception is $IBr^-(CO_2)_{15}$ whose recovery time at 770-nm is slightly higher than that for the 790-nm excitation; however, the difference is minimal, on the order of 10 ps.

More interesting trends are seen when we compare the results for the 770 nm excitation to the 790-nm simulations for the intermediate-sized clusters. In these clusters, we have formed once again a strong excited-state well whose presence is dominating the dynamics. While the 770-nm simulations still overestimate the recovery times, increasing the excitation energy by just 40 meV has decreased the GSR recovery times for the trapped species by a half to a quarter. More importantly, this has had the effect of bringing the simulated GSR recovery times into closer match with experiment. However, this finding is tempered by the fact that this effect is due to altering the excitation wavelength while keeping all other possible simulation parameters constant. As we will seen in the next section, the simulations can also be profoundly affected by the choice of the Lennard-Jones parameters for the solute-solvent short-range interactions.

4.7 Ground-State Recombination Sensitivity to Alteration of the Model Potential Parameters

In Section 2.2.2 it was pointed out that the standard Lennard-Jones (LJ) fit, tabulated in Table 2.3, may not be the ideal fit. From Figure 2.7, the standard fit, while a best compromise, was not the best that could be made to the coupled cluster with single, double, and iterative triple excitations (CCSD(T)) calculations carried out for the $Br^- \cdots CO_2$ interaction. An alternate set of LJ parameters were determined that matched the energetics of the CCSD(T) fit as shown in Figure 2.15. A similar set of LJ parameters were determined that matched the $Br^- \cdots CO_2$ T-shaped energetics predicted by a multireference configuration interaction (MRCI) calculation

of the system. This MRCI prediction is shown in Figure 2.7 and is shallower even than the standard LJ fit.

In order to test the effect of the other parameter sets, simulation for $IBr^-(CO_2)_{1-14}$ were run. For each cluster size, the ensemble was composed of 100 trajectories assembled in the same fashion as detailed in Section 3.1. The trajectories ran with a classical time-step of 1.0 fs for durations of 50 ps for $IBr^-(CO_2)_{1-6}$ and 3000 ps for $IBr^-(CO_2)_{7-14}$. The results for these simulations are shown in Figure 4.31.

The top plot in Figure 4.31 compares the simulated and experimental results to that using the more attractive CCSD(T) LJ fit to the $Br^- \cdots CO_2$ interaction. The effect on ground-state recombination (GSR) recovery times is quite a bit like that seen in the well depth sensitivity studies (Figure 4.30). However, the CCSD(T) LJ fit seems to have a much more pronounced increase in the simulated recovery time. While the effect on $IBr^-(CO_2)_5$ is to nearly match the experimental result, the GSR recovery time for $IBr^-(CO_2)_6$ is increased by an order of magnitude. For $IBr^-(CO_2)_7$ and $IBr^-(CO_2)_{12}$, the effect is an increase of **two** orders of magnitude. We note for completeness that, like the 840-nm results above, the CCSD(T) LJ fit simulations for $IBr^-(CO_2)_{8-12}$ were truncated in the number of completed trajectories, due to the lack of computation time.

This much larger effect of the CCSD(T) LJ parameters compared to the effect of changing the excitation wavelength is due to the size of each correction. Changing the excitation wavelength had the effect of only lowering the kinetic energy release (KER) of all clusters by a fixed amount upon excitation. However, the use of a more attractive $Br^- \cdots CO_2$ interaction causes any effect to be multiplied as more solvent molecules are added. Also, the minimal energy clusters, Figure 2.12, show that as clusters build to $IBr^-(CO_2)_8$, the solvent is primarily added on the bromine end. And, while these clusters were constructed with the standard LJ fit, the bromine end is more heavily favored with use of the CCSD(T) fit.

Proceeding to larger clusters, the effect of the CCSD(T) $Br^- \cdots CO_2$ LJ fit is less drastic. Indeed, the results move back into a near match with the GSR recovery times seen with the

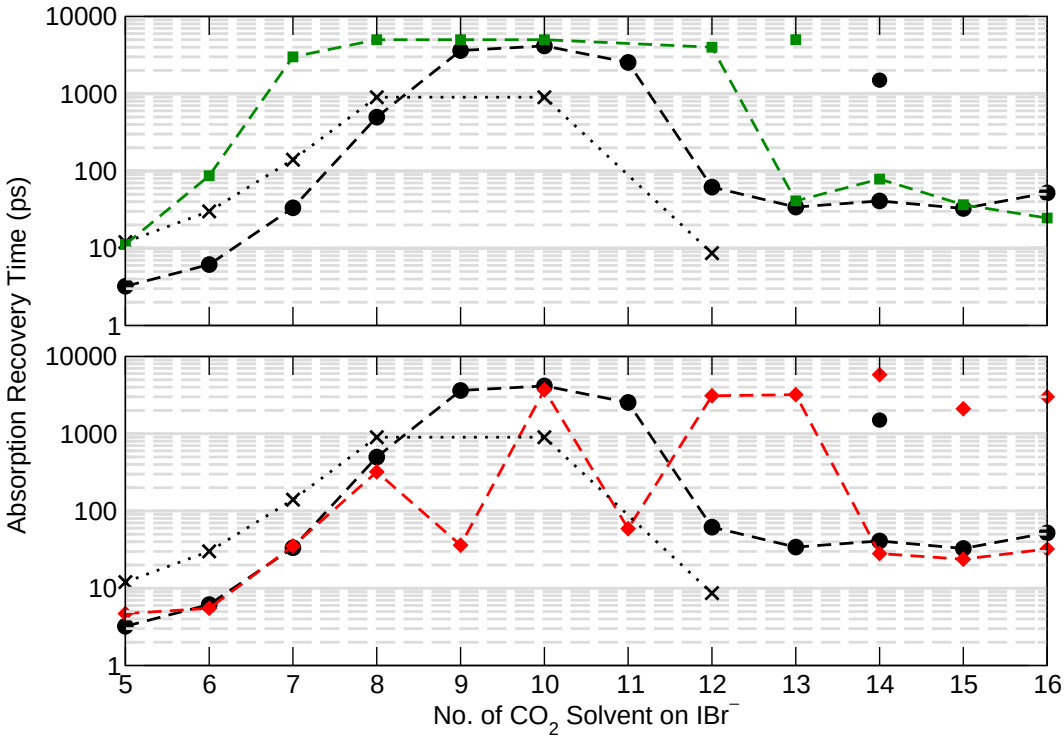

Figure 4.31: Simulated ground-state recombination times for near-infrared (790-nm) photoexcitation for the Lennard-Jones fits from CCSD(T) (top, green) and MRCI (bottom, red) $Br^- \cdots CO_2$ calculations as seen in Figure 2.7, as well as the normal Lennard-Jones fit from Table 2.3 (dashed with circles) and experimental results (dot with X's) from Dribinski, et al [80]. Experimental $IBr^-(CO_2)_{12}$ point is unpublished and preliminary [123].

standard fit. This is due to the fact that the added solvent molecules primarily interact with the iodine, rather than the bromine. Since the $I\cdots CO_2$ LJ parameters were not altered, one would expect these additional solvent molecules to have a smaller difference compared to the standard fit. The simulations do show the appearance of another double time scale point, $n_{CCSD(T)} = 13$, similar to that seen in the standard $IBr^-(CO_2)_{14}$, Section 4.5.3, showing that in the case of the CCSD(T) LJ fit, $IBr^-(CO_2)_{13}$ is acting more as a bridge between the long- and short-time recoveries.

As for the other LJ parameter set, that based on the weaker MRCI $Br^-\cdots CO_2$ fit, Figure 4.31 (bottom), the situation is more confused. With the smaller size clusters, $IBr^-(CO_2)_{5-8}$, the MRCI recovery times roughly matches that of the standard parameter set. As the $Br\cdots CO_2$ interaction is now lessened, one would expect that solvent motion on the excited state would be more labile, leading to faster GSR recovery times. After that, though, the MRCI results begin to wildly oscillate. Both $IBr^-(CO_2)_9$ and $IBr^-(CO_2)_{11}$ are extremely fast compared to the standard fit, yet $IBr^-(CO_2)_{12}$ and $IBr^-(CO_2)_{13}$ are orders of magnitude slower. At even larger cluster sizes, the MRCI results can only be fit to a double-exponential! One guess as to the reasons behind these oddities is the fact that the MRCI $Br^-\cdots CO_2$ interaction actually is less attractive than the $I^-\cdots CO_2$ interaction used in the standard model (and still used here, only the bromine was changed). It is possible that the clusters for $IBr^-(CO_2)_9$ and $IBr^-(CO_2)_{11}$ are actually more iodine-solvated so they can act more like the standard larger clusters from Section 4.5. Thus, the solvent motion necessary to reach the nonadiabatic transition zone would be all on the $+\Delta\Phi$ side rather than requiring the solvent to reorganize from a bromine-solvated to an iodine-solvated configuration.

Nevertheless, these results suggest that neither the CCSD(T) nor the MRCI LJ parameter sets provide a superior overall description of the solute-solvent interactions than the standard set.

4.8 Conclusions

In summary, early pump-probe absorption recovery experiments of the near-infrared (IR) photodissociation of $IBr^-(CO_2)_8$ found that ground-state recombination occurred on the order of a nanosecond, rather than the expected tens of picoseconds. In order to help explain these surprising findings, long-duration simulations of the near-IR photodissociation of $IBr^-(CO_2)_n$ were carried out. Our simulations also found a ground-state recombination (GSR) recovery time on the order of nanoseconds for $IBr^-(CO_2)_8$. Analysis of solute and solvent motion in the cluster over the duration of a trajectory through the use of solvent-flow plots found that this long-time recovery is due to the presence of a well on the excited A' state. Clusters are trapped in this well and must undergo a conformational transformation over a transition-state barrier to a more symmetric solvent configuration before relaxation to the ground state can occur.

Subsequent experiments and simulations of the ground-state recovery of $IBr^-(CO_2)_n$ from clusters as small as five solvent molecules to a complete solvent shell have shown strong agreement. Simulations broadly agree that, as the number of solvent molecules increase from five to eight, the GSR time increases by two orders of magnitude—from tens of picoseconds to nanoseconds. In the smaller clusters, our simulations tend to underestimate the GSR, while for the intermediate-sized clusters our simulations overestimate the recovery time.

We were also able to use our simulations to investigate the GSR recovery dynamics in larger cluster still not characterized in experiment. We predict a turnaround in GSR recovery times in larger clusters back to tens of picoseconds. $IBr^-(CO_2)_{12}$ is seen as the critical cluster size where the recovery dynamics change drastically. Analysis of the solvent environment of both the ground and excited A' state clusters show that this turnaround is due to a more favorable solvent configuration upon excitation which no longer requires traversal of a large transition-state barrier. Our simulations have also predicted a double time scale for recovery for $IBr^-(CO_2)_{14}$ due to a different excited-state well. This prediction has not yet been tested by experiment. Preliminary experimental findings on $IBr^-(CO_2)_{12}$, however, agree with the general trend of

a turnaround in recovery times, although future experiments on larger clusters have proved to be difficult. We have offered a partial explanation for this difficulty by calculating absorption spectra for large clusters in the ground state which predict a blue-shift in the $A' \leftarrow X$ absorption band away from the 790-nm excitation wavelength.

Sensitivity tests on the GSR recovery times were also performed. We found that the choice of excitation wavelength had a large effect on the dynamics of $IBr^-(CO_2)_n$ ground-state recombination in contrast to the small effects seen with photoproduct ratios in Chapter 3. Simulations of the effect of reduced kinetic energy release (KER) by use of a redder, 840-nm excitation greatly increased the recovery times of the intermediate-sized clusters, away from the experimental values. However, recent experiments have found a shallower D_0 for IBr^- very close to our calculated D_e. This new result means that zero-point energy (ZPE) becomes important and so simulations using slightly bluer, 770-nm excitation were performed. The slightly larger KER this excitation allows, relative to a 790-nm excitation, was found to improve the performance of our simulated recovery times relative to experiment in intermediate-sized clusters. This finding could present a possible avenue of exploration in the future. A survey of photoexcitations more energetic than 790 nm could provide a possible measure of the difference between our calculated potential energy curves for IBr^- and actual ones. That said, however, we must remember that this would only be exploring the effect of excitation wavelength keeping all other parameters of the simulation—most notably the Lennard-Jones parameters—constant.

Tests were also performed on the effect of using different Lennard-Jones (LJ) parameters for the $Br\cdots CO_2$ interaction in our model. Parameters which more closely matched the coupled cluster with single, double, and iterative triple excitations (CCSD(T)) calculations of the $Br^-\cdots CO_2$ interaction— in effect, a greater $Br\cdots CO_2$ attraction—led to a large enhancement of the excited-state well responsible for the long-duration dynamics and much longer recovery times. LJ parameters which modeled a shallower-than-standard $Br\cdots CO_2$ interaction led to similarly bad performance with both over- and underestimation of the recovery times. However, in this chapter and the previous, we have demonstrated that small changes in our model

of the $IBr^{-}(CO_2)_n$ system, can lead to large effects—both beneficial and detrimental—on the simulated dynamics.

Chapter 5

Dynamics of $IBr^-(CO_2)_n$ Ultraviolet Photodissociation

In this chapter we will explore the overall dynamics of $IBr^-(CO_2)_n$ ultraviolet (UV) (355-nm) photodissociation. We will first present a summary of the simulation methods used in constructing and running the trajectories used in our research. We will then present our simulated results for the product branching ratios for UV photodissociation at 355-nm excitation and compare these results to experiment. In doing so, we will notice that there are two separate regimes of comparison between experiment and theory. In the smaller clusters, we will show that simulation roughly agrees with experiment. However, with the larger clusters, simulation and experiment diverge with the growth of IBr^- as a major photoproduct. This is in sharp contrast to experiment where the recombined products are minimal. We will propose an explanation based upon spin-orbit quenching.

5.1 Ultraviolet Trajectory Simulation Methods

Ensembles for ultraviolet (UV) molecular dynamics (MD) simulations of $IBr^-(CO_2)_{0-14}$ are constructed via the following process. First, using the calculated minimum energy structures, see Section 2.2.4, the cluster is warmed for 40 ps at a temperature of 60 K, followed by a 100-ps run on the ground state to test that the cluster energetics are stable. After that, the ensembles are constructed using a 2-fs time-step run on the ground state that samples every 5 ps until 100 configurations are constructed.

To start the photoproduct trajectories, the configurations of the constructed ensemble

have their I-Br bond lengths adjusted to match the experimental photon energy, 355 nm. Since each of these excitations lie in the $B \leftarrow X$ absorption band, see Figure 2.9, only small adjustments are needed, on the order of 0.1-0.2 Å. Trajectories are then run for 50 ps or until the bond length exceeded 40 a_0 or more than 20 crossings of the ground-state well occur. A step-size of 1 fs is used for all trajectories which results in energy conservation on the order of $10^{-3}E_h$.

5.2 Simulated Ultraviolet Photodissociation Results

The results for the ultraviolet (UV) molecular dynamics (MD) simulations are shown in Figure 5.1. This figure details the three main product channels for the UV photodissociation of $IBr^-(CO_2)_n$: I^-, Br^-, and ground state recombined IBr^-.

As first glance, the simulations seem to agree poorly with experiment. In general, this disagreement is attributed to the large kinetic energy release (KER) the cluster receives at excitation. The simulations are run using a 355 nm, or nearly 3.5 eV photon. In the bare ion, this results in more than 1.5 eV of kinetic energy compared to the B state asymptote, see Figure 2.1. In contrast, the 790-nm simulations of Chapters 3 and 4 receive about 0.5 eV in the bare ion case which, as the cluster grows, isn't enough to escape from a solvent-induced well. Moreover, the expected weaknesses of the model, the Lennard-Jones (LJ) parameters for bromine, have more severe consequences at higher energy. As seen in previous chapters, a relatively small change in the $Br^- \cdots CO_2$ interaction can lead to substantial effects in the simulated photoproduct branching ratios and ground-state recombination (GSR) recovery time. In Section 5.3, we will perform a test of the sensitivity of the UV photoproduct branching ratios to the LJ parameter set.

However, the comparison of theory and experiment can still provide useful insight. In the next two sections, the analysis is partitioned into two regimes for UV photodissociation. In the first, the simulations for $IBr^-(CO_2)_{1-7}$ are examined where there seems to be a "shifted" agreement when compared to simulation. Then, the larger clusters are described where the simulations diverge sharply from the experimental results with the formation of a large GSR

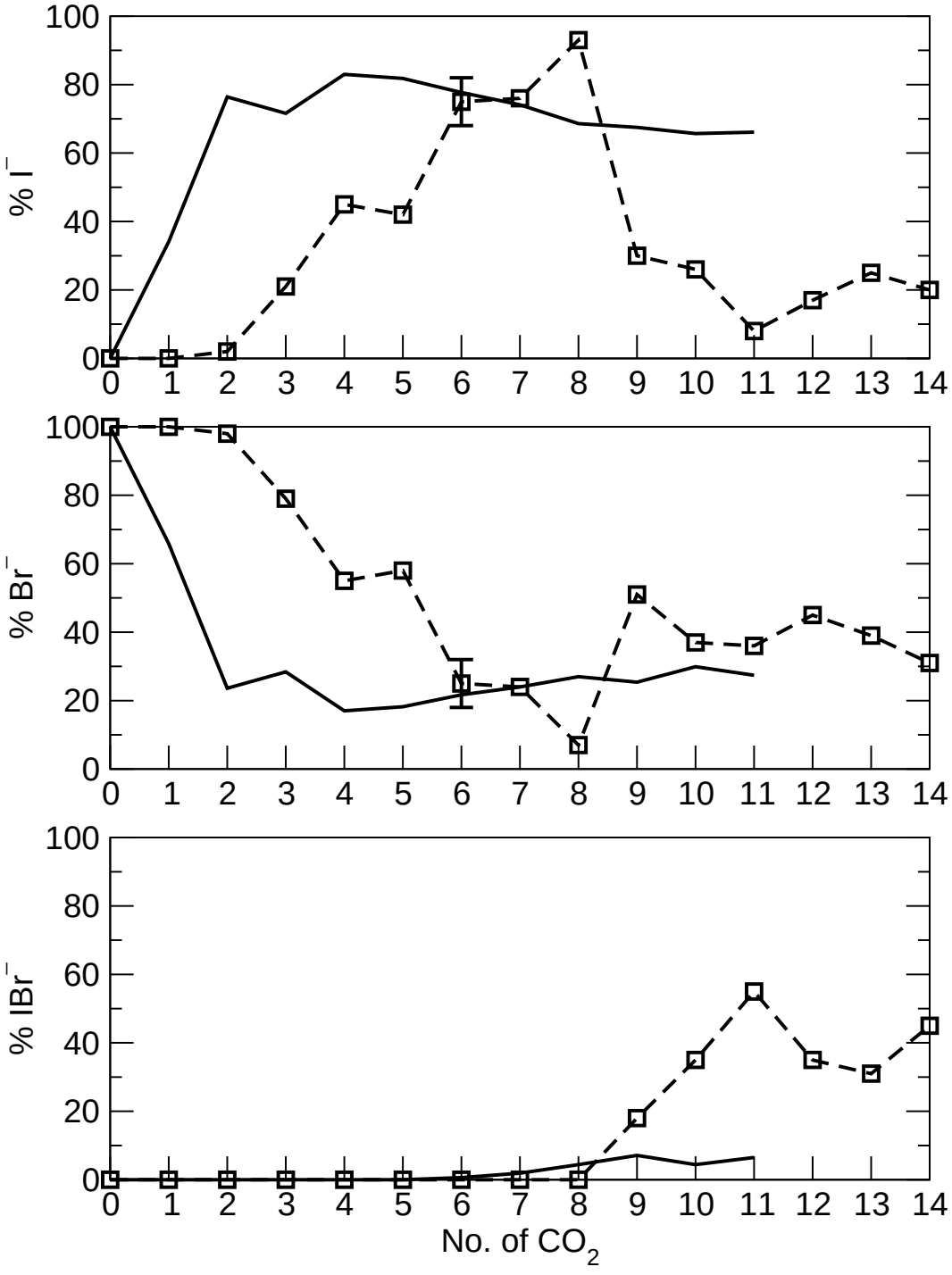

Figure 5.1: Ultraviolet (355 nm) simulated (dashed with square) photodissociation product branching ratios for $IBr^-(CO_2)_n$. Experimental results (solid) from Sanford, et al [79]. Error bars are 1σ for $n = 6$.

IBr^- channel in the simulations.

5.2.1 Ultraviolet Photodissociation in Small Clusters

In the smaller clusters, $IBr^-(CO_2)_{1-7}$, the only product channels of significance are I^- and Br^-. While simulation and experiment differ, they differ by what appears to be an overall shift. If one were to shift the simulated results in Figure 5.1 to the left by two cluster sizes (i.e., simulated $IBr^-(CO_2)_5$ moves to $IBr^-(CO_2)_3$), the agreement—pattern-wise—is quite good. For example, there is a broad drop-off in Br^- from $n_{expt} = 0 \rightarrow 2$, with concomitant increase of I^- product. The simulations show this same pattern occurring at $n_{sim} = 2 \rightarrow 4$. Also, the "dip" in I^- product at $n_{sim} = 5$ echoes that seen at $n_{expt} = 3$. Of course, although the pattern match is fairly good, our simulations do disagree about the magnitude of the two channels. The simulations show Br^- being the major product up to $IBr^-(CO_2)_5$, whereas in experiment it becomes the minor product by $IBr^-(CO_2)_2$.

For further analysis into the process of I^- and Br^- product formation in the UV photodissociation, two trajectories for $IBr^-(CO_2)_6$ that exemplify both channels are presented in Figure 5.2. This figure shows that the dissociation process is quite rapid. Both the Br^- channel, Figure 5.2(a), and the I^- channel, Figure 5.2(b) reach 15 Å of I-Br separation in under one picosecond. The Br^- product occurs with spin-orbit (SO) excited iodine as its companion neutral along the highest excited state as one would predict from the bare ion curves, Figure 2.1, where the B state dissociates to $Br^- + I^*$. Likewise, the I^- product dissociates with SO excited bromine after a nonadiabatic transition to a lower state.

Also important to note in Figure 5.2 is the behavior of the charge at the beginning of the trajectory. The UV $B \leftarrow X$ excitation is a charge transfer $\Sigma \rightarrow \Sigma^*$ transition. So, in the ground-state well, before excitation, the cluster has the solvent mainly around the bromine end, as shown in Figure 2.12, and the charge on the solute is located mainly on the solvated bromine. Upon excitation to the B state, though, the charge switches such that the solvent is now around the more neutral atom. Since this arrangement is not that favorable, the solvent shifts to favor

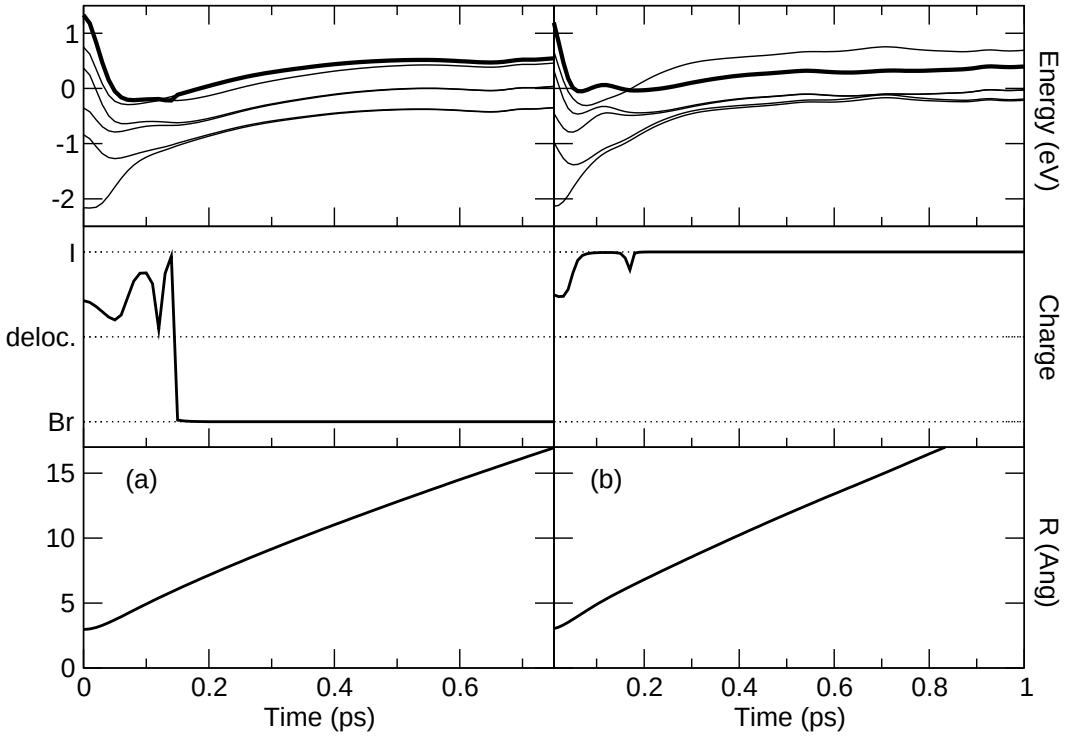

Figure 5.2: Ultraviolet (355-nm) photodissociation of two exemplar $IBr^-(CO_2)_6$ trajectories. The adiabatic energies are plotted in the first row as a function of time with the bold line being the occupied state. The second row plots the charge character of the trajectory over time. The third row plots the I-Br bond length over time. (a) shows a trajectory that dissociates to Br^-. (b) shows a trajectory that dissociates to I^-.

the iodine.

This early solvent shift can be better seen by use of a solvent flow plot first introduced in our analysis of the GSR dynamics of near-infrared (IR) photodissociation. Figure 5.3 shows the solvent flow plots for all $IBr^-(CO_2)_6$ UV photodissociation trajectories that end as Br^- product, Figure 5.3(a), and as I^- product, Figure 5.3(b). In each case there is a range of starting solvent configurations, i.e., a range of starting $\Delta\Phi$. Both sets begin at -$\Delta\Phi$ as the bromine is the solvated solute atom in the ground state. But, after excitation to the B state (brown) there is a rapid move to to a more symmetric configuration as the solvent shifts to solvate the iodide anion after which the two product channels diverge. For the Br^- product, the solute dissociates after reaching a symmetric configuration where the charge can transfer back to the bromine. The reason most of the trajectories end near zero $\Delta\Phi$ is because the dissociation is so rapid (Figure 5.2) that most of the Br^- product ends with at most one solvent molecule.

As for the I^- product, Figure 5.3(b), once again there are rapid solvent shifts at the start of the trajectory. However, instead of a charge transfer the symmetric configuration is reached, the solvent reorganization continues over to the iodine-solvated $+\Delta\Phi$ geometry. At the same time, a nonadiabatic hop occurs to a lower state that dissociates to I^-. Since the solvent was able to fully reorganize around the iodine, the trajectories dissociate with more solvent (and, thus, at larger absolute $\Delta\Phi$) than did the Br^-. Indeed, an analysis of the trajectories end on average with 2-3 solvent molecules.

5.2.2 Divergence of Simulation and Experiment with Large Clusters

Of course, the major difference between simulation and experiment as seen in Figure 5.2 is with the larger clusters, $IBr^-(CO_2)_{8-11}$. The simulations predict the appearance of ground-state recombined IBr^- product. At $IBr^-(CO_2)_9$, it becomes a significant product channel and by $IBr^-(CO_2)_{11}$ it is the major product of the simulated photodissociation. Experiment, on the other hand, barely shows any IBr^- product even in the largest clusters studied.

A possible explanation for this divergence begins with the observation that in the simula-

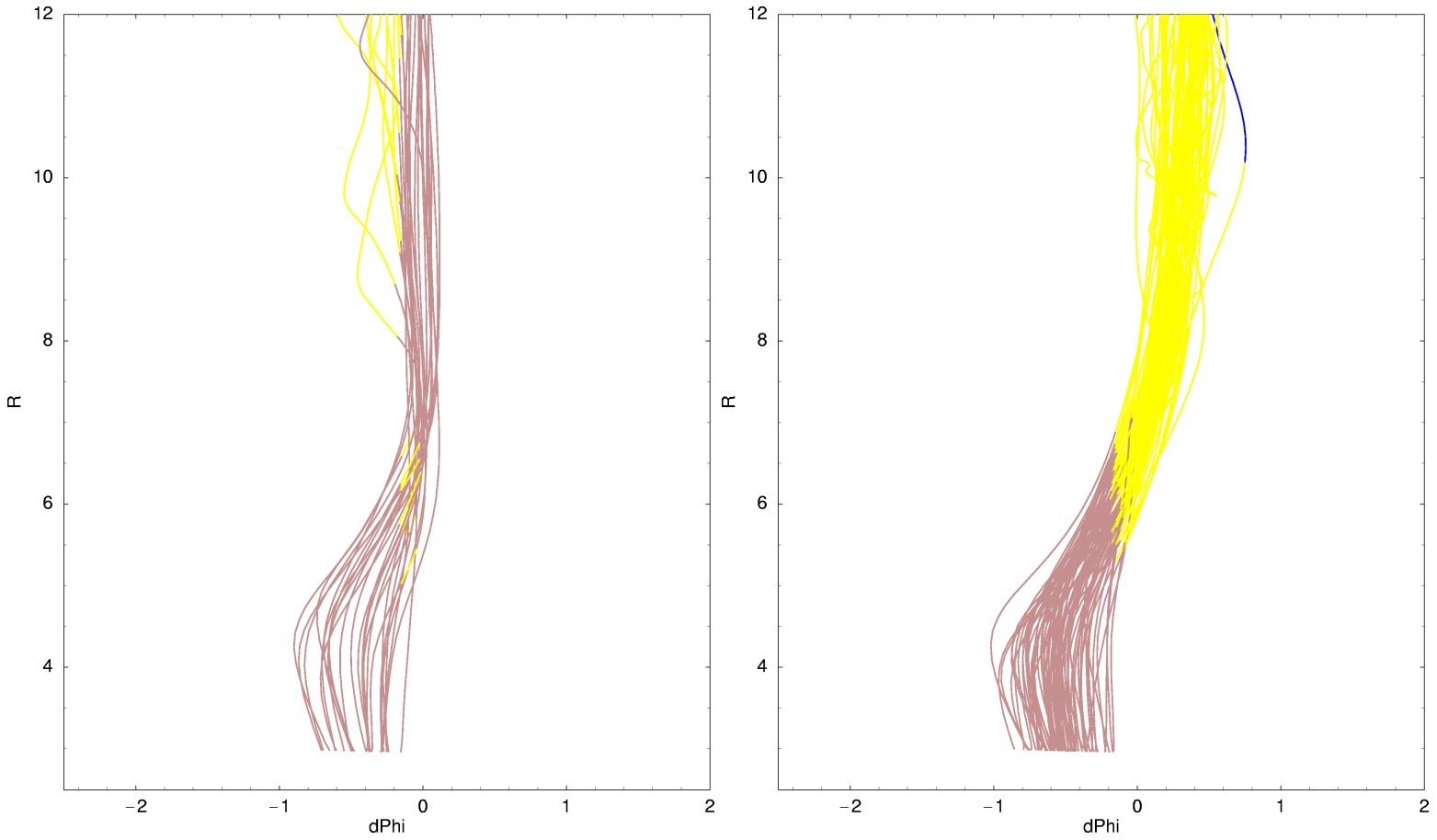

Figure 5.3: Plot of solvent coordinate versus solute bond length for ultraviolet (355-nm) trajectories for $IBr^-(CO_2)_6$ that end as (a) Br^- product and (b) I^- product. Brown, yellow, and blue represent trajectory dynamics on the fifth-, fourth-, and third-excited state, respectively. dPhi (=$\Delta\Phi$) is in eV and R is in Angstroms.

tions, SO quenching starts to become important in these clusters. In Figure 5.4, three exemplar trajectories are plotted for $IBr^-(CO_2)_{13}$. Although this is larger than any cluster yet studied experimentally, the size provides a clearer picture of the dynamics.

For the dissociation trajectories of the Br^- channel, Figure 5.4(a), and the I^- channel, Figure 5.4(b), unlike the $IBr^-(CO_2)_6$ trajectories in Figure 5.2, both the Br^- and I^- are produced not with the spin-orbit excited companion neutrals, but with their quenched analogues. Also, while the example I^- trajectory is nearly as fast as those shown for $IBr^-(CO_2)_6$, the Br^- trajectory is slower. This is attributed to exploration of the lower state much like that seen in the $IBr^-(CO_2)_8$ near-IR Br^- product solvent flow plot, Figure 4.9.

The final trajectory, Figure 5.4(c), shows a cluster that recombines as IBr^- in the ground state. This channel, which rarely is more than 10% of the total photoproduct in experiment, is a major product by $IBr^-(CO_2)_{11}$ in simulation. We also note that we see the first vibration of the ground-state recombined IBr^- solute at the latter times of Figure 5.4(c). We see the movement to the inner turning point and the associated rise in energy due to repulsion. At the same time we see the charge delocalize as the solute bond length decreases. The forces then cause the solute to separate, the charge localizes back on the bromine, and the pattern continues. Of course, like the other $IBr^-(CO_2)_{13}$ trajectories shown, this product channel also requires SO quenching to occur. Clearly, we must focus on this process and see whether it can help us explain the differences between experiment and simulation.

5.2.2.1 Spin-Orbit Quenching via Charge Transfer

In order to better understand the spin-orbit quenching (SOQ) process presented above, we refer back to the work of Delaney, Faeder, and Parson [40] on the simulation of UV photodissociation in $I_2^-(CO_2)_n$. In this study, they detailed a process of spin-orbit quenching via charge transfer (SOQ-CT) which helped explain the process of ground-state recombination in larger clusters. To facilitate our summary of this process, Figure 5.5 presents a visual summary of the dynamics of UV photodissociation in $I_2^-(CO_2)_n$. This figure is inspired by the classical Marcus

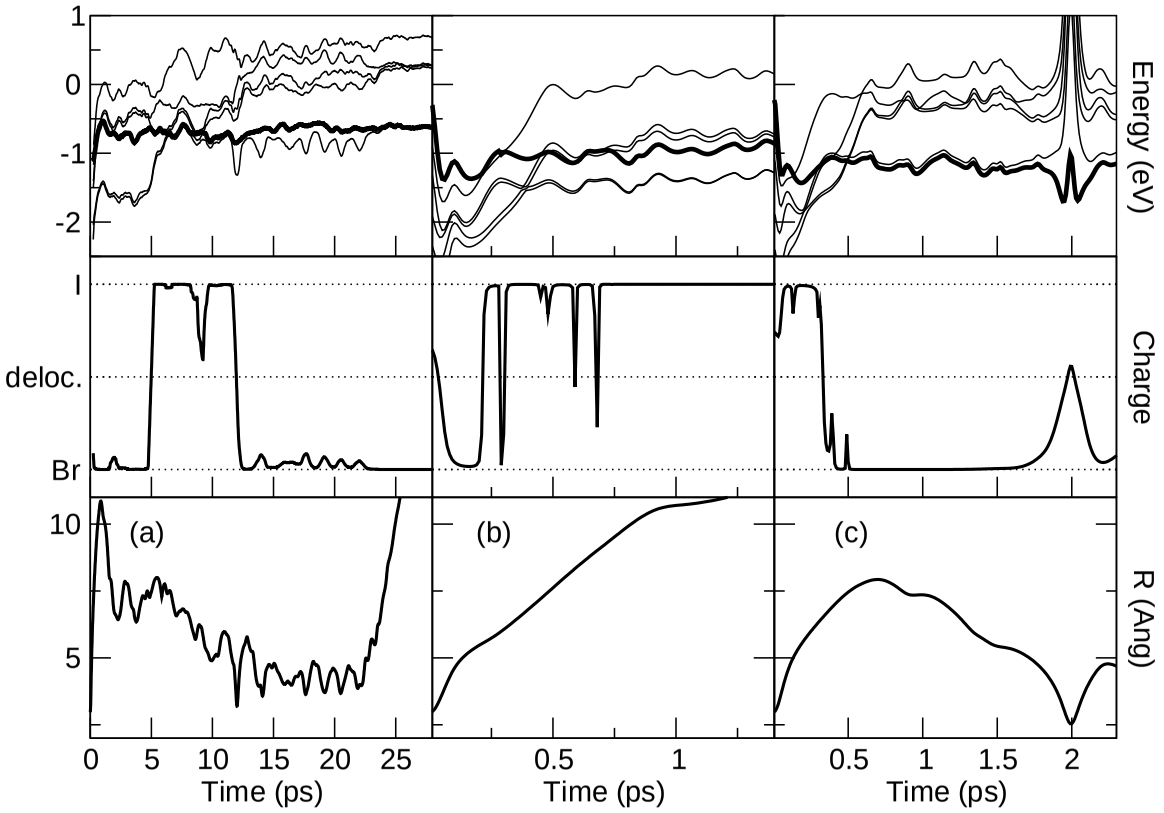

Figure 5.4: Ultraviolet (355-nm) photodissociation of three exemplar $IBr^-(CO_2)_{13}$ trajectories. The adiabatic energies are plotted in the first row as a function of time with the bold line being the current state. The second row plots the charge character of the trajectory over time. The third row plots the I-Br bond length over time. (a) shows a trajectory that dissociates to Br^-, with the energies plotted as a 50-point moving average to eliminate grassiness. (b) shows a trajectory that dissociates to I^-. (c) shows a trajectory that recombines in the ground state.

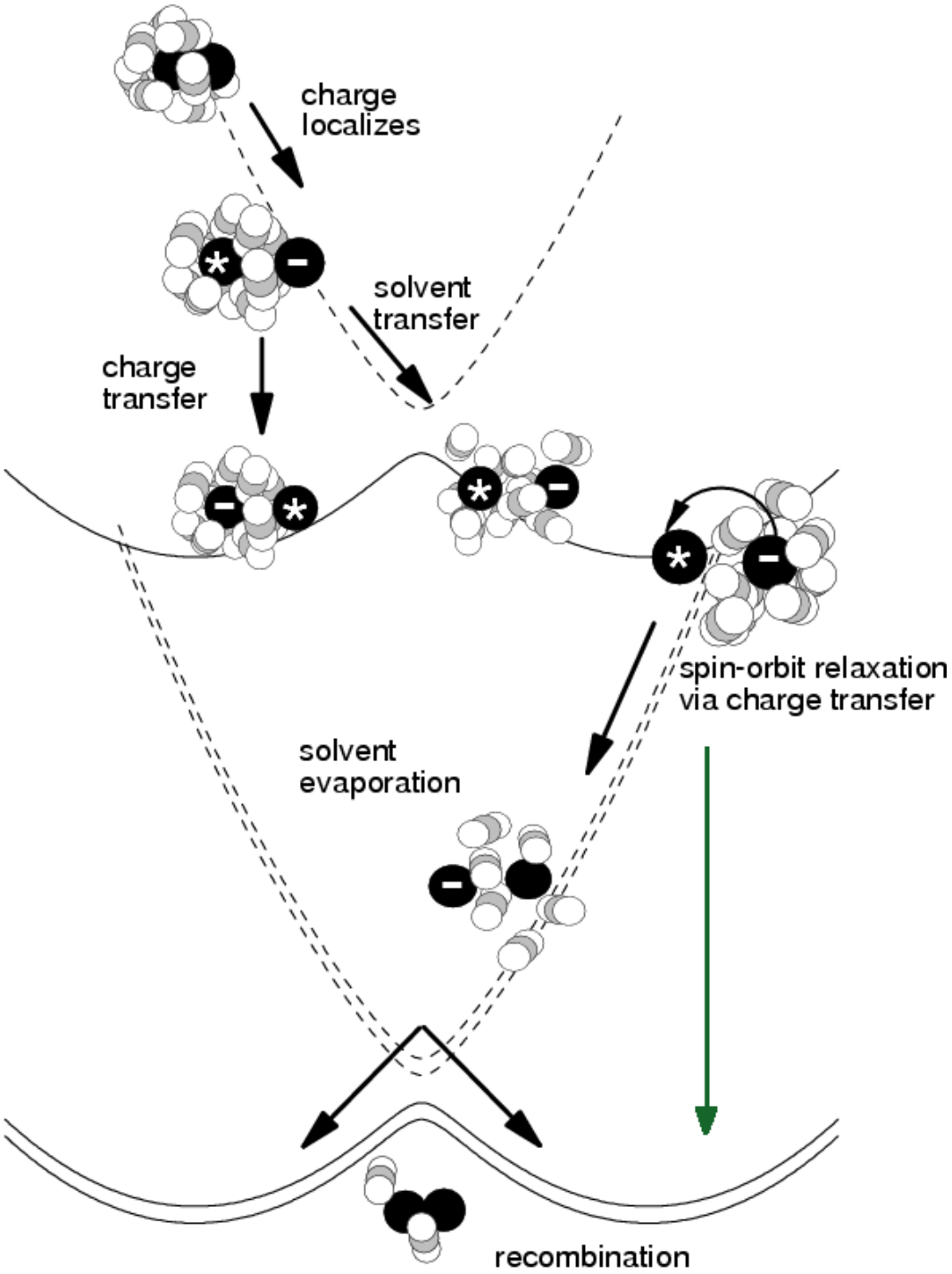

Figure 5.5: A summary of the dynamics of $I_2^-(CO_2)_n$ following ultraviolet photoexcitation with energy as the ordinate and solvent coordinate(=$\Delta\Phi$) as the abscissa. Dashed states exhibit "anomalous charge flow" where the charge and solvent move in opposition to each other. The asterisk denotes spin-orbit excited neutral. Green arrow represents path detailed in Section 5.2.2.2. Reproduced with permission from Delaney, Faeder, and Parson [40].

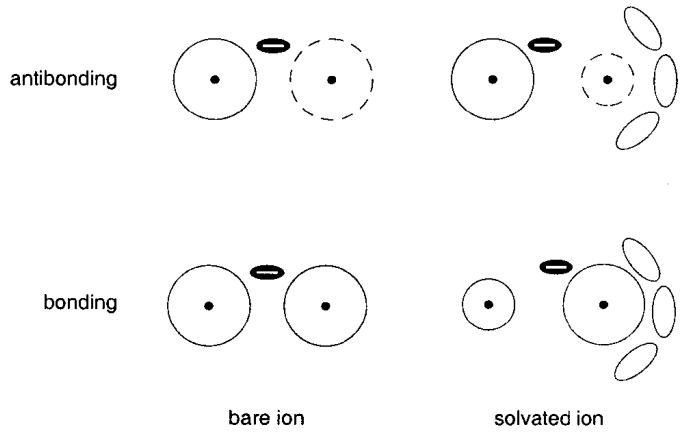

Figure 5.6: Illustration of anomalous charge flow in a diatomic anion. In the bare ion (left), the charge is equally shared between atoms in both the bonding and antibonding states. In the presence of solvent (right), the increased charge density due to solvation in the solvated atom in the bonding state leads to higher charge density for the unsolvated atom in the antibonding state to preserve orthogonality. Reproduced with permission from Parson, Faeder, and Delaney [29].

theory [42, 125, 126] where the familiar parabolas represent the adiabatic states of $I_2^-(CO_2)_n$ at large solute bond length where the I^- + I states (lower manifold) are essentially degenerate. As in this theory, the abscissa is the collective solvent coordinate, known as $\Delta\Phi$ in our work, and the ordinate is energy. Figure 5.5 also details another finding of the study by Delaney, et al, [40] that is crucial for our understanding of the spin-orbit quenching process. Namely, the dashed curves in Figure 5.5 represent states with "anomalous charge flow", a term introduced by Papanikolas and detailed in our group's work [23, 24, 27, 29, 35, 127] to indicate states where solvent and charge motion occurs in opposition to each other. While counterintuitive, a simple diatomic linear combination of atomic orbitals-molecular orbitals (LCAO-MO) picture, illustrated in Figure 5.6, shows how it arises. In the bare ion case, Figure 5.6(left), the bonding and antibonding states are orthogonal and the charge in each is shared equally between each atom. However, upon solvation, Figure 5.6(right), the charge prefers the solvated atom due to energetic reasons. Since the antibonding state must be orthogonal to the bonding state, the charge density in the antibonding state lies more on the **unsolvated** atom.

While both Figures 5.5 and 5.6 detail dynamics and charge flow in $I_2^-(CO_2)_n$, a homonu-

clear solute, the basic mechanics apply to $IBr^-(CO_2)_n$. The main difference is with Figure 5.5, where with $IBr^-(CO_2)_n$ the solvent coordinate symmetry is broken due to the difference in electron affinity and spin-orbit splittings of iodine and bromine. However, we believe that the figure is still of use in analyzing the dynamics of recombination in the UV photodissociation of $IBr^-(CO_2)_n$. To that end, Figure 5.7 presents an more detailed look at the dynamics of the recombining $IBr^-(CO_2)_{13}$ trajectory first shown in Figure 5.4(c). In this figure, we focus on the first 1000 fs of dynamics in this trajectory. In addition to the state energies, solute charge localization, and solute bond length, we also present the solvent coordinate, $\Delta\Phi$(=dPhi), as a function of time.

We begin our detailed look at this trajectory with the first 100 fs, where we see that after excitation to the B state, the charge localizes on iodine and the solvent begins to shift to a more symmetric—smaller $|\Delta\Phi|$—solvent configuration. Referring back to Figure 5.5, this is analogous to the first two "steps" illustrated at the top of the figure. Then, at approximately 125 fs, we transition to the a' state, marked in Figure 5.7 as the first dashed vertical line. At this point, the cluster undergoes solvent transfer to favor the iodide rather than the bromine, shown by the transition from negative to positive $\Delta\Phi$. This is analogous to following the right-hand path in Figure 5.5. Then, at $\approx$ 310 fs (second vertical line in Figure 5.7), the cluster reaches a large enough solvent coordinate so that the solvation environment compensates for the bromine spin-orbit splitting, the solute can then undergo spin-orbit quenching. At the same time, the charge character of the solute immediately switches from iodide to bromide as it moves to an antibonding, anomalous state. This is the SOQ-CT step seen in Figure 5.5. The potential energy is now converted into kinetic energy and solvent is boiled off as the cluster relaxes to the ground state. The transition to the ground state occurs in Figure 5.7 at $\approx$ 500 fs, all the while the cluster is moving to a more symmetric solvation geometry before finally stabilizing in a bromide-solvated configuration. This is as expected for ground-state recombined $IBr^-(CO_2)_n$ clusters.

We note for completion that, as mentioned above, both dissociation channels also proceed

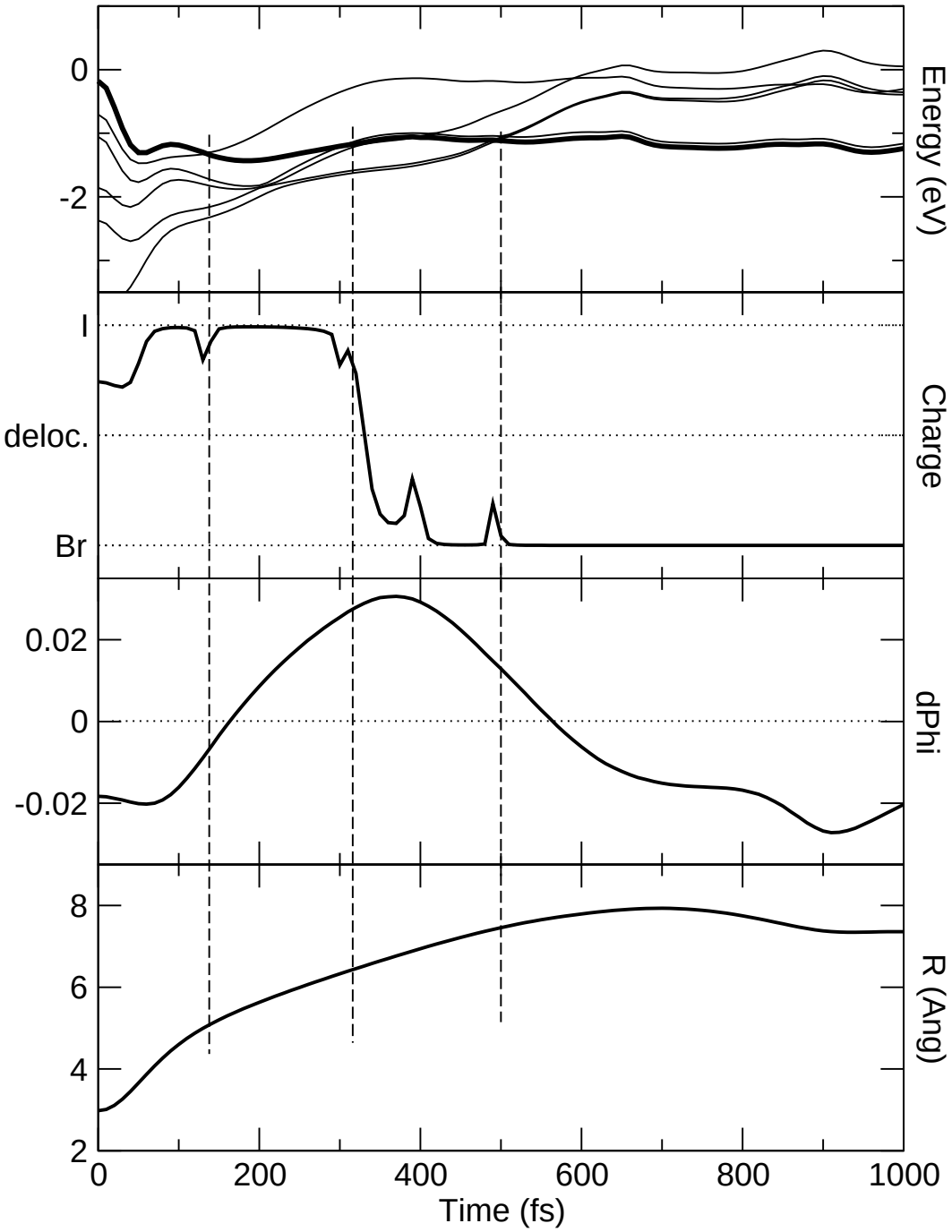

Figure 5.7: Details of the first 1000 fs of an $IBr^{-}(CO_2)_{13}$ trajectory that ends as ground-state recombined IBr^{-} product, seen previously in Figure 5.4(c). The plots detail as a function of time, from top to bottom, the adiabatic energies and the currently occupied state in bold, the charge localization on the solute, the solvent coordinate, $\Delta\Phi$(=dPhi), and the I-Br bond length. The three vertical dashed lines are used as guides for the eye for important point in the trajectory which are detailed in Section 5.2.2.1.

via spin-orbit quenching via charge transfer. In these cases, however, rather than removing the excess kinetic energy gained by the relaxation via solvent evaporation, the cluster instead "explodes" and leads to the dissociation channels. In the case of the Br^- channel, Figure 5.4(a), the energetics of the lower state are sufficient to allow transitory exploration before dissociation finally occurs. This occurs in much the same location as seen in the trapping dynamics of Chapter 4.

5.2.2.2 Spin-Orbit Quenching via Vibrational Deactivation

What we have detailed in the previous section is the recombination process seen in the simulations of UV photodissociation in both $I_2^-(CO_2)_n$ and $IBr^-(CO_2)_n$. However, as seen in Figure 5.1, in the larger clusters, the recombination channel is a very minor product when compared to the simulation. This implies that a different process must be occurring that could still lead to dissociating products, but would inhibit the recombination channel.

First, we hypothesize that ground-state recombination must occur via the SOQ-CT process. Partial support for this is in the similarity of the onset of GSR in both $I_2^-(CO_2)_n$ and $IBr^-(CO_2)_n$. In both the experiment [19] and simulation [40] of the UV photodissociation of $I_2^-(CO_2)_n$, the onset of GSR product was sharp and occurred at eight or nine solvent molecules in size. This sudden onset was due to the need for there to be enough solvent molecules to allow the solvent asymmetry to become large enough to overcome the spin-orbit splitting in the system (qv., Figure 5.5 and the intersection of the lower and upper states at large solvent coordinate). Similarly, in our simulations of UV photodissociation of $IBr^-(CO_2)_n$, we also see an abrupt opening of the IBr^- channel at larger cluster size,[1] followed by a sharp rise in the product channel, although it never reaches the dominance it has in $I_2^-(CO_2)_n$.

Moreover, we also hypothesize that the only SOQ process occurring, the only one of importance regarding our search for a possible mechanism for the difference between experiment and simulation, is quenching of bromine. We support this hypothesis with an example shown in

[1] While the onset is at eight solvent molecules much like $I_2^-(CO_2)_n$, we do not assume that this is a magic number for all systems.

Figure 5.8. In Figure 5.8 we present an "abbreviated" solvent flow plot of all the $IBr^-(CO_2)_{11}$ trajectories that completed as GSR product; similar plots can be shown for all GSR trajectories for the $IBr^-(CO_2)_n$ clusters that undergo it in silico. It is "abbreviated" in the sense that we only plot motion on the two highest excited states as well as indicating the transitions to the a state with the dots. We see that in every case, the SOQ transition seen is the $Br(^2P_{1/2}) \rightarrow Br(^2P_{3/2})$ relaxation. From our walkthrough of the trajectory in Figure 5.7, we know that once we move from the B state to the a' state (brown to yellow), we are in a normal charge flow state so the iodide ion is solvated and the spin-orbit excited neutral is the bromine.

Moreover, as additional evidence that perhaps the bromine SOQ-CT process is being frustrated in the experiment, we note that in Figure 5.1, the growth of the IBr^- channel seems due to the depletion of the I^- product. This is also supported by the observation that Br^- is relatively unchanged by the growth of IBr^-. So, if there was a process in the experiments that inhibits the bromine SOQ process for $IBr^-(CO_2)_n$ seen in the simulations that our model does not include, one would imagine the IBr^- would grow at the expense of the I^- product channel. The question for us now is, does there exist a SOQ process that our model would not be able to simulate that is efficient enough to compete with the charge-transfer process that the model does include?

We hypothesize that the answer involves the vibrations of CO_2. As noted in Chapter 2, our model treats the solvent as rigid as an approximation. Most of the time this approximation is valid as the present and other simulations have born out. We propose a spin-orbit quenching via vibrational deactivation (SOQ-VD) mechanism wherein the bromine is spin-orbit quenched via collisional deactivation by CO_2.

If one analyzes the vibrations of CO_2 [128], it is found that the symmetric stretch is found at $\nu_1 = (10^00) = 1388.19$ cm^{-1}, the asymmetric stretch is at $\nu_3 = (00^01) = 2349.16$ cm^{-1}, and their combination band, $\nu_1 + \nu_3 = (10^01)$, at 3714.78 cm^{-1}. From our table of IBr^- properties, Table 2.2.1.3, the experimental bromine spin-orbit splitting, $Br(^2P_{1/2}) \rightarrow Br(^2P_{3/2})$, is 0.4569 eV = 3685 cm^{-1}. This is nearly resonant, only 30 cm^{-1} different from the combination band

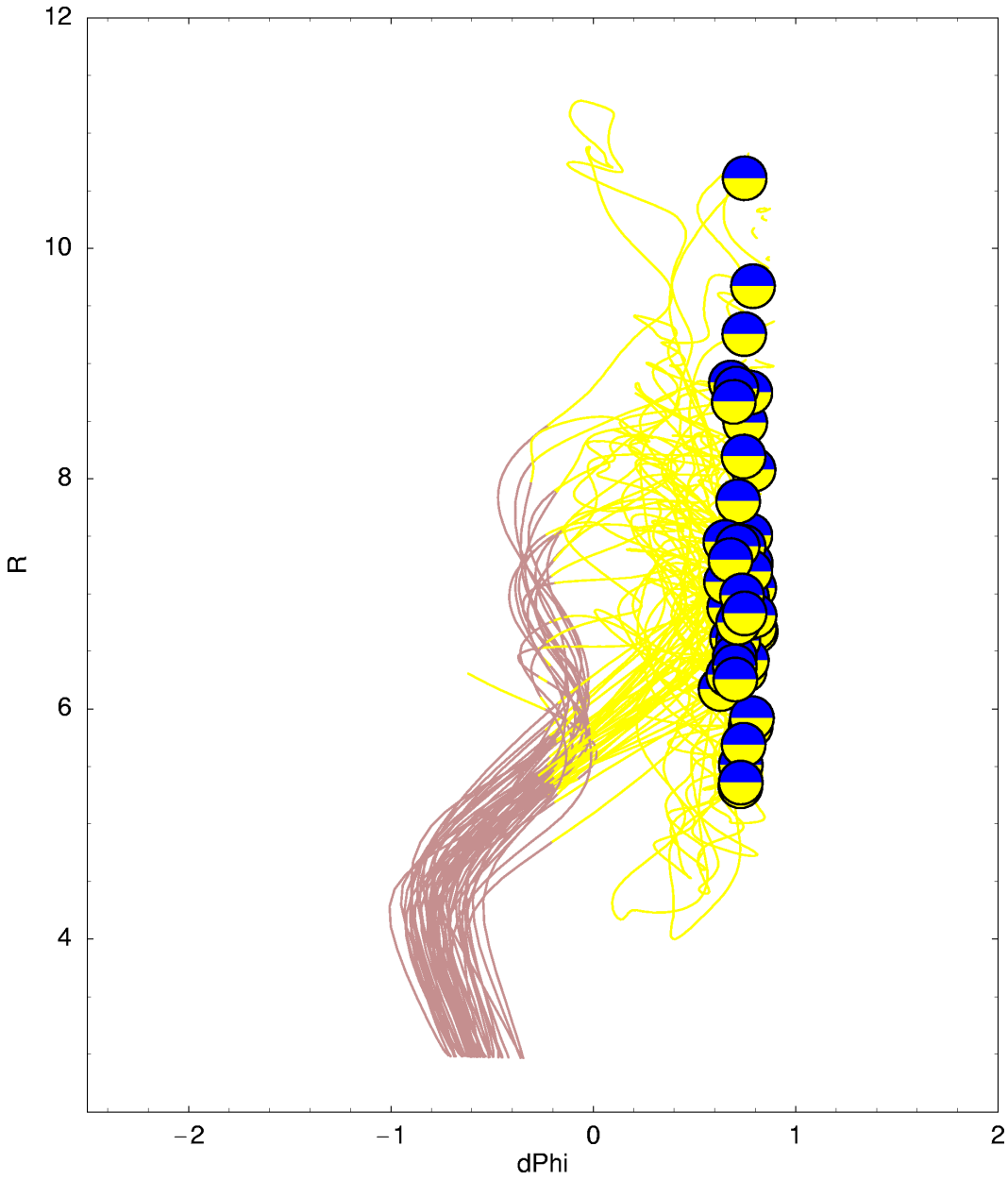

Figure 5.8: Plot of solvent coordinate versus solute bond length for all ultraviolet (355-nm) simulated $IBr^-(CO_2)_{11}$ trajectories that end as IBr^- on the ground state. Only the motion on two highest excited states are plotted for clarity. Yellow and brown represent trajectory dynamics on the fourth- and fifth-excited states, respectively, in analogy to Figure 2.1. The blue-and-yellow circles represent hops from the yellow to blue (next-lowest) states. dPhi (=$\Delta\Phi$) is in eV and R is in Angstroms.

excitation frequency.

Moreover, collisional $E-V$ quenching of SO excited halogens has been extensively studied for many decades [129]. One of the most important quenching processes studied has been the one considered here:

$$\mathrm{Br}(^2P_{1/2}) + \mathrm{CO_2}(00^00) \overset{E-V}{\rightarrow} \mathrm{Br}(^2P_{3/2}) + \mathrm{CO_2}(10^01). \tag{5.1}$$

It has been found that this $E-V$ transfer has a rapid rate coefficient, $k = 1.5 \cdot 10^{-11}$ cm^3/molecule/s [130], and produces $\mathrm{CO_2}(10^01)$ with a branching ratio of $\phi = 0.87 \pm 0.15$ [131–133]. Indeed, this $E-V$ transfer has been used as the pumping step for many $\mathrm{CO_2}$ lasers [134–137].

If we refer back to Figure 5.5, we can now include a possible new path that corresponds to the SOQ-VD process which we have noted with the green arrow. If we were to quench the bromine via the solvent vibrations **instead** of charge transfer, we could imagine taking the cluster located at the tail of the green arrow and just "removing the asterisk", i.e, SOQ of the bromine, but having no associated solvent reorganization. In that case, we would end up with a heavily solvated iodide anion and a loosely bound bromine that would undergo facile dissociation and would not be expected to recombine with any effectiveness.

Thus, we have shown that a SOQ-VD process for the quenching of SO excited bromine by $\mathrm{CO_2}$ does exist, and is efficient. We have seen in Figure 5.8 that the SOQ-CT process that would need to be inhibited in order to prevent ground-state recombination is that of $\mathrm{Br}(^2P_{1/2}) \rightarrow \mathrm{Br}(^2P_{3/2})$. Unfortunately, there is no good way at this time to simulate this via our model since we lack quantized vibrations of the solvent. However, even with our model's lack of ability to simulate this process, our hypothesis does have one benefit. We have put forth one possible reason why the $\mathrm{I_2^-(CO_2)}_n$ and $\mathrm{IBr^-(CO_2)}_n$ **experiments** are different due mainly to our simulations' lack of differences between the two systems!

5.3 Sensitivity of Ultraviolet Photoproduct Ratios to Lennard-Jones Parameters

In Section 2.2.2 it was shown that the standard $Br^- \cdots CO_2$ interaction Lennard-Jones (LJ) parameter fit, tabulated in Table 2.3, was slightly less attractive than the well depth for the $Br^- \cdots CO_2$ T-shaped geometry calculated at the coupled cluster with single, double, and iterative triple excitations (CCSD(T)) level of theory (Figure 2.7). In order to explore the effect of a tighter fit on the dynamics simulations, LJ parameters were determined that matched the energetics of the CCSD(T) fit as shown in Figure 2.15. Likewise, LJ parameters were determined that matched the $Br^- \cdots CO_2$ T-shaped energetics predicted by a internally-contracted multireference configuration interaction (icMRCI) calculation of the system as well. This multireference configuration interaction (MRCI) prediction is shown in Figure 2.7 and it is shallower than our standard LJ fit.

These two extra fits allow determination of the sensitivity of the product branching ratios for ultraviolet (UV) (355-nm) photodissociation simulations of $IBr^-(CO_2)_n$. In order to test the effect of the LJ fits, trajectories were assembled for $IBr^-(CO_2)_{1-14}$. Each ensemble was composed of 100 trajectories assembled in the same fashion as before. The trajectories ran with a classical time-step of 1.0 fs for durations of 100 ps for all cluster sizes. In each case, a trajectory is run until either the run-time duration is reached, until the bond length exceeds 40 a_0, or more than 20 crossings of the ground-state well occur after which that trajectory is considered recombined. The results for these simulations are shown in Figure 5.9. We note that, as shown in Figure 5.9, MRCI simulations were stopped after $IBr^-(CO_2)_8$ due to an obvious mismatch to both experiment and previous simulations.

Since there is such an obvious difference between the MRCI results and the standard results, their analysis is carried out first. The MRCI results, Figure 5.9 (red), show that from $IBr^-(CO_2)_0$ to $IBr^-(CO_2)_8$, the vast majority of product is Br^-. Indeed, of the 900 trajectories represented in Figure 5.9 for MRCI, only one $IBr^-(CO_2)_8$ trajectory ended as I^- products.

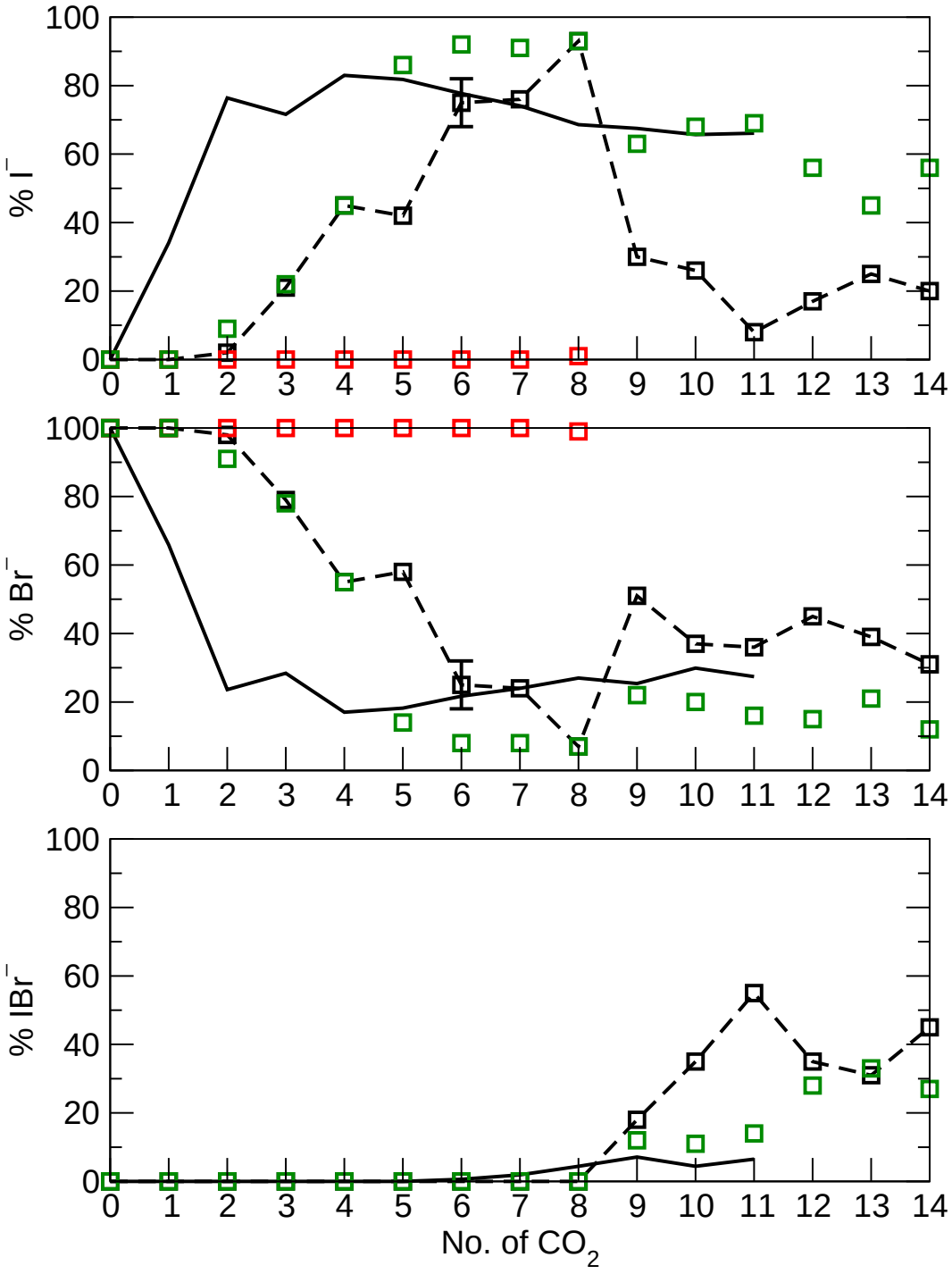

Figure 5.9: Branching ratios for UV (355-nm) photodissociation including results for tight Lennard-Jones fits to MRCI (red) and CCSD(T) (green) $Br^- \cdots CO_2$ data as seen in Figure 2.7, as well as the normal Lennard-Jones fit from Table 2.3 (dash with squares) and experimental data (line) from Sanford, et al [79].

The reason for this overwhelming preference for the Br^- product is that the MRCI $Br^- \cdots CO_2$ interaction is actually weaker than the $I^- \cdots CO_2$ interaction when those LJ parameters are used. Since the $B \leftarrow X$ transition is a charge transfer process, upon excitation the charge switches from bromine to iodine, and the solvent rapidly reorganizes to solvate the iodine while the solute continues to rapidly dissociate. Indeed, the solute dissociates faster than in the standard LJ fit trajectories because there is a smaller $Br \cdots CO_2$ interaction. Thus, the solvent isn't "holding on" to the bromine as tightly as it does in our standard LJ fit. Finally, this weaker $Br \cdots CO_2$ interaction leads to final Br^- products that are largely without solvent. Even in the $IBr^-(CO_2)_8$ clusters, the MRCI LJ Br^- product is produced as 80% $Br^-(CO_2)_0$!

Whereas the MRCI LJ fit produces a rather simple distribution, the CCSD(T) fit has a much more interesting effect on the UV photodissociation dynamics. Figure 5.9 (green) shows that the more attractive CCSD(T) $Br^- \cdots CO_2$ interaction leads to a better fit with experiment. Indeed, by $IBr^-(CO_2)_5$, the Br^- channel is too low due to extra I^- product production. In analogy to the MRCI results, the stronger bromine-solvent interaction delays the dissociation of the solute enough to allow more product to undergo nonadiabatic transition to the lower state leading to more I^- product. Unfortunately, though, the shifted pattern match that was observed with the standard LJ parameters has been lost, especially at $IBr^-(CO_2)_5$.

The larger clusters see the reappearance of spin-orbit quenching. And, as with the standard LJ trajectories, Figure 5.4, the larger cluster I^- and Br^- product is produced with spin-orbit (SO) quenched neutral. Moreover, the appearance of SO quenching again opens the ground-state recombination (GSR) IBr^- product channel at $IBr^-(CO_2)_9$. While the CCSD(T) IBr^- channel never reaches the heights that the standard fit did at $IBr^-(CO_2)_{11}$ (in fact, it's fairly close to the experiment), it is still a major product, often more prevalent than Br^-.

Thus, as with the near-infrared photodissociation dynamics, Figure 3.9, the CCSD(T) LJ fit provides a closer match to experiment. In the case of UV photodissociation, though, there is not the opportunity to test the CCSD(T) LJ fit against time-resolved absorption recovery data, due to the absence of ground-state recombination IBr^- product in experiment. The lack

of experimental product ratio data at larger cluster sizes also prevents one from determining whether IBr^- product becomes as important as the simulations say it does. Access to this data could help shed light on whether the $E-V$ hypothesis in Section 5.2.2 is plausible or whether it is the LJ parameters that cause the overestimation of IBr^- product in the standard simulations.

5.4 Conclusions

Simulations of the ultraviolet (UV) (355 nm) photodissociation of $IBr^-(CO_2)_n$ were performed and compared to experiment. We found that the large kinetic energy release associated with the $B \leftarrow X$ transition led to worse agreement when compared to our simulations' performance in the near-infrared (IR) case. We saw that at small cluster sizes our simulations roughly agree with experiment and tend to replicate the pattern of the photoproduct branching ratios. This pattern, however, was "shifted" to higher mass clusters in the simulations leading to a delayed onset of the Br^- product channel. The two product channels proceeded with rapid dissociation on the order of a few picoseconds. We also saw that since the $B \leftarrow X$ excitation is a charge-transfer $\Sigma \rightarrow \Sigma^*$ transition, rapid solvent motion occurs quickly upon excitation. This is because at the moment of promotion to the B state, the solvent shifts from the neutral bromine atom in order to solvate the now anionic iodide.

The major difference between experiment and simulation occurred at larger clusters. This difference was attributed to the existence of an alternate spin-orbit quenching process in the experiment not seen in simulation. We showed that the spin-orbit quenching process needed for ground-state recombination in the simulation was that of spin-orbit quenching via charge transfer. This process allows the formation of ground-state recombined IBr^- as a significant product channel in the simulation—something not seen in experiment up to a cluster size of eleven solvent molecules. We then attempted to explain this dichotomy by proposing a process which could compete with spin-orbit quenching via charge transfer (SOQ-CT) in the experimental system that our model does not include. Through use of the solvent flow plots, we proposed that the major spin-orbit quenching process occurring in the experimental system was

spin-orbit quenching via vibrational deactivation of the $Br(^2P_{1/2}) \rightarrow Br(^2P_{3/2})$ transition by CO_2. The CO_2 $\nu_1 + \nu_3$ combination band has near-resonance with the spin-orbit splitting of bromine, only 30 cm^{-1} different, and, according to the literature, the collisional deactivation of spin-orbit excited bromine by CO_2 is fast and efficient. The absence of CO_2 vibrations in the simulation model would lead to the simulations neglecting this possible pathway. While we have no experimental evidence that this is the process causing the divergence of experiment and simulation in the larger clusters, it is an avenue worth exploring.

Finally, tests were performed on the sensitivity of the UV photodissociation to the Lennard-Jones (LJ) parameter set used in our model. We found that using LJ parameters that led to a weaker $Br^- \cdots CO_2$ interaction essentially closed the I^- channel. We propose that due to the weak $Br \cdots CO_2$ interaction the cluster dissociated so fast that there was no time for the $B \rightarrow a'$ transition necessary to form I^- product. Use of the stronger $Br^- \cdots CO_2$ interaction from the coupled cluster with single, double, and iterative triple excitations (CCSD(T)) LJ parameters led to a better fit with experiment with I^- product dominating in most clusters. This was attributed to increased time for the cluster to achieve the nonadiabatic transition necessary for I^- product formation. Moreover, the CCSD(T) LJ parameters also led to a decrease in the ground-state recombination (GSR) IBr^- product, although it is still a significant channel at larger cluster sizes. Lack of GSR IBr^- product in the experiment precludes us from using time-resolved experimental data as a second check on both the efficacy of the LJ parameters, as done with the near-IR simulations. Moreover, the experimental difficulties with generation of large clusters also precludes us from knowing whether GSR product occurs at the highest cluster masses. In the next chapter, we will discuss whether new time-resolved photoelectron imaging experiments on $IBr^-(CO_2)_n$ will allow us another tool to assess the validity of our solvent-mediated spin-orbit quenching hypothesis.

Chapter 6

Future Directions

We believe that not all has been said about $IBr^-(CO_2)_n$ either theoretically or experimentally. The unique features of this system could allow for collaborative work in areas not usually explored. We first focus on new work being undertaken currently by the Lineberger group. This work involves photoelectron imaging of IBr^- and $IBr^-(CO_2)_n$. We speculate on whether we could use the model for CO_2 solvation of IBr^- developed in Chapter 2 to simulate the photoelectron spectra for $IBr^-(CO_2)_n$. Second, we speculate on the effect of including solvent vibrations in our model. As including these vibrations could affect the solute-solvent interactions already shown to be of primary importance in this and previous work, it is something that must be considered. Then, we will have a much more ambitious speculation: that the trapped metastable species seen in our study of ground-state recombination (GSR) dynamics of $IBr^-(CO_2)_n$ might be used as a new "ground-state cluster" to explore. Finally, we propose revisiting the less well-understood dynamics of $ICl^-(CO_2)_n$ clusters in the wake of the insights developed in this thesis.

6.1 Photoelectron Imaging of IBr^-

An area of study in the Lineberger [1,2,111,123,138–145], Sanov [113,146–155], and Neumark [56–60,66,68,71–74,156,157] groups is the use of time-resolved photoelectron spectroscopy and imaging to explore the dynamics of solvated ions. In recent work, Sanov and coworkers [113] have shown that time-resolved photoelectron imaging can be used to map out excited states in

bare IBr^-, Figure 2.3. If the Lineberger group were able to extend this technique to solvated $IBr^-(CO_2)_n$, the research could dovetail quite nicely with our own.

The proposed experiments will involve a near-infrared (IR) pump pulse and a UV probe pulse to detach the electron. As the first pulse is the same near-IR excitation studied in the present work, Figure 3.1 can give us an idea of what might be seen. As solvent molecules are added to IBr^-, the photoelectron spectra would be able to follow the rise and fall of the various product channels seen in Figure 3.5. The photoelectron experiments promise to provide insights to the energetics of the cluster that complement those achieved by the absorption recovery experiments. In analogy to Sanov [113], following the peaks of the spectra as a function of time would provide experimental data about the evolution of the various electronic states as the cluster is solvated.

Also of interest would be study of the excited-state trapping of $IBr^-(CO_2)_n$. We are intrigued by the possibility that time-resolved photoelectron spectra might provide information about long-lived excited states seen in the simulations, and the mechanism of its decay. We imagine that there might be two peaks assigned to the IBr^- channel, one for the A' trapped IBr^- and the other for the recombining IBr^- peak. The evolution of the magnitude of the signal of these two peaks over time could provide another measure of the recovery time for recombination. We base this possibility on previous work done by Neumark [57] who used femtosecond photoelectron spectroscopy to follow the dynamics of $I_2^-(Ar)_n$ clusters as previously studied by the Lineberger group [15, 16, 45]. By following the evolution of the photoelectron spectra for $I_2^-(Ar)_{20}$ over several picoseconds, they were able to resolve a signal growing in on the tens-of-picoseconds scale attributed to transitions of recombined I_2^- product, a finding later supported by our group [25]. If extraction of the energetics of the excited-state well were possible, it would be interesting to see how the experimental results compare to solvated potential energy surfaces (PESs) such as Figure 4.4. In any event, any energetic information about the well or the transition state would provide further insight for analysis of both experiment and simulation.

Speculations about the possible results of future experiments, of course, isn't really the

domain of this thesis. Rather, the question for this chapter is whether our group would be able to help to model the photoelectron imaging experiment. In previous work by this group, Faeder and Parson were able to model the time-resolved photoelectron spectra for I_2^- in argon clusters [25]. They modeled the time-dependent photoelectron signal at energy E with pump-probe delay Δ using a quasi-classical golden rule expression,

$$\sigma(E,\Delta) \propto \Big\langle \int_{-\infty}^{\infty} dt \exp[-\gamma_{\rm pp}(t-\Delta)^2] \times \sum_f |\mu_{if}(\mathbf{R}(t))|^2 \exp\{-\gamma_{\rm d}(E)[h\nu - E - (V_{\rm IX}^f(\mathbf{R}(t)) - V_{\rm IX^-}^i(\mathbf{R}(t)))]^2\} \Big\rangle \tag{6.1}$$

where the angle brackets denote an average over all trajectories, $\mathbf{R}(t)$ is the nuclear configuration at time t, μ_{if} is the transition dipole for detachment of an electron from state i of IBr^- to state f of IX (I_2^- in Ref. 25), $V_{\rm IX^-}^i$ and $V_{\rm IX}^f$ are the energies of the initial and final states, and $h\nu$ is the probe laser energy. The parameters $\gamma_{\rm d}(E)$ and $\gamma_{\rm pp}$ come from the electron detector width and a convolution of the pump and probe laser widths.

In order to transfer this model to $IBr^-(CO_2)_n$, we would need several new pieces of information. First, we would need both the IBr^- and IBr potential energy surfaces. The first have been provided in this work in Figure 2.1. The IBr potential curves, however, are more complicated. Several low-lying bound states are known to spectroscopic accuracy ($X\ ^1\Sigma^+$, [158,159]; $A\ ^3\Pi_1$, [158,159]; $A'\ ^3\Pi_2$, [160]; $B\ ^3\Pi_{0^+}$, [158,161], $B'\ ^3\Sigma_{0^+}^-$, [158,161]) and it is probable that some of these would be the most significant neutral curves needed for inclusion, along with the repulsive $Y\ 0^+$ and $C\ ^1\Pi_1$ states [114]. However, these states are only a fraction of the total; the I(^{2}P) and Br(^{2}P) interaction results in 23 spin-orbit coupled states [162, 163]. Patchkovskii has recently calculated [164] all 23 states for IBr at the multireference quasi-degenerate second-order perturbation (MRQDPT2) level of theory, including all scalar and spin-orbit relativistic effects. These curves are presented along with those for IBr^- in Figure 6.1 where the bold curve in the anion is the A' state, and the bold curves in the neutral correspond to states accessible from A' by the one-electron rule. We would also need to include the $I\cdots CO_2$ and $Br\cdots CO_2$ interactions which we have already determined and are tabulated in Table 2.3. As

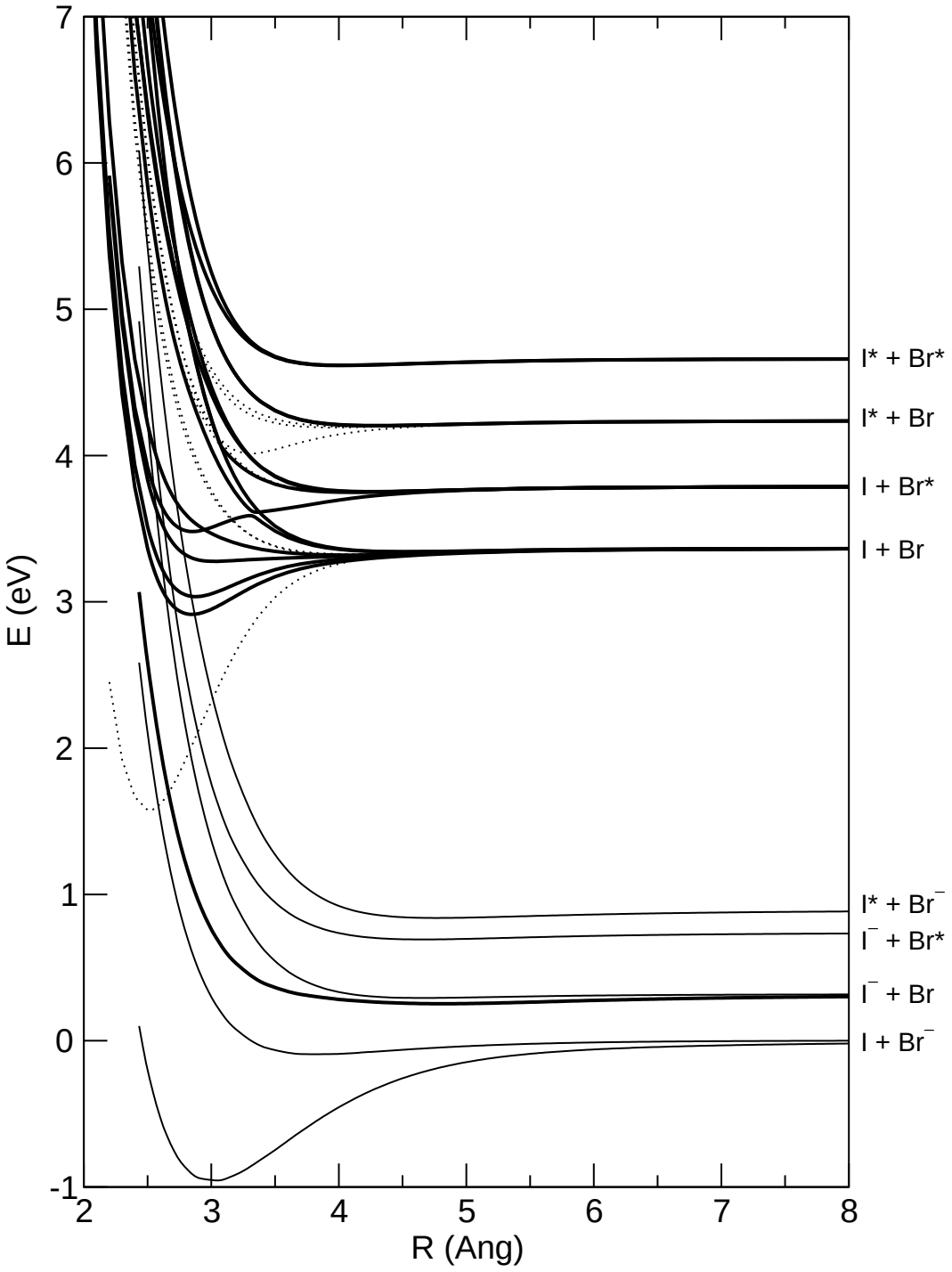

Figure 6.1: Potential energy curves for the six lowest spin-orbit states of IBr^- and the 23 states of IBr calculated by Patchkovskii [164]. The bold curve for IBr^- corresponds to the A' state. The bold and dotted curves in IBr correspond to states accessible and forbidden, respectively, by the one-electron rule from the A' state in IBr^-.

for the other parameters in Equation 6.1, μ_{if}, $\gamma_{\mathrm{d}}(E)$, and γ_{pp}, we would follow the prescriptions from the previous work.

Using this approach, Faeder and Parson were able to successfully model the time-dependent photoelectron spectra [57] of the dissociation of $I_2^-Ar_6$ and the dissociation and recombination of $I_2^-Ar_{20}$. This represents both of the domains we would hope to explore in the study of $IBr^-(CO_2)_n$. However, given the difficulties we have had in modeling CO_2 loss (and, thus, vibrational relaxation) as seen in Section 3.3, we would expect the modeling of this phenomenon via simulated photoelectron spectra would be less successful than that seen for I_2^- in argon. We would also hope that, if the spectroscopic challenges could be overcome, experiments could be undertaken to study the larger clusters, especially $IBr^-(CO_2)_{14}$. The photoelectron study would provide more evidence for the existence or lack thereof of the excited-state trapping for this cluster.

In addition to photoelectron spectroscopy following near-IR excitations, we might consider a study of the ultraviolet (UV) dynamics of $IBr^-(CO_2)_n$ with this method. Such experiments could help shed light on the questions raised in Chapter 5. Specifically, the photoelectron study might be able to resolve the question of spin-orbit (SO) quenching in the larger clusters. As discussed in Section 5.2.2, our simulations show evidence for a solvent-induced spin-orbit quenching via charge transfer (SOQ-CT) process which leads to a significant portion of UV photoproduct ending as ground-state recombination (GSR) IBr^- product. This contrasts with experiment where IBr^- is a very minor channel, see Figure 5.1. Our hope is that the energetics seen in the photoelectron studies would be able to help us elucidate whether a hypothesized spin-orbit quenching via vibrational deactivation (SOQ-VD) process due to collisional deactivation by CO_2 were possible and occurring.

6.2 Incorporation of Intramolecular CO_2 Vibrations

If, as we speculate in Chapter 5, the near-resonance between the bromine spin-orbit (SO) splitting and the vibrations of CO_2 allows for efficient deactivation of the spin-orbit excited

bromine, an obvious future direction of study is the inclusion of the intramolecular CO_2 vibrations in our model. This is easier said than done, however, because these vibrations would have to be treated quantum mechanically. The mechanism proposed in Section 5.2.2 involves a combination of both the symmetric and asymmetric stretches of CO_2, we would then also require a model for the electronic-vibrational energy transfer.

In addition to investigation of possible $E-V$ quenching of bromine, the inclusion of CO_2 vibrations would allow for further investigation of the effect of the bending vibration in CO_2 on dynamics. In our model, we keep the solvent rigid as a first approximation. But, while CO_2 has no permanent dipole in its equilibrium geometry, upon distortion it can develop one. Since even rigid solvent motion has shown a great effect on $IBr^-(CO_2)_n$ dynamics, the possibility of a dipole moment on the solvent could affect the dynamics even more. Ladanyi and Parson [28] previously investigated the effects of a flexible CO_2 model on the dynamics of $I_2^-(CO_2)_n$ and found that, in this system, the normal low-frequency bends of CO_2 did not significantly affect the dynamics. Rather one had to increase the bending force constant by 5 times in order to any large effects.

That said, we can partially speculate on how the inclusion of CO_2 bends would affect the $IBr^-(CO_2)_n$ dynamics. Ladanyi and Parson showed that the effect of the inclusion of a bend was to strengthen the intermolecular interactions. Since the $Br^- \cdots CO_2$ geometry is known in experiment to distort the CO_2 to a larger degree than for $I^- \cdots CO_2$ [53], we would expect that the bend would have a larger effect in $IBr^-(CO_2)_n$. In this work we have already investigated the effect of a larger $Br^- \cdots CO_2$ interaction on the dynamics of $IBr^-(CO_2)_n$. In Sections 3.5 and 4.7, we saw that the inclusion of a stronger $Br^- \cdots CO_2$ interaction was minor at best and often detrimental, especially in regards to the ground-state recombination (GSR) dynamics. Thus, we might expect that the investigation of the effect of the CO_2 bend would not be useful. The problem is that the inclusion of the bends would not just strengthen the $Br^- \cdots CO_2$ interaction, but also the $I^- \cdots CO_2$. As it is the differences between these interactions that have led to much of the interesting dynamics seen in this work, it might still be useful to

integrate the Ladanyi-Parson model for CO_2 bending into our model.

6.3 Excitation of Trapped Metastable Clusters

In this section, we speculate about the use of the trapped species we have seen as a starting point for new studies. While the photoelectron investigations discussed in Section 6.1 are probably the best way to extend the study of the trapping in $IBr^-(CO_2)_n$, there are other possibilities.

Focusing on $IBr^-(CO_2)_8$, we saw that the long-time ground-state recombination was due to trapping in an excited-state well on the A' state, see Figures 4.4 and 4.6, located at a $-\Delta\Phi$ solvent configuration. To explore the properties of this metastable state, a simulated spectrum for a set of trapped configurations of $IBr^-(CO_2)_8$ was calculated (Figure 6.2(a)) and an associated potential energy surface (PES) for a trapped configuration is shown in Figure 6.2(b). We note that the PES shown in Figure 6.2(b) is generated from a single $IBr^-(CO_2)_8$ cluster configuration in the excited-state well, but is compared to the simulated spectrum in Figure 6.2(a) which was generated as an average of all configurations in a trajectory which spent 50 ps in the excited state well. Thus the interpretation of the average spectrum in terms of the PES should not be taken too literally; it is shown rather as an indicator of the range of state energies explored by a cluster in the well.

With these caveats kept in mind, Figure 6.2(a) does suggest that the metastable state might be used as a novel "initial condition" for photodissociation studies. Such studies could allow probing of the B state at a lower kinetic energy release (KER) than is generated with $B \leftarrow X$ ultraviolet (UV) excitation. A lower KER could allow us to investigate B state dynamics where the dissociation is not so severe. Experimentally, this might make spin-orbit (SO) quenching more likely as the solute atoms would remain close together for a longer time. Similar spectra are expected for the other species, $IBr^-(CO_2)_{9-10}$, that also have long lifetimes due to this well.

It should be emphasized that it is hard to assign the peaks in this spectrum to the

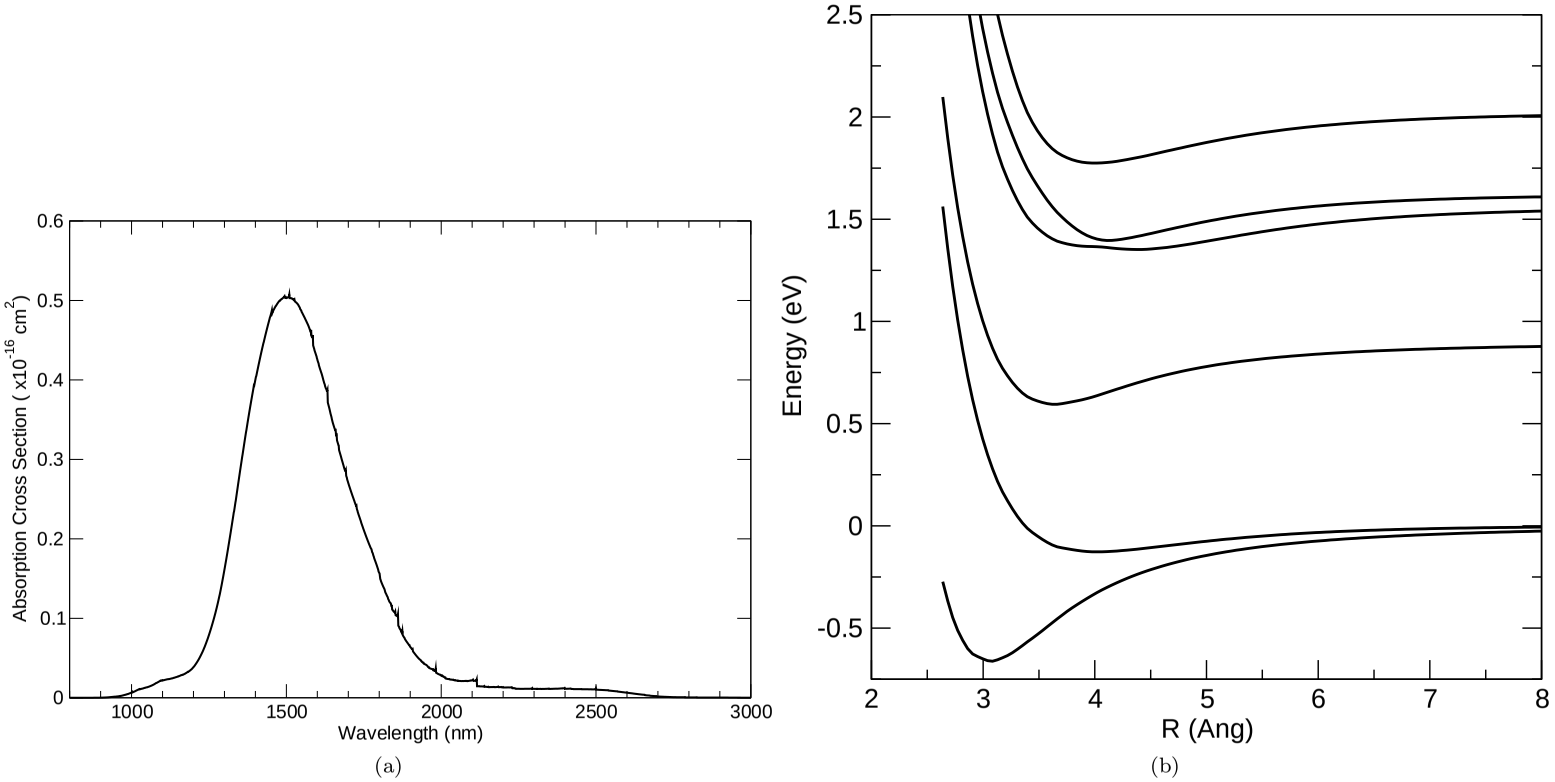

Figure 6.2: (a) Simulated absorption spectrum for $IBr^-(CO_2)_8$ trajectories trapped in the A' state well. (b) Potential energy surface for an $IBr^-(CO_2)_8$ configuration that is trapped in the A' well.

corresponding states in the familiar bare ion curves, Figure 2.1. Since the B state dissociates to Br^- one would expect that as the bromine end of the solute is solvated, the B state would be lowered in energy relative to states that would prefer iodine solvation. Thus, it is possible that the larger peak in fact corresponds to $B \leftarrow A'$ excitation. But, on the basis of the energetics shown in Figure 6.2(b), this peak would correspond to either the a' state, as this is an $\Omega = 1/2$ state like the A', or the a state, but both states are so close together neither is easily separated.

Our simulations also predicted an excited-state well for $IBr^-(CO_2)_{14}$. In analogy to $IBr^-(CO_2)_8$, we can construct a spectrum, Figure 6.3(a), and a PES, Figure 6.3(b), for a configuration in the well. We see that the larger peak has now red-shifted from the analogous peak in the $IBr^-(CO_2)_8$ well spectrum, Figure 6.2(a), reflecting the shifts in the states seen in the $IBr^-(CO_2)_{14}$ PES, Figure 6.3(b).

Of course, it is much easier to run trajectories of $a \leftarrow A'$ or similar excitations than to perform the associated experiment. This author freely admits that the experimental setup to probe such an excitation (i.e., 1500-nm lasers, infrared optics, etc.) may be too difficult to pursue. Plus, the predicted absorption cross sections in Figure 6.2(a) are on the order of that of the $A' \leftarrow X$ peak in the bare ion spectrum, Figure 2.9. Thus, the same experimental difficulties seen in the larger $IBr^-(CO_2)_n$ clusters could come into play. Moreover, beyond the practical difficulties of such an experiment is the fact that only a narrow range of cluster sizes, $IBr^-(CO_2)_{8-10}$, could be probed in this way.

6.4 Revisiting $ICl^-(CO_2)_n$ Dynamics

In our group's previous simulations of $ICl^-(CO_2)_n$, it was noted that for medium-sized clusters, $ICl^-(CO_2)_{4-6}$, ICl^- was formed in the A' well and often remained there until the simulation completed at 50 ps. In experiment [46, 76, 77], the major product channel for these sizes was ICl^- as well, but the small number of solvent molecules attached to the ICl^- implies that the ion has relaxed to the ground state by the time it reaches the mass detector. One hypothesis for this apparent discrepancy between experiment and simulations is that there is

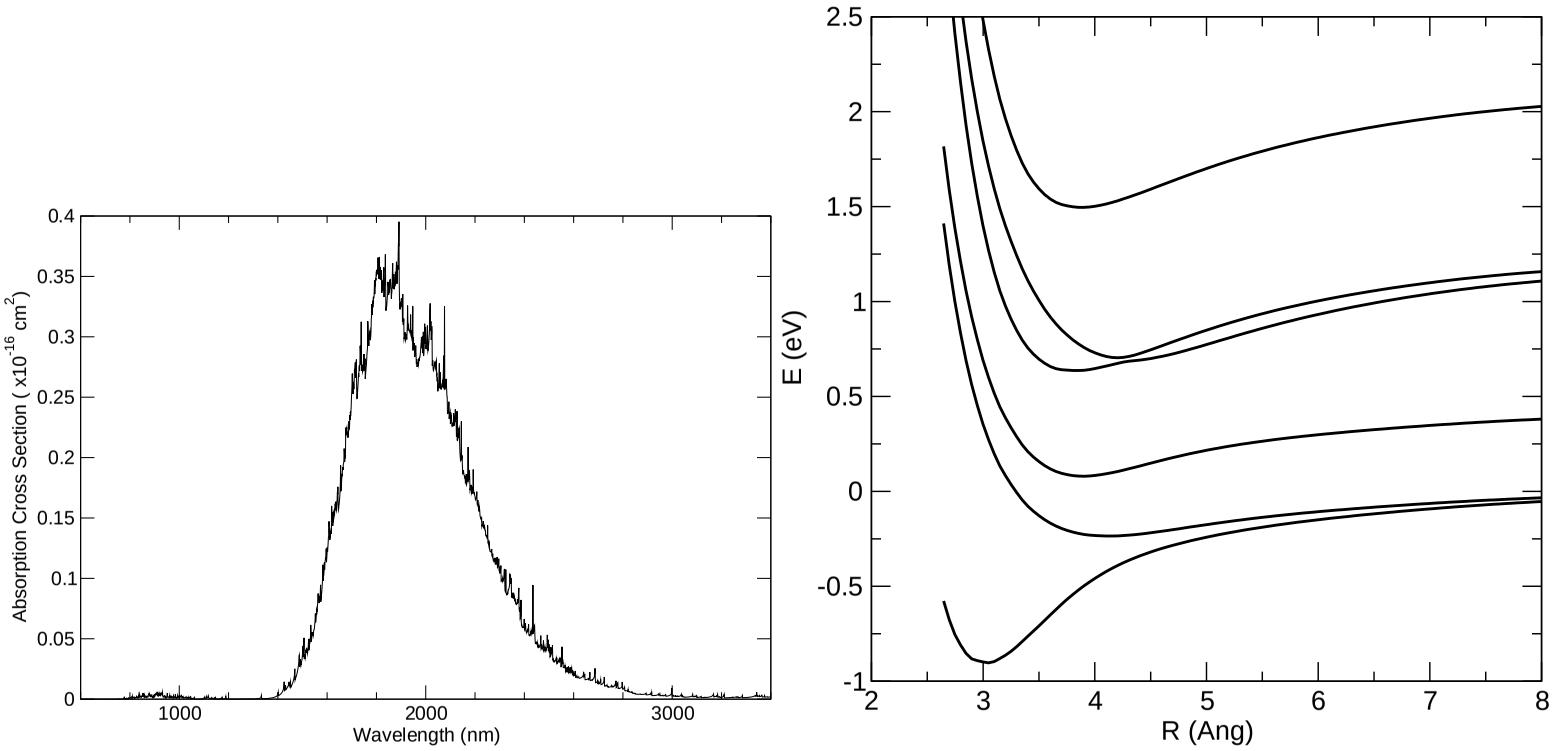

(a) (b)

Figure 6.3: (a) Simulated absorption spectrum for an $IBr^-(CO_2)_{14}$ trajectory trapped in the A' well on the $+\Delta\Phi$ side. (b) Potential energy surface for $IBr^-(CO_2)_{14}$ configuration that is trapped in the A' well.

in fact no real disagreement—the electronic relaxation is simply far too slow to be observers in the simulation. This situation is very similar to what we have explored for $IBr^-(CO_2)_n$ in Chapter 4.

The obvious first step would be to run long-time simulations in order to see if the ground-state recombination occurs eventually. Unfortunately, there are no time-resolved experiments on the recombination of $ICl^-(CO_2)_n$ due to the extremely low absorption cross-section for ICl^-, see Figure 2.11. Without these, it will take more trial-and-error with the long-time simulations to select the correct run-time. In $IBr^-(CO_2)_8$, we had the luxury of knowing that recombination did take place after 50 ps, albeit by at least 5 ns. Since the $Cl^- \cdots CO_2$ is such a strong attraction, it is entirely possible that the $ICl^-(CO_2)_5$ A' state might in fact harbor an even stronger well than that found in $IBr^-(CO_2)_8$. If the $IBr^-(CO_2)_n$ and $ICl^-(CO_2)_n$ ground-state recombination (GSR) processes were to have similar excited-state mechanics, we would expect to need to form a symmetric solvent configuration in order to reach the nonadiabatic transition geometry. The $ICl^-(CO_2)_n$ model predicts that $Cl^- \cdots CO_2$ is 100 meV stronger than the $I^- \cdots CO_2$. In this study, we have seen that making the $Br^- \cdots CO_2$ interaction about 20 meV larger, Figure 2.15, has had a dramatic effect on the GSR dynamics of $IBr^-(CO_2)_n$ in Section 4.7. Thus, the much larger $Cl^- \cdots CO_2$ interaction could necessitate 10-ns+ molecular dynamics (MD) simulations. Luckily, the advances in computer hardware make such a simulation quite possible at this time. We could then use the solvent-flow plots pioneered in $I_2^-(CO_2)_n$ simulations and used here with great success to more fully map out the solute-solvent concerted dynamics.

Bibliography

[1] A. Sanov and W. C. Lineberger, Phys. Chem. Chem. Phys. **6**, 2018 (2004).

[2] A. Sanov and W. C. Lineberger, Phys. Chem. Comm. **5**, 165 (2002).

[3] J. Franck and E. Rabinowitch, Trans. Faraday Soc. **30**, 120 (1934).

[4] J. Zimmerman and R. M. Noyes, J. Chem. Phys. **21**, 2086 (1950).

[5] F. W. Lampe and R. M. Noyes, J. Am. Chem. Soc. **76**, 2140 (1954).

[6] D. Booth and R. M. Noyes, J. Am. Chem. Soc. **82**, 1868 (1960).

[7] L. F. Meadows and R. M. Noyes, J. Am. Chem. Soc. **82**, 1872 (1960).

[8] T. Chuang, G. Hoffman, and K. Eisenthal, Chem. Phys. Lett. **25**, 201 (1974).

[9] D. J. Nesbitt and J. T. Hynes, J. Chem. Phys. **77**, 2130 (1982).

[10] A. L. Harris, J. K. Brown, and C. B. Harris, Ann. Rev. Phys. Chem. **39**, 341 (1988).

[11] M. L. Alexander, Ph.D. thesis, University of Colorado, 1987.

[12] M. Alexander, N. Levinger, M. Johnson, D. Ray, and W. C. Lineberger, J. Chem. Phys. **88**, 6200 (1988).

[13] N. E. Levinger, Ph.D. thesis, University of Colorado, 1990.

[14] J. Papanikolas, J. Gord, N. Levinger, D. Ray, V. Vorsa, and W. C. Lineberger, J. Phys. Chem. **95**, 8028 (1991).

[15] V. Vorsa, P. J. Campagnola, S. Nandi, M. Larsson, and W. C. Lineberger, J. Chem. Phys. **105**, 2298 (1996).

[16] V. Vorsa, S. Nandi, P. J. Campagnola, M. Larsson, and W. C. Lineberger, J. Chem. Phys. **106**, 1402 (1997).

[17] M. E. Nadal, S. Nandi, D. W. Boo, and W. C. Lineberger, J. Chem. Phys. (1998), to be submitted.

[18] S. Nandi, A. Sanov, N. Delaney, J. Faeder, R. Parson, and W. C. Lineberger, J. Phys. Chem. A **102**, 8827 (1998).

[19] A. Sanov, T. Sanford, S. Nandi, and W. C. Lineberger, J. Chem. Phys. **111**, 663 (1999).

[20] A. Sanov, J. Faeder, R. Parson, and W. C. Lineberger, Chem. Phys. Lett. **313**, 812 (1999).

[21] L. Perera and F. G. Amar, J. Chem. Phys. **90**, 7354 (1989).

[22] F. G. Amar and L. Perera, Z. Phys. D **20**, 173 (1991).

[23] J. Faeder, N. Delaney, P. Maslen, and R. Parson, Chem. Phys. Lett. **270**, 196 (1997).

[24] N. Delaney, J. Faeder, P. E. Maslen, and R. Parson, J. Phys. Chem. A **101**, 8147 (1997).

[25] J. Faeder and R. Parson, J. Chem. Phys. **108**, 3909 (1998).

[26] P. E. Maslen, J. Faeder, and R. Parson, Mol. Phys. **94**, 693 (1998).

[27] J. Faeder, N. Delaney, P. Maslen, and R. Parson, Chem. Phys. **239**, 525 (1998).

[28] B. M. Ladanyi and R. Parson, J. Chem. Phys. **107**, 9326 (1997).

[29] R. Parson, J. Faeder, and N. Delaney, J. Phys. Chem. A **104**, 9653 (2000).

[30] V. S. Batista and D. F. Coker, J. Chem. Phys. **105**, 4033 (1996).

[31] V. S. Batista and D. F. Coker, J. Chem. Phys. **106**, 7102 (1997).

[32] V. S. Batista and D. F. Coker, J. Chem. Phys. **106**, 6923 (1997).

[33] C. Margulis and D. F. Coker, J. Chem. Phys. **110**, 5677 (1999).

[34] I. Last and T. F. George, J. Chem. Phys. **86**, 3787 (1987).

[35] P. E. Maslen, J. M. Papanikolas, J. Faeder, R. Parson, and S. V. ONeil, J. Chem. Phys. **101**, 5731 (1994).

[36] P. E. Maslen, J. Faeder, and R. Parson, Chem. Phys. Lett. **263**, 63 (1996).

[37] J. Faeder, Ph.D. thesis, University of Colorado, 1998.

[38] A. J. Stone, The Theory of Intermolecular Forces (Oxford, New York, 1996).

[39] S. Hammes-Schiffer and J. C. Tully, J. Chem. Phys. **103**, 8528 (1995).

[40] N. Delaney, J. Faeder, and R. Parson, J. Chem. Phys. **111**, 651 (1999).

[41] N. Delaney, Ph.D. thesis, University of Colorado, 1999.

[42] R. A. Marcus, Ann. Rev. Phys. Chem. **15**, 155 (1964).

[43] D. Ray, N. Levinger, J. Papanikolas, and W. C. Lineberger, J. Chem. Phys. **91**, 6533 (1989).

[44] J. Papanikolas, V. Vorsa, M. Nadal, P. Campagnola, J. Gord, and W. C. Lineberger, J. Chem. Phys. **97**, 7002 (1992).

[45] J. Papanikolas, V. Vorsa, M. Nadal, P. Campagnola, H. Buchenau, and W. C. Lineberger, J. Chem. Phys. **99**, 8733 (1993).

[46] M. Nadal, Ph.D. thesis, University of Colorado, 1996.

[47] J. M. Papanikolas, Ph.D. thesis, University of Colorado, 1994.

[48] V. Vorsa, Ph.D. thesis, University of Colorado, 1996.

[49] A. E. Johnson, N. E. Levinger, and P. F. Barbara, J. Phys. Chem. **96**, 7841 (1992).

[50] D. A. V. Kliner, J. C. Alfano, and P. F. Barbara, J. Chem. Phys. **98**, 5375 (1993).

[51] J. Alfano, Y. Kimura, P. K. Walhout, and P. F. Barbara, Chem. Phys. **175**, 147 (1993).

[52] P. K. Walhout, J. C. Alfano, K. A. M. Thakur, and P. F. Barbara, J. Phys. Chem. **99**, 7568 (1995).

[53] D. W. Arnold, S. E. Bradforth, E. H. Kim, and D. M. Neumark, J. Chem. Phys. **102**, 3493 (1995).

[54] D. W. Arnold, S. E. Bradforth, E. H. Kim, and D. M. Neumark, J. Chem. Phys. **102**, 3510 (1995).

[55] I. Yourshaw, Y. Zhao, and D. M. Neumark, J. Chem. Phys. **105**, 351 (1996).

[56] B. J. Greenblatt, M. T. Zanni, and D. M. Neumark, Chem. Phys. Lett. **258**, 523 (1996).

[57] B. J. Greenblatt, M. T. Zanni, and D. M. Neumark, Science **276**, 1675 (1997).

[58] B. J. Greenblatt, M. T. Zanni, and D. M. Neumark, Faraday Discuss. **108**, 101 (1997).

[59] M. T. Zanni, T. R. Taylor, B. J. Greenblatt, B. Soep, and D. M. Neumark, J. Chem. Phys. **107**, 7613 (1997).

[60] K. R. Asmis, T. R. Taylor, C. S. Xu, and D. M. Neumark, J. Chem. Phys. **109**, (1998).

[61] M. T. Zanni, V. S. Batista, B. J. Greenblatt, W. Miller, and D. M. Neumark, J. Chem. Phys. **110**, 3748 (1999).

[62] B. J. Greenblatt, M. T. Zanni, and D. M. Neumark, J. Chem. Phys. **111**, 10566 (1999).

[63] V. S. Batista, M. T. Zanni, B. J. Greenblatt, D. M. Neumark, and W. Miller, J. Chem. Phys. **110**, 3736 (1999).

[64] M. T. Zanni, A. V. Davis, C. Frischkorn, M. Elhanine, and D. M. Neumark, J. Chem. Phys. **112**, 8847 (2000).

[65] B. J. Greenblatt, M. T. Zanni, and D. M. Neumark, J. Chem. Phys. **112**, 601 (2000).

[66] M. T. Zanni, A. V. Davis, C. Frischkorn, M. Elhanine, and D. M. Neumark, J. Chem. Phys. **113**, 8854 (2000).

[67] A. V. Davis, M. T. Zanni, C. Frischkorn, M. Elhanine, and D. M. Neumark, J. Elec. Spectro. Rel. Phen. **112**, 221 (2000).

[68] D. M. Neumark, Ann. Rev. Phys. Chem. **52**, 255 (2001).

[69] A. V. Davis, R. Wester, A. E. Bragg, and D. M. Neumark, J. Chem. Phys. **117**, 4282 (2002).

[70] R. Wester, A. V. Davis, A. E. Bragg, and D. M. Neumark, Phys. Rev. A **65**, 051201(R) (2002).

[71] H. Gomez, T. R. Taylor, and D. M. Neumark, J. Chem. Phys. **117**, 8181 (2002).

[72] A. V. Davis, R. Wester, A. E. Bragg, and D. M. Neumark, J. Chem. Phys. **119**, 2020 (2003).

[73] A. V. Davis, R. Wester, A. E. Bragg, and D. M. Neumark, J. Chem. Phys. **118**, 999 (2003).

[74] A. Stolow, A. E. Bragg, and D. M. Neumark, Chem. Rev. **104**, 1719 (2004).

[75] N. Delaney, J. Faeder, and R. Parson, J. Chem. Phys. **111**, 452 (1999).

[76] M. E. Nadal, P. D. Kleiber, and W. C. Lineberger, J. Chem. Phys. **105**, 504 (1996).

[77] T. J. Sanford, Ph.D. thesis, University of Colorado, 2004.

[78] T. Sanford, D. Andrews, J. Rathbone, M. Taylor, F. Muntean, M. Thompson, A. B. McCoy, R. Parson, and W. C. Lineberger, Faraday Discuss. **127**, 383 (2004).

[79] T. Sanford, S.-Y. Han, M. A. Thompson, R. Parson, and W. C. Lineberger, J. Chem. Phys. **122**, 054307 (2005).

[80] V. Dribinski, J. Barbera, J. P. Martin, A. Svendsen, M. A. Thompson, R. Parson, and W. C. Lineberger, J. Chem. Phys. **125**, 133405 (2006).

[81] A. J. Stone, Chem. Phys. Lett. **83**, 233 (1981).

[82] A. J. Stone and M. Alderton, Mol. Phys. **56**, 1047 (1985).

[83] A. J. Stone, Chem. Phys. Lett. **155**, 102 (1989).

[84] A. J. Stone, Chem. Phys. Lett. **155**, 111 (1989).

[85] C. A. Hunter, J. K. M. Sanders, and A. J. Stone, Chem. Phys. **133**, 395 (1989).

[86] S. L. Price, A. J. Stone, and M. Alderton, Mol. Phys. **52**, 987 (1984).

[87] A. J. Stone and R. J. A. Tough, Chem. Phys. Lett. **110**, 123 (1984).

[88] L. Greengard, The Rapid Evaluation of Potential Fields in Particle Systems (MIT Press, Cambridge, MA, 1988).

[89] L. Greengard and V. Rokhlin, J. Comput. Phys. **73**, 325 (1987).

[90] C. A. White and M. Head-Gordon, J. Chem. Phys. **101**, 6593 (1994).

[91] C. A. White, B. G. Johnson, P. M. W. Gill, and M. Head-Gordon, Chem. Phys. Lett. **230**, 8 (1994).

[92] L. Verlet, Phys. Rev. **159**, 98 (1967).

[93] J. C. Tully, J. Chem. Phys. **93**, 1061 (1990).

[94] B. J. Schwartz, E. R. Bittner, O. V. Prezhdo, and P. J. Rossky, J. Chem. Phys. **104**, 5942 (1996).

[95] W. H. Press, S. A. Teukolsky, W. T. Vetterling, and B. P. Flannery, Numerical Recipes in C: The Art of Scientific Computing, 2nd ed. (Cambridge University Press, New York, 1992).

[96] H.-J. Werner, P. J. Knowles, R. Lindh, M. Schütz, P. Celani, T. Korona, F. R. Manby, G. Rauhut, R. D. Amos, A. Bernhardsson, A. Berning, D. L. Cooper, M. J. O. Deegan, A. J. Dobbyn, F. Eckert, C. Hampel, G. Hetzer, A. W. Lloyd, S. J. McNicholas, W. Meyer, M. E. Mura, A. Nicklass, P. Palmieri, R. Pitzer, U. Schumann, H. Stoll, A. J. Stone, R. Tarroni, and T. Thorsteinsson, MOLPRO, version 2002.6, a package of ab initio programs, 2003, see http://www.molpro.net.

[97] H.-J. Werner, P. J. Knowles, J. Almlöf, R. D. Amos, M. J. O. Deegan, S. T. Elbert, C. Hampel, W. Meyer, K. Peterson, R. Pitzer, A. Stone, and P. R. Taylor, Molpro, version 94.3, a package of ab initio programs, 1994.

[98] H. A. Kramers, Proc. Amsterdam Acad. **33**, 959 (1930).

[99] M. J. Klein, Am. J. Phys. **20**, 65 (1952).

[100] H. Stoll, B. Metz, and M. Dolg, J. Comput. Chem. **23**, 767 (2002).

[101] H. Stoll, private communication.

[102] K. A. Peterson, D. Figgin, E. Goll, H. Stoll, and M. Dolg, J. Chem. Phys. **119**, 11113 (2003).

[103] A. J. Sadlej, Theoretica Chimica Acta **79**, 123 (1991).

[104] A. J. Sadlej, Theoretica Chimica Acta **81**, 339 (1992).

[105] H.-J. Werner and P. J. Knowles, J. Chem. Phys. **89**, 5803 (1988).

[106] P. J. Knowles and H.-J. Werner, Chem. Phys. Lett. **145**, 514 (1988).

[107] P. J. Knowles and H.-J. Werner, Theor. Chim. Acta **84**, 95 (1992).

[108] J. A. Pople, R. Seeger, and R. Krishnan, Int. J. Quantum Chem. **S11**, 149 (1977).

[109] C. E. Moore, Atomic Energy Levels, Vol. 35 of National Standards Reference Data Series, 2nd ed. (National Bureau of Standards, Washington, DC, 1971).

[110] T. M. Miller, in Electron Affinities, 73rd ed., edited by D. R. Lide (Chemical Rubber, Boca Raton, 1993).

[111] R. Calvi and W. C. Lineberger, private communication.

[112] R. J. Le Roy, LEVEL 7.7: A Computer Program for Solving the Radial Schrödinger Equation for Bound and Quasibound Levels, University of Waterloo Chemical Physics Research Report CP-661, 2005, see the "Computer Programs" link at http://leroy.uwaterloo.ca.

[113] R. Mabbs, K. Pichugin, and A. Sanov, J. Chem. Phys. **122**, 174305 (2005).

[114] E. Wrede, S. Laubach, S. Schulenburg, A. Brown, E. R. Wouters, A. J. Orr-Ewing, and M. N. R. Ashfold, J. Chem. Phys. **114**, 2629 (2001).

[115] C. G. Gray and K. E. Gubbins, Theory of Molecular Fluids (Clarendon, Oxford, 1984), Vol. 1.

[116] C. S. Murthy, S. F. O'Shea, and I. R. McDonald, Mol. Phys. **50**, 531 (1983).

[117] Y. Zhao, C. C. Arnold, and D. M. Neumark, J. Chem. Soc. Faraday Trans. **89**, 1449 (1993).

[118] R. A. Kendall, T. H. Dunning, Jr., and R. J. Harrison, J. Chem. Phys. **96**, 6796 (1992).

[119] T. H. Dunning, Jr., J. Chem. Phys. **90**, 1007 (1989).

[120] G. Herzberg, Molecular Spectra and Molecular Structure. I. Spectra of Diatomic Molecules, 2nd ed. (Van Nostrand, New York, 1950).

[121] E. J. Heller, J. Chem. Phys. **68**, 2066 (1978).

[122] P. C. Engelking, J. Chem. Phys. **87**, 936 (1987).

[123] J. Martin, J. Darr, and W. C. Lineberger, private communication.

[124] J. I. Steinfeld, J. S. Francisco, and W. L. Hase, Chemical Dynamics and Kinetics, 2nd ed. (Prentice-Hall, Inc., Upper Saddle River, NJ, 1998).

[125] M. D. Newton and N. Sutin, Ann. Rev. Phys. Chem. **35**, 437 (1984).

[126] G. C. Schatz and M. A. Ratner, in Quantum Mechanics in Chemistry (Prentice Hall, Englewood Cliffs, 1993), Chap. 10.

[127] J. M. Papanikolas, P. E. Maslen, and R. Parson, J. Chem. Phys. **102**, 2452 (1995).

[128] I. Suzuki, J. Mol. Spec. **25**, 479 (1968).

[129] D. Husain and R. J. Donovan, in Advances in Photochemistry, edited by J. N. Pitts, Jr, G. S. Hammond, and W. A. Noyes, Jr (Wiley-Interscience, New York, 1971), Vol. 8, pp. 1–75.

[130] R. O. Johnson, G. P. Perram, and W. B. Roh, J. Chem. Phys. **104**, 7052 (1996).

[131] H. Reisler and C. Wittig, J. Chem. Phys. **69**, 3729 (1978).

[132] A. Hariri and C. Wittig, J. Chem. Phys. **67**, 4454 (1977).

[133] A. J. Sedlacek, R. E. Weston, and G. W. Flynn, J. Chem. Phys. **93**, 2812 (1990).

[134] R. O. Johnson, S. J. Karis, G. P. Perram, and W. B. Roh, Appl. Phys. B **66**, 411 (1998).

[135] A. B. Peterson, C. Wittig, and S. R. Leone, Appl. Phys. Lett. **27**, 305 (1975).

[136] A. B. Peterson, C. Wittig, and S. R. Leone, J. Appl. Phys. **47**, 1051 (1976).

[137] R. L. Pastel, G. D. Hager, H. C. Miller, and S. R. Leone, Chem. Phys. Lett. **183**, 565 (1991).

[138] J. B. Kim, P. G. Wenthold, and W. C. Lineberger, J. Chem. Phys. **108**, 830 (1998).

[139] F. Muntean, M. S. Taylor, A. B. Mccoy, and W. C. Lineberger, J. Chem. Phys. **121**, 5676 (2004).

[140] G. J. Rathbone, T. Sanford, D. Andrews, and W. C. Lineberger, Chem. Phys. Lett. **401**, 570 (2005).

[141] A. Sanov, T. Sanford, L. J. Butler, J. Vala, R. Kosloff, and W. C. Lineberger, J. Phys. Chem. A **103**, 10244 (1999).

[142] R. L. Schwartz, G. E. Davico, and W. C. Lineberger, J. Electron Spectrosc. Relat. Phenom. (2000).

[143] R. L. Schwartz, G. E. Davico, J. B. Kim, and C. W. Lineberger, J. Chem. Phys. **112**, 4966 (2000).

[144] M. S. Taylor, F. Muntean, W. C. Lineberger, and A. B. Mccoy, J. Chem. Phys. **121**, 5688 (2004).

[145] M. S. Taylor, J. Barbera, C. P. Schulz, F. Muntean, A. B. Mccoy, and W. C. Lineberger, J. Chem. Phys. **122**, 054310 (2005).

[146] E. Surber and A. Sanov, J. Chem. Phys. **116**, 5921 (2002).

[147] R. Mabbs, E. Surber, and A. Sanov, Analyst **128**, 765 (2003).

[148] E. Surber and A. Sanov, J. Chem. Phys. **118**, 9192 (2003).

[149] R. Mabbs, K. Pichugin, E. Surber, and A. Sanov, J. Chem. Phys. **121**, 265 (2004).

[150] R. Mabbs, E. Surber, L. Velarde, and A. Sanov, J. Chem. Phys. **120**, 5148 (2004).

[151] E. Surber, R. Mabbs, T. Habteyes, and A. Sanov, J. Phys. Chem. A **109**, 4452 (2005).

[152] R. Mabbs, E. Surber, and A. Sanov, J. Chem. Phys. **122**, 054308 (2005).

[153] F. A. Akin, L. K. Schirra, and A. Sanov, J. Phys. Chem. A **110**, 8031 (2006).

[154] T. Habteyes, L. Velarde, and A. Sanov, Chem. Phys. Lett. **424**, 268 (2006).

[155] L. Velarde, T. Habteyes, and A. Sanov, J. Chem. Phys. **125**, 114303 (2006).

[156] A. Osterwalder, M. J. Nee, J. Zhou, and D. M. Neumark, J. Chem. Phys. **121**, 6317 (2004).

[157] A. A. Hoops, J. R. Gascooke, A. E. Faulhaber, K. E. Kautzman, and D. M. Neumark, Chem. Phys. Lett. **374**, 235 (2003).

[158] W. G. Brown, Phys. Rev. **42**, 355 (1932).

[159] T. Yukiya, N. Nishimiya, and M. Suzuki, J. Mol. Spec. **214**, 132 (2002).

[160] D. T. Radzykewycz, C. D. Littlejohn, M. B. Carter, J. O. Clevenger, J. H. Purvis, and J. Tellinghuisen, J. Mol. Spec. **166**, 287 (1994).

[161] W. H. Eberhardt and W. Sullivan, J. Mol. Spec. **70**, 270 (1978).

[162] R. S. Mulliken, Phys. Rev. **61**, 277 (1942).

[163] R. S. Mulliken, J. Chem. Phys. **55**, 288 (1971).

[164] S. Patchkovskii, Phys. Chem. Chem. Phys. **8**, 926 (2006).

Appendix A

List of Acronyms

BO	Born-Oppenheimer
CASSCF	complete active-space self-consistent field
CC	coupled cluster
CCSD	coupled cluster with single and double excitations
CCSD(T)	coupled cluster with single, double, and iterative triple excitations
CI	configuration interaction
CISD	singles-and-doubles configuration interaction
CPP	core polarization potential
CSF	configuration state function
DM	distributed multipole
DMA	distributed multipole analysis
EA	electron affinity
ECP	effective core potential
eKE	electron kinetic energy
FWHM	full-width half-maximum
GSR	ground-state recombination
HF	Hartree-Fock
icMRCI	internally-contracted multireference configuration interaction
IR	infrared
KER	kinetic energy release
LCAO-MO	linear combination of atomic orbitals-molecular orbitals
LJ	Lennard-Jones

MCDHF	multiconfigurational Dirac-Hartree-Fock
MCSCF	multiconfigurational self-consistent field
MD	molecular dynamics
MFP	Maslen, Faeder, and Parson
MRCI	multireference configuration interaction
MRCISD	singles-and-doubles multireference configuration interaction
MRQDPT2	multireference quasi-degenerate second-order perturbation
NACME	nonadiabatic coupling matrix element
PE	potential energy
PES	potential energy surface
SA-MCSCF	state-averaged multiconfigurational self-consistent field
SA-CASSCF	state-averaged complete active-space self-consistent field
SBE	sequential binding energy
SCF	self-consistent field
SO	spin-orbit
SOQ	spin-orbit quenching
SOQ-CT	spin-orbit quenching via charge transfer
SOQ-VD	spin-orbit quenching via vibrational deactivation
TDSE	time-dependent Schrödinger equation
UV	ultraviolet
ZPE	zero-point energy

Appendix B

Table of Ground-State Recombination Dynamics

No. of CO_2	Duration (ps)	No. of Traj.	No. of GSR Product	Extrap. GSR Product[a]	τ_{sim} (ps)	τ^{b}_{expt} (ps)
5	20	1796	711	—	3.43 ± 0.06	12 ± 0.5
6	20	1000	440	—	6.97 ± 0.18	30 ± 5
7	200	237	155	—	33.4 ± 0.7	140 ± 20
8	2000	100	75	—	498 ± 23	900 ± 100
9	4000	100	54	76	3620 ± 60^{c}	—
10	4000	90	44	70	4150 ± 120^{c}	900 ± 100
11	3000	100	74	87	2540 ± 60^{c}	—
12	300	223	181	—	61.8 ± 2.1	$\approx 10^{d}$
13	300	250	199	—	34.1 ± 1.6	—
14	3000	100	96	—	40.9 ± 1.9 1500 ± 440	—
15	150	100	99	—	32.7 ± 2.8	—
16	150	100	97	—	52.0 ± 3.1	—

[a] A_0 in Eqn. 4.1
[b] Ref. 80
[c] Lower bound to time constant
[d] Unreported. Ref. 123

Table B.1: Ground-state recombination (GSR) recovery dynamics of near-IR (790 nm) photodissociation of $IBr^{-}(CO_2)_n$. All simulations performed with 1.0 fs time step. A trajectory was considered dissociated once I-Br bond length reached 40 a_0 or recombined after 20 crossings of the ground state well.